HOLLOW CONDENSATES, TOPOLOGICAL LADDERS AND QUASIPERIODIC CHAINS

BY

KARMELA PADAVIC-CALLAGHAN

DISSERTATION

Submitted in partial fulfillment of the requirements
for the degree of Doctor of Philosophy in Physics
in the Graduate College of the
University of Illinois at Urbana-Champaign, 2020

Urbana, Illinois

Doctoral Committee:

Professor Michael Stone, Chair
Professor Smitha Vishveshwara, Director of Research
Assistant Professor Bryce Gadway
Professor Alexey Bezryadin

Abstract

This thesis presents three distinct topics pertaining to the intesection of condensed matter and atomic, molecular and optical (AMO) physics. We theoretically address the physics of hollow Bose-Einstein condensates and the behavior of vortices within them then discuss localization-delocalization physics of one-dimensional quasiperiodic models, and end by focusing on the physics of localized edge modes and topological phases in quasi-one-dimensional ladder models. For all three topics we maintain a focus on experimentally accessible, physically realistic systems and explicitly discuss experimental implementations of our work or its implications for future experiments.

First, we study shell-shaped Bose-Einstein condensates (BECs). This work is motivated by experiments aboard the International Space Station (ISS) in the Cold Atom Laboratory (CAL) where hollow condensates are being engineered [1]. Additionally, shell-like structures of superfluids form in interiors of neutron stars and with ultracold bosons in three-dimensional optical lattices. Our work serves as a theoretical parallel to CAL studies and a step towards understanding these more complex systems. We model hollow BECs as confined by a trapping potential that allows for transitions between fully-filled and hollow geometries. Our study is the first to consider such a real-space topological transition. We find that collective mode frequencies of spherically symmetric condensates show non-monotonic features at the hollowing-out point. We further determine that for fully hollow spherically symetric BECs effects of Earth's gravity are very destructive and consequently focus on microgravity environments. Finally, we study quantized vortices on hollow condensate shells and their response to system rotation. Vortex behavior is interesting as a building block for studies of more complicated quantum fluid equilibration processes and physics of rotating neutron stars interiors. Condensate shell's closed and hollow geometry constrains possible vortex configurations. We find that those configurations are stable only for high rotation rates. Further, we determine that vortex lines nucleate at lower rotation rates for hollow condensates than those that are fully-filled.

Second, we analyze the effects of quasiperiodicity in one-dimensional systems. Distinct from truly disordered systems, these models exhibit delocalization in contrast to well-known facts about Anderson localization [2]. We study the famous Aubry-Andre-Harper (AAH) model, a one-dimensional tight-binding model

that localizes only for sufficiently strong quasiperiodic on-site modulation and is equivalent to the Hofstadter problem at its critical point. Generalizations of the AAH model have been studied numerically and a generalized self-dual AAH model has been proposed and analytically analyzed by S. Ganeshan, J. Pixley and S. Das Sarma (GPD) in Ref. [3]. For extended and generalized AAH models the appearance of a mobility edge i.e. an energy cut-off dictating which wavefunctions undergo the localization-delocalization transition is expected. For the GPD model this critical energy has been theoretically determined. We employ transfer matrices to study one-dimensional quasiperiodic systems. Transfer matrices characterize localization physics through Lyapunov exponents. The symplectic nature of transfer matrices allows us to represent them as points on a torus. We then obtain information about wavefunctions of the system by studying toroidal curves corresponding to transfer matrix products. Toroidal curves for localized, delocalized and critical wavefunctions are distinct, demonstrating a geometrical characterization of localization physics. Applying the transfer matrix method to AAH-like models, we formulate a geometrical picture that captures the emergence of the mobility edge. Additionally, we connect with experimental findings concerning a realization of the GPD model in an interacting ultracold atomic system.

Third, we consider a generalization of the Su-Schrieffer-Heeger (SSH) model. The SSH chain is a one-dimensional tight-binding model that can host localized bound states at its ends. It is celebrated as the simplest model having topological properties captured by invariants calculated from its band-structure. We study two coupled SSH chains i.e. the SSH ladder. The SSH ladder has a complex phase diagram determined by inter-chain and intra-chain couplings. We find three distinct phases: a topological phase hosting localized zero energy modes, a topologically trivial phase having no edge modes and a phase akin to a weak topological insulator where edge modes are not robust. The topological phase of the SSH ladder is analogous to the Kitaev chain, which is known to support localized Majorana fermion end modes. Bound states of the SSH ladder having the same spatial wavefunction profiles as these Majorana end modes are Dirac fermions or bosons. The SSH ladder is consequently more suited for experimental observation than the Kitaev chain. For quasiperiodic variations of the inter-chain coupling, the SSH ladder topological phase diagram reproduces Hofstadter's butterfly pattern. This system is thus a candidate for experimental observation of the famous fractal. We discuss one possible experimental setup for realizing the SSH ladder in its Kitaev chain-like phase in a mechanical meta-material system. This approach could also be used to experimentally study the Hofstadter butterfly in the future.

Presented together, these three topics illustrate the richness of the intersection of condensed matter and AMO physics and the many exciting prospects of theoretical work in the realm of the former combining with experimental advances within the latter.

To Mom, Dad and BT.

Acknowledgments

I wrote one of my college admissions essays about the first physics class I had ever taken. I described what I learned in that class – that the real world can be modeled through mathematical equations – as inspiration for every piece of work I had undertaken afterwards. The tie between my junior-in-high-school self, having just moved to a far away foreign country while my family remained in Croatia, and physics was so strong that I wanted high-powered admissions officers to judge me based on those first few moments of amazent with it that I had experienced in the seventh grade. In other words, for more than a decade I have wanted much else other than to be a physicist and do physics. This thesis is a culmination of that desire and there are many who have made it possible for me to grow into the physicist I decided I would become all the way back then.

First and foremost, my gratitude goes to Prof. Smitha Vishveshwara who has advised, mentored and guided me since my first day in Urbana-Champaign. The norm within her group has always been to dream big, to chase odd topics whenever we really cared for them, to never say no to an unconventional idea and always work in good faith, with a cheery attitude and lots of optimism. In the early years of my doctoral work, this was very valuable to me. Having worked with Prof. Vishveshawara on many outreach projects involving the intersection of physics and the arts, I will also always appreciate her ability to wear many hats, play many roles (sometimes quite literally) and pull it all off with a smile. I am thankful for her showing me that this is who a physicst can be in addition to all the academic excellence she has corralled my way.

Regardless of friendly attitudes and long-dreamed dreams, graduate school has been a long and challenging process, full of self-discovery and sometimes painful growth along all axes of my being a person. I do not think I would have been able to take this all on without the endless emotional and practical support from my family and spouse. As they have all lived far away from me for the vast majority of my time in Urbana-Champaign, even just the endless conversations and infinite text-message chains have meant a world to me. I have traveled a tremendous amount in the past six years and my husband's willingness to tag along or take his own doctoral work on trains, buses and planes has been immensely helpful. Working on our degrees at the same time has so often been both inspiring and comforting. (*Bennett, you are the true MVP*

of this endeavor.)

Over the years I have had many great teachers and collaborators. In this vein, I owe thanks to Profs. B. Gadway, E. Fradkin, R. Leigh, T. Hughes and M. Stone at UIUC and Profs. C. Prodan at NJIT, C. Lannert at Smith College, N. Lundblad at Bates College, D. Sen at IIS, Dr. Kuei Sun at Univeristy of Texas and Dr. Wade DeGottardi. Especially I want to thank the members of my thesis committe for devoting some of their time to my work. I have also been inspired and humbled by many discussions with my group-mates Varsha Subrahmanyan and Suraj S. Hegde. I mentored Varsha in her first year of graduate school and have always been grateful for the coincidence of her subsequently joining the same research group – I have always been amazed by her work as a physicist and her curiosity and kindness as a person. I fondly remember a spring semester in which we attended a comic book convention together, and our many lunches at the Red Herring. Suraj, on the other hand, has been something of an informal mentor to me for years and truly showed me the ropes on so much of the work presented below. Our shared interest in cooking (his sambhar remains legendary) and yoga was just an added bonus. I hope that my influence on younger members of our group, including laying out this thesis in what I hope to be an easy-to-read manner, will be at least partly as positive as Suraj's influence has been on me. Over the last year, I have also had a chance to collaborate with F. Alex An and found this work to be fun and inspiring. I hope we can both carry the good spirit of our meetings into our respective future work.

Finally, I want to loudly and boldy acknowledge all of my collabrators when it comes to mentoring, diveristy advocacy and labor organizing efforts I have taken part in at UIUC over the years. Co-leading Illinois GPS, co-founding the retreat for Women and Gender Minorities in Physics and Astronomy, consulting for the Access Network and taking various roles within the leadership of the Graduate Employee Organization have all been important experiences and bolstered my faith in the academic and scientific communities being on a constant path of self-improvement. There are too many incredible graduate students who volunteered their precious time and energy to these efforts to fit into this paragraph but Brianne, Gloria, Will, Eli, Luis, Cristina and Ryan are at the top of my list. I have also learned a tremendous amount from my many mentors in the Access Network and Joel, Gina, Ben and Chandra all deserve my thanks. In the grand scheme of things, the nearly six years I have spent in the Physics Department at UIUC are likely not much, but even over that short time-span, it feels as if the conversations have changed and ideas about diversity, equity and inclusion became more of staple of how we think about ourselves as a community of incredibly gifted individuals. This gives me lots of hope, and I will be leaving Urbana-Champaign knowing that it can only become a better place. Here, I wish all the best to Shubhang, Preetha, Devyn, Daniel, Anabel, Shraddha and all other amazing organizers that will keep this work going. Support of Prof. L. Cooper and Ms. V.

Wimmer were instrumental in all these efforts and I will always believe that we are all incredibly lucky to have them in our corner.

More than any other place in which I have lived by myself, Urbana-Champaign has been and felt like a home. I have cherished having small-town routines, shopping at the farmer's market, having favorite yoga teachers and sources of coffee that never failed me. It would be absurd to thank the whole city, but with every year I have been a little more convinced that it would have been impossible for me to complete the work presented below anywhere else.

Table of Contents

List of Figures

List of Abbreviations

AAH	Aubry-Andre Harper
AMO	atomic, molecular and optical
BEC	Bose-Einstein condensate
CAL	Cold Atoms Laboratory
GPD	Ganeshan, Pixley and Das Sarma
GP	Gross-Pitaevskii
ISS	International Space Station
MI	Mott insulator
SF	superfluid
SSH	Su-Schrieffer-Heeger
SPME	single-particle mobility edge

Chapter 1

Introduction

This thesis presents three separate theoretical studies aiming to answer three questions (1) How are hollow quantum objects different than those that are fully filled? (2) How are periodic systems having irrational period (i.e. quasiperiodic systems) different than those with a rational one? and (3) What physics results if a prototypical topological model – the Su-Schrieffer-Heeger (SSH) chain – is doubled?

While these three studies are distinct and self-contained, they are unified by being motivated by both simple theoretical concepts (eg. changes in physical topology, quasiperiodicity and localized edge modes) and recent advances in experimental physics. In that sense, this thesis aims to be an example of the richness of quantum phenomena and the diveristy of questions they give rise to as well as of the value of theory working in concert with experiments.

Part 1: Hollow Bose-Einstein condensates

Physics of BEC shells is relevant for a variety of systems. In ultracold atomic systems, condensate shells are expected in Bose-Fermi mixtures and in optical lattice systems where Mott-insulating regions confine layers of superfluid shells. In neutron stars, shells consisiting of superfluid and superconducting matter have been proposed as constituents of the stars' interior structures. Our work on shell-shaped BECs is a step towards understanding the physics of these rich systems. Below, we employ analytical solutions to the Gross-Pitaevskii equation within the hydrodynamic and Thomas-Fermi approximations, as well as its numerical solutions, to determine static and dynamic properties of filled and hollow spherically symmetric BECs. We consider the so-called bubble trap, currently employed in CAL experiments, that can confine a filled spherical BEC or a hollow three-dimensional BEC shell. Connecting with these experiments is of significant interest as its microgravity environment allows for more successful realizations of BEC shells than in terrestrial laboratories. Modeling different bubble trap regimes, we study the transition from a fully filled to a thin hollow condensate – a change in physical topology of the system and a crossover from three to two dimensions. Our work is a first comprehensive study of such a real space topological change.

Due to having a hollow core and an inner surface, BEC shells exhibit properties completely different from filled condensates. Most strikingly, collective mode frequency spectra have non-monotonic features across

the hollowing-out transition. These hollowing-out signatures are the physical outcome of the emerging inner surface. Our work hence suggest a non-destructive method for confirming the existence of this surface and the central hollow region. Further connecting with experimental concerns, we analyze the effects of gravity on condensate shells and determine critical experimental parameters for realizing three-dimensional (as opposed to disk-like) hollow BECs. We find that engineering these systems on Earth is not experimentally feasible at this time. Thus, our studies are related to experimental efforts in microgravity environments where condensate shells could be more stable. As such, our work contributes to a possible new direction for experiments centering quantum superfluid systems in novel geometries.

Extending our work on hollow BECs, we study emergence and behavior of point-vortices or vortex lines in rotating BEC shells having various thicknesses. Topological concerns constrain vortices to appear in pairs carrying opposite circulation for any closed and spherically symmetric BEC geometry. These vortex-antivortex pairs can lower the energy of the condensate by overlapping and effectively annihilating. We find that fast rotation in the very thin shell regime can prevent annihilation by pinning the vortex and the anti-vortex to the two poles of the condensate shell. For thicker shells, vortex lines are nucleated at lower rotation speeds than in the case of a fully-filled system. Examining the possibility of a bent vortex line we find that straight vortices aligned with the rotation axis are most stable and least energetically costly in rotating three-dimensional BEC shells. Here, we use the Gross-Pitaevskii equation and heavily base our analytical approach on literature on vortices in classical superfluids, potential flows and studies of defects on nematic shells. This work is a natural extension of considering systems with spherically symmetry, relates to extensive exprimental work on vortices in more anisotropic traps, and also serves as a starting point for analyses of more chaotic and turbulent superfluid flows. Further, it generalizes past work on two-dimensional, annular BECs. [8].

Part 2: Quasiperiodicity in one-dimension

The Aubry-Andere-Harper (AAH) model is a well studied example of a one-dimensional system having a quasiperiodic on-site modulation (in its tight-binding form). Unlike a truly disordered one-dimensional system, the AAH model undergoes a localization-delocalization transition as the strength of quasiperiodicity is increased. When generalized or extended to include long-ranged hoppings or multiple harmonic-like on-site terms, it also features mobility edges – critictical energies separating localized and delocalized states existing at the same quasiperiodicity strength. We use the transfer matrix formalism to develop a geometric picture of the localization-delocalization transition for AAH and AAH-like models.

Transfer matrices can characterize localization physics through Lyapunov exponents or the inverse localization length of the wavefunction. Due to their symplectic nature transfer matrices can be represented

as points on a torus. Products of such matrices then form toroidal curves related to eigenstates of the model. We examine such toroidal curves characterizing systems with known quasiperiodicity or disorder patterns as well as those stemming from some predetermined wavefunction forms. The aim of these studies is to construct a dictionary of curves for various localization regimes and wavefunctions of one-dimensonal tight-binding systems. To that end, we obtain distinct toroidal curves for localized, delocalized and critical regimes of the AAH model, demonstrating a geometrical characterization of localization physics. Further, we study the GPD model from Ref. [3] i.e. an AAH-like quasiperiodic one-dimensional model known to have mobility edges. Our geometrical representation of the transfer matrix method succesfully captures mobility edge physics. Finally, mobility edge physics has been probed in ultracold atomic experiments where nonlinear interactions between atoms play a non-negligible role. In collaboration with one such experiment in the group of Prof. Bryce Gadway at the University of llinois Urbana-Champaign (UIUC), we model the effect of interactions on the GPD model through numerical simulations. In concert with experimental observations, we find strong deviations from the single-particle, non-interacting predictions in that mobility edge shifts towards lower energy values.

Part 3: Topological ladder models

The Su-Schrieffer-Heeger (SSH) model is a prototypical example of a one-dimensional system supporting topological phases defined by zero energy states localized at its edges. Using the SSH chain as a building block, we study a ladder-like, quasi-one-dimensional system having rich toplogical properties. Experimentally most relevant, we show that two coupled SSH chains can act as an analog of the Kitaev chain, a topological superconductor model having Majorana end modes in its topological phases. In the case of the SSH ladder, these modes are Dirac fermions (or bosons) instead and therefore better suited for observation and direct measurements. Extending the SSH ladder model to quasiperiodic couplings, we suggested a new way for realizing the Hofstadter butterfly in experiments as a topological phase diagram.

When the SSH ladder is characterized by two alternating values of intra-chain couplings and its two legs are off-set by one unit cell, its topological phase hosts localized edge states having spatial wavefunction profiles equivalent to those of localized Majorana modes in the Kitaev chain. When the two legs are not off-set, localized modes on their edges hybridize and the system behaves as a weak topological insulator. For four distinct intra-chain couplings, the phase diagram is more complex than in the Kitaev-like regime, but topological phases still only support a single pair of dispersionless modes. For quasiperiodic inter-chain couplings in the Kitaev-like regime, the topological phase diagram is the Hofstadter butterfly. We suggest that the Hofstadter butterfly could then be imaged by detecting edge modes of the quasiperiodic SSH ladder: non-trivial parts of the topological phase diagram correspond to topological phases having localized edge

modes. To make this proposal more concrete, we discuss an experimental realization of the Kitaev-like SSH ladder in a meta-material system in collaboration with the group of Prof. Camelia Prodan group at the New Jersey Institute of Technology (NJIT). We show that the localized edge modes in the Kitaev-like regime of the SSH ladder can be observed in a system composed of precisely patterened mechanical spinners and outline a proposed experimental technique employed by collaborators.

Organization of Thesis

The organization of this thesis is as follows. Part I includes Chapters 2 to 8 and provides a detailed and exhaustive study of hollow Bose-Einstein condensates. In Chapter 2, we summarize some basics of the physics of Bose-Einstein condensation in trapped, interacting dilute gases. Similarly, in Chapter 3 we establish standard methods for studying vortices in BECs including a few illustrative examples in two-dimensional condensates and a discussion of vortex-vortex interactions. Chapter 4 introduces hollow BEC shells. Here, we explicitly address the experimental setup and capabilities of the CAL experiments in addition to enumerating other trapping potenials capable of hosting hollow, spherically symmetric condensates. We build on this setup in Chapter 5 by examining the limiting cases of the hollowing-out transition – the fully-filled sphere and the very thin shell condensate geometries – and address the transition between the two. Chapter 6 focuses on the physics of hollowing out in greater detail. In this Chapter, we differentiate between signatures of the transition in the spectra of radial and surface collective modes, respectively, and empahsize the importance of the details of the central density vanishing. We proceed to connect our work to realistic experimental systems in Chapter 7 and determine system parameters necessary for realizing condensate shells robust to the destructive effects of gravity. After determining that experiments in microgravity are the most feasible, we provide estimates for potentially observable collective mode frequencies and establish gravity-induced coupling of radial excitations. Chapter 8 closes Part I of this thesis by building on Chapter 3, discussing vortex physics on a nearly-two-dimensional condensate shell and the effects of rotating it. We also present preliminary results on physics of vortex lines in thicker (three-dimensional) BEC shells.

Part II of this thesis is devoted to studies of one-dimensional quasiperiodic systems. In Chapter 9 we introduce the transfer matrix method for representing localization-delocalization physics through curves on a torus and provide examples of its use. Chapter 10 narrows this technique to the AAH model and its generalization proposed in Ref. [3]. Additionally, we give an overview of the current state of mathematical and experimental research on AAH and AAH-like models and a heuristic argument for the difference in toroidal curves characterizing different regimes of these models. We end by again connecting to an experimental study in Chapter 11. The focus here is on a specific ultracold atomic realization of the GPD model. We describe the experimental technique used and relate observations to our numerical simulations. These simulations

capture the importance of inter-atomic interactions.

Part III of this thesis focuses on topological ladder models and consists of Chapters 12 and 13. In Chapter 12 we present a comprehensive study of the SSH ladder system utilizing transfer matrix methods. We obtain the topological phase diagram as a function of couplings within the SSH ladder, discuss the regime in which it is equivalent to the Kitaev chain and the case of quasiperiodic inter-chain hopping which results in a fractal topological phase diagram. Further, we use a Zak phase method to capture finite size effects relevant for experimental studies. In the same vein, we relate this work to realistic systems by outlining an implementation of the SSH ladder as a spinner ladder of reconfigurable, acoustic meta-materials in Chapter 13.

Part I: Hollow Bose-Einstein Condensates

Chapter 2

Trapped, Interacting Bose-Einstein Condensates

Following the work of Bose on photon statistics, in 1925 Einstein predicted that in a gas of non-interacting, massive bosons, below a certain temperature the lowest energy single-particle state would be macroscopically occupied. Such a state of ultracold bosons, with macroscopic occupation of the lowest quantum state, is known as a Bose-Einstein condensate. In this Chapter, we outline the basic physics of Bose-Einstein condensation of trapped, interacting dilute gases. In Section 2.1, we review the mathematical definition of BEC then proceed to discuss its ground state wavefunction in Section 2.2. Anticipating the discussion of collective modes of spherically symmetric hollow BECs later on, Section 2.3 focuses on the hydrodynamic model of elementary excitations of the condensate. We conclude this Chapter by briefly outlining some experimental studies related to hollow and other ultracold bosonic systems in Section 2.4.

2.1 Bose-Einstein Condensation

The possibility of Bose-Einstein condensation can be inferred from studying the Bose distribution function alone. Namely, for a gas of non-interacting bosons the mean occupation number of the single-particle state ν is given by

$$f^0(\epsilon_\nu) = \frac{1}{e^{(\epsilon_\nu - \mu)/kT} - 1}, \tag{2.1}$$

where ϵ_ν is the energy of the state. In this expression, μ the chemical potential introduced to reflect the fact that the total number of particles in the system N is conserved. It is defined so that N is equal to the sum of the occupancies of individual energy levels. At high temperatures the chemical potential is smaller than the energy of the lowest single-particle state $\epsilon_{\min}$. In this regime

$$f^0(\epsilon_\nu) \approx e^{-(\epsilon_\nu - \mu)/kT} \tag{2.2}$$

and the mean occupation of any state is much smaller than unity. As the temperature is lowered the chemical potential and the mean occupation number for a given ϵ_ν increase, but the chemical potential cannot exceed $\epsilon_{\min}$ as this would make the Bose distribution function of Eq. (2.1) negative (unphysical) when evaluated for the lowest single-particle state. The mean occupation number of any excited single-particle state therefore must be smaller than $1/(e^{(\epsilon_\nu-\epsilon_{\min})/kT}-1)$. Since the total number of particles in excited states is then less than N, the remaining particles must reside in the single-particle ground state, whose occupation number can be arbitrarily large – the system has a Bose-Einstein condensate!

Bose-Einstein condensation is therefore a thermodynamic phase transition driven by particle statistics. It is a direct consequence of the fundamental difference between fermions and bosons on the microscopic quantum level. A Bose gas undergoes Bose-Einstein condensation at some critical temperature T_c. Below the critical temperatureT_c normal gas particles coexist with condensed atoms. They are only separated in momentum space where all condensed particles are in the zero momentum single-particle state. As the temperature of the gas is lowered the fraction of particles in the condensed state increases.

In order to see that a true phase transition occurs, the heat capacity can be calculated as [9]

$$\frac{C(T)}{\alpha Nk}=\begin{cases}(\alpha+1)\frac{\zeta(\alpha+1)}{\zeta(\alpha)}\left(\frac{T}{T_c}\right)^{\alpha}, & T<T_c\\ 1+(\alpha-1)\frac{\zeta(\alpha)}{2^{\alpha+1}}\left(\frac{T_c}{T}\right)^{\alpha}, & T>T_c\end{cases} \tag{2.3}$$

where $\zeta(\alpha)$ is the Riemann zeta function and α is determined by the shape of the confining potential for the BEC (for a gas confined by rigid walls $\alpha=3/2$ and for a three-dimensional harmonic-oscillator trapping potential $\alpha=3$).

The heat capacity $C(T)$ has a cusp at $T=T_c$ which implies that the associated free energy is not analytic and the Bose gas undergoes a phase transition at this temperature. Critical temperature can be calculated by setting $N(T=T_c)=N_{\text{excited}}$ as when the total number of particles in the excited states N_{excited} is less than their total number N, macroscopic occupation of the lowest energy state takes place. In other words, we use the fact that T_c is the highest temperature at which the system has a BEC. The number of particles in excited states is

$$N_{\text{excited}}=\int_0^\infty d\epsilon g(\epsilon)f^0(\epsilon) \tag{2.4}$$

and takes on its greatest value for $\mu=0$. Here, $g(\epsilon)$ denotes the density of states. We then define the critical

temperature by writing

$$N = N_{\text{excited}}(T_c, \mu = 0) = \int_0^\infty d\epsilon g(\epsilon) \frac{1}{e^{\epsilon/k_B T_c} - 1}. \tag{2.5}$$

Following some algebra,

$$k_B T_c = \frac{N^{1/\alpha}}{[C_\alpha \Gamma(\alpha)\zeta(\alpha)]^{1/\alpha}} \tag{2.6}$$

where $\Gamma(\alpha)$ is the gamma function and C_α a constant determined from the density of states [9].

A crucial factor for calculating T_c, and the condensate's thermodynamic properties is the trapping potential that confines it and controls its shape. As an extreme example, Bose-Einstein condensation cannot occur for $T \neq 0$ in a two-dimensional box potential (having rigid walls) but a two-dimensional Bose gas can condense at non-zero temperature if the bosons are harmonically confined. For an isotropic harmonic potential, i.e. a filled sphere geometry, the critical temperature takes the form $T_c \approx 4.5(f/100\text{Hz})\text{N}^{1/3}$ nK. In typical experiments the frequencies used for harmonic traps are on the order of 100 Hz (or larger) so that for particle numbers N in the range from 10^4 to 10^8 the transition temperatures T_c lie in the range from 100 nK to 10 μK. In this thesis, we will most often reference experiments using ^{87}Rb atoms. For 10^5 ultracold ^{87}Rb atoms forming a filled sphere BEC (in a spherical box trap i.e. having very sharp boundaries compared to the harmonic confinement case) of radius 8.6 μm or a thick shell (in a spherical box trap having a sharp inner and outer boundary) having 14 μm and 15 μm (note that these two geometries have the same volume), critical temperature is on the order of $T_c \sim 200$ nK [10]. We note that that Eq. (2.6) is given for an idealized, non-interacting Bose gas with no internal degress of freedom (for instance, spin).

Further, critical temperature and overall properties of the condensate also depend on interatomic interactions and particle number. Concerning the latter, T_c decreases for finite N since ϵ_{min} is non-zero due to zero-point energy. The presence of interactions between atoms affects the shape of the condensate once it is released from the trap, plays a role in its dynamics and affects the structure of the ground state wavefunction. We address the issue of interatomic interactions in more detail below.

2.1.1 Scattering lengths and effective interactions

Two-body interactions between atoms dominate in ultracold atomic gases. Condensed atoms are in their electronic ground states so these interaction consist of scattering between different hyperfine states. From a theoretical point of view, studies of these gases are partly appealing because at low energies the effective interactions between condensed atoms can be characterized solely by the s-wave scattering length a_s.

This quantity can be accessed experimentally; the use of photoassociation spectroscopy and the study of Feschbach resonances, (instances when a low-energy bound state in one scattering channel modifies scattering in another channel) have made it possible to precisely measure scattering lengths. For polarized alkali atoms, often used in experiments, scattering lengths are typically two orders of magnitude larger than the size of the atom in question, mostly due to van der Waals interactions (van der Waals coefficients are large for alkali elements). The s-wave scattering length, a_s determines the shape of the scattered wavefunction when the simplest picture of inter-particle interactions is adopted. At very low energies, when it is sufficient to only consider s-wave scattering, the total scattering cross section is also determined purely by a_s as $\sigma = 8\pi a_s^2$. The numerical value of the scattering length depends on the details of the interatomic potential.

The scattering length, a_s, is additionally important for calculating effective interactions. Effective interactions are introduced in order to avoid having to evaluate short-range correlations between atoms whenever a many-body wave function is calculated. They describe long-wavelength, low-frequency degrees of freedom of the system when the interactions with the degrees of freedom at shorter wavelengths have been taken into account. This is justified since for most configurations of ultracold gas systems the many-body wave function varies slowly in space and typically the gases used in experiments are quite dilute so condensed atoms are rarely close together. More formally, to first order in the interaction the scattering length is given by the first order term in the Born series. Low-energy scattering behavior can then be obtained by using an effective two-body interaction U_{eff} in the Born approximation so that

$$\int d\mathbf{r} U_{\text{eff}}(\mathbf{r}) = \frac{4\pi\hbar^2 a_s}{m} \equiv U_0. \tag{2.7}$$

In coordinate space the effective interaction between two particles at positions $\mathbf{r}$ and $\mathbf{r}'$, respectively, may be taken to have the contact form $U_{\text{eff}}(\mathbf{r}, \mathbf{r}') = U_0\delta(\mathbf{r} - \mathbf{r}')$, where δ is the Dirac delta function. While a more detailed discussion of effective interactions is deferred to the references, the form of U_{eff} given in Eq. (2.7), with a positive value of a_s, is used extensively in this thesis.

2.2 Ground state of trapped bosons

We proceed to consider a Bose-Einstein condensate of interacting atoms and confined by an experimentally controllable trapping potential. Zero-temperature properties of the non-uniform Bose gas when the scattering length a_s is much smaller than the mean inter particle spacing are described by the Gross-Pitaevskii (GP) equation. This non-linear Schrodinger equation can be derived through a mean-field approach i.e. a Hartree approximation. Below, we outline this derivation then present a particular solution of the Gross-Pitaveskii

equation obtained by applying the Thomas-Fermi approximation.

2.2.1 The Gross-Pitaevskii equation

In the condensed state all bosons are in the same single-particle state $\phi(\mathbf{r})$. For the N-particle system then $\Psi(\mathbf{r}_1, \mathbf{r}_2, \ldots, \mathbf{r}_N) = \Pi_{i=1}^{N} \psi(\mathbf{r}_i) = \Pi_{i=1}^{N} N^{1/2} \phi(\mathbf{r}_i)$ normalized so that $\int d\mathbf{r} |\phi(\mathbf{r})|^2 = 1$. Given that the density of particles, $n(\mathbf{r})$, is typically equated to the amplitude of the wavefunction, this normalization condition amounts to the intuitive constraint $\int d\mathbf{r} n(\mathbf{r}) = N$. The effective Hamiltonian for the condensate reads

$$H = \sum_{i=1}^{N} \left[\frac{\mathbf{p}_i^2}{2m} + V(\mathbf{r}_i) \right] + U_0 \sum_{i<j} \delta(\mathbf{r}_i - \mathbf{r}_j) \tag{2.8}$$

where $V(\mathbf{r})$ is the external (trapping) potential. The expectation value of this Hamiltonian for $\Psi(\mathbf{r}_1, \mathbf{r}_2, \ldots, \mathbf{r}_N)$ is given by, neglecting terms of order $1/N$ (in typical experiments N is on the order of 10^5),

$$E[\psi(\mathbf{r})] = \int d\mathbf{r} \left[\frac{\hbar^2}{2m} |\nabla \psi(\mathbf{r})|^2 + V(\mathbf{r}) |\psi(\mathbf{r})|^2 + \frac{1}{2} U_0 |\psi(\mathbf{r})|^4 \right]. \tag{2.9}$$

where the last term accounts for interatomic interactions, as discussed above. We use integration by parts to obtain the first term in Eq. (2.8) while the interaction term has a pre-factor of $N(N-1)/2$ that counts the number of ways of making pairs of bosons. The latter is approximated as $N^2/2$ for large N.

The Gross-Pitaevski equation is derived by minimizing the energy of Eq. (2.9) with respect to independent variations of $\psi(\mathbf{r})$ and $\psi(\mathbf{r})^*$ subject to the normalization constraint on Ψ. This can be carried out by introducing the chemical potential μ as a Lagrange multiplier i.e. minimizing $E - \mu N$ at fixed μ. Consequently, the time-independent Gross-Pitaevskii equation reads

$$-\frac{\hbar^2}{2m} \nabla^2 \psi(\mathbf{r}) + V(\mathbf{r}) \psi(\mathbf{r}) + U_0 |\psi(\mathbf{r})|^2 \psi(\mathbf{r}) = \mu \psi(\mathbf{r}). \tag{2.10}$$

Solving the GP equation is equivalent to finding the ground state of the condensate.

2.2.2 The Thomas-Fermi Approximation

Before examining solutions of Eq. (2.10), it is worth estimating various energy scales for a BEC in a comonly used harmonic trap $V(r) = \frac{1}{2} m \omega_0^2 r^2$. If the spatial extent of the condensate cloud is $\sim R$, its potential energy will be on the order of $\sim m\omega_0^2 R^2/2$ and the kinetic energy term on the order of $\sim \hbar^2/2mR^2$. Here, according to the Heisenberg uncertainty principle, the typical momentum is $\sim \hbar/R$. We conclude that when interactions between condensed atoms are not important, BEC energy varies as $1/R^2$ for small R and R^2

for large R. The energy contribution due to interactions is on the order of $nU_0 \sim U_0 N/R^3$. Consequently, for repulsive interactions the minimum of the total energy is shifted to larger values of R so that for large values of Na_s the kinetic energy term, which scales as $1/R^2$, becomes less important. In the limit of strong interactions the kinetic energy contribution can therefore be neglected. We can then estimate the size of the condensate cloud as $R \sim S_l(Na_s/S_l)^{1/5}$ by minimizing the sum of potential and interaction energies. Similarly, the energy per particle is approximately $E/N \sim \hbar\omega_0(Na/S_l)^{2/5}$. The length scale $S_l = \sqrt{\hbar/m\omega_0}$ here is the characteristic length for the harmonic oscillator potential. The quantity Na/S_l can be taken as a dimensionless measure of the strength of the interatomic interactions within the condensate.

Motivated by these heuristic arguments, the Thomas-Fermi approximation consists of solving the GP equation, Eq. (2.10), while neglecting the kinetic energy contribution. This approach is appropriate for large condensates. More precisely, an approximate wavefunction amplitude for large N is simply

$$|\psi(\vec{r})|^2 = n(\mathbf{r}) = \frac{\mu - V(\mathbf{r})}{U_0} \tag{2.11}$$

in the region where $\mu > V(\vec{r})$ for all $\vec{r}$, and $\psi(\vec{r}) = 0$ for all other $\vec{r}$. Within the Thomas-Fermi approximation, the size of the condensate cloud $\vec{R}$ can then be obtained by solving $V(\vec{R}) = \mu$ for a specific choice of trapping potential. An important feature of this solution is that it corresponds to a condensate cloud that has sharp edges. In a real, physical BEC, condensate density should vanish more gradually at the edges of the trapping potential.

2.3 Hydrodynamic equations

We finish the theoretical warm-up portion of this Chapter by discussing elementary excitations of homogenous and inhomogenous BECs, focusing specifically on the hydrodynamic model. Hydrodynamic equations follow from the time-dependent Gross-Pitaevskii equation (TDGPE):

$$i\hbar\frac{\partial\psi(\mathbf{r},t)}{\partial t} = -\frac{\hbar^2}{2m}\nabla^2\psi(\mathbf{r},t) + V(\mathbf{r})\psi(\mathbf{r},t) + U_0|\psi(\mathbf{r},t)|^2\psi(\mathbf{r},t). \tag{2.12}$$

In order for TDGPE to be consistent with its time independent counterpart, Eq. (2.10), condensate wavefunction has to take the stationary form

$$\psi(\mathbf{r},t) = \psi(\mathbf{r})e^{-i\mu t/\hbar}. \tag{2.13}$$

Since $\partial E/\partial N = \mu$, this expression reflects the fact that, microscopically, ψ can be thought of as the matrix element of the annihilation operator $\hat{\psi}$ between ground states with N and $N-1$ particles:

$$\psi(\vec{r},t) = \langle N-1|\hat{\psi}(\vec{r})|N\rangle \propto e^{-i(E_N - E_{N-1})t/\hbar}. \tag{2.14}$$

Alternatively, Eq. (2.12) can be derived from the action principle with an appropriate Lagrangian, as shown in Ref. [9].

The hydrodynamic formalism consists of reformulating Eq. (2.12) as a set of equations, governing the behavior of the condensate density $n = |\psi|^2$ and the gradient of its phase. The latter determines the local velocity of the condensate. The first of these equations – the continuity equation – reads

$$\frac{\partial n}{\partial t} + \nabla \cdot (n\mathbf{v}) = 0 \tag{2.15}$$

where the BEC velocity is defined by

$$\mathbf{v} = \frac{\hbar}{2mi}\frac{(\psi^*\nabla\psi - \psi\nabla\psi^*)}{|\psi|^2}. \tag{2.16}$$

The form of Eq. (2.15) is identical to the classical expression for an ideal fluid. However, the velocity field v here is always a potential flow. Denoting the phase of the condensate wavefunction as ϕ, its velocity is given by

$$\mathbf{v} = \frac{\hbar}{m}\nabla\phi. \tag{2.17}$$

Note that for non-singular ϕ the motion of the condensate must always be irrotational as $\nabla \times v = (\hbar/m)\nabla \times \nabla\phi = 0$. We revisit the implications of this property in detail in Chapter 8 as it gives rise to vortex behavior.

The second hydrodynamic equation governs the motion of the condensate velocity. It reads

$$m\frac{\partial \mathbf{v}}{\partial t} = -\nabla(\tilde{\mu} + \frac{1}{2}mv^2) = -\nabla\left(V + nU_0 - \frac{\hbar^2}{2m\sqrt{n}}\nabla^2\sqrt{n} + \frac{1}{2}mv^2\right). \tag{2.18}$$

This expression is the equivalent of the Euler equation for a classical inviscid fluid. An important difference between the two is that the term $\frac{\hbar^2}{2m\sqrt{n}}\nabla^2\sqrt{n}$, referred to as quantum pressure, is not present for a classical ideal fluid. This term describes forces due to spatial variations in the magnitude of the condensate wavefunction. For a regime where the Thomas-Fermi approximation is valid the kinetic energy contribution to the BEC energetics is negligible and since this contribution gives rise to quantum pressure, for condensates with

$Na_s/S_c >> 1$ (with S_c some characteristic length) quantum pressure can always be neglected in Eq. (2.18). It is worth noting that typically liquids cannot be described only in terms of local density and local velocity, unless the temperature is very low.

Further, Eqs. (2.15) and (2.18) can be used to derive equations of motion for small density disturbances by expanding $n = n_{\rm eq} + \delta n$. Assuming that $\mathbf{v}$ and δn are small and linearizing Eqs. (2.15),(2.18) and the quantity $\tilde{\mu}$ gives

$$m\frac{\partial^2 \delta n}{\partial t^2} = \nabla \cdot (n_{\rm eq} \nabla \delta\tilde{\mu}). \tag{2.19}$$

This equation describes low-lying excitations of a trapped, interacting BEC. To further simplify, we neglect quantum pressure and consider density deviations with harmonic time-dependence, $\delta n \propto e^{-i\omega t}$ so that

$$-m\omega^2 \delta n = \nabla n_{\rm eq} \cdot \nabla \delta n + n_{\rm eq} \nabla^2 \delta n. \tag{2.20}$$

We emphasize that this expression can be used regardless of the method by which the equilibrium density profile, $n_{\rm eq}$, is calculated. As an example, if the density profile is determined by the Thomas-Fermi approximation

$$m\omega^2 \delta n = \nabla V \cdot \nabla \delta n - [\mu - V(\mathbf{r})] \nabla^2 \delta n. \tag{2.21}$$

Here, $\mu = V(R)$ can be used for condensates of fixed size R.

Eigenvalues and eigenvectors of Eq. (2.21) correspond to oscillation frequencies, ω, and oscillation modes of the condensate. The eigenproblem formulated in this equation is the starting point for investigations of the dynamics of hollow, shell-shaped condensates presented in the following Chapters.

2.4 Experimental realizations of BEC

We end this Chapter by commenting on experimental studies of Bose-Einstein condensates. The prediction of Bose-Einstein condensation predates its experimental realization by more than 80 years. A large part of the challenge that was experimentally realizing a BEC is that at low temperatures most substances do not remain gaseous. While this difficulty prompted proposals for realizations of BEC in spin-polarized hydrogen, where attractive interatomic interactions are very weak, dramatic advances in cooling of alkali atoms [11] ultimately made them the preferred species in experiments. In the Nobel prize winning 1995 experiments [12, 13] room-

temperature gas of rubidum atoms was trapped and cooled by lasers to about 20 μK, then further trapped magnetically by the Zeeman interaction with an inhomogenous magnetic field. Once the rubidium atoms were trapped in this way, the atomic cloud was cooled even more by evaporation. The rate of evaporation was enhanced by applying a radio-frequency magnetic field which flipped the electronic spin of the most energetic atoms thus causing them to be repelled from the magnetic field minimum. Strikingly, no cryogenic apparatus was involved in this procedure that cooled the atomic cloud to, then record-low, temperatures on the order of 100 nK. In contemporary experiments a wide variety of species and isotopes have been used to carry out Bose-Einstein condensation and temperatures on the picokelvin scale [14] have been achieved.

Realization of Bose-Einstein condensation in dilute ultracold atomic gases proved to be the beginning of a rich field of experimental research. Through advancements in cooling, control and manipulation techniques, BECs have become a powerful setting for studies of quantum phases of matter and emulation of traditional condensed matter systems [15], going as far as realizing molecular condensates [16, 17] and atomic hydrogen BECs [18] while condensation in even more novel elements such as ^{48}Ti is currently being explored [19]. We particularly note that bosonic condensates have been succesfully engineered in a wide variety of geometries ranging from quasi-one-dimensional and quasi-two-dimensional [20, 21, 22, 23, 24] to annular [25, 26], box-shaped [27] and double well [28]. It is further meaningful to note that the use of optical lattices [29, 30, 31] has made it possible to study artificial crystals of ultracold bosons, including the effects of disorder [32, 33, 34, 35] that can be precisely added to the system by the means of additional laser beams. Experimental techniques making it possible for these systems to be shaken [36], rotated [37, 38, 39, 40] or stirred [41, 42] have also expanded the scope of BEC studies. In recent years, the field has further advanced in terms of experimental control, culminating in the ability to address single ultracold atoms [43, 44, 45] by, for instance, using so-called optical tweezers [46, 47] or Rydberg states [48, 49]. These powerful tools could be used for quantum computation in the future. As another extreme, many-body localized states can also be engineered in bosonic condensates [50, 51]. Finally, BECs have been shown to be versatile and useful settings for high precision measurements [52, 53] and quantum metrology [54, 55]. Studies of hollow, spherically symmetric BECs presented in this thesis can be seen as another offshoot of an incredibly rich field that constantly pushes past new frontiers. They build on previous work concerning annular or ring-shaped condensates and introduce new physics by being three-dimensional, closed and compact. The hollowing-out transition in particular, discussed in detail in Chapters 4 and 6, is a new avenue for observing dimensional crossover and a change in physical topology of the condensate. In Chapter 4 we focus on hollow BECs, including outlining specific avenues for experimental realization. We hope our work will spark experiments going beyond the current efforts aboard the International Space Station [56, 1] and add meaningfully to the existing body of research.

Chapter 3

Vortices in Bose-Einstein Condensates

Studies of rotating BECs [41, 38, 39, 40] and phase imprinting of vortices carrying quantized rotation [57, 58] were among the first experimental studies to have been conducted following the realization of Bose-Einstein condensation in 1995. More generally, vortex structures are ubiquitous in experiments with BECs and understanding their behavior is a starting point for models of turbulence in ultracold quantum gases. Emergence of quantized vortices upon system rotation has als been used to confirm presence of superfluidity in helium droplet studies [59, 60, 61]. In this thesis, we mostly focus on hollow spherically symmetric condensates and the behavior of vortices in systems with this geometry is likely to have strong implications for vortex motion in the shell structures in the interiors of neutron stars [62, 63]. Consequently, we devote this Chapter to establishing some standard methods for studying vortex physics in BECs in general, then build on them by working in the setting of hollow and rotating BEC shells in Chapter 8. The approaches and ideas presented here are well known in the literature and provide a strong foundation for that work. First, in Sec. 3.1 we observe how single-valuedness of the macroscopic wavefunction leads to quantization of circulation and gives rise to quantized vortices. We proceed to approximate the cost maintaining a vortex within a BEC in Sec. 3.2 and connect vortex physics to rotating condensates in Sec. 3.3. In Sec. 3.4 we present the complex potential formalism standard for studying vortices in two-dimensional classical fluid and comment on using it to describe quantum superfluids as well. Finally, Sec. 3.5 utilizes all previous discusion to describe the motion of vortices in two-dimensional condensates.

3.1 Quantization of Circulation

One of the distinct features of quantum superfluids is the emergence of quantized vortices in response to rotation. This is a direct consequence of the condensate velocity being proportional to the gradient of the phase of the condensate wavefunction. For a macrosocopic wavefunction of the form $\Psi = fe^{iS}$, the velocity

field associated with superfluid flow is given by

$$\vec{v} = \frac{\hbar}{m}\vec{\nabla}S. \tag{3.1}$$

In other words, condensate flow is a potential flow and therefore has to be irrotational $\nabla \times v = 0$. At the same time, since the condensate wavefunction has to be single-valued, when evaluated around a closed countour its phase can only change by a multiple of 2π. Circulation Γ around a closed contour consequently reads

$$\Gamma = \oint v \cdot d\mathbf{l} = \frac{\hbar}{m} 2\pi\ell = \ell\frac{h}{m} \tag{3.2}$$

where ℓ is an integer. Namely, circulation around a closed contour is quantized in units of h/m.

To see how this purely quantum mechanical constraint leads to development of vortices, we consider a condensate in a trap that is invariant under rotation about the z-axis with $S = \ell\phi$. Here, the condensate flow is azimuthal only. From quantization of circulation it follows that

$$v_\phi = \ell\frac{\hbar}{m\rho} \tag{3.3}$$

with ρ the radial coordinate in the $x - y$ plane. It is clear that v_ϕ increases rapidly as ρ approaches the rotation axis (z-axis), seemingly leading to singular behavior. To avoid the infinite kinetic energy associated with divergent velocity, condensate density $n = |f|^2$ vanishes at the rotation axis thus creating a vortex core. The size of the vortex core is given by the healing length of the condensate, $\xi^2 = \frac{\hbar^2}{2mnU_0}$.

This length scale captures the variation of the condensate density near an infinitely hard wall [9]. At the wall, the condensate wavefunction must vanish and ξ is the distance over which it increases from zero to the value in the condensate bulk (far away from the wall). According to the Gross-Pitaevskii equation, the condensate wavefunction in the bulk is governed by the competition between inter-atomic interactions and kinetic energy. Setting the two to be equal

$$\frac{\hbar^2}{2m\xi^2} = nU_0 \tag{3.4}$$

describes the distance ξ over which the condensate wavefunction restores its bulk value when in some way disrupted or perturbed i.e. the healing length. We proceed to estimate the energy cost of maintaining a vortex core of this size that is devoid of condensed atoms.

3.2 Energy cost of vortex core

To estimate the energy associated with the existence of a vortex core in a Bose-Einstein condensate hosting some rotational flow, we follow Ref. [9] and consider the simple case of a BEC in a trap with axial symmetry. We note that as long as the vortex is assumed to be point-like and the healing lenght much smaller than the overall size of the condensate, the details of the trapping potential are essentially irrelevant for this computation. The energetics of the vortex are only really significantly affected by such considerations if the vortex is very close to the edge of the condensate where the trapping potential determines the BEC density gradients that can cause vortex motion. In what follows, we typically study vortices in the bulk of the condensate and explictly address boundary effects when appropriate.

For a large, axially symmetric BEC, we assume that the wavefunction, in cylindrical polar coordinates, takes the form

$$\psi(\vec{r}) = f(\rho, z)e^{i\ell\phi}, \tag{3.5}$$

where the amplitude $f = |\psi|$ is a real function. This amplitude can be calculated from the Gross-Pitaevskii equation, Eq. (2.10),

$$-\frac{\hbar^2}{2m}\left[\frac{1}{\rho}\frac{\partial}{\partial\rho} + \frac{\partial^2 f}{\partial z^2}\right] + \frac{\hbar^2}{2m\rho}\ell^2 f + V(\rho, z)f + U_0 f^3 = \mu f. \tag{3.6}$$

Given our discussion above, we simplify this expression by taking $V(\rho, z) \approx 0$ i.e. treating the BEC as near uniform, and set $\ell = 1$ as multiply quantized vortex lines are rarely seen in experiments. The vortex hence extends along the z-axis and the wave-function does not depend on z. In the literature, it is common to obtain the precise structure of a vortex core by solving Eq. (3.6), or an equivalent, near the vortex and far away from it, then matching the two solutions [64]. Here, at large distances form the axis, the centrifugal term $\propto 1/\rho^2$ in the GP equation is small and negligible so f can be approximated as $f \approx f_0 = \sqrt{\mu/U_0}$. Close to the rotation axis, on the other hand, $f \propto \rho$. The crossover between these two behaviors occuse at a distance from the z-axis of the order of the healing length ξ, in line with our discussion in the previous Section. For convenience, we rescale all variables with respect to ξ and f_0 and work with dimensionless quantities $x = \rho/\xi$ and $\chi = f/f_0$. The dimensionless GP equation is equal to

$$-\frac{1}{x}\frac{d}{dx}\left(x\frac{d\chi}{dx}\right) + \frac{\chi}{x^2} + \chi^3 - \chi = 0. \tag{3.7}$$

To find the energy associated with the vortex we consider the total energy of a large, axially symmetric

condensate hosting a vortex and subtract the total energy of a uniform gas with the same number of particles per unit length ν contained within a cylinder of radius R. As in previous Sections, we take the energy per unit volume of a uniform gas to be $\bar{n}^2 U_0/2$ where $\bar{n}$ is the average density of the condensate. This quantity, the average density, is not the same in the condensate hosting a vortex state as the core of the vortex is empty – a hole in the density near the z-axis. Comparing condensates having the sume number of particles, the vortex state has a larger density away from the z-axis than the uniform system. We caclulate ν in terms of f and f_0 as

$$\nu = \pi R^2 f_0^2 - \int_0^R 2\pi\rho d\rho (f_0^2 - f^2) \tag{3.8}$$

so that for the uniform system the energy per unit length reads

$$\epsilon_0 = \frac{1}{2}\pi R^2 f_0^4 U_0 - f_0^2 U_0 \int_0^R 2\pi\rho d\rho (f_0^2 - f^2) \tag{3.9}$$

where we have neglected terms of the order of $f_0^4 U_0 \xi^4/R^2$ since we are assuming that the size of the condensate is much larger than its healing length, $R >> \xi$. As the total energy per unit lenght of the vortex state is given by

$$\epsilon = \int_0^{\rho_0} 2\pi\rho d\rho \left[\frac{\hbar^2}{2m}\left(\frac{df}{d\rho}\right)^2 + \frac{\hbar^2}{2m}\frac{f^2}{\rho^2} + \frac{1}{2}U_0 f^4\right], \tag{3.10}$$

subtracting the uniform contribution Eq. (3.9) and re-writing it in terms of the re-scaled units gives the energy contribution of the vortex line itself as

$$\epsilon_v = \frac{\pi\hbar^2}{m} f_0^2 \int_0^{R/\xi} x dx \left[\left(\frac{\partial\chi}{\partial x}\right)^2 + \frac{\chi^2}{x^2} + \frac{1}{2}(1-\chi^2)^2\right]. \tag{3.11}$$

For $\rho >> \xi$, the second term in the integrand of Eq. (3.11) dominates. We conclude that, to logarithmic accuracy [9], the energy per unit length of the vortex is

$$\epsilon_v \approx \pi n \frac{\hbar^2}{m^2} \log(R/\xi). \tag{3.12}$$

This is the energetic cost of the vortex core being a structure empty of condensed particles maintained within the BEC. A more accurate result can be obtained by evaluating Eqs. (3.7) and (3.11) numerically. In our future discussions, we will use Eq. (3.12) as a starting point and present more detailed numerical results when appropriate (for instance, for a harmonically trapped BEC we will add a well-known numerical factor

to the argument of the logarithm).

3.3 Rotating condensates

We now turn to a discussion or rotating BECs and the connection between rotation and nucleation of vortices. To explicity show that rotation about the z-axis is related to azimuthal flow, we consider the Lagrangian for a rotating BEC as

$$\mathcal{L} = \int d\vec{r}\Psi^* i\hbar(\partial_t + (\vec{\Omega}\times\vec{r})\cdot)\Psi - \frac{\hbar^2}{2m}\vec{\nabla}\Psi\vec{\nabla}\Psi^* - V(\vec{r})|\Psi|^2 - \frac{1}{2}U_0|\Psi|^4 \tag{3.13}$$

where $i\hbar(\vec{\Omega}\times\vec{r}) = -\Omega\hat{L}$ and the angular momentum operator $\hat{L} = -i\hbar(\vec{r}\times\vec{\nabla})$. Taking $\vec{\Omega} = \Omega\hat{z}$ and separating the amplitude and phase of the condensate wavefunction as above, Eq. (3.13) becomes

$$\mathcal{L} = \int d\vec{r} f^*(i\hbar\partial_t - \Omega\hat{L}_z - i\Omega(\hat{L}_z S))f - V(r)|f|^2 - \frac{1}{2}|f|^4 - \frac{\hbar^2}{2m}f^*(\vec{\nabla}^2 f + 2i\vec{\nabla}S\cdot\vec{\nabla}f + |\vec{\nabla}S|^2 f) \tag{3.14}$$

where we have used integration by parts and

$$-\vec{\nabla}^2\Psi = (-\vec{\nabla}^2 f + |\vec{\nabla}S|^2 f - i(\vec{\nabla}^2 S) - 2i\vec{\nabla}S\cdot\vec{\nabla}f)e^{iS}. \tag{3.15}$$

As there should be no imaginary terms in the Lagrangian, we can infer the phase of the rotating condensate shell by requiring that

$$-f^*\Omega L_z f = -\frac{\hbar^2}{2m}(2i)f^*\vec{\nabla}S\cdot\vec{\nabla}f \tag{3.16}$$

Since $-\Omega L_z = -\vec{\Omega}\cdot\hat{L} = i\hbar(\vec{\Omega}\times\vec{r}\cdot\vec{\nabla})$, the previous expression is equivalent to

$$f^* i\hbar(\vec{\Omega}\times\vec{r})\cdot\vec{\nabla}f = -\frac{i\hbar^2}{m}f^*\vec{\nabla}S\cdot\vec{\nabla}f \tag{3.17}$$

which, finally, implies

$$v_{\rm rot} = \vec{\nabla}S = -\frac{m}{\hbar}(\vec{\Omega}\times\vec{r}) = -\frac{m\Omega}{\hbar}(y\hat{x} - x\hat{y}) = \frac{m\Omega}{\hbar}\hat{\phi}. \tag{3.18}$$

In other words, rotating a BEC adds a uniform background flow of magnitude $v_{\rm rot} = \frac{\hbar}{m}\vec{\nabla}S = \Omega$ to the condensate. A condensate having a vortex along the z-axis with circulation Ω would have the same effect

on the motion of condensed atoms.

From the point of view of the total energy of the condensate, it is simple to see that for a BEC that is either rotating or being stirred fast enough the vortex state can become preferrable. In the rotating frame

$$E_{\text{rot}} = E - \Omega \cdot L \tag{3.19}$$

where L is the angular momentum vector and Ω the angular velocity of the rotation. Denoting the energy of a state with angular momentum component L along the rotation axis (i.e. some flow around this axis) as E_L, we conclude that such a state is energetically favorable compared to the state with no condensate flow, having E_0, when

$$\Omega_c = \frac{E_L - E_0}{L}. \tag{3.20}$$

This defines Ω_c as the critical rotation speed for creation of defects and excitations carrying angular momentum, such as vortices. This definition of Ω_c is rather general and only relies on our ability to calculate E_L and E_0 which do, in turn, depend on the geometry of the condensate, the number of condensed particles and other details of the particular system being considered.

3.4 Potential flows and parallels with vortices in classical inviscid fluids

Studying vortices in BECs, especially in flat two-dimensional condensates or near-two-dimensional systems being very strongly confined along one dimension, our approach can often be informed by investigations of inviscid fluids in classical hydrodynamics. Such fluids have zero or negligible viscosity. To further motivate parallels between flows in such fluids and in BECs we recall that within the Gross-Pitaevskii formalism counterparts of both the continuity and Euler equations (Eqs. (2.15 and (2.18), respectively) apply in the so-called hydrodynamic regime. Here, in addition to the fluid flow being irrotational, it is also assumed to be incompressible, $\nabla \cdot v = 0$. This condition that the divergence of the flow velocity vanishes is equivalent to requiring that mass be conserved and density within a moving volume of fluid remain constant. In calculations, we also often assume that the flow can only be tangential or parallel to the condensate boundaries. The accuracy of this assumption depends on the trapping potential. For a potential with sufficiently hard walls, this assumption is equivalent to requiring number conservation – atoms cannot flow out of the condensate. However, for a condensate cloud with more realistic edges where the BEC density diminishes

gradually rather than abruptly, assuming that, in azimuthally symmetric geometries, no flow is present in the radial direction may introduce some errors.

For two-dimensional classical inviscid fluids, it is costumary to introduce a complex potential w [65, 66] having real and imaginary components as

$$w = \chi + i\psi. \tag{3.21}$$

Components of condensate flow, in polar coordinates, are then

$$v_\rho = -\frac{1}{\rho}\frac{\partial \psi}{\partial \phi},\ v_\phi = -\frac{\partial \psi}{\partial \rho} \tag{3.22}$$

In classical hydrodynamics, ψ is idenitified as the stream function. It is constant along a streamline. The difference between stream function values between any two points in the flow is equal to the rate of volume flow across a unit area through a line connecting the two points. For a quantum superfluid, χ matches the phase of its macroscopic wavefunction (in other words $\chi = S$ in our previous notation). Due to the single-valuedness of this wavefunction, χ has to be invariant under shifts by mutiples of 2π in order to be physically meaningful in discussions of quantum fluids. As noted in Ref. [67], this quantum constraint can change the dynamics of objects like vortices in BECs compared to the analogous classical problems. The two parts of the complex potential w, ψ and χ, satisfy the Cauchy-Riemann equations [65, 66] so the flow field can be defined in terms of either.

As an example, for a single point-like vortex at the center of an unbounded two-dimensional superfluid having circulation Γ_0, the complex potential reads

$$w_{\text{vortex}} = \frac{i\Gamma_0}{2\pi}\ln(z) \tag{3.23}$$

where $z = \rho e^{i\phi}$. From Eq. (3.22) it follows that $v_\rho = 0$ and $v_\phi = \frac{1}{\rho}$ or, correcting the units, $\vec{v}_{\text{vortex}} = \frac{\hbar}{m\rho}\hat{\phi}$ exactly as in Eq. (3.3).

Since for incompressible flow w obeys the Laplace equation $\nabla^2 w = 0$, standard solution techniques are applicable. Analogously to electromagnetism, we can use the method of images when appropriate boundary conditions are given. As noted above, we will typically constrain solutions by requiring the flow field be tangentially to condensate boundary only. In this formalism, vortices act as sources and sinks (depending on the orientation of their circulation), in analogy with electric charges. For example, the equivalent of an electromagnetism problem in which an electron is situated at some fixed distance above a conducting plane

would be a vortex in a two-dimensional superfluid near a wall with the boundary condition that no flow perpendicular to the wall should be present. In this case, a valid formulation of the complex potential would be to add a vortex with equal and opposite circulation on the other side of the wall. This approach is quite fruitful for two-dimensional condensates in disk and ring geometries and will be employed repeatedly in some of the discussions that follow.

Further, as Eq. (3.22) shows, the flow field of the condensate can be calculated from the complex potential thus allowing for further calculations of the circulation associated with that flow and the condensate kinetic energy, respectively

$$\begin{aligned} \Gamma(\rho) &= \rho \int_{-\pi}^{\pi} d\phi v_\phi \\ KE &= \frac{1}{2}\bar{n} \int d^2\rho |v|^2 \end{aligned} \tag{3.24}$$

for $\bar{n}$ some appropriately averaged value of condensate density [68].

3.4.1 BEC disks

In Chapter 8, we will often perform calculations for three-dimensional BEC shells by treating them as a collection of two-dimensional slices perpendicular to the rotation axis (typically the z-axis so the slices are parallel to the $x-y$ plane). While this approach assumes that the flow (and interactions) between such slices is unimportant, it nevertheless captures, as discussed in Sec. 8.3.1, some essential features of simple three-dimensional vortex configurations. It is therefore informative to consider complex potentials and flow fields of two-dimensional BECs in ring and disk geometries hosting vortices at the rotation axis or radially offset from it.

The simplest case – a point vortex at the rotation axis in a disk BEC – is essentially given by Eq. 3.23 with a constant term added to account for the fact that flow has to vanish at the condensate boundary. Namely,

$$w_{\text{disk}} = \frac{i\Gamma_0}{2\pi} \ln(z/R) \tag{3.25}$$

vanishes for $z = R$. If the vortex is not positioned at the center of the disk but rather at some $z = r_v < R$, the complex potential $w(z, r_v)_{\text{disk}}$ can be obtained by the method of images; the flow will be the same as if

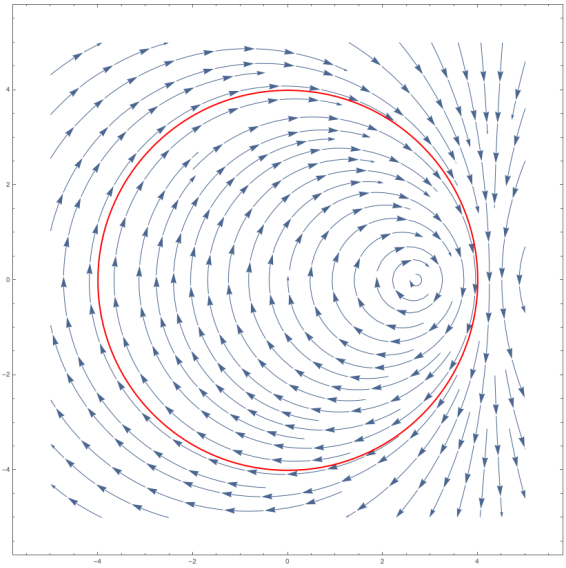

Figure 3.1: Plot of the streamlines corresponding to the complex potential of Eq. (3.26) describing a disk BEC with an off-center vortex of unit vorticity. The red lines denote condensate boundaries where the flow vanishes.

therewere an equal and opposite vortex at $z = R^2/r_v$ so that

$$w(z, r_v)_{\text{disk}} = \frac{\Gamma_0}{2\pi} \ln\left(\frac{z - r_v}{z - R^2/r_v}\right). \tag{3.26}$$

Streamlines corresponding to the complex potential of Eq. (3.26) are shown in Fig. 3.1. Physical quantities such as components of condensate velocity can be obtained by taking derivatives of the imaginary component of w as per Eq. (3.22): $v_\rho = -(1/\rho)\partial_\phi \text{Im}[w]$ and $v_\phi = -\partial_\rho \text{Im}[w]$.

3.4.2 Annular BEC

We proceed to consider vortices in two-dimensional annular BEC. This geometry is the two-dimensional counterpart to the hollow condensate shell and has been achieved experimentally [25, 26]. While not all experimental efforts result in perfectly two-dimensional condensate annuli, toroidal BECs up to 40 times wider than they are thick have been realized thus succesfully emulating the near-2D regime.

For a point-vortex situated inside the annular BEC, we again use the method of images, starting with the problem of a vortex between two hard walls then transforming the coordinates in order for the two walls to form the inner and outer boundary of the annulus [68]. The vortex configuration with two straight parallel boundaries is analogous to the probelm of a single charge between two grounded conducting plates in electromagnetism. It is know that this problem can be solved by adding infinitely many positive and

negative image charges; the superfluid problem is solved in the same way. More precisely, for one boundary at $z = 0$, with z a complex variable, and one at $z = \delta$ with the vortex at $z = a$, the boundary condition of no flow transverse to either boundary is satisfied when an image vortex is placed at $z = 2m\delta + a$ and the corresponding antivortex at $z = 2m\delta - a$ for m an integer. In other words, the vortices and antivortices are simple zeroes and simple poles of the function

$$g(z) = \frac{\sin(\frac{2\pi}{\delta}(z-a))}{\sin(\frac{2\pi}{\delta}(z+a))} \tag{3.27}$$

so that the complex potential encoding the flow of the superfluid, assuming vortex circulation Γ_0, can be written as

$$w_{\text{annulus}}(z) = \frac{i\Gamma_0}{2\pi} \ln\left[\frac{\sin(\frac{2\pi}{\delta}(z-a))}{\sin(\frac{2\pi}{\delta}(z+a))}\right]. \tag{3.28}$$

To transform to an annular region in the complex z plane, we substitute

$$z \to \ln(z/R_{\text{in}}) \tag{3.29}$$

for R_{in} the inner radius of the annulus and $z = re^{i\phi}$. Following this transformation, the lines Re(z) = const correspond to circles $\ln(r/R_{\text{in}}) = \text{const}$ so we have to take $\delta = \ln(R/R_{\text{in}})$ for the outer radius of the annular BEC to be equal to R. Similarly, we take $a = \ln(R_{\text{in}}/r_{\text{v}})$ for a vortex located at $(r_{\text{v}}, 0)$. Putting these results together

$$w_{\text{annulus}}(z) = \frac{i\Gamma_0}{2\pi} \ln\left[\frac{\sin(\gamma \ln(z/r_{\text{v}}))}{\sin(\gamma \ln(zr_{\text{v}}/R_{\text{in}}^2))}\right] \tag{3.30}$$

where we have defined the constant $\gamma = \pi/2\ln(R_{\text{in}}/R)$. Further, we obtain the stream function

$$\psi_{\text{annulus}}(z) = \frac{\Gamma_0}{8\pi} \frac{(\cos(2\ln(R_{\text{in}}/r_v)) - \cos(2\ln(r/R_{\text{in}}))\cosh(2\gamma\phi))^2 + \sinh^2(2\gamma\phi)\sin^2(2\ln(R_{\text{in}}/r_v))}{(\sin^2(\gamma\ln(rr_v/R_{\text{in}}^2))\cosh^2(\gamma\theta) + \cos^2(\gamma\ln(rr_v/R_{\text{in}}^2))\sinh^2(\gamma\phi))^2}. \tag{3.31}$$

Here, it is important to recall that, as discussed above, due to the single-valuedness of the condensate wavefunction $\text{Re}[\text{w}_{\text{annulus}}]$ has to be invariant under the transformation $\theta \to \theta + 2\pi$. From Eq. (3.30) we find

$$\text{Re}[\text{w}_{\text{annulus}}(\text{z})] = \frac{\Gamma_0}{2\pi} \arctan\left(\frac{\sinh(2\gamma\phi)\sin(2\ln(\text{R}/\text{r}_{\text{v}}))}{\cos(2\ln(\text{r}/\text{R}))\cosh(2\gamma\phi) - \cos(2\ln(\text{R}/\text{r}_{\text{v}}))}\right) \tag{3.32}$$

which is not periodic in θ.

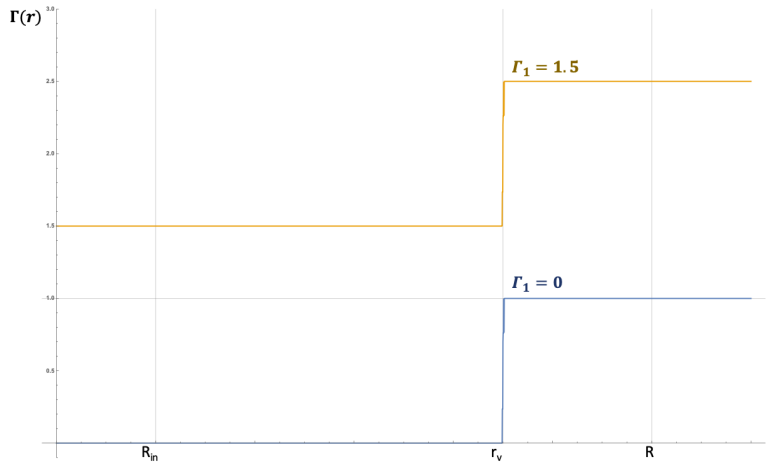

Figure 3.2: Plot of the circulation Γ associated with the condensate flow around a point vortex in a two-dimensional annular BEC. Calculated according to Eq. (3.24), the circulation is a step function changing value at the position of the vortex. Its value for $< R_{\rm in} < r < r_v$ is determined by the amount of vorticity associated with the inner boundary of the condensate annulus denoted by Γ_1. Blue line shows the case when $\Gamma_1 = 0$ and the only vorticity in the condensate is due to the point vortex situated at $r = r_v$; the yellow line shows the same vortex configuration with $\Gamma_1 = 1.5$ units of vorticity winding around the inner boundary of the BEC.

In order to remedy this, we note that following the conformal transformation (from the configuration with two straight walls to the annulus), the image vortices are found at

$$\begin{aligned} z_+ &= \left(\frac{R}{R_{\rm in}}\right)^{2m} \frac{1}{r_v} \\ z_- &= \left(\frac{R}{R_{\rm in}}\right)^{2m} \frac{r_v}{R_{\rm in}^2} \end{aligned} \tag{3.33}$$

which is also true if we take

$$w_{\rm annulus}(z) = \frac{\Gamma_1}{2\pi} \ln(z/R_{\rm in}) + \frac{\Gamma_0}{2\pi} \ln\left(\frac{\vartheta_1(-i/2 \ln(z/r_v), R_{\rm in}/R)}{\vartheta_1(-i/2 \ln(z r_v/R_{\rm in}^2), R_{\rm in}/R)}\right) \tag{3.34}$$

where ϑ_1 is the Jacobi theta function as in Ref. [67] and Γ_1 added in order to give the physically correct circulation around the vortex. More precisely, $\frac{\Gamma_1}{2\pi} \ln(r/R)$ has to be chosen in such a way that adding its contribution to those of all the image vortices returns (via Eq. (3.24)) total circulation of Γ_0 associated with the actual, physical vortex piercing the annular condensate. To make this evident, we plot circulation as given by Eq. (3.24) in Fig. 3.2.

The function $\vartheta_1(z, q)$ has simple zeroes at complex points $z = m\pi + n\pi\tau$ for some integers m and n and $q = e^{i\pi\tau}$ [67]. Plots of the stream function derived from Eq. (3.34) are shown in Fig. 3.3 where the image

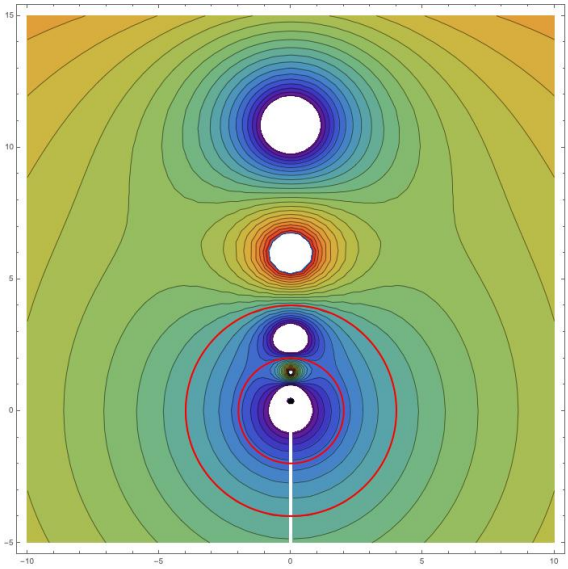

Figure 3.3: Plot of the stream function ψ corresponding to the complex potential of Eq. (3.34) utilizing the Jacobi theta function. The red lines denote the annular BEC. The succession of image vortices is seen as a number of singularities along the y-axis. Note that their vorticities alternate sign as expected.

vortices can be clearly identified. The stream function itself reads

$$\psi_{\text{annulus}}(z) = \frac{\Gamma_1}{2\pi}\ln(r/R_{\text{in}}) + \frac{\Gamma_0}{2\pi}\ln\left|\frac{\vartheta_1(-i/2\ln(z/r_v), R_{\text{in}}/R)}{\vartheta_1(-i/2\ln(zr_v/R_{\text{in}}^2), R_{\text{in}}/R)}\right|. \tag{3.35}$$

3.5 Motion of vortices in two-dimensional condensates

We proceed to discuss how the complex potential formalism of the preceding Section can be used to determine vortex motion. The dynamical behavior of simple structures such as a single vortex can be seen as building blocks for more complicated instances of turbulence in fluids that have been perturbed in some way, thus marking this discussion as a necessary starting point for future studies of that physics.

3.5.1 Vortex precession and static configurations

As in the electromagnetism analogy, solutions to the Laplace equation $\nabla^2 w(z)$ that introduce image vortices feature non-stationary vortices. A charge positioned next to a grounded conducting plane experiences a force due to the opposite image charge on the plane's other side and a vortex in a superfluid moves due to the flow of the image vortex on the other side of its boundary. It is worth noting that for azimuthally symmetric traps, vortices situated on the z-axis – the axis of symmetry – can satisfy the condition of only causing flow tangential to the trap boundaries without any image vortices being introduced and therefore

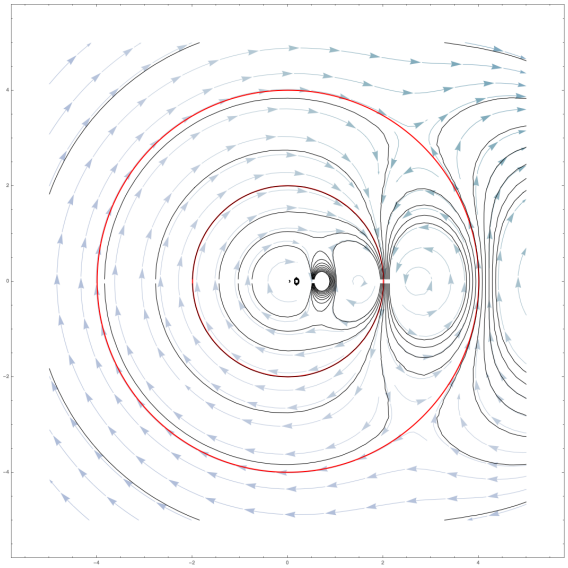

Figure 3.4: Streamlines and condensate velocity profile for an annular BEC containing an off-center vortex. The red lines denote the boundaries of the condensate, the blue arrows indicate condensate flow as determined in Eq. (3.38) and black countours correspond to the stream function corresponding to Eq. (3.34).

remain stationary. Any vortex off-set from that symmetry axis, however, will move within the condensate. Following Ref. [67] the motion of the vortex is determined by

$$v_v = \frac{\hbar}{m} \lim_{z \to r_v} \left(w'(z) - \frac{1}{z - r_v} \right) \tag{3.36}$$

where the first term references the definitions of Eq. (3.22) and the second serves to prevent v_v from becoming singular (recall that for $z \to r_v$ the condensate density vanishes).

For the two two-dimensional cases discussed above, Eq. (3.36) yields

$$\begin{aligned} v_{\text{annulus}} &= \frac{\hbar}{2mr_v\pi} \left(\Gamma_1 - \frac{\Gamma_0}{2} + \frac{i\Gamma_0}{2} \frac{\vartheta_1'(-i\ln(r_v/R), R_{\text{in}}/R)}{\vartheta_1(-i\ln(r_v/R), R_{\text{in}}/R)} \right) \\ v_{\text{disk}} &= \frac{\hbar\Gamma_0}{2m\pi} \frac{r_v}{R^2 - r_v^2} \end{aligned} \tag{3.37}$$

In either geometry the vortex is not static and, in fact, executes a precession since its speed changes sign as it moves within the condensate, as shown in Fig. 3.5.

Quantities in Eq. (3.37) should be considered alongside simply using Eq. (3.22) to obtain the components of the overall flow of the superfluid. For instance, in the case of the annular geometry, the velocity field of

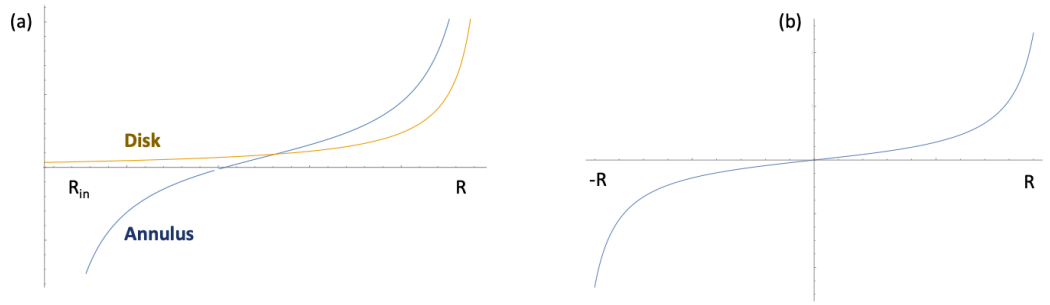

Figure 3.5: Vortex speeds as a function of vortex position for a two-dimensional annulus **(a)** and a two-dimensional disk geometry **(b)**. For the disk geometry the vortex can only be static when its core is at the center of the condensate while for the annulus BEC there is a static configuration for $r_v = \sqrt{RR_{\rm in}}$ and $\Gamma_1 = 0$.

the condensate reads

$$v_x = \mathrm{Im}\left[\frac{\Gamma_1}{z\pi} - \frac{i\Gamma_0}{4\pi}t(z)\right]$$
$$v_y = \mathrm{Re}\left[\frac{\Gamma_1}{z\pi} - \frac{i\Gamma_0}{4\pi}t(z)\right]. \tag{3.38}$$

where we have defined

$$t(z) = \frac{\vartheta_1'(-i/2\ln(z/r_v), R_{\rm in}/R)}{\vartheta_1(-i/2\ln(z/r_v), R_{\rm in}/R)} - \frac{\vartheta_1'(-i/2\ln(zr_v/R_{\rm in}^2), R_{\rm in}/R)}{\vartheta_1(-i/2\ln(zr_v/R_{\rm in}^2), R_{\rm in}/R)}. \tag{3.39}$$

This flow is shown in Fig. 3.4 together with streamlines corresponding to the stream function given by Eq. (3.35). The connection between Eqs. (3.37) and this expression is that the precessional velocity of the vortex is the same as that of a blob of superfluid carried by the flow of Eq. (3.38) at the position of the vortex core $z = r_v$.

Given this connection, we proceed to comment on vortex motion. More precisely, if we consider a two-dimensional condensate disk hosting an off-axis vortex, the speed of the vortex only vanishes for $r_v = 0$ and increases without bound as $r_v \to R$. In this geometry it is then energetically favorable for the vortex to be at the exact position of the rotation axis and therefore not move. Moreover, any configuration with a vortex away from the rotation axis is inherently unstable if any dissipation mechanism is present. This is not the case for the annular condensate as the vortex speed can vanish for $\Gamma_1 = 0$ and $r_v = \sqrt{RR_{\rm in}}$. The hollow topology can host a static vortex configuration provided there is no additional vorticity around the inner boundary of the condensate [67]. However, this static configuration is not necessarily stable against small pertubations either as it is not a true energy minimum for all values of Γ_1 or systems under rotation,

as noted in Ref. [68].

Finally, we note that in both the disk and annulus configurations, our analysis disregarded density inhomogeneities due to the condensate being confined by a trapping potential. Similar to bouyant forces in classical fluids, vortices in superfluids are drawn to areas of low condensate density gradients. Throughout this Section, we assume hard condensate boundaries and take $n(\rho, \theta) \approx \bar{n}$ to be constant in all calculations, but in a more realistic physical system the behavior of the vortex would be altered very close to the boundary [69]. As noted above, the nature of the boundary – sharp and sudden or more gradual – also affects the motion of the vortex as in the latter case the method of images technically becomes irrelevant.

3.6 Interactions between vortices

Having discussed the case of a single vortex at length, we proceed to discuss vortex configurations featuring mutliple defects. In a configuration consisiting of mutiple vortices each vortex is moved by flows due to the other vortex cores. We have previously employed this argument to show that a vortex in a two-dimensional BEC may or may not, depending on the condensate geometry, execute a precession due to image vortices (boundary effects). The same kind of interaction is present in vortex configurations involving two or more physical vortices. The total energy of the condensate consequently has to include a term accounting exactly for the flow due to one vortex carrying another. We will refer to this as an interaction energy between the vortices. This vortex-vortex interaction is an important factor in determining the most energetically favorable vortex state of a condensate cloud having many defects.

In general, there are two contributions to the total energy of the condensate due to vortices. First, there is an energy cost associated with maintaining zero condensate density at the position of the vortex core. Second, as a vortex carries vorticity, the condensate flows around it and kinetic energy is associated with that flow. Interactions between vortices are a consequence of that flow as noted above so vortex-vortex interaction energy arises from kinetic energy calculations. An analogous electromagnetic system is a collection of parallel, current-carrying wires. Here, each individual wire is in a magentic field due to the other wires which leads to a Lorentz force between them. For instance, two parallel wires carrying currents in the same directions will repel while they will attract if the direction of the current is reversed in one of the wires. Similarly, two vortices may attract or repel dependening on the direction of flows i.e. vorticities they are associated with.

To make this idea more concrete, we consider the energy funciontional

$$E[\psi] = \int d^3r \left[\frac{\hbar^2}{2m}(|\nabla f|^2 + f^2|\nabla S|^2) + V(r)f^2 + \frac{1}{2}U_0 f^4 \right]. \tag{3.40}$$

with $|f|^2$ the condensate density and S the phase of its wavefunction as before. Suppose the condensate in question is just a thin layer of superfluid on a flat two-dimensional plane. In this case, working in polar coordinates, a single vortex carrying one unit of angular momentum and situated at $(x, y) = (x_1, y_1)$ can be encoded by taking $S_1 = \arctan\left(\frac{y-y_1}{x-x_1}\right)$. Similarly, another vortex can be added by taking $S = S_1 + S_2$ where $S_2 = \arctan\left(\frac{y-y_2}{x-x_2}\right)$ is determined by the position of the second vortex $(x, y) = (x_2, y_2)$. Now, the second term in Eq. (3.40) reads

$$E[\psi] = \int d^3r \left[\frac{\hbar^2}{2m} f^2 |\nabla(S_1 + S_2)|^2 = \int d^3r \left[\frac{\hbar^2}{2m} f^2 (|\nabla S_1|^2 + |\nabla S_2|^2 + 2\nabla S_1 \cdot \nabla S_2) \right] \right. \tag{3.41}$$

Recalling that $v \propto \nabla_S$, we can identify terms proportional to integrals of $|v_1|^2$, $|v_2|^2$ and $v_1 \cdot v_2$ with v_i denoting the flow around a particular vortex. While $|v_i|^2$ terms can be thought of as just kinetic energies of the flow around each individual vortex (note that these contribute to the cost of the vortex core as discussed in Sec. 3.2), the $v_1 \cdot v_2$ term quantifies the way each vortex interacts with the flow of the other. This is the energy associated with the vortex-vortex interaction.

In the flat plane, this interaction term can be calculated for a pair of equidistant vortices, one at $(\rho, \phi) = (+a, 0)$ and one at $(-a, 0)$, having opposite vorticities by extracting v from their complex potential

$$w_{\text{pair}} = \frac{i\Gamma_0}{2\pi} \ln \left[\frac{re^{i\phi} + a}{re^{i\phi} - a} \right]. \tag{3.42}$$

As in Ref. [68], carrying out this calculation with an ansatz for the condensate density $f(\rho) = \rho(\rho^2 + \xi)$, where ξ is the healing length of the superfluid (the size of the vortex core), and assuming large vortex-antivortex separation a, yields

$$KE_{\text{pair}} = \frac{h^2}{2\pi m^2} \bar{n}(\ln(2a/\xi) + 1/4) \tag{3.43}$$

It follows that the two defects experience an attractive force when they are sufficiently close together. It is known that in a classical inviscid fluid a vortex-antivortex pair can come close together to form a dipole and execute a stable motion without the two vortices annihilating [66]. In particular, from Eq. (3.42), either vortex would move in the $\hat{y}$ direction with velocity having magnitude inversely proportional to a.

The same has been shown, through experiments [70, 71, 72] and both analytical [67, 73, 74] and numerical studies [75, 76], to be true for inhomogenous i.e. trapped BEC.

Closing this Chapter, we move on from summarizing and outlining standard techniques and concepts for studying BECs, at equilibrium, having collective motions, and hosting vortices, and focus on a specific condensate geometry that have not been a major of focus of study prior to our work. More precisely, the next five Chapters present an exhaustive study of three-dimensional, spherically symmetric and hollow BEC shells. In Chapter 4 we introduce condensate shells and discuss their experimental realization, then determine collective motions of such condensates in Chapter 5. Next, in Chapter 6 we conduct a detailed analysis of the hollowing-out transition that transforms a fully-filled spherically symmetric BEC into a thin, hollow condensate shell. Chapter 7 address the destructive effects of gravity and consequent experimental concerns when it comes to realizing hollow BECs in laboratory settings. Finally, in Chapter 8 we return to issues of vorticity and rotation, studying vortex physics on the surface of a hollow condensate shell as dictated by its thickness and rotation rate. The work presented in these five Chapters (Chapters 4-8) has been published in Refs. [77, 78] and we adapt some of the discussion below from those journal articles. Physics of vortex-antivortex pairs on shell-shaped BECs is addressed in Ref. [79]. This publication particularly informs the discussion in Chapter 8. All three of these studies have been completed in collaboration with Prof. C. Lannert (Smith College and Univeristy of Massachussets – Amherst) and Dr. Kuei Sun (The Univeristy of Texas at Dallas – Richardson).

Chapter 4

Introduction to Hollow BECs

A fully three-dimensional, hollow BEC geometry – a condensate shell – is fundamentally of interest for a number of reasons. In addition to the novelty of the topologically non-trivial shape of a condensate shell in real space, a transition between a fully filled condensate and its hollow counterpart contains rich physics. Tuning between the filled sphere and thin shell condensate geometries offers a means of achieving dimensional crossover from a solid three-dimensional (3D) shape to a two-dimensional (2D) one akin to a thin layer of superfluid glued to the surface of a sphere. The thin shell limit is interesting in its own right given that it provides a setting for studying two-dimensional condensate physics in the presence of non-trivial curvature. Further, the point at which the sphere initially hollows represents a change in topology. Unlike in other studies of topological transitions in quantum fluids, which require measuring Berry phases and other global invariants in momentum space, this topological change takes place in real space and is reflected in the physical density of the condensate. To encode this topological change more formally, we note that the filled sphere and hollow shell correspond to different second homotopy groups – for the filled condensate, a spherical surface within the hollow BEC that surrounds its center cannot be continuously deformed into a point. In terms of dimensional crossover and topological change, the hollowing out of the spherical BEC is a higher dimensional analog of annular and toroidal BECs [26, 25] that have been experimentally realized and extensively studied in the past.

Shell-shaped BECs appear in a range of strongly correlated systems, in diverse settings engineered in labs or naturally occuring in astronomical objects. As an example, it is well known that shell-shaped condensate regions occur in 3D optical lattice systems of ultracold bosons [31, 80, 81, 82], produced by the interplay between weak tunneling-to-interaction ratio (or strong lattice potential) [83, 84, 85] and inhomogeneous boson density due to harmonic confinement [86, 87, 88]. Here, superfluid (SF) regions are confined by surrounding Mott-insulator (MI) regions of the same bosons creating an effective trapping potential [89, 90], rather than by an external trap. Additionally, condensate shells occur in Bose-Fermi mixtures [91, 92, 93]. In this case, a shell of condensed Bose gas forms due to phase separation of ultracold bosons from a filled-sphere core of ultracold fermions. In superfluid helium droplets, introduction of other molecules in the center of the droplet

leads to development of superfluid solvation shells around it [60, 61]. At the astronomical scale, signals from neutron stars acting as radio pulsars have motivated models of their interiors as consisting of macroscopic quantum states of matter, some possibly being shells of superfluid neutron matter [94, 95, 63, 62]. Studying a single BEC shell in various thickness regimes is meaningful as a building block for theoretical understanding of these, more complex, systems featuring shell-shaped superfluid structures. Currently, the most promising experimental setting for manipulating and analyzing a single condensate shell having tunable thickness is NASA's Cold Atom Laboratory (CAL) aboard the ISS. We start this Chapter by addressing some of the details of this experimental setup in Sec. 4.1 then offer a more general discussion of trapping potential hosting filled and hollow spherically symmetric BECs in Sec. 4.2. This discussion includes the "bubble trap" utilized by CAL. We end by establishing the hollowing-out transition from a filled-sphere condensate to a hollow condensate shell in Sec. 4.3 thus setting up the much more detailed discussion of the same process in the next Chapter.

4.1 Cold Atom Laboratory and ultracold atoms in space

CAL posesses the unique capability of realizing BECs in orbit, where the constant freefall environment makes it possible to conduct experiments largely free of gravitational perturbations. This is of marked importance as destructive gravitational effects have prevented the realization of BEC shells on Earth [96, 97] so far. We address the details of shell deformation due to gravity i.e. gravitationa sag in Chapter 7 and focus on accessible microgravity environments here. One planned experiment on board involves the first creation of a hollow shell BEC [56, 1] using an rf-dressed "bubble trap" potential [98, 99]. Such traps have been proposed almost two decades ago but have not been fully utilized for confinements of three-dimensional BECs until the lauch of CAL in May 2018. Previously, realization of BEC in microgravity had been succesful in the ZARM drop tower [100] and the MAIUS sounding rocket [101, 102] in Germany. Additionally, normal fluid shells were studied during space shuttle launches [103].

CAL was developed by the Jet Propulsion Laboratory beginning in 2016 and is currently in operation aboard the ISS. It is an atom-chip-base BEC machine with capacity and capability for a number of experimental studies. The procedure by which CAL produces shell-shaped condensates follows two steps. First, a condensate is prepared in a "bare trap". Then the rf dressing signal is ramped upwards giving rise to an adiabatic potential confinig the condensed bosons into a shell geometry. It is important to note that in experiments that have been conducted thus far various inhomogeneities play an important role for characterizing BEC shells [56]. These inhomogeneities are a product of technical minutiae of the CAL machine and present

a departure from the assumption of perfect spherical symmetry as employed in theoretical studies presented in this thesis. More precisely, the condensate shells realized in CAL are ellipsoidal and complete density coverage around the surface of the shell is not always achieved [1]. However, some of these inhomogeneities could potentially be compensated through additional microwave dressing fields and CAL's operation is set to continue and improve throughout 2019. A second-generation orbital microgravity atom-chip ultracold atomic physics facility, BECCAL [102], is currently under development in Germany, jointly supported by NASA and the German Space Agency DLR thus presenting even more future opportunities for experimental studies of hollow BECs. The work presented here is therefore at the forefront of a new and growing area of ultracold atomic research. Our studies, as elaborated on in the following chapters, serve as a foundation for experimental work that is bound to continue developing in orbit in the future.

Turning to these studies, we proceed to establish equilibrium properties of hollow shell BECs. As discussed in Chapter 2 equilibrium density profiles of BECs are determined by the choice of trapping potential and details such as widths and maximum radii of trapped condensates are also influenced by the strength of interactions between the atoms. We consider a harmonic trap for the filled sphere geometry and a radially shifted harmonic trap for the thin shell condensate. A "bubble trap" proposed in the literature [98] and related to the experimental CAL trap can be tuned between these two limiting cases. Studying these two limiting cases – filled sphere and very thin shell BEC – sets us up for a comprehensive discussion of the hollowing-out transition in Section 4.3. Further, we consider a generalized trapping potential which can tune the rate of growth of condensate equilibrium density in the center of the system as it hollows. Hence we identify the effect of density on the creation of an inner boundary. We analyze the equilibrium condensate density in all of these trapping potentials and note that the Thomas-Fermi approximation, Eq. (2.11), is a good approximation for many analyses. Since it models sharp boundaries for the condensate, the hollowing-out features found in these cases are rather sharp and abrupt as well. Accounting for realistic condensate profiles and softer, more gradually vanishing, boundaries requires going beyond the Thomas-Fermi approximation. To that end we consider ground-state densities determined through numerical methods. Numerical studies presented in this Chapter have been conducted by Prof. C. Lannert as part of a collaborative research project.

4.2 Trapping potentials for spherically symmetric BECs

We begin by defining trapping potentials that host the limiting cases of the filled spherical condensate and the thin condensate shell, then discuss two trapping potentials that can capture the physics of the intermediate

(thick) shell regime and the hollowing-out transition. We adopt dimensionless length units, rescaled by an oscillator length $S_l = \sqrt{\hbar/(2m\omega)}$, where ω is a relevant frequency, for instance, of the bare harmonic confining trap prior to rf dressing.

As the simplest and best understood case, we start by analyzing the spherically symmetric harmonic trap, which produces a fully filled spherical condensate. The associated trapping potential takes the form

$$V_0(r) = \frac{1}{2} m\omega_0^2 S_l^2 r^2, \tag{4.1}$$

where ω_0 is the single-particle frequency of small oscillations and r is the dimensionless radial distance from the origin (spherical center).

The radially shifted harmonic trap realizes the opposite limit of a very thin spherical condensate shell

$$V_{\rm sh}(r) = \frac{1}{2} m\omega_{\rm sh}^2 S_l^2 (r - r_0)^2, \tag{4.2}$$

where the location of potential minimum r_0 is nonzero, and $\omega_{\rm sh}$ is the frequency of single-particle oscillations near this radius. Several salient features of the equilibrium density and collective mode structure of the thin shell limit are well captured by analyzing condensates in this radially shifted potential. In addition, this potential is a good approximation for any trapping potential with a radially shifted minimum in the thin shell limit.

At the same time, the potential of Eq. (4.2) is unphysical for situations where the condensate density is finite close to the trap center; the slope of the potential is discontinuous at $r = 0$. For a more realistic trap producing a hollow condensate, we consider a "bubble trap" [98, 96, 97] that utilizes adiabatic potentials. More precisely, it is achievable in cold atomic settings by employing time-dependent, radio frequency induced adiabatic potentials within a conventional magnetic trapping geometry. Its form is given by

$$V_{\rm bubble} = m\omega_0^2 S_l^2 \sqrt{(r^2 - \Delta)^2/4 + \Omega^2}, \tag{4.3}$$

where Δ and Ω are the effective (dimensionless) detuning between the applied rf-field and the energy states used to prepare the condensate and the Rabi coupling between these states, respectively. The minimum of this potential is found at $r = \sqrt{\Delta}$ and the frequency of single-particle small oscillations around it is $\sqrt{\Delta/\Omega}\omega_0$.

Parameters Δ and Ω allow for tuning between the filled condensate and the thin shell. When $\Delta = \Omega = 0$, the bubble-trap potential reduces to a harmonic trap with frequency ω_0. For large Δ, it is approximated

near its minimum by a radially shifted harmonic trap, Eq. (4.2), with frequency $\omega_{\rm sh} = \sqrt{\Delta/\Omega}\omega_0$. Slowly increasing or decreasing the trap parameter Δ results in a continuous deformation between the two limiting geometries of a filled sphere and a thin spherical shell. This is the hollowing-out transition resulting in a change in the BEC's topology.

While this change is topological in nature (an inner surface is created), because condensates have continuous density profiles, hollowing-out in a real system would be more gradual and the density at the center would become smaller until it is effectively zero. In order to capture this and tune the detailed behavior of the condensate density during the hollowing transition, we study the general radially shifted trapping potential

$$V_{\rm gt}(r) = \frac{1}{2} m\omega_{\rm gt}^2 R^2 S_l^2 \Big[\Big(\frac{r}{R} \Big)^{\alpha} - \gamma \Big]^2, \tag{4.4}$$

where R represents the (dimensionless) characteristic size of the system (the sharp outer boundary under the Thomas-Fermi approximation). In this expression, $0 \leq \gamma \leq 1$ is a dimensionless parameter that tunes the radially shifted trap minimum thus realizing the evolution between filled sphere and thin shell, and α determines the polynomial growth of condensate density in the radial direction from the boundary. The radially shifted harmonic trap of Eq. (4.2) is a special case of the general trap having $\alpha = 1$.

4.3 Evolution of equilibrium density from filled sphere to thin shell

Having enumerated the trapping potentials used in our studies, we next find the equilibrium density profiles of condensates confined to these traps.

First, using the Thomas-Fermi approximation of Sec. 2.2.2 we formulate the condensate density $n_{\rm eq}(\mathbf{r})$ and boundary $n_{\rm eq}(\mathbf{R}) = 0$ as determined by the trap geometry and the total number of particles $N = \int n_{\rm eq}(\mathbf{r}) d\mathbf{r}$. This approximation can be used to show that a BEC in the bubble trap with a slowly changing detuning Δ transitions from a filled sphere to a hollow shell when $\Delta = R^2/2$ (where we have set $\Delta = \Omega$ for convenience).

4.3.1 Beyond Thomas-Fermi

A more accurate numerical solution for the ground state of the GP equation (for any value of interaction strength) can be found using an imaginary-time algorithm [104]. In Fig. 4.1, we show the evolution of the numerical ground state in the bubble trap as the detuning Δ is varied from 0 to 200 (corresponding to

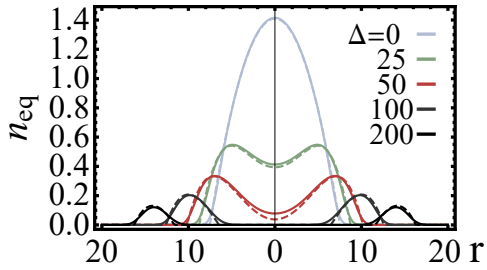

Figure 4.1: Ground-state density profiles $n_{\rm eq}(r)$ in the bubble trap for $\Delta = 0$ (lighter blue curves), 25 (light green), 50 (dark red), 100 (darker gray), and 200 (black). The various values of Δ show the evolution from the spherical (filled) condensate in a harmonic trap at $\Delta = 0$ to a thin-shell condensate for large Δ. The solid (dashed) curves are obtained from the numerical solution of the GP equation (the Thomas-Fermi approximation). Here, we use $\Delta/\Omega = 1$ and an interaction constant $u = 10,000$.

evolution from a filled, harmonically trapped, sphere to a thin spherical shell) with $\Delta/\Omega = 1$ fixed. The equilibrium density given by the Thomas-Fermi approximation is shown for comparison. While for the most part the density profiles match each other, those found through the exact numerical calculation show a more realistic, smooth decrease in density at the edges of the condensate. In these numerical calculations, we usee a relatively large value of dimensionless interaction strength $u = 8\pi N a_s/S_l = 10,000$. Here S_l is the oscillator length for the harmonic trap when $\Delta = 0$. For ^{87}Rb and a bare trap frequency of 10–100 Hz, for instance, this corresponds to $N = 2 \times 10^5$ to 5×10^4 atoms.

Taking into account the analyses and arguments above, in what follows, we either employ the Thomas-Fermi approximation or the numerical ground state, as appropriate. We follow this discussion of static properties of hollow BECs by turning to their collective modes in the next Chapter.

Chapter 5

Collective Modes of Hollow BECs

This Chapter marks the beginning of our identification and discussion of salient features differentiating the physics of filled and hollow BECs that is the focus of the first third of this thesis and addresses the first big question laid out in its introduction. More concretely, this Chapter is devoted to studying collective modes of spherically symetric condensates that are filled, hollow or undergoing a transition from one topology to the other. We focus on collective modes in part because they are experimentally practical – collective modes have been observed in BECs since some of the earliest ultracold atomic studies and they offer a non-destructive way to detect a central hollow region that cannot be directly imaged in a three-dimensional condensate. The discussion of collective modes here is organized as follows. First, in Sec. 5.1, we outline analytical and numerical methods we use in order to study collective modes. Sec. 5.2 shows the results of applying these methods to two limiting geometries of the fully filled sphere confined by a quadratic potential and the very thin hollow shell confinedby a radially shifted quadratic potential. In Sec. 5.2.3 we explicitly address surface modes as the existence of an additional surface capable of hosting excitations is the biggest difference between filled and hollow condensates. Finally, Sec. 5.3 addresses signatures of the hollowing-out transition from a filled sphere to a thin hollow shell BEC in the collective mode frequency spectrum.

5.1 Methods and approaches for dynamics of collective modes

In this Section we lay out methods for studying condensate dynamics. More precisely, we aim to analyze collective motions of spherically symmetric BECs and present four complementary methods for doing so appropriate in different regimes. The first method uses a hydrodynamic approach, as in Sec. 2.3, combined with Thomas-Fermi equilibrium density profiles discussed in Sec. 2.2.2. This method specializes our previous discussion to spherically symmetric BECs and provides a good approximation for collective mode spectra in any spherically symmetric trap. Second, we employ a fully numerical approach that mimics the experimental excitation of collective oscillations through sudden changes in trap potential. While more realistic, this method can only capture low-lying collective modes due to finite resolution. A third, hybrid, method uses

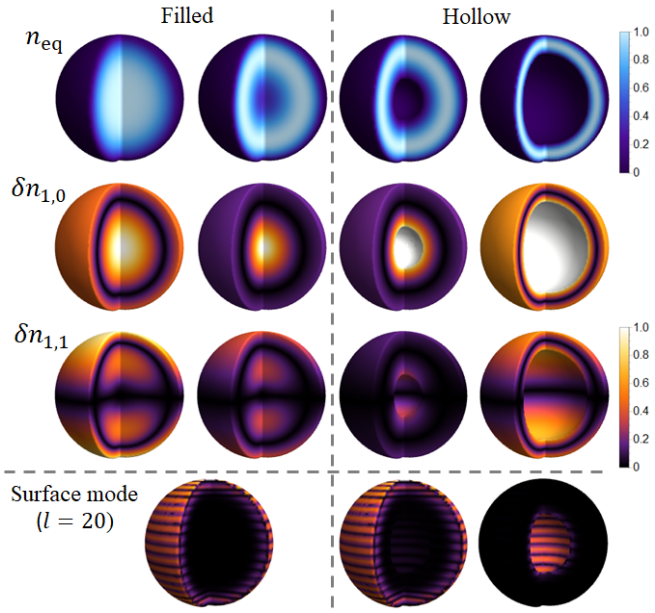

Figure 5.1: Top row: schematic equilibrium density profiles of a spherical BEC evolving from filled (left two panels) to hollow (right two) geometries. The middle two columns are close to the hollowing transition. Second and third rows: density deviation of collective modes $(\nu, \ell) = (1, 0)$ and $(1, 1)$, respectively, for the corresponding equilibrium density profile in the same column. Bottom row: density deviation of high angular momentum ($\ell = 20$) surface modes on a filled BEC (left, on the outer surface only) and a hollow BEC (right, on either the inner or outer surface). The density and density deviations are scaled by colors in the corresponding bar graph.

the hydrodynamic equations, Eq. (2.21), but applied to the numerical ground-state density. This method has the advantages of the simpler Thomas-Fermi hydrodynamic approach, but with realistic treatment of the gradually vanishing condensate boundaries. Finally, a fourth method focuses on surface modes localized to the boundary of the system by linearizing the hydrodynamic eigenproblem close to the edges of the condensate.

5.1.1 Hydrodynamic treatment for spherically symmetric condensates

First, we describe the condensate's collective dynamics in terms of small density oscillations in the hydrodynamic regime introduced in Sec. 2.3. We will use this expression for specific trap geometries under a number of assumptions about the nature of the collective modes. In this framework, to obtain Eq. (2.19), we assume that δn is small i.e. deviations away from the equilibrium density and amplitude of the collective mode oscillations are small. As a consequence any terms contributing to condensate dynamics that are greater than linear in δn are negligible. Similarly, the higher derivatives of δn are negligible if the oscillations in the condensate density are smooth, i.e., δn varies only on length scales much larger than the local coherence length $a_d\sqrt{a_d/a_s}$ where a_d is the interparticle spacing [9]. The second derivative of $n_{\rm eq}$, associated with the

kinetic energy arising from the density variation due to the trap, is also negligible in the strong interaction (Thomas-Fermi) limit. All of these factors contribute to the simplicity of Eq. (2.21) which we use a starting point here.

For traps with spherical symmetry, we can decompose $\delta n(\mathbf{r}) = D(r)Y_{\ell m_\ell}(\theta, \varphi)$, where $Y_{\ell m_\ell}$ are the usual spherical harmonics and find that Eq. (2.21) reduces to

$$\frac{mS_l^2}{U}\omega^2 r^2 D = -\frac{d}{dr}\left(r^2 n_{\rm eq}\frac{dD}{dr}\right) + \ell(\ell+1)n_{\rm eq}D. \tag{5.1}$$

Using the Thomas-Fermi equilibrium density profile of Eq. (2.11) the eigenproblem becomes

$$mS_l^2\omega^2 D \quad = \quad \frac{dV}{dr}\frac{dD}{dr} - [V(R) - V(r)] \times \left[\frac{dD^2}{dr^2} + \frac{2}{r}\frac{dD}{dr} - \frac{\ell(\ell+1)}{r^2}D\right]. \tag{5.2}$$

Here, we note that the hydrodynamic approach can be applied for any equilibrium density profile. While for the most part we will use the density obtained from the Thomas-Fermi approximation, we will use the numerical ground-state density found from the imaginary-time algorithm for comparison.

Equations (5.1) and (5.2) have analytic solutions in two limiting cases of filled sphere and thin shell, which are studied in Sec. 5.2, or can be analyzed with perturbation theory, as for the finite thin-shell case in Sec. 5.2.2 or for the gravity effects studied in Sec. 7.2. In general, our eigenproblem is of the Sturm–Liouville form and can hence be treated with a finite-difference method, whose technical details are presented in Appendix A. Our hydrodynamic results for the evolution between filled sphere and hollow shell in Sec. 5.3 and Ch. 6 are obtained from the finite-difference method.

5.1.2 Surface modes

We proceed to highlight the case of collective modes localized near the edges of the condensate—its surface modes. Following the earlier work in Ref. [105], we note that in order to identify surface modes it is appropriate to expand the Thomas-Fermi equilibrium density profile about $\mathbf{r} = \mathbf{r}_b$ for $V(\mathbf{r}_b) = \mu$, the position of the condensate boundary. Here, the Thomas-Fermi equilibrium density profile can be expressed as

$$n_{\rm eq}(\mathbf{r}) = \frac{\mathbf{F}\cdot(\mathbf{r}-\mathbf{r}_b)}{U}, \tag{5.3}$$

where $\mathbf{F} = -\nabla V(\mathbf{r}_b)$.

Denoting the direction of ∇V by x and the position of the boundary (which is a 2D equipotential surface)

by $x = x_b$, we can estimate the size of the region near the boundary within which this treatment of the condensate equilibrium density is reliable. Recalling that the Thomas-Fermi approximation follows from neglecting the contribution of the kinetic energy in the GP equation, Eq. (2.10), we estimate that kinetic energy dominates for $x_b - x \leq \delta_{\rm sm}$ where

$$\delta_{\rm sm} = \left(\frac{\hbar}{2m|\mathbf{F}|}\right)^{1/3}. \tag{5.4}$$

If the trapping potential varies slowly on the length scale $\delta_{\rm sm}$, it is then a good approximation to expand the potential and the Thomas-Fermi equilibrium density about $r = r_b$ as suggested above [9].

Next, we solve the hydrodynamic equations for the linearized potential $V(x) = Fx$ with x defined so that it vanishes at r_b. In the y and z directions, defined relative to x, there is translational invariance so a density oscillation (collective mode) described by $\delta n = \delta n(x, y, z)e^{-i\omega t}$ must correspond to a plane wave in these two variables. As in Ref. [105], we chose the z-direction as the direction of propagation of this collective excitation and denote its wave number by q. Consequently, this mode only has x and z dependences and we can rewrite the hydrodynamic equation as

$$mS_l^2\omega^2\delta n(x,z) \quad = \quad F\frac{\partial\delta n(x,z)}{\partial x} + Fx\left[\frac{\partial^2\delta n(x,z)}{\partial x^2} + \frac{\partial^2\delta n(x,z)}{\partial z^2}\right]. \tag{5.5}$$

Solutions to this expression can take the form

$$\delta n(x,z) = f(qx)e^{qx+iqz} \tag{5.6}$$

for some smooth function $f(qx)$. In this ansatz, the exponential factor in the variable x corresponds to an exponential decay away from the condensate boundary, consistent with our modeling a density oscillation concentrated at the condensate surface. We obtain the frequencies for modes described by Eq. (5.6) as

$$mS_l^2\omega_{\rm in,out}^2 = (1 + 2\nu_{\rm in,out})F_{\rm in,out}q_{\rm in,out}, \tag{5.7}$$

while the modes themselves are of the form

$$\delta n(x,y,z,t) \quad = \quad C_{\nu_{\rm in,out}}L_{\nu_{\rm in,out}}(-2q_{\rm in,out}x) \times e^{q_{\rm in,out}x + iq_{\rm in,out}z - i\omega_{\rm in,out}t},$$

where $C_{\nu_{\rm in,out}}$ is the overall magnitude and $L_{\nu_{\rm in,out}}$ are Laguerre polynomials. For these modes, indices $\nu_{\rm in,out}$ count the number of radial nodes of a collective excitation confined to a boundary surface of the BEC.

The specific behavior of surface modes, depending on the exact physical topology of the condensate, is further discussed in Sec. 5.2.3 for the limiting case of a thin hollow shell geometry and in Secs. 5.3.2 and 6.3 for the evolution between the filled sphere and hollow shell in the bubble, Eq. (4.3), and general traps, Eq. (4.4) respectively.

5.1.3 Sudden quench numerics

While the hydrodynamic treatment described above is adequate for obtaining the collective mode spectrum for all condensate geometries and trapping potentials being discussed, our numerical simulations serve as a good complement. Moreove, they capture physics beyond the hydrodynamic regime for the bubble trap geometry, which can access the filled sphere and thin shell limits as well as the evolution between them. Taking inspiration from experimental methods for exciting collective modes of trapped BECs [106], we theoretically probe the excitations of the system by direct simulation of the GP equation after a small and sudden change in the trap potential takes the system slightly out of equilibrium. These simulations were carried by Prof. C. Lannert as a part of a long-standing collaboration.

The details of the numerical approach are as follows. After first finding the numerical ground state of the GP equation describing a BEC confined by the bubble trap for one set of values of trap parameters Δ_0 and Ω_0, we time-evolve this initial state using the GP equation with different values of trap parameters Δ and Ω. This results in time-oscillating features in the time evolved condensate wavefunction $\psi(\mathbf{r}, t)$. The frequencies of these oscillations can be extracted by using a fast-Fourier transform in the time domain. For small changes ($\Delta_0 - \Delta \ll \Delta_0$ and likewise for Ω) these simulations should probe the linear response and low-lying modes of the system.

In practice, we use the explicit time-marching method of Ref. [107] to time evolve the initial numerical ground state (found in Sec. 4.3) for two types of quenches. In one case, we let $\Delta/\Omega \neq \Delta_0/\Omega_0$ change while keeping $\Delta = \Delta_0$ fixed, which fixes the mean radius of the shell but allows the tightness of the confinement to change. For a hollow shell, this quench is expected to primarily excite modes in which the thickness of the shell oscillates. Alternatively, we change $\Delta \neq \Delta_0$ while keeping $\Delta/\Omega = \Delta_0/\Omega_0$ fixed so that the tightness of the trap is constant while the mean radius of the shell varies. This method is found to equally excite modes with both even and odd values of ν (which denotes the number of radial nodes in the collective mode). The two methods agree when the same mode frequencies are resolvable. Because these quenches both preserve spherical symmetry, they only probe spherically symmetric ($\ell = 0$) modes of the system. In principle, appropriate quenches could be designed to probe nonsymmetric states as well (such as an offset of the center of the trap in the x direction, resulting in excitation of the center-of-mass modes). In what

follows, we concentrate on numerical resolution of the spherically symmetric modes only.

5.2 Collective modes: limiting cases

In this Section, we apply the hydrodynamic approach of Sec. 5.1.1 to a filled spherical condensate and a thin condensate shell. This detailed treatment establish the full frequency spectrum and associated mode behaviors of the two limiting cases for the more general system that can undergo a hollowing transition. Since this system is spherically symmetric, its collective modes can be characterized by two quantum numbers: one for the number of radial nodes, ν, and one for the orbital angular momentum denoted by the index ℓ. We find that the presence of an inner boundary in condensate shells produces features that are not found in fully filled spherical BECs even for the same quantum numbers. These results provide a check for the full evolution between these two limits when analyzing the bubble trap and other trapping potentials supporting a hollowing-out transition in subsequent Sections. Moreover, they additionally provide a better understanding of the intermediate crossover regime.

5.2.1 Filled sphere: Quadratic potential

We begin our discussion of the two limiting condensate topologies by reviewing the results of applying the hydrodynamic approach to the well-understood case of a condensate in a spherically symmetric harmonic trap, Eq. (4.1), $V_0 = \frac{1}{2}m{\omega_0}^2 S_l^2 r^2$. We assume the strong interaction regime where the Thomas-Fermi approximation is applicable.

Solving Eq. (5.2), one obtains [108, 9]

$$\omega_{\nu,\ell}^{\mathrm{sp}} = \omega_0\sqrt{\ell + 3\nu + 2\nu\ell + 2\nu^2}, \tag{5.8}$$

where ν is a radial index as above and ℓ is an index of the orbital angular momentum. We see from Eq. (5.8) that in addition to the trivial mode $\omega_{0,0}^{\mathrm{sp}} = 0$, which corresponds to a uniform density deviation but does not exist in real physical systems, any nonzero mode has frequency $\omega_{\nu,\ell}^{\mathrm{sp}} \geq \omega_0$. A schematic density deviation profile for $(\nu,\ell) = (1,0)$ $[(1,1)]$ is presented in the leftmost panel of the second (third) row of Fig. 5.1. We see that ν and ℓ count the nodes, at which the density deviation vanishes, in radial and angular directions, respectively. The $\ell = 0$ modes exhibit only the radial expansion and contraction (spherically symmetric) and are referred to as breathing modes. The $\ell = 1$ modes exhibit a center-of-mass oscillation between the southern and northern hemispheres and are referred to as sloshing or dipole modes. The breathing, sloshing, and quadrupole ($\ell = 2$) modes have been experimentally observed [106, 109, 110, 111] to be in

good agreement with the theoretical predictions.

5.2.2 Thin shell: Radially shifted quadratic potential

As discussed in Sec. 4.2, shell-shaped BECs can be realized by using a radially shifted harmonic trapping potential, Eq. (4.2),

$$V_{\rm sh}(\mathbf{r}) = \frac{1}{2} m\omega_{\rm sh}^2 S_l^2 (r - r_0)^2. \tag{5.9}$$

Here, the potential minimum – condensate density maximum – appears at $r = r_0$. Given the shell's outer radius $R = R_{\rm out} = r_0 + \delta$ and $\delta < r_0$, the Thomas-Fermi approximation yields the inner radius $R_{\rm in} = r_0 - \delta$. The condensate shell has two distinct radii, $R_{\rm in}$ and $R_{\rm out}$, in contrast to a single outer radius R for the fully filled spherical condensate. Evaluating the integral $N = \int n_{\rm eq}(\mathbf{r}) d\mathbf{r}$, we find the relationship between the total number of particles, N, and the shell's dimensionless thickness, 2δ:

$$N = \frac{8\pi m\omega_{\rm sh}^2 S_l^2}{3U} \delta^3 (r_0^2 + \frac{\delta^2}{5}). \tag{5.10}$$

If $\delta \ll r_0$, this reduces to

$$2\delta = \left(\frac{3UN}{\pi m\omega_{\rm sh}^2 S_l^2 r_0^2} \right)^{1/3}. \tag{5.11}$$

We define the "thin shell limit" by $c \equiv r_0/\delta \gg 1$ and solve Eq. (5.2) for the collective modes in this limit.

To that end, we let $\eta = \frac{r - r_0}{\delta}$ (so $-1 \leq \eta \leq 1$), $\lambda = (\omega/\omega_{\rm sh})^2$, as well as $y(\eta)/(\eta + c) = D(r)$ and express Eq. (5.2) as

$$\Big[(1 - \eta^2) \frac{d^2}{d\eta^2} - 2\eta \frac{d}{d\eta} + 2\lambda + \frac{2\eta}{\eta + c} - \ell(\ell + 1) \frac{1 - \eta^2}{(\eta + c)^2} \Big] y = 0. \tag{5.12}$$

In the limit of a very thin shell ($c \to \infty$), we can ignore the last two terms in Eq. (5.12). The solutions are Legendre polynomials $y_\nu(\eta) = \sqrt{\frac{2\nu+1}{2}} P_\nu(\eta)$ having eigenfrequencies

$$\omega_{\nu,\ell}^{\rm sh} = \omega_{\rm sh} \sqrt{\nu(\nu + 1)/2}. \tag{5.13}$$

Similar to our analysis in the filled sphere case, for the thin shell we identify nonzero breathing mode frequencies higher than the characteristic trapping frequency. In contrast to the filled case, however, thin shell collective modes characterized by differenr ℓ values are all nearly degenerate compared with the radial energy scale. The rightmost panel of second (third) row of Fig. 5.1 shows a schematic density deviation profile for $(\nu, \ell) = (1, 0)$ $[(1, 1)]$. We note that for these modes, the nodal structures is similar to the filled

sphere case. At the same time, for a very thin shell the energy associated with a collective mode is largely unaffected by the number of angular nodes. In other words, the radial behavior of the collective mode determines its eigenfrequency. We note that this degeneracy of ℓ modes has previously been shown [112] to characterize the collective modes of thin ring-shaped BECs as well. Additionally, we note that, unlike the indices $\nu_{\rm in,out}$ of Eq. (5.7), here ν denotes the number of radial zeros of a collective mode spanning the full extent of the condensate shell.

For a slightly thicker shell in which c deviates from the infinite limit, we calculate the correction to $\omega^{\rm sh}_{\nu,\ell}$ by treating the last two terms in Eq. (5.12) perturbatively. We obtain

$$\left(\frac{\omega^{\rm sh}_{\nu,\ell}}{\omega_{\rm sh}}\right)^2 = \frac{\nu(\nu+1)}{2}\left[1+\frac{4c^{-2}}{(2\nu-1)(2\nu+3)}\right]+\frac{c^{-2}\ell(\ell+1)}{4}\left[1-\frac{1}{(2\nu-1)(2\nu+3)}\right]. \tag{5.14}$$

The leading corrections to the frequency are of the order $O(c^{-2})$. In a shell with a large but finite c, the frequency spectrum of the lowest lying collective modes (low ν and ℓ indices) has the form of bands corresponding to different ν separated by $O(\omega_{\rm sh})$, with each band having fine levels corresponding to different ℓ separated by $O(c^{-2}\omega_{\rm sh})$. As a result, the two energy scales for radial and angular motions are well separated in a thin shell. As the thickness of the shell increases, the effects of the angular oscillations on its collective mode frequency and energy become more prominent.

In the $\nu = 0$ case, we obtain purely angular collective modes of the condensate shell

$$\omega^{\rm sh}_{0,\ell} = c^{-1}\omega_{\rm sh}\sqrt{\ell(\ell+1)/3}. \tag{5.15}$$

Accordingly, we expect the collective modes of a very thin shell that do not have any radial nodes to correspond to very low (but still nonzero) frequencies. Such low-frequency excitations (compared with the trap frequency) do not exist in the filled-sphere condensate.

Additionally, we note that the presence of an inner boundary for a shell condensate can have important effects on its collective modes. In the limit of large ℓ ($\gg c$), the term $\ell(\ell+1)(1-\eta^2)/(\eta+c)^2$ in Eq. (5.12) dominates. This term behaves as a potential barrier between the inner and outer boundaries $\eta = \pm 1$, respectively, and favors low-frequency modes localizing on either the inner or outer shell surface (potential minimum). This is different from the filled-sphere condensate, which does not have an inner boundary. We proceed to discuss these surface modes below, and later in Sec. 5.3.2, we show how this effect causes a sudden change in the spectrum of large ℓ modes as a bubble-trap system evolves from a filled sphere to a hollow shell.

5.2.3 Surface modes

Since the most striking difference between a fully filled spherical BEC and its hollow counterpart is the presence of an additional, inner boundary for the latter, we employ the techniques presented in Sec. 5.1.1 in order to study the collective modes localized at condensate boundaries. Noting that only hollow three-dimensional condensate structures provide more than one two-dimensional surface which can support these collective excitations, we highlight this discussion as adding new physics to know studies of surface excitations in BECs.

For collective modes localized at the outer edge of the fully filled spherical condensate it is known that [105]

$$\omega_{\nu,\ell}^{\rm sp} = \omega_0 \sqrt{\ell(2\nu+1)}. \tag{5.16}$$

This expression isexactly the large $\ell \gg 1$ limit of the collective mode frequencies given by Eq. (5.8).

To study the modes confined to the inner and outer surfaces of the hollow condensate shell we first consider the radially shifted quadratic potential of trapping frequency ω_{sh} in Eq. (4.2) and obtain

$$m S_l^2 \omega_{\rm in,out}^2 = (1+2\nu_{\rm in,out}) F_{\rm in,out} q_{\rm in,out}, \tag{5.17}$$

or, more precisely,

$$\omega_{\rm in,out}^{\rm sh} = \omega_{\rm sh} \sqrt{\ell(1+2\nu_{\rm in}) \frac{|R-r_0|}{r_{\rm in,out}}}, \tag{5.18}$$

where we identify the wave numbers $q = \ell / r_{\rm in,out}$ and calculate $r_{\rm in} = 2r_0 - R$ and $F_{\rm in,out} = \pm \omega_{\rm sh}^2 (R - r_0)$. Here, collective modes on the inner surface have a higher frequency, for the same number of radial and angular nodes (ν and ℓ), than those on the outer surface. Recalling that the radially shifted trapping potential captures the salient characteristics of thin BEC shell dynamics, we note that these expressions are only representative of condensate behavior for $r_0 \approx R$. This implies that in the thin shell limit, where the areas of the inner and the outer boundary are comparable, frequencies of surface modes hosted on either are nearly equivalent as well. At the same time, this analysis is only applicable to shells of thickness $\delta > 2\delta_{\rm sm}$ as in thinner condensate shells kinetic energy near condensate boundaries cannot be neglected [recall Eq. (5.4)] so surface modes exhibit significant overlap and thus cannot be treated as fully confined to either condensate boundary.

This thin-shell result can be compared with the case of a more general, thicker condensate shell described

by the bubble trap of Eq. (4.3). In this case, the surface modes of the condensate have frequencies given by

$$\omega^2_{\rm in,out} = \frac{\omega_0^2 \ell (R^2 - \Delta)}{\sqrt{(\Delta - R^2)^2/4 + \Omega^2}}(2\nu + 1), \tag{5.19}$$

where the wave number associated with each surface mode is $q_{\rm in,out} = \ell/R_{\rm in,out}$. In other words, for the bubble trap, $F_{\rm in}q_{\rm in} = F_{\rm out}q_{\rm out}$ leads to a degeneracy in the frequency of surface modes at the inner and outer surfaces. This degeneracy implies that for a hollow condensate with two surfaces that are separated by a substantial thickness, even though the inner surface is smaller in area, its stiffness is lower and can support more oscillations per unit distance (since $q_{\rm in} > q_{\rm out}$), bringing the frequency of oscillations with ν nodes on the two surfaces into alignment.

In terms of surface modes, we can then identify two different regimes for spherically symmetric BECs: the fully filled BEC sphere where only the outer condensate boundary is available for localization of oscillations, and a hollow BEC shell of nontrivial thickness where the oscillations confined to the inner boundary attain the same frequencies as those confined to its outer surface. In the very thin shell limit, these modes overlap, and their radial nodes do not remain well separated. In all of these regimes the form of the collective modes is functionally the same up to factors that explicitly depend on $r_{\rm in,out}$ thus capturing the effects of two boundaries and finite thickness in the case of hollow condensates. In the following Sections, we discuss the way in which these two regimes (filled and hollow) connect through a hollowing-out transition.

5.3 Collective modes: evolution from filled sphere to thin shell

In this Section, we examine the evolution of a fully filled spherical condensate to a hollow, thin shell geometry and the effect of this change in physical BEC topology on the system's collective modes. In the extreme limits of the filled sphere and thin shell, we have given analytic predictions in Sec. 5.2 above.

We start by showing that the collective mode structure progression for breathing modes as the system deforms from a filled sphere to a thin hollow shell is characterized by a distinctive feature—a dip in frequency in Sec. 5.3.1. The dip occurs at the point in parameter space when the density at the center of the condensate first begins to vanish i.e it identifies the hollowing transition. We find that at this transition, density deviations for the radial collective modes localize near the hollowing region. We argue that since the condensate density in this region is highly reduced, the stiffness associated with these modes is also lowered at this point, accounting for the reduced collective mode frequencies.

Density deviations characterized bt high angular momentum (high ℓ values) are mainly confined to the boundary surface of the condensate. They are equivalent to surface modes discussed in Sec. 5.2.3. The effect

of an emerging surface on surface mode frequencies is rather strong. In Sec. 5.3.2, we detail the evolution of the surface mode structure through the hollowing-out transition and find a distinct rearrangement of the spectrum when the inner surface first emerges. We argue that with a new surface present any nodes in the transverse (radial) direction can be distributed between the two (inner and outer) boundary surfaces. Consequently, energetic cost of hosting these nodesis reduced and mode frequencies change suddenly and dramatically.

Throughout this Section, we analyze systems in the bubble trap potential of Eq. (4.3). We begin with a survey of the evolution of the spherically symmetric mode frequencies and the corresponding condensate density distortions, using the Thomas-Fermi approximation and the hydrodynamic approach. We then corroborate and deepen this analysis using the quench numerics approach of Sec. 5.1.3. Finally, we analyze finite angular momentum modes with $\ell \neq 0$, including surface modes ($\ell \gg 1$). A more focused analysis is performed in Ch. 6 using different trapping potentials to show that the frequency dip and the surface mode redistribution are robust for a variety of spherically symmetric configurations.

5.3.1 Evolution of spherically symmetric modes in the bubble trap

We begin our analyses by solving the hydrodynamic differential problem in a bubble trap geometry in the Thomas-Fermi limit, given by Eq. (5.2), using a finite-difference method. This calculation is carried out over a range of mean shell radii $\sqrt{\tilde{\Delta}} \equiv \sqrt{\Delta}/R$ thus allowing us to obtain frequencies corresponding to the same collective mode at various stages of the evolution between a filled sphere ($\Delta = \tilde{\Delta} = 0$) and a very thin shell ($\Delta \approx R^2$ or $\tilde{\Delta} \approx 1$). We keep the outer edge of the condensate R fixed while the total number of atoms is allowed to vary—this corresponds to working with constant chemical potential μ. This analysis is expected to capture the physics of a condensate in the strong interaction limit. Finite-difference calculations have been conducted by collaborator Dr. K. Sun.

The Thomas-Fermi density profile gives densities corresponding to a filled sphere at $\tilde{\Delta} = 0$, a filled sphere with depleted central density for $0 < \tilde{\Delta} < 0.5$, and a truly hollow shell for $0.5 < \tilde{\Delta} < 1$. The thin-shell limit is $\tilde{\Delta} \to 1$. The hollow shell has an inner boundary at $R_{\rm in} = R\sqrt{2\tilde{\Delta} - 1}$, while filled geometries (regardless of central density depletion) have no inner boundary. The sharp transition between the filled and hollow systems is demarcated by the condition $\tilde{\Delta} = 0.5$. In finite-difference numerics, we section the interval $[0, R]$ ($[R_{\rm in}, R]$) for the filled (hollow) case into 2^d lattice sites and turn the relevant differential equation into a generalized eigenproblem for a finite-size $(2^d + 1) \times (2^d + 1)$ matrix (see more details in Appendix A). We choose a sufficiently large d that guarantees the convergence of the solution. The data points presented below are for $d = 16$ (unless mentioned otherwise).

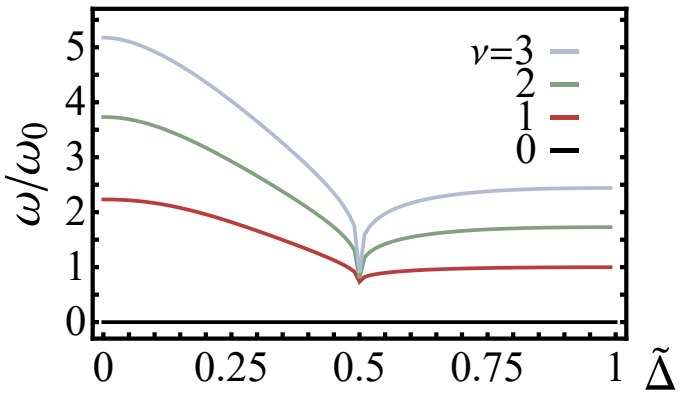

Figure 5.2: Oscillation frequencies ω, found via the hydrodynamic equation, Eq. (5.2), with Thomas-Fermi equilibrium profiles, of the three lowest-lying nonzero spherically symmetric ($l = 0$) collective modes $\nu = 1, 2, 3$ (dark red, green, and light blue curves, respectively) vs the bubble-trap detuning $\tilde{\Delta}$ [given $\Delta/\Omega = 1$ in Eq. (4.3)]. The zero mode (black) is also presented for comparison. As $\tilde{\Delta}$ increases, the BEC evolves from a filled sphere $\tilde{\Delta} = 0$ toward a hollow thin shell $\tilde{\Delta} \to 1$, through a hollowing transition at $\tilde{\Delta} = 0.5$. In the sphere and thin-shell limits, the frequencies agree with the exact solutions of Eqs. (5.8) and (5.13), respectively. Around the transition point, the collective-mode evolution is characterized by a dip in frequency, which is singular in the Thomas-Fermi approximation due to the appearance of a sharp new boundary.

In Fig. 8.6, we plot the oscillation frequencies for the lowest-lying spherically symmetric ($\ell = 0$) collective modes, including a zero mode and three nonzero modes, as a function of $\tilde{\Delta}$, representing the deformation of the condensate from a filled sphere ($\tilde{\Delta} = 0$) to a thin shell ($\tilde{\Delta} \to 1$). We recall that the zero mode $\nu = 0$, corresponding to a constant density-deviation profile and denoted in this Figure, is not physically detectable for any $\tilde{\Delta}$. We find that the collective mode frequency curves do not cross each other so that these collective modes do not become degenerate away from any non-monotonic features in the frequency spectrum. Further, we determine that the set of frequencies we have calculated can distinguish between different stages of the hollowing-out deformation. Frequency values in the two limiting cases are consistent with those predicted for the filled-sphere and thin-shell limits in Eqs. (5.8) and (5.13), respectively. There is a frequency dip in each of the three physical modes when the shell develops an inner boundary at $\tilde{\Delta} = 0.5$. The frequencies monotonically decrease (increase) with $\tilde{\Delta}$ if $\tilde{\Delta} < 0.5$ (> 0.5). We have confirmed the stability of this dip structure as the continuum limit is approached by increasing the number of simulation points up to $d = 23$. The frequency dip presents a clear signature for the hollowing transition in the system. The physical behavior giving rise to this feature is explored below and in more detail in the next Chapter.

We now turn to the behavior of the density deviations $\delta n(r)$ [recalling that the collective modes of the condensate correspond to $\delta n(\mathbf{r}) = D(r)Y_{\ell m}(\theta, \varphi)$] and their evolution as the system transitions from a filled sphere to a thin shell. In Fig. 5.3, we show δn for the lowest three modes and the equilibrium density $n_{\rm eq}$ at six values of $\tilde{\Delta}$. We see that at any stage in the evolution between the sphere and the thin shell,

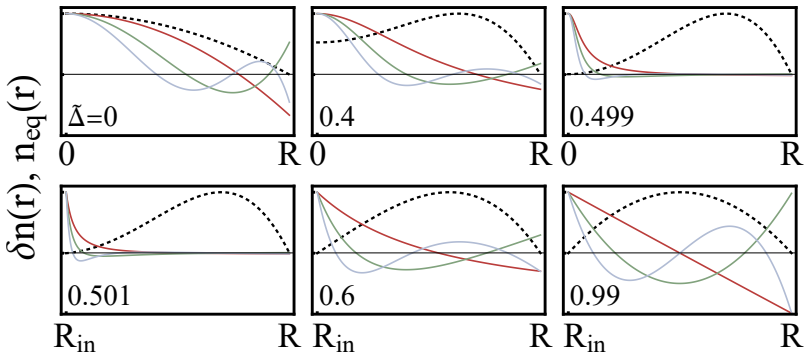

Figure 5.3: Normalized density deviation profiles $\delta n(r)$ of the three physical breathing modes in Fig. 8.6 (same convention) and equilibrium profile $n_{\rm eq}(r)$ (dashed curves). Individual panels correspond to three filled cases $\tilde{\Delta} = 0$, 0.4, and 0.499, and three hollow cases 0.501, 0.6, and 0.99 (as labeled inside). Around the hollowing-out transition, the density deviation profiles tend to concentrate on the spherical center. This is energetically favorable and related to the development of frequency dip, as discussed in Sec. 6.2.

the number of nodes in δn is always equal to the mode index ν, and the maximum excitation amplitude occurs at the center if the center is filled and at the inner boundary $r = R_{\rm in}$ if the center of the system is hollow. When $\tilde{\Delta}$ increases from zero, the central equilibrium density starts to diminish. As we approach the hollowing transition at $\tilde{\Delta} = 0.5$, the central density drops to zero and the density deviations attain large amplitudes, localizing at the center of the system. Note that we still assume a strong interaction such that the hydrodynamic approach is valid, i.e., for given scattering length a_s and characteristic interparticle spacing a_d, $a_d\sqrt{a_d/a_s}$ is small compared with the length scale of the inter-atomic interaction. For $\tilde{\Delta} > 0.5$, i.e., the hollow-shell regime, the density remains zero at $R_{\rm in}$ ($\neq 0$) and the density deviations delocalize from $R_{\rm in}$ as $\tilde{\Delta}$ increases. We recover the Legendre polynomials in the density-deviation profiles in the thin shell limit of $\tilde{\Delta} = 0.99$, as we have shown in Sec. 5.2.2.

We emphasize the frequency dip at the hollowing transition $\tilde{\Delta} = 0.5$ and the concentration of density deviations around the center as the main results of this Section. In assessing the generality of this frequency drop as a signature of a hollow condensate, realistic factors such as moderate interaction strength and nonsharp boundaries need to be taken into account.

Addressing the latter, we employ methods for analyzing collective modes beyond the Thomas-Fermi approximation (this approximation models condensate boundaries as sharp and abrupt). To that end, we recall that the hydrodynamic formalism for the BEC's dynamical behavior can be applied to any equilibrium density profile: we apply it to the numerical ground state of the GP equation. In Fig. 5.4 we plot the frequencies of the $\nu = 1, 2, 3$ spherically symmetric ($\ell = 0$) collective modes calculated by using hydrodynamic equation, Eq. (5.1), with the GP equilibrium density profile found by employing the imaginary-time algorithm. We see that the limiting behavior of the collective mode frequencies is consistent with our discussion in Sec. 5.2

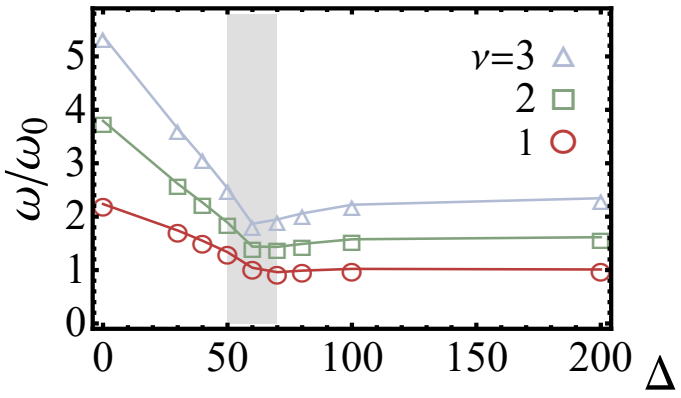

Figure 5.4: Oscillation frequencies ω, found via the hydrodynamic equation, Eq. (5.1), with equilibrium profiles given by the numerical solution to the GP equation, of the three lowest-lying nonzero spherically symmetric ($l = 0$) collective modes $\nu = 1, 2, 3$ (circles, squares, and triangles, respectively) vs the bubble-trap detuning Δ. The bubble-trap parameters are set by $\Delta/\Omega = 1$ and the interaction strength is $u = 10^4$. The equilibrium profiles corresponding to five of the data points are shown in Fig. 4.1. Compared to the Thomas-Fermi results in Fig. 8.6, the dip in frequency is softened but clearly presents a hollowing transition region (shaded region) between filled and hollow topologies.

regardless of whether we use the Thomas-Fermi density profile or the more realistic numerical GP result. The dip feature is still present, indicating the development of an inner boundary, but the GP profiles give a less sharp frequency dip compared to the Thomas-Fermi results. In fact, the transition itself spreads across a region, as opposed to a single point. The softened dip feature here reflects the transition region (shaded) between filled and hollow behaviors in analogy to its being indicative of the hollowing transition at a single point in parameter space in Fig. 8.6. The sharpness of the frequency dip in our previous calculation is associated with the use of the Thomas-Fermi approximation in which the density profile decreases to zero at condensate edges suddenly rather than gradually (as shown in Fig. 4.1). We discuss the importance of the rate of central density vanishing for signatures of the hollowing deformation in the collective mode frequency spectrum in detail in Sec. 6.2

To capture the most general physics beyond both the Thomas-Fermi approximation and the hydrodynamic approach, we perform sudden quench numerical simulations using the method described in Sec. 5.1.3. We simulate BECs throughout their evolution in a bubble-trap from a filled sphere at $\Delta = 0$ to a thin shell at large values of Δ. Figure 5.5 shows the measured frequencies of the three lowest lying nonzero spherically symmetric collective modes as a function of Δ ranging from 0 to 200, holding $\Delta/\Omega = 1$ and the total number of particles N fixed.

We highlight the general agreement of the frequency spectrum found using this method with the hydrodynamic results shown in Figs. 8.6 and 5.4. Further, we here also obtain a more rounded dip feature than that calculated by using the Thomas-Fermi approximation. This supports the idea that the sharpness

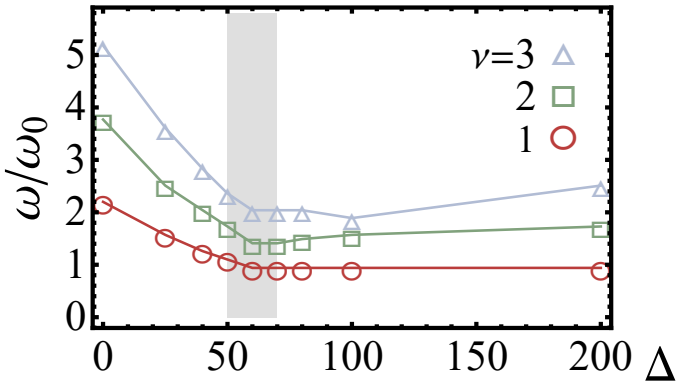

Figure 5.5: Oscillation frequencies ω, found via quench numerics, of the three lowest-lying nonzero spherically symmetric ($l = 0$) collective modes $\nu = 1, 2, 3$ (same convention as Fig. 5.4) vs the bubble-trap detuning Δ. The bubble-trap parameters are set by $\Delta/\Omega = 1$ and the interaction strength is $u = 10^4$. In going beyond the Thomas-Fermi approximation of Fig. 5.4, the singularity in the dip feature around the hollowing transition is softened and spread across the shaded region. However, the drop in frequency from the filled $\Delta = 0$ point and the asymptote to the thin-shell limit for large Δ persists and the spectrum demonstrates that the collective-mode features through the topological transition are robust beyond the hydrodynamic approximation.

of the frequency dip is related to the suddenness with which the sphere hollows as a function of Δ. We observe that the frequency of the $\nu = 1$ mode (shown in red) shows behavior very similar to the results of the hydrodynamic approach with the numerical ground state. As also found with the hydrodynamic approach applied to the numerical ground state, the frequencies of the three modes are well separated when the sphere hollows out, i.e., at the value of Δ where the frequency dips.

Figure 5.6 shows condensate density deviations from equilibrium determined by numerical time evolution after a quench for values of Δ that results in the deformation from the filled sphere to the thin shell. These density deviations generally reflect those found from the hydrodynamic approach in the Thomas-Fermi approximation (Fig. 5.3) – they also show localization of oscillations to the inner boundary for $\Delta \approx 60$ where the frequency dip occurs as the center of the system becomes hollow.

Arguably these numerical results are more representative of true physical behavior of an experimental system than those obtained using the hydrodynamic approach, which involves a number of previously noted assumptions. The similarity between the two results, especially prominent for hollow shells, justifies the use of the more numerically efficient Thomas-Fermi hydrodynamic approximation. Most importantly, it corroborates our prediction that the dip in the frequency at the values of Δ where the system transitions between the filled sphere and hollow shell is a physical feature that could be observed in an experimental setting.

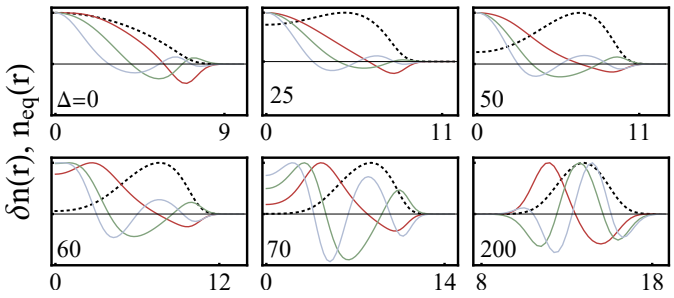

Figure 5.6: Density deviation profiles $\delta n(r)$ of the three breathing modes in Fig. 5.5 (same convention) and equilibrium profile $n_{\rm eq}(r)$ (dashed curves). Individual panels correspond to $\Delta = 0$, 25, 50, 60, 70, and 200 (as labeled inside). The radial coordinate (x axis) is presented in the same units as Fig. 4.1. Similar to the hydrodynamic results in Fig. 5.3, the density deviation profiles tend to concentrate (but less significantly so) around the spherical center in the hollowing transition region.

5.3.2 Evolution of modes having $\ell \neq 0$ in the bubble trap

We turn to examining the evolution of collective modes having $\ell \neq 0$ as the condensate is hollowed. In contrast to the discussion in the previous Section, these modes exhibit angular oscillations and are not spherically symmetric. Considering high ℓ modes in general, we note that in the eigenvalue problem of Eq. (5.1) or (5.2), the nonzero ℓ brings in the term $[V(R)-V(r)]\ell(\ell+1)/r^2 \propto n_{\rm eq}(r)\ell(\ell+1)/r^2$, often called a "centrifugal" term because of its relationship with the angular momentum of the system. Without this term ($\ell = 0$), the right-hand side (RHS) of Eq. (5.2) has only r-derivative terms, which naturally guarantee a (unphysical) zero-frequency mode $\nu = 0$ having a uniform density-deviation profile. We show below that this mode shifts to a finite frequency and hence becomes a physical solution as the centrifugal term contributes for any nonzero ℓ. In addition, if ℓ is large enough such that the centrifugal term dominates over the derivative terms, we expect the low-frequency modes to be strongly affected by the potential minima, which correspond to condensate boundaries where $n_{\rm eq} = 0$. In this case, a filled condensate with only an outer boundary is quite different from a hollow condensate which has both an inner and an outer boundaries. The high-ℓ collective modes can consequently drastically change when the (bubble-trap) system starts to hollow out.

To pin down the effect of increasing ℓ on the collective mode response to the hollowing-out transition, we first study the simplest, $\ell = 1$, case. Figure 5.7(a) shows the $\nu \leq 3$ modes obtained from the hydrodynamic approach using Thomas-Fermi equilibrium profiles. We see that the $\nu = 0$ mode here has a finite (and hence physically detectable) frequency that is of the order $O(\omega_{\rm sh})$ on the filled-sphere side and almost zero in the thin-shell limit, in agreement with the limiting cases studied in Secs. 5.2.1 and 5.2.2. The monotonically decreasing frequency curve also shows how these two different energy scales continuously connect through

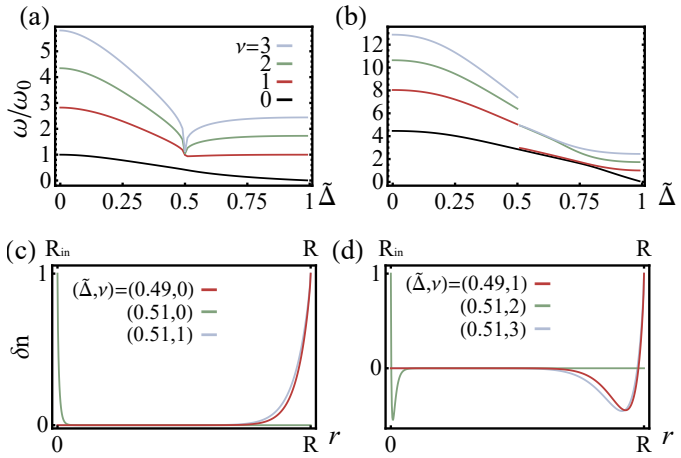

Figure 5.7: **(a)** [**(b)**] Oscillation frequencies ω vs $\tilde{\Delta}$ for $\ell = 1$ ($\ell = 20$) and $\nu = 0, 1, 2, 3$ (same convention as Fig. 8.6). The $\ell = 1$ (low-ℓ) modes exhibit similar features, including the dip across the hollowing transition $\tilde{\Delta} = 0.5$, as the $\ell = 0$ modes in Fig. 8.6, except that the $\nu = 0$ mode here has nonzero frequency. The $\ell = 20$ (high-ℓ) modes exhibit sudden drops at the transition. **(c)** Density deviation profiles δn corresponding to one mode $(\tilde{\Delta}, \nu) = (0.49, 0)$ (dark red) right before the hollowing (axis on bottom), and two modes $(0.51, 0)$ (green) and $(0.51, 1)$ (light blue) right after it (axis on top) in panel **(b)**. **(d)** Same convention as panel **(c)** except for modes $(0.49, 1)$ right before the hollowing and $(0.51, 2)$ and $(0.51, 3)$ right after it. Panels **(c)** and **(d)** confirm that the high-ℓ modes are surface modes—with density deviation localizing around the condensate surfaces. Before the hollowing ($\tilde{\Delta} = 0.49$), the density deviations of all modes localize around the only surface $r = R$, while after the hollowing ($\tilde{\Delta} = 0.51$), half of them remain around the outer surface $r = R$ and the other half redistribute around the emerging inner surface $r = R_{\rm in} \approx 0$.

the deformation. The three $\nu > 0$ modes exhibit qualitative features and dip structures similar to those of the $\ell = 0$ case, except the filled-sphere frequencies in the $\ell = 1$ case increase by $O(\omega_{\rm sh})$ due to the angular oscillation.

We next study a large-ℓ case where the centrifugal term dominates. Figure 5.7(b) shows the same $\nu \leq 3$ modes for $\ell = 20$. We see that the $\nu = 0$ curve again continuously decreases to zero as we proceed from the filled sphere to the thin shell. For the $\nu > 0$ modes, the dip structure disappears, and all frequency curves exhibit a sudden drop as the hollowing occurs at $\tilde{\Delta} = 0.5$. The $\nu = 1$ mode makes a drop to become nearly degenerate with the $\nu = 0$ mode, and the $\nu = 2$ and $\nu = 3$ modes become equal and continue the evolution of the $\nu = 1$ mode before the drop. In fact, the νth mode right before the hollowing point and the (2ν)th and $(2\nu + 1)$th modes right after it are nearly degenerate such that the νth-mode frequency curve appears to split into two upon the hollowing transition.

We further investigate this splitting in the high-ℓ spectrum by comparing the radial density-deviation profiles $\delta n(r)$ of three nearly degenerate modes—one just before the hollowing ($\tilde{\Delta} = 0.49$) and two just after the hollowing ($\tilde{\Delta} = 0.51$). In panels (c) and (d) of Fig. 5.7 we plot the density deviation profiles for six specific modes corresponding to oscillation frequency curves in Fig. 5.7(b). From these calculations, it is

evident that before the hollowing transition, the modes concentrate near the outer boundary. After hollowing one of the nearly degenerate pair modes localizes near the outer boundary while the other does near the newly created inner boundary. This indicates that the inner minimum of the centrifugal term provides a hollow condensate with additional degrees of freedom for accommodating its collective modes. As the shell becomes thinner, the pair of nearly degenerate modes further split due to a coupling between them through the r-derivative terms in Eq. (5.2).

To summarize, our work here shows that the frequencies of pure angular modes ($\nu = 0$, $\ell \neq 0$) of a spherical condensate decrease during the evolution to a shell condensate and that high angular modes qualitatively change when the inner boundary is created. These results may lead to development of non-destructive methods for experimental observation of the change in central density structure of hollowing three-dimensional condensates. The following Chapter builds on this work by more rigorously connecting the properties of non-monotonic features in the frequency spectra of all collective modes (characterized by both $\ell = 0$ and $\ell \neq 0$) to the rate of decrease of central condensate density as the system undergoes the hollowing-out transition.

Chapter 6

The Hollowing-Out Transition

In this Chapter, we use the generalized radially shifted trapping potential of Eq. (4.4) in order to study the signatures of the hollowing transition for a range of spherically symmetric condensate geometries. These geometries differ in the rate of decrease of the equilibrium density of the BEC near the system's center where the hollowing-out takes place. Below, we provide physical interpretations for the universal nonmonotonic signatures of the hollowing transition in the BEC collective mode frequency spectrum as well as for the more detailed features of these signature that depend on specific hollowing-out conditions.

In Sec. 6.1, we discuss the general radially shifted potential given in Eq. (4.4) characterized by the two parameters γ, which tunes the BEC geometry from filled sphere to hollow shell, and α, which controls the decay of the equilibrium density near the center of the system as it hollows. In Sec. 6.2, by varying the behavior of the central density, we show that the radial collective mode spectrum exhibits a universal dip at the hollowing transition, but that the sharpness of the dip depends on α. We further present an energetic argument followed by a variational calculation lending insights into the concentration of density deviations near the hollowing center associated with the frequency dip. In Sec. 6.3, we show that while the hollowing transition always leads to additional surface modes on the inner surface, the mode frequencies depend on the surface stiffness, which in turn depends on α. The frequency degeneracy of the inner and outer surface modes, which we have observed in the bubble trap, corresponds to a special case where $\alpha = 2$. In Sec. 6.4, we study the hollowing-out physics in a 2D system and show that the collective-mode features are dimension independent.

6.1 General radially shifted potential and density effects

In this Chapter we focus on the trapping potential given in Eq. (4.4):

$$V_{\rm gt}(r) = \frac{1}{2} m\omega_{\rm gt}^2 R^2 S_l^2 \Big[\Big(\frac{r}{R} \Big)^{\alpha} - \gamma \Big]^2,$$

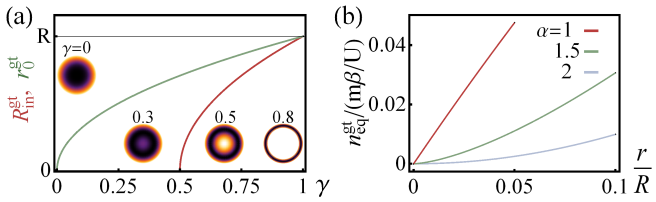

Figure 6.1: **(a)** Thomas-Fermi inner boundary $R_{\rm in}^{\rm gt}$ (dark red) and maximum-density position $r_0^{\rm gt}$ (green) vs γ for a condensate in the general trap, given by Eq. (4.4) for $\alpha = 2$. Insets from left to right: schematic density profiles of the condensate at $\gamma = 0$, 0.3, 0.5, and 0.8, respectively. **(b)** Thomas-Fermi density profiles $n_{\rm eq}^{\rm gt}(r)$ around the center for $\alpha = 1$ (dark red), 1.5 (green), and 2 (light blue) at the hollowing transition $\gamma = 0.5$.

where γ is a dimensionless parameter that tunes the condensate between sphere and shell geometries, α tunes the condensate equilibrium density profile near the hollowing center, and R specifies a characteristic size of the BEC.

To understand the geometry of a condensate confined by this trap, we focus on the Thomas-Fermi density profile,

$$n_{\rm eq}^{\rm gt}(\mathbf{r}) = n_0^{\rm gt}\left[1-\left(\frac{r}{R}\right)^{\alpha}\right]\left[\left(\frac{r}{R}\right)^{\alpha}-(2\gamma-1)\right], \tag{6.1}$$

with an overall magnitude $n_0^{\rm gt} = m(\omega_{\rm t}^{\rm gt})^2 S_l^2 R^2/(2U)$. The condensate has its outer boundary at $r = R$ (where $n_{\rm eq}^{\rm gt}$ vanishes) and its density maximum at $r = \gamma^{1/\alpha}R \equiv r_0^{\rm gt}$. This density profile shows that the general trap produces a filled sphere condensate for $\gamma = 0$, a thin-shell condensate for $\gamma \to 1$, and transitions between them as γ is varied.

At $\gamma = 0$, the condensate has a fully-filled spherical geometry with density $n_{\rm eq}^{\rm gt} \propto 1-(r/R)^{2\alpha}$. This equilibrium density profile monotonically decreases as one moves radially out (away) from the origin. As γ starts to increase from zero, the maximum density position shifts to a finite radius. For $0 < \gamma < 0.5$, the condensate density at the origin, $n_{\rm eq}^{\rm gt}(0) = n_0^{\rm gt}(1-2\gamma)$, remains finite and the origin is a local density minimum. At $\gamma = 0.5$, the condensate density at the origin becomes zero, signaling the transition from filled to hollow geometry. For $\gamma > 0.5$, the system is a hollow shell having an inner boundary at

$$R_{\rm in}^{\rm gt} = (2\gamma-1)^{1/\alpha}R. \tag{6.2}$$

As $\gamma \to 1$, the condensate approaches the thin-shell limit, where $V^{\rm gt}(\mathbf{r})$ can be approximated by the thin-shell potential of Eq. (4.2) having parameter values $r_0 = r_0^{\rm gt}$ and $\omega_{\rm t}^{\rm sh} = \gamma^{1-1/\alpha}\alpha\omega_{\rm t}^{\rm gt} \sim \alpha\omega_{\rm t}^{\rm gt}$ (and hence $c = 1/[\gamma^{-1/\alpha}-1] \gg 1$).

In Fig. 6.1(a), we plot the Thomas-Fermi inner boundary $R_{\rm in}^{\rm gt}$ and the maximum-density position $r_0^{\rm gt}$ as

a function of the parameter γ and schematic density profiles (insets) for $\alpha = 2$ (quartic double-well) case. These curves show both functions evolving continuously, while the schematics show the density at four stages of the evolution: sphere ($\gamma = 0$), thick shell with filled center (0.3), thick shell at the hollowing transition (0.5), and thin shell (0.8). The variable α determines the power law of the equilibrium profile's growth at the center of the system as $n_{\rm eq}^{\rm gt} \propto r^{\alpha}$. In Fig. 6.1(b), we plot the Thomas-Fermi profiles near the center of the system at the hollowing transition ($\gamma = 0.5$) for various α. For the bubble-trap potential, the Thomas-Fermi density corresponds to $\alpha = 2$, while the numerical GP solution behaves as $\alpha < 2$ since the condensate wave function has a continuous "tail" at its boundaries.

In Sec. 5.3, we discussed the collective mode frequency spectra for breathing modes in the Thomas-Fermi approximation and using the numerical ground state density, for the hollowing transiton achieved by using the bubble-trap potential. We found some universal features (e.g., a dip in the frequency spectrum), as well as some notable differences (e.g., the sharpness of the dip). Here, we analyze the collective modes in the general potential of Eq. (4.4) while varying α with the explicit aim to distinguish between universal signatures of the hollowing transition from those that depend on the central density profile. In the following two Sections, we present a detailed analysis of the effect of α on the spectra of the purely radial and surface collective modes. We note that for $\alpha \leq 1$, the density profile has a kink (discontinuity in its derivative) at the center, which leads to divergent kinetic energy density $|\partial_r \psi(0)|^2$ and is hence unphysical. Consequently, in what follows we only consider $\alpha > 1$.

6.2 Spherically symmetric modes at the hollowing transition

In our previous discussion we identified a dip in the frequency spectrum of radial collective modes when the spherical BEC in bubble trap starts to hollow out at its center in calculations carried out by using both the hydrodynamic treatment and sudden quench numerics. However, the results based on a Thomas-Fermi equilibrium density profile show a sharper dip (as in Fig. 8.6) than those based on densities obtained by numerically solving the GP equation (as in Figs. 5.4 and 5.5). Additionally, for values of Δ near the hollowing transition, the former have density deviations more localizing near the trap center ($r = 0$) than the latter. Since the most significant difference between the Thomas-Fermi and GP equilibrium density profiles lies in the central region at the hollowing transition, and the concentrated density deviations are mainly determined by the equilibrium density near the center [through Eq. (2.20)], it is reasonable to hypothesize that the shape of central equilibrium density and the sharpness of the frequency dip are closely related. In this Section, we use the general-trap profile of Eq. (6.1) to verify this relationship and confirm that the GP equilibrium

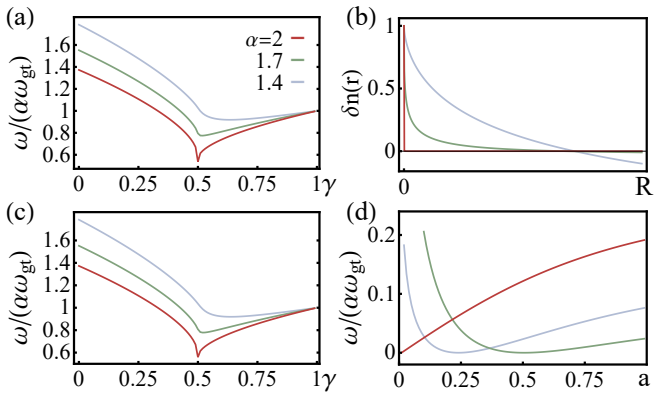

Figure 6.2: **(a)** Oscillation frequencies ω for the lowest nonzero breathing mode ($\nu = 1$, $\ell = 0$) as a function of γ for $\alpha = 2$ (dark red), 1.7 (green), and 1.4 (light blue), obtained by solving the hydrodynamic equation for the general-trap Thomas-Fermi profiles in Eq. (6.1). **(b)** The corresponding density deviation profiles δn at the hollowing transition, $\gamma = 0.5$. **(c)** Oscillation frequencies ω obtained from the variational method. **(d)** Variational frequency function at $\gamma = 0.5$. Panels (b)–(d) have the same convention as panel (a). Panels (a) and (b) show the dependence of the frequency dip sharpness and the concentration of density deviation profiles on the growth rate of the equilibrium density profile from the hollowing-out center. Panels (c) and (d) show that the dependence originates from the orthonormality and energy minimization of collective mode.

density profile leads to a less sharp frequency dip. Such a rounded dip should better characterize results in real experimental systems. We further provide evidence that the frequency dip is always accompanied by the concentration of density deviations at the hollowing transition based on energetics arguments and a variational calculation.

The shape of the central density of a hollowing condensate can be characterized by a power-law index α, such that $n_{\rm eq}(r) \propto r^{\alpha}$. As we have shown in Sec. 6.1, the general-trap potential can both tune through the sphere-to-shell evolution and control the index α. It is therefore ideal for studying the effects of differing central density depletion rates during the hollowing transition. In other words, tuning α at $\gamma = 0.5$, the transition point between filled and hollow topologies, can help theoretically isolate the effects of the central density growth ($\propto r^{\alpha}$). For a bubble-trap potential, the central Thomas-Fermi profile varies as r^2 when the system is hollowing out. However, the solution of the GP equation is distinctly different due to relatively smooth "tail" near the center associated with a relatively large kinetic energy contribution in this region, which is ignored in the Thomas-Fermi approximation. A more realistic description of the frequency dip in a bubble traps can then be captured by the density growth of modified profile with $\alpha < 2$ than by the original Thomas-Fermi approach.

Figure 6.2(a) shows the frequency of the lowest nonzero radial collective mode ($\nu = 1$, $\ell = 0$) as a function of γ at various $\alpha \leq 2$, obtained by hydrodynamics calculations. The frequency dip we have already underlined in previous calculations is clearly identifiable near $\gamma = 0.5$ in all three curves, but its sharpness

changes with the growth rate α. More precisely, we see that for $\alpha < 2$, the frequency-dip structure is smoother and the minimum-frequency point shifts slightly to $\gamma > 0.5$. In Fig. 6.2(b), we plot the density deviation profiles $\delta n(r)$ corresponding to each α in Fig. 6.2(a) at $\gamma = 0.5$. We see that the density deviations become less concentrated at the center as α decreases from 2. As a result, the $\alpha = 2$ density growth, leading to sharp frequency dips and highly concentrated density deviations, agrees with the results for a bubble-trap system and Thomas-Fermi density profiles (as in Figs. 5.3 and 5.4). On the other hand, the $\alpha < 2$ density growth, leading to less sharp frequency dip and less concentrated density deviations, agrees with the results using the numerically calculated GP density profiles (as in Figs. 5.4, 5.5, and 5.6). Thus, the general-trap model captures the main features of the spherically symmetric collective mode frequency spectra during the hollowing transition. We conclude that for a bubble-trap system, using the Thomas-Fermi profile in a general trap and setting $\alpha < 2$ can mimic the more realistic GP profile without the need for numerics.

We proceed to discuss the relationship between the frequency dip and the concentration of density deviations at the hollowing transition. To that end, we first provide an energetic argument for interpreting the frequencies of the collective modes. The νth collective mode has a radial density deviation profile that is orthogonal to all the lower-frequency modes and minimizes the energy (frequency). This is a direct result of the orthonormality of the eigen-solutions of Eq. (2.20) re-written in dimensionless units as

$$-\frac{mS_l^2}{U}\omega^2\delta n = \nabla n_{\rm eq}\cdot\nabla\delta n + n_{\rm eq}\nabla^2\delta n.$$

We see from Eq. (2.20) that the equilibrium density profile contributes to two terms, $n_{\rm eq}$ and $\nabla n_{\rm eq}$. For most of the evolution from a filled sphere to a thin shell, these two terms are not simultaneously zero: at the filled center $\nabla n_{\rm eq}(0) = 0$ but $n_{\rm eq}(0) \neq 0$, and at the inner boundary of a fully hollow shell, $n_{\rm eq}(R_{\rm in}) = 0$ but $\nabla n_{\rm eq}(R_{\rm in}) \neq 0$. At least one of these two terms increases the energy (frequency) and hence disfavors the concentration of density deviations.

However, when the system is at the hollowing transition, both of these terms can become very small in the central region, i.e., the whole differential operator on RHS of Eq. (2.20) nearly vanishes. In this case, a concentration of density deviation profiles near the center of the system will have a very small energy (frequency) expense and should hence be favored in the low-frequency modes of the system. By the same argument, density deviation profile spreading away from the center will result in a higher frequency and be more energetically costly. This very small contribution from the RHS of Eq. (2.20) also leads the mode frequencies to be much lower than those in the fully-filled sphere and the very thin hollow shell (where either $n_{\rm eq}$ or $\nabla n_{\rm eq}$ contributes)—hence forming a dip in the frequency spectrum.

We strengthen this energetic argument by solving Eq. (5.1) for the first breathing mode ($\nu = 1, \ell = 0$) by a variational calculation. We consider a variational density deviation profile $D_1(r)$ that has one node ($\nu = 1$) and is orthogonal to the zero mode ($\nu = 0$) with a uniform density deviation D_0. We then solve for $D_1(r)$ by minimizing the oscillation frequency functional. Our variational ansatz reads,

$$D_1(r) = \frac{1}{(r/a)^2 + 1} - b. \tag{6.3}$$

This density deviation profile has a node at $r = a\sqrt{b^{-1} - 1}$. Orthogonality to the zero mode can be guaranteed by choosing b such that $\int D_0 D_1(r) r^2 dr = 0$. With this ansatz, we compute the frequency ω as the expectation value of the differential operator of Eq. (5.1), namely,

$$\frac{mS_l^2}{U}\omega^2 = \frac{\int n_{\rm eq}(\partial_r D_1)^2 r^2 dr}{\int D_1^2 r^2 dr}. \tag{6.4}$$

The solution, the form of D_1, can then be obtained by minimizing ω with respect to the only free parameter a.

In Fig. 6.2(c), we plot variational results for various values of α. We see that the frequency dips upon the hollowing out and that the dependence of dip sharpness on the density profile is identical to results in Fig. 6.2(a) given by the hydrodynamic equation. In Fig. 6.2(d), we plot the frequency of this mode at the hollowing transition, $\gamma = 0.5$, as a function of the variational parameter a, which is also the full width at half maximum of the density deviation profile. In the $\alpha = 2$ case (with a sharp dip in the spectrum), $a \to 0$ directly leads to the minimization of frequency, which causes density deviations to be localized at the center of the system. For $\alpha < 2$ cases (exhibiting a more smooth dip feature), the frequency minimization occurs at nonzero a, giving density deviations with some small, but nonzero, width. These variational results not only agree with those given the hydrodynamic equation but also corroborate the energetic argument that the density deviations localizing near the hollowing center is directly related to the dip in frequency.

We conclude that independent of the specific shape of the confining trap, any condensate system that transitions between a filled sphere and a hollow shell will display a universal signature of the hollowing. Specifically, radial collective mode spectrum generically exhibits a frequency minimum at the hollowing transition. This is a rather remarkable result since it allows one to deduce the appearance of a hollowing region deep within the condensate by imaging lowest-lying collective excitations of the system, which can be observed on even the outer surface, possibly even nondestructively.

6.3 Surface modes at the hollowing transition

We now turn to large-ℓ collective modes, which manifest themselves as distortions localized near the boundary i.e. the condensate's surface modes [105]. Localization of these modes to boundaries is due to the dominant centrifugal term $\ell(\ell+1)n_{\rm eq}$ in Eq. (5.1), which becomes small only near the boundary, where $n_{\rm eq}=0$. A hollow spherical shell supports similar minima in this term on both its inner and outer surfaces. When the system transitions from being fully-filled to being hollow, the creation of the new inner boundary enables localization of large-ℓ density deviations to the inner surface. The availability of the emerging surface doubles the surface mode spectrum such that half of modes remain at the outer surface but the other half redistribute to the inner surface.

Surface mode frequencies are determined by the properties of the surfaces, as discussed in Sec. 5.2.3 and seen specifically in Eq. (5.7). Focussing on the general-trap potential in the shell region, $\gamma \geq 0.5$, we linearize the trapping potential and the corresponding Thomas-Fermi equilibrium density close to the inner and outer boundaries, $R_{\rm in}$ and $R_{\rm out}=R$, respectively, in order to find

$$n_{\rm eq}^{\rm TF}(x_{\rm in,out}) = -\frac{F_{\rm in,out}}{U}x_{\rm in,out}, \tag{6.5}$$

with $F_{\rm in,out} = -\nabla V_{\rm gt}(R_{\rm in,out})$ and $x_{\rm in,out} \leq 0$ the local variable pointing along the direction of $F_{\rm in,out}$. Employing the equilibrium density profile of Eq. (6.1) to leading order in $|r-R_{\rm in,out}|$ in the hydrodynamic equation of motion, Eq. (5.5) yields the wave number associated with each surface mode given by $q_{\rm in,out} = \ell/R_{\rm in,out}$ and

$$\begin{aligned}
\omega_{\rm out}^2 &= \alpha\omega_{\rm gt}^2 S_l^2 \ell(1-\gamma)(2\nu_{\rm in,out}+1),\\
\omega_{\rm in}^2 &= \alpha\omega_{\rm gt}^2 S_l^2 \ell(2\gamma-1)^{1-2/\alpha}(1-\gamma)(2\nu_{\rm in,out}+1).
\end{aligned} \tag{6.6}$$

As before, indices $\nu_{\rm in}$ and $\nu_{\rm out}$ in these expressions count the nodes of radial oscillations confined to the inner or the outer boundary surface, respectively (rather than counting the total number of radial nodes $\nu_{\rm in}+\nu_{\rm out}$ across the entire shell which is denoted by ν).

We note that for the $\alpha=2$ case [including the bubble-trap one in Fig. 5.7(b)], there is a degeneracy in the frequency of surface modes at the inner and outer surfaces: $\omega_{\rm in}^2=\omega_{\rm out}^2$. If $\alpha\neq 2$, this double degeneracy no longer exists, but the frequency spectrum still exhibits a clear drop due to the mode redistribution to the newly emerging inner surface. In Fig. 6.3(a) [Fig. 6.3(b)], we plot the oscillation frequency spectrum of the high-angular-momentum mode $\ell=20$ for the general-trap case with $\alpha=2$ (1.85). We see that near

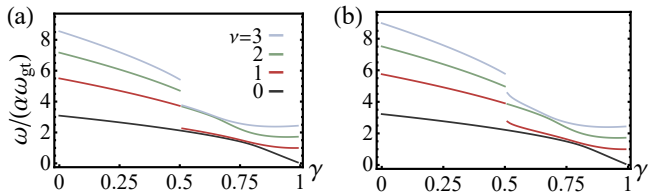

Figure 6.3: **(a)** [**(b)**] Oscillation frequencies ω of high-angular-momentum modes $\ell = 20$ in the general-trap case vs γ for $\nu = 0, 1, 2, 3$ (same convention as Fig. 8.6) and $\alpha = 2$ (1.85). Comparing (a) and (b), we see that the sudden drop of surface-mode frequency is a universal feature for the hollowing transition, but the degeneracy between outer and inner surface modes of hollow condensates only occurs at $\alpha = 2$.

the hollowing-out region $\gamma \gtrsim 0.5$, the double degeneracy occurs at $\alpha = 2$ but no longer exists at $\alpha = 1.85$, in agreement with the surface-mode characteristics in Eq. (6.6). In the thin-shell region $\gamma \lesssim 1$, the modes strongly couple with each other and are no longer degenerate (neither localize near the surface anymore). The restructuring of the large-ℓ surface mode spectrum is a direct and universal signature of a newly emerging surface and hence the hollowing transition.

We conclude this part of our discussion by emphasizing two main results.First, we find that the sharpness of the dip in the collective mode frequency spectrum at the hollowing transition depends on the rate of central condensate density decay. Consequently, the experimentally observed spectrum should also exhibit a universal dip upon the transition, regardless of its deviation from the very idealized Thomas-Fermi equilibrium density profile. More precisely, the dip is less sharp than the predictions using Thomas-Fermi approximation as the more realistic equilibrium density distribution have continuous "tails" at the boundaries. Second, we conclue that while the sudden drop of the surface-mode spectrum is a universal signature of the emergence of an additional surface upon the hollowing transition, the double degeneracy between inner and outer surface modes of a hollow shell only occurs for specific geometries, including that of the bubble-trap confinement.

6.4 The hollowing transition in two dimensions

We end this Chapter by investigating whether the hollowing-out physics we have found for a 3D spherical system also occurs in an analogous 2D geometry as a natural extension of our study of universal signatures of such a transition. In more detail, we obtain the collective-mode frequency spectra of a condensate in a 2D bubble trap, which realizes the hollowing transition from a filled disk to a hollow ring. The trap takes the same form as the 3D bubble trap of Eq. (4.3) except the coordinates are restricted to the x-y plane ($z = 0$). The 2D density deviation profile for a circularly symmetric condensate has the form $\delta n(\mathbf{r}) = D(r)e^{i\ell\phi}$.

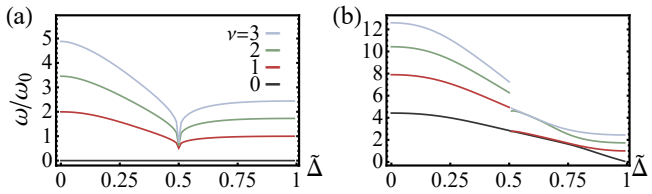

Figure 6.4: **(a)** [**(b)**] Oscillation frequencies ω of a 2D condensate vs 2D bubble-trap parameter $\tilde{\Delta}$ for breathing modes $\ell = 0$ (edge modes $\ell = 20$) and $\nu = 0, 1, 2, 3$ (same convention as Fig. 8.6). Both panels show the same collective-mode features in the filled-to-hollow evolution and upon the hollowing transition as in 3D cases, indicating that the hollowing-out physics is dimension independent.

Employing this form in hydrodynamical equation of Eq. (5.1) yields the differential eigenequation,

$$\frac{mS_l^2}{U}\omega^2 rD = -\frac{d}{dr}\left(rn_{\rm eq}\frac{dD}{dr}\right) + \frac{\ell^2 n_{\rm eq}}{r}D. \tag{6.7}$$

In Fig. 6.4, we show the 2D collective-mode spectrum for the Thomas-Fermi equilibrium density profile $n_{\rm eq}$, which exhibits a sharp hollowing transition at $\tilde{\Delta} = 0.5$ (just as in the 3D case). Panel (a) shows that the breathing mode ($\ell = 0$) frequencies are nonmonotonic as a function of $\tilde{\Delta}$ – they develop a sharp dip at the 2D hollowing transition. A variational analysis confirms that the frequency dip in this 2D system can be derived from the orthonormality and energy minimization of the collective modes and is associated with the density deviation concentrating in the central hollowing region. Figure 6.4(b) shows that the high-ℓ ($\ell = 20$) mode frequencies exhibit a sudden drop at the transition. Examining the density deviation profiles, we find that the high-ℓ modes are edge modes, analogous to the surface modes in the 3D case. The frequency drop of these edge modes at the hollowing transition results from the redistribution of half of the radial nodes to the emerging inner edge of the ring. Performing a similar analysis for the edge modes in this disk geometry as we did for the surface modes in the spherical geometry, we confirm that the degeneracy of outer and inner edge modes in the hollow region is due to the quadratic growth rate of the equilibrium density profile from the center, a specific property of the bubble trap.

In summary, by considering a radially symmetric system in two dimensions, we see that signatures of the hollowing transition exhibited by the collective-mode spectrum are the same in both three and two dimensions. This indicates that the signatures are due to the physics of central hollowing, rather than details of geometry or dimension. We remark that both disk-shaped and ring-shaped BECs have been well studied theoretically [112, 113] and experimentally [26, 25]. The transition regime between these 2D topologies is potentially achievable but has not been studied, to our knowledge. Our findings not only detail the collective-mode physics in the transition regime but also reveal universal features in hollowing-out condensate systems.

Chapter 7

Effects of Gravity on Hollow BECs and Experimental Concerns

So far we have examined equilibrium profiles and dynamical behavior of spherically symmetric BECs as their real-space topology is changed from filled to hollow. We now turn to a discussion of gravitational effects which cannot be neglected in experimental shell traps on Earth. Crucially, unlike in a harmonically trapped system, in a shell-shaped trapped system the gravitational force tends to cause sag: mass accumulation at the lower vertical points in the system and a depletion around the highest. This gravitational sag has been experimentally shown to produce quasi-two-dimensional systems having no closed shell-like surfaces, and strong confinement in the direction of gravitational acceleration, under ordinary gravitational conditions on Earth [97, 96]. In Sec. 7.1, we estimate the gravitational strength at which the density of the top region of the condensate becomes completely depleted for a thin-shell geometry within the Thomas-Fermi approximation. Further, we calculate the precise value for the critical number of atoms needed to produce a closed thin-shell structure given some gravitational field in its environment. Turning to dynamics in Sec. 7.2, we analyze the effect of low gravity on the collective mode structure of a very thin condensate shell by using a perturbative treatment. We find that gravity couples modes with adjacent angular momentum indices. This is consistent with the fact that a condensate shell in a gravitational field is not fully spherically symmetric. Our estimates show that for typical cold atomic experimental settings, microgravity facilities are the most promising for studying the rich collective mode structure of closed condensate shells. We explicitly present some of these estimates as well as calculate other experimentally relevany quantities such as atomic densities and collective mode frequencies in Sec. 7.3.

7.1 Behavior of equilibrium density and open shells

First, we identify the condition for treating gravity as a small effect compared to the strength of interactions between the atoms in the condensate. We work in the strong interaction and thin shell limits of the radially shifted harmonic potential discussed in Sec. 5.2.2. This geometry can be achieved by the bubble trap of Eq. (4.3). In order to arrive at this condition, we consider the case in which the effect of gravity shifts the

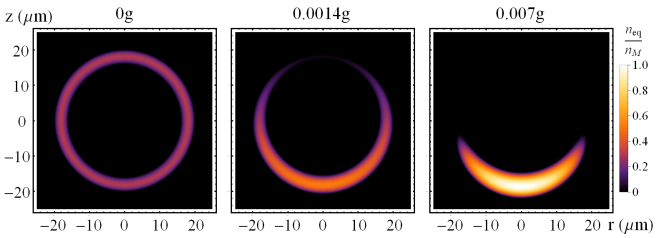

Figure 7.1: Thomas-Fermi density profiles for condensates confined by the bubble trap without gravity (left) and under the influence of gravitational fields $0.0014g$ (middle) and $0.007g$ (right), where g is the gravitational acceleration on Earth. These profiles are generated for 10^5 ^{87}Rb atoms forming a condensate shell with outer radius 20 μm and thickness 4 μm in the absence of gravity. The colors in the bar graph represent density normalized by $n_M = 3.1 \times 10^{13}/\text{cm}^3$. As the strength of the gravitational field increases, we observe a density depletion at the top of the condensate shell and a density maximum at its bottom.

trap minimum by an amount much smaller than the thickness of the BEC shell. The latter is determined by the strength of interatomic interactions. More precisely, as noted in Sec. 5.2.2, the thickness of the condensate shell can be obtained from the Thomas-Fermi density profile after fixing the number of particles, N, as was found in Eq. (5.11),

$$\delta = \frac{1}{2}\left(\frac{3UN}{m\pi\omega_{\text{sh}}^2 S_l^2 r_0^2}\right)^{1/3}.$$

The displacement of the trap minimum away from its center due to gravity [114] is equal to

$$r_{\text{disp}} = \frac{g}{\omega_{\text{sh}}^2 S_l}. \tag{7.1}$$

Hence, the influence of gravity is small compared to the strength of interactions in the condensate when

$$r_{\text{disp}} \ll \delta. \tag{7.2}$$

When this condition is satisfied, we expect the BEC shell to be largely unchanged in shape despite the influence of gravity. In experimental efforts of Refs. [96, 97], the quantity analogous to Eq. (7.1) is reported to be comparable to the entire size of the condensate cloud. In this case, the condition for weak gravity we have identified in Eq. (7.2) is clearly violated and a radical, flattening deformation of the condensate shell is found by the authors.

As an intermediate stage between these two possibilities—weak gravity that does not change the shape of the condensate shell and very strong gravity that effectively collapses it into a quasi-two-dimensional geometry—we consider a set of experimental parameters for which gravity deforms the BEC shell to have most density at its bottom and a heavily depleted top region. This change in condensate density is shown for the bubble trap and multiple values of gravitational field smaller than Earth's gravity in Fig. 7.1. The

deformation away from a fully connected geometry and to a more open shape akin to a part of a hyperboloid rather than a sphere is clear even for gravitational acceleration values on the order of a thousand times smaller than those typically measured on Earth.

To examine this gravitational deformation analytically, we work within the Thomas-Fermi approximation and consider the thin-shell limit of the potential described by Eq. (4.2) with an added gravitational term. Specifically, adding $-gr\cos\theta$ to the potential and completing the square, we obtain

$$V(r,\theta) = \frac{m\omega_{\rm sh}^2 S_l^2}{2}\left[(r-r_0)+\frac{g\cos\theta}{\omega_{\rm sh}^2 S_l}\right]^2 + \left(mgS_l r_0\cos\theta - \frac{mg^2\cos^2\theta}{2\omega_{\rm sh}^2}\right), \tag{7.3}$$

where r_0 is the trap minimum in the absence of gravity. For the bubble trap, the frequency of small single-particle oscillations is given by $\omega_{\rm sh} = \sqrt{\Delta/\Omega}\omega_0$ and the trap minimum is $r_0 = \sqrt{\Delta}$. In other words, this treatment is relevant for the thin shell regime of the bubble trap in realistic experiments.

The potential in Eq. (7.3) is equivalent to a radially shifted harmonic trap in the variable $r - r_0$, with the trap minimum vertically displaced away from the center of the condensate shell. This vertical displacement is equivalent to adding a potential term

$$V_{\rm offset}(\theta) = mgS_l r_0\cos\theta - \frac{mg^2\cos^2\theta}{2\omega_{\rm sh}^2}. \tag{7.4}$$

From the Thomas-Fermi equilibrium density, Eq. (2.11), we see that the density at the top of the shell vanishes when the chemical potential is equal to $\mu_c = V_{\rm offset}(\theta = 0)$. This corresponds to the condensate shell "opening up" and can, in extreme cases, lead to the shell approaching a quasi-two-dimensional geometry as in Refs. [96, 97]. More precisely, in the regime of strong gravity, the extreme sag deforms the hollow shell into a disk-like geometry that is strongly confined in the direction of gravitational acceleration in addition to being confined by the trapping potential.

When the chemical potential attains the critical value μ_c, the inner and the outer radii of the shell are the solutions of $\mu_c - V(r) = 0$. Previously, when the effects of gravity were not take into account, we typically fixed the outer radius of the condensate as $r = R$, with R being some constant chosen in accordance with experimental data. Once gravity is accounted for, the condensate shell is not perfectly spherically symmetric, so there is no longer a single, θ-independent, outer radius R. Similarly, in the presence of gravity, the thickness of the shell varies with the polar angle as

$$\delta(\theta) = 2r_0\sqrt{\tilde{g}(1-\cos\theta)(2-\tilde{g}-\tilde{g}\cos\theta)}, \tag{7.5}$$

where we have introduced the dimensionless parameter $\tilde{g} = g/S_l r_0 \omega_{\rm sh}^2$. We take the condensate shell corresponding to the potential of Eq. (7.3) to be very thin for $\tilde{g} \ll 1$ and refer to these values of $\tilde{g}$ as the thin shell limit in analogy with our discussion in Sec. 5.2.2.

We note that $\delta(0) = 0$, as expected since we have chosen the chemical potential to cause a density depletion at the top of the condensate shell. Additionally, for $\theta = 0$ we find $r_{\rm max} = r_{\rm min} = r_0 - \frac{g}{\omega_{\rm sh}^2 S_l}$. Since these values should correspond to coordinates on top of the BEC shell we require that

$$r_0 > \frac{g}{\omega_{\rm sh}^2 S_l}. \tag{7.6}$$

This is a rather natural constraint given that in the classical problem of an oscillator in a gravitational field, the frequency of oscillation is given by $\omega = \sqrt{g/L}$ for L the size of the object that is oscillating. In other words, the condition in Eq. (7.6) requires the trapping frequency to be larger than the oscillation frequency naturally associated with gravitational effects. These observations fully characterize the geometry of the condensate shell deformed by gravity. By providing this detailed discussion of such BEC shapes we therefore make strong contact with current and future experimental studies where gravitational effects are likely to be of import.

Further, particle number conservation is important in experimental settings and within our formalism it requires

$$N_c = 2\pi \int_{r_{\rm min}}^{r_{\rm max}} \int_0^{\pi} n_{eq}(r,\theta) r^2 \sin\theta dr d\theta, \tag{7.7}$$

which, evaluated in the thin shell limit, is equivalent to

$$N_c = \frac{128 m \pi g^{3/2} r_0^{7/2} S_l^{1/2}}{15 U \omega_{\rm sh}}. \tag{7.8}$$

Since this expression only includes the gravitational acceleration and trap parameters (the minimum of the harmonic trapping potential r_0 and the frequency of single-particle oscillations around the trap minimum $\omega_{\rm sh}$), it can be used to predict at what particle number the effects of gravity will cause a density depletion at the top of the condensate shell.

Accordingly, given fixed trap parameters, a value of N can be chosen in such a way that the thin condensate shell keeps an approximately uniform density profile regardless of gravitational effects—choosing a number of atoms larger than N_c guarantees a smaller deformation of the shape of the BEC shell under the influence of gravity. In the limit of $g \to 0$ the number of atoms needed in order to form a condensate

shell robust to the influence of gravity, N_c, vanishes and it also diminishes as $\omega_{\rm sh}$, the trapping frequency, is increased. In other words, an equivalent of the weak gravity regime can be reached by using tighter confinement for the trapped atoms as well.

Furthermore, Eq. (7.8) implies that given a fixed number of atoms forming the condensate, a critical value of the gravitational constant g_c can be estimated as

$$g_c = \frac{(15U\omega_{sh}N)^{2/3}}{(128m\pi)^{2/3}r_0^{7/3}S_l^{1/3}}. \tag{7.9}$$

In experimental setups where the measured value of g is larger than g_c, the condensate shell is expected to open up on top, rather than maintaining its bubble-like shape, as depicted in Fig. 7.1. If the effective value of the gravitational constant can be lowered through experimental techniques or use of special microgravity facilities, we propose that realizing $g_{\rm eff}$ smaller than g_c will result in a robust shell-like geometry of the condensate.

Under experimental conditions within which the value of gravitational acceleration cannot be changed, the expression in Eq. (7.8) suggests a way in which shell-shaped condensates can also be achieved and maintained without significant gravitational sag. In cases where $N \gg N_c$ is within the range of plausible experimental parameters, gravity can be treated as a small effect on an otherwise stable condensate shell of approximately uniform thickness. We proceed to examine the collective motions of condensate shells under such conditions.

7.2 Collective modes in presence of gravity

Having characterized the behavior of equilibrium density profiles of hollow BEC shells in the presence of gravity, we turn to a discussion of condensate shell dynamics under the same environmental conditions. In particular, we consider including gravity in the hydrodynamic formalism. Within this approach, we use the gravitational GP equation and apply the Thomas-Fermi approximation with gravity explicitly accounted for.

First, we consider adding a gravitational potential term to Eq. (2.10) so that $V(\mathbf{r}) = V_{\rm trap}(r) + mgz$ and consequently obtain

$$\frac{-\hbar^2}{2m}\nabla^2\psi(\mathbf{r},t) + V_{\rm trap}(r)\psi(\mathbf{r},t) - mgz\psi(\mathbf{r},t) + U_0|\psi(\mathbf{r},t)|^2\psi(\mathbf{r},t) = i\hbar\partial_t\psi(\mathbf{r},t), \tag{7.10}$$

a GP equation having explicit dependence on the strength of gravity. The corresponding Thomas-Fermi

density profile reads

$$n_{\rm eq}(\mathbf{r}) = \frac{\mu - V_{\rm trap}(r) - mgz}{U}. \tag{7.11}$$

Repeating the arguments of Sec. 2.3 we find that hydrodynamic equations appropriate for a BEC in a nonzero gravitational field are

$$\omega^2 \delta n(\mathbf{r}) = \frac{1}{mS_l^2}\frac{\partial V_{\rm trap}(r)}{\partial r}\frac{\partial \delta n(\mathbf{r})}{\partial r} + \frac{g}{S_l}\cos\theta\frac{\partial \delta n(\mathbf{r})}{\partial r} - \frac{g}{rS_l}\sin\theta\frac{\partial \delta n(\mathbf{r})}{\partial \theta} - \left[\frac{\mu - V_{\rm trap}(r)}{mS_l^2} - \frac{gr}{S_l}\cos\theta\right]\nabla^2\delta n(\mathbf{r}) \tag{7.12}$$

This expression, Eq. (7.12), is the nonzero gravity equivalent of Eq. (2.20) with the Thomas-Fermi equilibrium density profile, Eq. (7.11). As in previous Sections, here we use dimensionless length units rescaled by $S_l = \sqrt{\hbar/(2m\omega)}$.

We proceed to treat the gravitational terms in this equation perturbatively. More precisely, we assume that the trap parameters have been chosen in accordance with Eq. (7.8) so that the shape of the shell is largely unchanged by gravitational effects. Additionally, we find that choosing $N \geq N_c$ satisfies the condition in Eq. (7.2), thus justifying our treatment of the condensate shell thickness as effectively uniform. The analysis presented here consequently characterizes the collective modes of a condensate shell experiencing minimal gravitational sag.

As shown in Sec. 5.2.2, for a very thin condensate shell the collective modes are analytically described by

$$\delta n(\mathbf{r}) = \sqrt{\frac{\nu(\nu+1)}{2}} P_\nu\left(\frac{r - r_0}{\delta}\right) Y^l_{m_\ell}(\theta, \phi), \tag{7.13}$$

where $P_\nu(x)$ are the Legendre polynomials, with the corresponding frequencies given by Eq. (5.13),

$$\omega^{\rm sh}_{\nu,\ell} = \omega_{\rm sh}\sqrt{\nu(\nu+1)/2}.$$

Corrections to these frequencies due to the effects of gravity are then given by the eigenvalues of a matrix with entries equal to

$$\langle \delta n(\mathbf{r})^\ell_{\nu,m_\ell} | V_g(r,\theta) | \delta n(\mathbf{r})^{\ell'}_{\nu',m'_\ell}\rangle = \frac{g}{S_l}\langle \delta n(\mathbf{r})^\ell_{\nu,m_\ell}| - \frac{1}{r}\sin\theta\frac{\partial}{\partial\theta} + \cos\theta\frac{\partial}{\partial r} + r\cos\theta\nabla^2 | \delta n(\mathbf{r})^{\ell'}_{\nu',m'_\ell}\rangle. \tag{7.14}$$

In the thin-shell limit, $c \gg 1$, we only consider the matrix elements of Eq. (7.14) to leading order in c^{-1}, or equivalently, the thickness of the condensate shell, δ. Carrying out this calculation (see more details in

Appendix B), we find

$$\langle \delta n(\mathbf{r})^{\ell}_{\nu,m_\ell} | V_g(r,\theta) | \delta n(\mathbf{r})^{\ell'}_{\nu',m'_\ell} \rangle \approx \frac{g\delta r_0}{S_l} \frac{\nu(\nu+1)}{2\nu+1} \times [f(\ell,\ell',m_\ell,m_{\ell'})\delta_{\ell,\ell'+1} + g(\ell,\ell',m_\ell,m_{\ell'})\delta_{\ell,\ell'-1}], \quad (7.15)$$

where the numerical factors $f(\ell,\ell',m_\ell,m_{\ell'})$ and $g(\ell,\ell',m_\ell,m_{\ell'})$ are also given in Appendix B. Noting the Kronecker δ functions in Eq. (7.15), we conclude that for a fixed ν and ℓ finding the eigenfrequencies and eigenmodes of the system under the influence of gravity is reduced to diagonalizing a matrix with nonzero entries only for

$$\{\nu',\ell',m'_\ell\} = \{\nu, \ell \pm 1, m_\ell\}. \quad (7.16)$$

Consequently, the effect of weak gravity (gravity in the regime where it can be treated perturbatively) on the collective modes of the spherically symmetric thin condensate shell is to mix modes with adjacent angular momentum indices. If a collective mode with a fixed number of radial nodes ν and a fixed number of angular modes ℓ is induced under conditions of weak gravity in a thin shell BEC, the number of angular nodes will therefore change while the radial density-deviation profile will remain the same. Since the overlap between the collective modes under consideration, Eq. (7.15), is weighted by both the thickness of the shell and the minimum of the harmonic trapping potential, the mixing effect will be more or less prominent depending on the size of the condensate shell. We further strenghten this conclusion by noting that the same inference of gravitationally induced mode mixing can be obtained by making an ansatz $\delta n(r,\theta,\phi) = D(r)\sum_{\ell=0}^{\infty}\sum_{m_\ell=-\ell}^{\ell} C_{\ell m_\ell} Y^{\ell}_{m_\ell}(\theta,\phi)$, for $C_{\ell m_\ell}$ some appropriate set of constants, and seeking a complete solution to the eigenproblem of Eq. (7.12).

Finally, we emphasize that Eq. (7.15) is obtained not only in the weak gravity regime but also the thin shell limit so the mode mixing effect on a thicker shell would be qualitatively different than on a thin one. To gain insight into the behavior of a thicker shell described by a smaller value of c (larger δ), we note that evaluating the matrix element of Eq. (7.15) to quadratic order (see Appendix B for more details) in the shell thickness yields terms such as

$$2\delta^2 \begin{pmatrix} \nu & 1 & \nu' \\ 0 & 0 & 0 \end{pmatrix}^2, \quad (7.17)$$

where we use the Wigner-j symbol. As this symbol is proportional to a Clesbsh-Gordan coefficient, we can identify a selection rule for this expression. More precisely, terms of this form vanish unless $\nu' = \nu \pm 1$. Consequently, we posit that away from the thin-shell limit (assuming that gravity can still be treated as weak compared to the strength of inter-atomic interactions), gravitational pull leads not only to the mixing

of modes with adjacent angular node indices ℓ but also those with adjacent radial node indices ν. The practical impact of the analysis of gravitational effects presented in this Section is discussed below.

7.3 Experimental Feasibility and Estimates

Having presented an extensive study of spherically symmetric hollow condensates and their behavior in various limits ranging from the fully-filled sphere geometry to a nearly-two-dimensional thin hollow shell, we turn to a discussion of experimental feasibility of achieving these configurations. We start by providing a few estimates for experimentally measurable quantities, such as condensate density and collective mode frequency in Sec. 7.3.1, then turn to the striking effects of Earth's gravity on condensate shells and their feasibility in microgravity experiments in Sec. 7.3.2.

7.3.1 Estimates in the absence of gravity

As a realistic example, we consider a fully filled spherical ^{87}Rb condensate made up of $N = 10^5$ atoms, confined by the potential of Eq. (4.1) with the bare frequency $\omega = 2\pi \times 500$ Hz and having condensate size of $R = 10$ μm. The maximum equilibrium density of such a system is on the order of 10^{16} cm^{-3}. For a condensate shell of the same size, an equivalent confining frequency and characterized by $c = r_0/\delta \approx 1000$, we find that the same quantity is on the order of 10^{18} cm^{-3}. Comparing their respective breathing mode frequencies shown in Fig. 8.6 we find that the $(\nu, \ell) = (1, 0)$ mode in the filled condensate corresponds to $\omega^{\rm sp}_{1,0} \approx 2\pi \times 1.12$ kHz while the same mode in the thin shell is characterized by $\omega^{\rm sh}_{1,0} \approx 2\pi \times 0.50$ kHz with the correction given by Eq. (5.14) on the order of 10^{-6}% and therefore negligible. Recalling our discussion in Sec. 5.3.1 and Fig. 8.6, we use these estimates to predict that when the $(\nu, \ell) = (1, 0)$ mode is induced in the fully filled spherical condensate, if the system transitions to a thin shell, its eigenfrequency decreases from $2\pi \times 1.12$ kHz to a value slightly smaller than $2\pi\omega \approx 2\pi \times 0.50$ kHz at the hollowing transition and then increases to reach this value in the very-thin-shell limit. More simpl put, the adiabatic change in the condensate shape from a filled sphere to a very thin, hollow shell results in approximately halving the lowest lying collective mode frequency. Similarly, we calculate $\omega^{\rm sp}_{2,0} \approx 2\pi \times 1.87$ kHz and $\omega^{\rm sh}_{2,0} \approx 2\pi \times 0.87$ kHz – 53% decrease from the fully filled sphere limit to the thin hollow shell geometry. More generally, for all low-lying, $\ell = 0$ modes that are experimentally accessible, we predict the decrease in the collective mode frequency at the hollowing point, compared to the oscillation frequency of the same mode in the fully filled spherical BEC to be rather prominent, on the order of 50% or more. Somewhat higher spherically symmetric modes, such as $\nu = 3$, are good candidates for experimental detection of the further decrease of collective mode

frequency at the hollowing point compared to the thin-shell limit as well. The collective mode with $\nu = 3$ shows a 20% change between the hollowing point and the thin-shell limit, which makes it suitable for full observation of nonmonotonicities in the collective mode frequency spectrum of a hollowing BEC. Further, collective modes with low angular momentum values, such as $\ell = 1$ or $\ell = 2$, exhibit frequency dip features similar to those in frequencies of spherically symmetric $\ell = 0$ modes. In a realistic experimental system that might not have perfect spherical symmetry, such low-ℓ collective modes would be the most likely candidate for study.

Comparing collective modes with $\nu = 1$ but different ℓ, we find that $\omega^{\rm sp}_{1,1} \approx 2\pi \times 1.41$ kHz while $\omega^{\rm sp}_{1,10} = 2\pi \times 2.96$ kHz and $\omega^{\rm sp}_{1,20} = 2\pi \times 4.03$ kHz. Identifying large ℓ modes, such as $\ell = 10$ and $\ell = 20$, with excitations of the condensate localized to a particular boundary surface, we highlight that these surface modes typically have high oscillation frequencies compared to fully spherically symmetric modes having the same number of radial nodes ν but fewer oscillations in the angular direction. Given our calculations in Sec. 5.2.2, this effect of increasing ℓ is not present in the thin-shell limit since all of the collective modes in this configuration are degenerate with respect to a change in the number of their angular nodes.

For $\ell = 20$, we further examine the drop in collective mode frequency due to the redistribution of surface modes when an inner boundary is available. Noting that collective modes with total number of radial zeros equal to 2ν and $2\nu + 1$ become degenerate immediately after the hollowing out transition takes place, we find that $\omega^{\rm sp}_{1,20} = 2\pi \times 4.03$ kHz and $\omega^{\rm sp}_{0,20} = 2\pi \times 2.24$ kHz in the sphere limit drop to $\omega^{\rm sh}_{1,20} = 2\pi \times 1.50$ kHz. This drop constitutes a decrease on the order of 60% and 30%, respectively. Consequently, we identify the redistribution of surface modes as a rather strong effect on collective mode frequencies.

Finally, repeating our analysis for a thicker shell with $c \approx 20$, we find that the corrections to the collective mode frequencies of the shell due to its nontrivial thickness become approximately 3% of the value obtained while assuming the thin-shell condition $c \to \infty$ is satisfied. As this is not a very large correction, we conclude that a number of our thin-shell results can potentially be observed in experiments even when creating a very thin condensate shell is not feasible.

7.3.2 Estimates in the presence of gravity and feasibility

We proceed to turn to the effects of gravity in experimentally realistic systems. In contrast to fully filled spherical condensates that are simply shifted by gravity with no effect on their shape, the geometry of a hollow condensate shell is, as we have shown in Ch. 7, rather sensitive to the presence of a gravitational field. Accordingly, experimental parameters such as the trapping frequency, interatomic interaction strength, and the number of atoms in the condensate have to be chosen to satisfy the criteria given by Eq. (7.8). Otherwise,

the density of the condensate shell is heavily depleted on its top while the majority of atoms pool at its bottom and a fully connected, three-dimensional condensate shape cannot be realized.

In the presence of ordinary gravity, Eq. (7.8) constrains the shell radius to be rather small or the trapping frequencies to be rather high. Consequently, a realization of a robust, fully shell-shaped BEC on Earth presents an experimental challenge. We estimate that a thin condensate shell made up of ^{87}Rb atoms confined by a trap with a bare frequency of $2\pi \times 500$ Hz and size on the order of $R \sim 10\mu$m would have to be made up of $N_c \sim 10^7$ atoms in order to maintain approximately uniform density and robust shape under the influence of gravity. As current experimental efforts [1, 56] show that even lower bare frequencies are optimal for experiments using an rf-dressed bubble trap, we conclude that the number of atoms needed in order for the condensate shell to maintain its shape despite gravitational sag is impractically high. In other words, experimental investigations of the behavior and properties of ^{87}Rb BEC shells in Earth's gravity are not feasible and microgravity environments need to be sought. For example, we estimate that for a ^{87}Rb condensate shell composed of 200,000 atoms, as is the case in Ref. [97], and having the same size ($R \sim 10\mu$m) would show significant lack of density on its top and largely consist of a pool of atoms at the trap bottom unless (effective) gravitational acceleration in its environment was smaller than $g_c \sim 0.2$ m/s^2.

While gravitational sag is often compensated for in experimental studies of ultracold atomic systems on Earth, the shell-shaped geometry makes standard methods such as magnetic levitation or the use of the dipole force challenging. Since the bubble trap employs a dressed-state potential, magnetic levitation is not feasible because the atoms in the condensate are in superpositions of all internal magnetic states. Further, though a dipole force due to a gradient of optical intensity (for instance, achieved by using a far-detuned Gaussian beam) could in principle be used to counteract the effects of gravity, the need for high precision in designing such a gradient makes this approach very difficult. Consequently, we identify microgravity environments, rather than terrestrial setups with gravitational compensation, as an optimal choice for experimentally realizing hollow BEC shells.

In cases where a thin shell can be produced, most likely in microgravity environments such as the ZARM drop tower [100] and the Matter-Wave Interferometry in Microgravity (MAIUS) sounding rocket [101, 102] in Germany, and NASA's Cold Atom Laboratory aboard the International Space Station [56, 1], we estimate the corrections to the frequencies of the collective modes due to their mixing under the influence of gravity as well. While the magnitude of these corrections depends on the specific ℓ values of the unperturbed modes, we generally estimate them to be rather small. In particular for the $\nu = 1, \ell = 1, m_\ell = 0$ mode of a thin ^{87}Rb condensate shell of the size on the order of 1 μm and trapped by a potential having bare frequency of $\omega_0 = 2\pi \times 500$ Hz in microgravity $g \approx 10^{-5}$, we find the fractional correction to the collective mode frequency

ω to be $\omega_{\rm grav}/\omega = 1.00015$. This is a change in the collective mode frequency of approximately 0.015 %, which is below the detection limit in experiments. The magnitude of gravitational mode mixing corrections increases in size with increasing ν, and similarly with increasing ℓ. For instance, for high-ℓ collective modes such as described by $\nu = 1$ and $\ell = 20$ the effect of gravity leads to a 2.5 % change in collective mode frequency. As this is still a small correction, we take the strength of gravity rather than the magnitude of ℓ or ν to be the dominant factor for the importance of mode mixing. In other words, the presence or absence of mode-mixing effects in thin, spherically symmetric condensate shells can be interpreted as an indicator of the strength of gravity in experiments where a fully covered shell is realized.

More precisely, we propose that since the change in the frequencies of the collective modes due to mode mixing is rather small in microgravitational environments, the presence of large frequency corrections due to mode mixing points toward a larger value of gravitational acceleration. For instance, recalling that we estimated that the condensate shell in Ref. [97] would retain its shape for $g_c \approx 0.2$ m/s^2 we calculate that the frequency of the $(\nu, \ell) = (1, 0)$ breathing mode in a thin shell of the same size ($R \sim 10\mu$m) in a gravitational field determined by g_c would change approximately 27% due to mode mixing. This correction is almost 20,000 times larger than it would be in microgravity. Additionally, a similar mode-mixing behavior would be observed in condensate shells with anisotropy along the z-direction, or clouds closer to an elongated "cigar-shape" rather than a sphere. We conclude that the absence of strong experimental signatures of mode mixing offers a confirmation of both very small values of gravitational acceleration in the environment of the condensate shell and also its full spherical symmetry.

Concluding with this Section, the preceeding four Chapter of this thesis present an extensive and detailed study of static and dynamic properties of spherically symmetric BECs spanning fully-filled and hollow geometries. In these Chapters we have discussed equilibrium denisty profiles, the hollowing transition, collective modes having only radial nodes and collective modes confined to condensate surfaces, signatures of the hollowing in the frequency spectra of both types of these collective excitations, effects of gravity on the equilibrium and low-lying excitation physics of thin hollow BEC shells and their experimental feasibility on Earth and in specialized microgravity facilities. However, we have not so far considered any external manipulations of these systems, such as rotation, or presence of topological defects, such as vortices. In the next Chapter, we end our discussion of filled and hollow spherically symmetric BECs by discussing excatly those concerns. Importance of spherical symmetry throghout our discussion makes it natural to consider the effects or rotating the condensate and vortices are ubiquitous in experimental studies and of great theoretical interests with respect to studies of turbulence and re-equilibration following some perturbation in superfluids. Hence, the following Chapter and its focus on vortices and rotation in shell-shaped BECs rounds out our

work on these systems and establishes a foundation for understanding even richer physics in systems where such superfluid geometries occur spontaneously.

Chapter 8

Vortices and Rotation Effects on Hollow BECs

Since we have so far mostly focused on hollow condensates having spherical symmetry it is natural to study their behavior under rotation. As discussed in Chapter 3, typically rotation results in nucleation of vortices. Closed surfaces and non-zero curvature, both features of hollow BEC shells, are superfluid properties that can significantly influence the behavior and arrangement of vortices [115, 116]. Further, previous works concerning vorticity in toroidal or annular condensates underlined the importance of the central hollow regions of these geometries, for instance as being able to host a multiply quantized "giant" vortex state [117, 118, 119, 8], these ideas provide strong motivation for exploring vorticity in three-dimensional condensate shells. Generating vortices through rotating BEC shells could possibly be executed within one of the on-going CAL experiments as well. Moreover, rotating condensate shells are parallel to structures proposed to occur in interiors of neutron stars which adds further importance to understanding vortex structures in these systems. In neutron stars, motion of vortices within superfluid shell layers has been suggested to have signatures in the radiofrequency signals of those stars measured on Earth [95, 120, 63, 62]. Studying vortex motion in BEC shells may be a step towards understanding this significantly more complex physics.

In what follows, we first discuss the constraints on possible vortex configurations on the surface of a very thin BEC shell due to its topology in Sec. 8.1.1, describe superfluid flows due to vortices on such a condensate shell in Sec. 8.1.2, then adapt the discussion of interactions between vortices from Sec. 3.6 to the case of a curved surface in Sec. 8.1.3. We study rotating hollow nearly-two-dimensional shells in Sec. 8.2, arguing for most likely arrangements of vortices having opposite circulations based on energetics in Sec. 8.2.1 and Sec. 8.2.2 based on analytic and numerical calculations, respectively. In Sec. 8.2.3, we briefly comment on the changes in condensate shape caused by rotation. In Sec. 8.3 we start to address three-dimensional hollow BEC shells. Here, we present an intuitive argument connecting "flat" two-dimensional systems and three-dimensional shells in Sec. 8.3.1 and complement it with numerical simulation results in Sec. 8.3.2. We specifically focus on the physics of a vortex-antivortex pair symmetrically positioned about the equator of the shell and investigate shell thickness and rotation parameters that pin it to the rotation axis. This is in

contrast to their moving toward the shell equator and annihilating. We conclude by commenting on stability of vortex lines and outlining related future work in Sec. 8.4.

8.1 Two-dimensional condensates on closed curved surfaces

Before addressing fully three-dimensional condensate shells (shells with non-negligible thickness) we first pin-point the consequences of the condensate shell having curvature and being hollow. To that end, we study a two-dimensional BEC shell. Practically, this discussion applies to condensates in the thin shell limit. Mathematically, it can be thought off as applying to a two-dimensional superfluid film that has been wrapped on top of a spherical surface. While we do not comment on the subtleties of the Bose-Einstein condensation phase transition in this geometry here, recent experimental [56, 1] and theoretical works [10, 121] have increasingly brought it within the realm of physical accessibility. Throughout this Section, we use the designation thin shell to mean that the condensate is quasi-two-dimensional and all radial degrees of freedom can be neglected.

8.1.1 Constraints on allowed vortex configurations

For a condensate with a closed and compact geometry there are topological constraints on possible vortex configurations. Namely, for a collection of vortices (i) the total sum of their circulations (vorticities) has to vanish and (ii) the sum of their topological charges has to satisfy the Poincare-Hopf theorem. These constraints have been identified for not only closed condensate shells, but also a broader class of compact surfaces, including toroidal surfaces of revolution discussed in Ref. [67].

More formally, the first constraint reads

$$\sum_i \ell_i = 0 \tag{8.1}$$

where i indexes each vortex with circulation, or angular momentum, ℓ_i. This circulation is determined with respect to the rotation axis of the vortex. For instance, if a vortex is positioned on the z-axis, ℓ_i is the same as the angular momentum measured about that axis. To derive Eq. (8.1) we consider a line integral of the condensate velocity

$$\oint \nabla S \cdot dl = \oint v \cdot dl \tag{8.2}$$

evaluated around a small loop on the surface of the BEC shell that does not encircle any vortices. This

integral counts the circulations within the loop as, using Stokes' theorem, we can write

$$\oint v \cdot dl = \int\int \nabla \times v \cdot dA. \tag{8.3}$$

Here

$$\nabla \times v = \sum_i \ell_i \delta(\theta - \theta_i)\delta(\phi - \phi_i) \tag{8.4}$$

since the velocity field of the condensate has to be irrotational everywhere except at the position of each vortex (singular defect). However, the same loop divides the condensate shell surface into two parts – one containing no vortices and one containing all of the vortices. Since the two have to produce the same result when integration in Eq. (8.2) is carried out, it follows that the circulations of all vortices have to add up to zero. One clear implication of this constraint is that a spherical condensate shell cannot support a single vortex because that is a vortex configuration having non-zero total circulation. The simplest allowed vortex configuration on a thin BEC shell is a pair of vortices with opposite circulations – a vortex antivortex pair reminiscent of an electric dipole.

Further, the shape of condensate flow stemming from the vortices has to be related to the spherical shell topology by the Poincare-Hopf theorem [122]. Concretely, given a vector field everywhere tangent to the sphere, the topological indices associated with its zeroes and singularities have to add up to its Euler characteristic. Adopting the notation of topological charges q_i for the ith vortex, the Poincare-Hopf theorem requires that

$$\sum_i q_i = 2. \tag{8.5}$$

Topological charge is calculated as the algebraic sum of the number of revolutions of a unit vector perpendicular to the flow around the defect (shown as a bold line in the schematic in Fig. 8.1) along a small counter-clockwise oriented curve with the defect at its center [123]. Specifically, any vortex, regardless of the direction or amount of circulation it carries, has $q = +1$ while stagnation points in the flow contribute $q = -1$. This is illustrated in Fig. 8.1. The configuration consisting of two vortices with opposite ciruclations (vortex antivortex pair) satisfies this topological constraint since their total topological charge is given by $q_1 + q_2 = +1 + 1 = +2$.

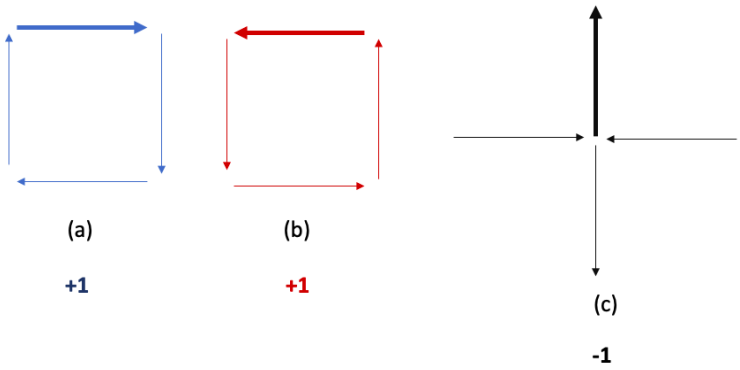

Figure 8.1: Representation of topological charges associated with vortices and stagnation points in the flow relevant for the discussion of the Poincare-Hopf theorem. Schematics in **(a)** and **(b)** represent flow around point vortices with opposite circulations (for instance, $\ell = 1$ and $\ell = -1$) while flow with features as in **(c)** would, for example, be found between two vortices with identical circulations.

8.1.2 Phase and flow profiles for vortices on 2D shells

As a building block towards more complex vortex configurations satsfying all the topological and geometric constraints particular to shell-shaped condensates, we first consider the structure of the condensate wavefunction phase for a single point-like vortex on the BEC shell. For a vortex at either pole of the condensate shell, superfluid flow simply swirls about the z-axis so that $\vec{v} = \frac{\hbar}{m}\nabla S$ is in the ϕ direction. We can infer its magnitude from the quantization conditions (single-valuedness of the wavefunction) as in Eq. (3.3). To calculate the flow field $\vec{v}$ when a vortex is present at a point on the shell distinct from the z-axis, having position given by some (θ_v, ϕ_v) instead, we use the Green's function, Γ, on the sphere which is derived in the next Section. More precisely,

$$\vec{v} = \nabla_{\vec{u}} \sum_i \frac{\ell_i h}{m} \Gamma(\vec{u}, \vec{u}_v) \tag{8.6}$$

for vortices carrying angular momentum ℓ_i and $\vec{u}_v = \{\theta_v, \phi_v\}$. Following Ref. [115] and Eq. (8.24) below, we use this expression to find the flow profile for a vortex anti-vortex pair residing at $\theta = \alpha$ and $\theta = \pi - \alpha$ i.e. two vortices with opposite circulations placed symmetrically with respect to the equator

$$\begin{aligned} v_\theta &= \frac{\hbar}{2mR} \frac{2\cos\alpha(\cos\phi\sin\alpha + \sin\theta)}{(1+\cos\phi\sin\theta\sin\alpha)^2 - (\cos\alpha\cos\theta)^2} \\ v_\phi &= \frac{\hbar}{2mR} \frac{\cot\theta\csc\theta\sin(2\alpha)\sin\phi}{(\cos\alpha\cot\theta)^2 - (\csc\theta + \cos\phi\sin\alpha)^2}. \end{aligned} \tag{8.7}$$

We explicitly note that throughout this Chapter we use dimension-full units so that, for instance, R in the above expression is on the order of microns. A schematic of this vortex configuration is shown in Fig. 8.2. The flow pattern for $\alpha \neq 0$ is not purely azimuthal and has a nonzero θ-component in contrast to vortices residing on the poles of the shell. As is intuitive, v_θ is small for small α so $v \approx v_\phi \hat{\phi}$ for such vortex-antivortex configurations.

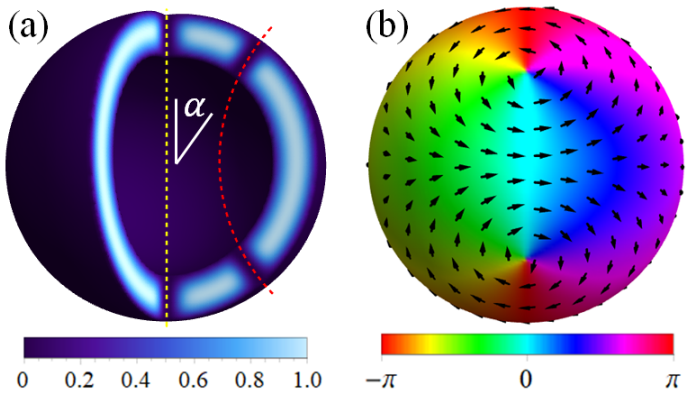

Figure 8.2: (a) A schematic density profile of a shell-shaped BEC comparing a vortex-antivortex pair at the poles, rotating about the z axis (straight dashed line) with another such pair at polar angle $\theta = \alpha$ (antivortex at $\pi - \alpha$) rotating about a curved dashed line. (b) Vector field showing superfluid flow for the vortex-antivortex pair at $\theta = \alpha$. The $+x$ direction points out of page, and the colors represent the phase S of the BEC wavefunction.

8.1.3 Interactions between vortices on a spherical surface

Similar to the case of planar or flat two-dimensional condensates (as in Sec. 3.6), in a configuration consisiting of mutiple vortices each individual vortex is moved by flows around the other vortex cores. This increases the kinetic energy of the condensate. We calculate the kinetic or interaction energy between a vortex and an antivortex on the surface of the sphere. We assume that condensate thickness is very small so that only the phase of the wavefunctions, S, is relevant and the density of the superfluid is uniform. Equivalently, the energy functional reads

$$E[S] = \frac{\hbar^2 \rho_{2\mathrm{D}}}{2m} \int d^2u |\nabla S|^2 + \rho_{2\mathrm{D}}^2 \int d^2u V(\vec{u}) + \frac{1}{2} U_0 \rho_{2\mathrm{D}}^4 \int d^2u. \tag{8.8}$$

where $\rho_{2\mathrm{D}}$ is the condensate density and $d^2u = R\sin(\theta) d\theta d\phi$ with (θ, ϕ) the usual spherical polar coordinates.

Following Refs. [124, 115, 116], the kinetic energy contribution to Eq. (8.8) can be evaluated by calculating

the Green function on the surface of a sphere. Working with the usual metric $g_{\alpha,\beta}$ for a shell of fixed radius

$$g_{\alpha,\beta} = \begin{pmatrix} R^2 & 0 \\ 0 & R\sin^2\theta \end{pmatrix} \tag{8.9}$$

(here $g = \det g = R^4 \sin^2\theta$), the energy cost of some vortex configuration due to the associated condensate flow can be written as

$$KE = \frac{\hbar^2 \rho_{2\mathrm{D}}}{2m} \int d\vec{u}\sqrt{g} g^{ij} \partial_i S \partial_j S. \tag{8.10}$$

We define the curl of the velocity field as

$$\rho_{\mathrm{vort}}(\vec{u}) = \gamma^{ij} \partial_i \partial_j S \tag{8.11}$$

where γ^{ij} is the covariant antisymmetric tensor. Consequently, we can rewrite Eq. (8.10) as

$$KE = \frac{\hbar^2 \rho_{2\mathrm{D}}}{2m} \int d\vec{u}\sqrt{g} \int d\vec{u}' \sqrt{g'} \rho_{\mathrm{vort}}(\vec{u}) \Big(-\frac{1}{\triangle} \Big)_{uu'} \rho_{\mathrm{vort}}(u'). \tag{8.12}$$

For $\Gamma(\vec{u}, \vec{u}')$ the inverse of the Laplacian on the spherical shell we further have

$$KE = \frac{\hbar^2 \rho_{2\mathrm{D}}}{2m} \int d\vec{u}\sqrt{g} \int d\vec{u}' \sqrt{g'} \rho_{\mathrm{vort}}(\vec{u}) \Gamma(\vec{u}, \vec{u}') \rho_{\mathrm{vort}}(u'). \tag{8.13}$$

Before solving for the Green function $\Gamma(\vec{u}, \vec{u}')$, we comment on the curl of the condensate flow velocity v, denoted as $\rho_{\mathrm{vort}}(\vec{u})$. First, the velocity field of the condensate is a gradient field and therefore irrotational unless there are singularities in the phase. In other words, $\rho_{\mathrm{vort}}(\vec{u})$ should be identically zero in the absence of vortices. Second, we can use Stokes theorem to infer its form for condensates hosting some vortices. Assuming $S = \sum_j S_j$ with S_j determined by the position of the jth vortex, as in Eqs. (8.3) and (8.4) we can write

$$\oint v \cdot d\vec{l} = \oint \nabla S \cdot d\vec{l} = \sum_j \oint \nabla S_j \cdot d\vec{l} = \sum 2\pi \ell_j \tag{8.14}$$

where ℓ_j is the angular momentum associated with the jth vortex. At the same time, by Stokes' theorem,

we can write

$$\oint v \cdot d\vec{l} = \int\int \nabla \times \nabla S \cdot d\vec{A} = \sum 2\pi\ell_j \tag{8.15}$$

so that identifying the integrand on the right hand side with $\rho_{\rm vort}$ we find

$$\rho_{\rm vort}(\vec{u}) = \sum_j 2\pi\ell_j \delta(\vec{u} - \vec{u}_j). \tag{8.16}$$

More explicitly, $\rho_{\rm vort}$ is the distribution of vortices over the surface of the sphere. The kinetic energy of Eq. (8.13) then has the form of a sum over all vortex pairs on that surface with the Green function encoding their interactions.

As in Ref. [124] we calculate the Green function Γ by working with spherical harmonics. We start with

$$\nabla^2_{\vec{u}}\Gamma(\vec{u},\vec{u}') = \frac{\delta(\vec{u},\vec{u}')}{\sqrt{g}} - \frac{1}{4\pi R^2} \tag{8.17}$$

where the factor of $\sqrt{g}$ ensures that the delta function returns unity when integrated over the surface of the spherical condensate shell.

The second factor in Eq. (8.17) is introduced in order to cancel any divergent terms once the delta function is expanded. To physically motivate the introduction of this term it is useful to recall that the Green function of the Laplacian can be interpreted as the steady temperature response of the system to a unit point-source of heat. Since a spherical shell is a closed system, heat injected into it by a point-source cannot escape. To prevent energy build-up and make time-independent temperature response possible, the shell has to be brought into contact with a reservoir that uniformly absorbs heat at the same rate at which it is pumped in. The $1/4\pi R^2$ term in Eq. 8.17 represents such a subtraction for a spherical shell of surface area $4\pi R^2$ [124].

Expanding the delta function in terms of spherical harmonics as

$$\frac{\delta(\vec{u},\vec{u}')}{\sqrt{g}} = \frac{\delta(\theta-\theta')\delta(\phi-\phi')}{R^2\sin\theta'} = \frac{1}{R^2}\sum_{\ell=0}^{\infty}\sum_{m=-\ell}^{m=\ell} Y_\ell^m(\theta,\phi)Y_\ell^{m*}(\theta',\phi'). \tag{8.18}$$

we obtain

$$\nabla^2_{\vec{u}}\Gamma(\vec{u},\vec{u}') = \frac{1}{R^2}\sum_{\ell=1}^{\infty}\sum_{m=-\ell}^{m=\ell} Y_\ell^m(\theta,\phi)Y_\ell^{m*}(\theta',\phi') \tag{8.19}$$

where now the ℓ sum starts from $\ell = 1$ since the $\ell = 0$ constant term canceled with the second term in Eq. (8.17). Further, we can use the well known identity

$$\nabla^2 Y_\ell^m(\theta,\phi) = -\frac{\ell(\ell+1)}{R^2} Y_\ell^m(\theta,\phi) \tag{8.20}$$

and integration by parts in an integral of the form $\int dA' \nabla^2 \Gamma Y_{\ell'}^{m'}$ to conclude that

$$\Gamma(\vec{u},\vec{u}') = -\sum_{\ell=1}^{\infty} \sum_{m=-\ell}^{m=\ell} \frac{Y_\ell^m(\theta,\phi) Y_\ell^{m*}(\theta',\phi')}{\ell(\ell+1)}. \tag{8.21}$$

The expression in Eq. (8.21) can be simplified by using the addition theorem for spherical harmonics

$$P_\ell(\vec{x}\cdot\vec{y}) = \frac{4\pi}{2\ell+1} \sum_{m=-\ell}^{m=\ell} Y_\ell^m(\vec{x}) Y_\ell^{m*}(\vec{y}) \tag{8.22}$$

and the following two facts about Legendre polynomials:

$$\begin{aligned} \sum_l \frac{P_\ell(\cos\beta)}{\ell} &= -\ln\left(\frac{1+\sin(\beta/2)}{\sin(\beta/2)}\right) \\ \sum_l \frac{P_\ell(\cos\beta)}{\ell+1} &= \ln\left(\frac{\sin(\beta/2)}{1+\sin(\beta/2)}\right) - 1. \end{aligned} \tag{8.23}$$

Combining Eq. (8.21), (8.22) and (8.23) finally gives

$$\Gamma(\vec{u},\vec{u'}) = -\sum_{\ell=1}^{\infty} \frac{2\ell+1}{\ell(\ell+1)} \frac{P_\ell(\cos\beta)}{4\pi} = \frac{1}{4\pi} \ln\left(\frac{1-\cos\beta}{2}\right) + \frac{1}{4\pi} \tag{8.24}$$

for β the angle between the directions $\vec{u} = \{\theta,\phi\}$ and $\vec{u} = \{\theta',\phi'\}$ on the shell. The kinetic energy of the vortex configuration, dropping all constant terms, then follows from Eqs. (8.16) and (8.13) so that

$$KE = -\frac{\pi\hbar^2\rho_{2\mathrm{D}}}{2m^2} \sum_{i\neq j} \ell_i \ell_j \ln(1-\cos\beta_{ij}). \tag{8.25}$$

In Eq. (8.25), β_{ij} is the angular separation between the vortices measured with respect to the center of the condensate (central angle). This quantity is analogous to the flat plane separation between the vortices in Eq. (3.43) and can be calculated as

$$\cos(\beta_{ij}) = \cos\theta_i \cos\theta_j + \sin\theta_i \sin\theta_j \cos(\phi_i - \phi_j). \tag{8.26}$$

We note that in evaluating the energy functional Eq. (8.8) we did not account for the energy associated with maintaining the empty vortex core. From Sec. 3.2, we know that far away from the vortices such terms are logarithmic in the ratio of the condensate size and the size of the vortex core i.e. $E_c \propto \ln(R/\xi)$.

We can now use Eq. (8.25) to estimate the interaction energy between a vortex antivortex pair on a nearly two-dimensional spherical condensate shell again. Assuming that they are situated at $(\theta, \phi) = (\pm\alpha, 0)$ as before Eq. (8.26) implies that

$$KE_{\text{pair}} = \frac{\pi\hbar^2\rho_{2\text{D}}}{2m^2}\ln(1+\cos(2\alpha)) = \frac{\pi\hbar^2\rho_{2\text{D}}}{m^2}\ln(\cos(\alpha)). \tag{8.27}$$

This interaction energy decreases as α increases towards the equator $\theta = \pi/2$. When $\alpha \approx \pi/2$ the two vortices are essentially at the same position so the net flow of the condensate greatly diminishes. It has been shown in the literature that in oblate BECs similar annihilations between pairs of counter-circulating vortices can occur and result in formation of less energetically costly defects [125]. We argue that a similar mechanism applies on the surface of a sphere – the oppositely directed flows around each respective vortex core require too much kinetic energy for the dipole-like configuration to be preferred. As this analysis changes when the system is rotated, we revisit it in the following Section.

8.2 Rotating two-dimensional shells

Experimentally, vortices in BEC can be engineered by rotating or stirring [37, 39, 38, 40] the condensate cloud or by using the more controlled technique of phase imprinting [57, 58]. In the latter case, the vortex can be created at specific point in the condensate while in the former vortices typically arise close to the rotation axis, assuming some critical rotation rate has been achieved as in Eq. (3.20). We turn to studying the effects of rotation on vortices in a thin, quasi-two-dimensional spherical BECs.

8.2.1 Analytic energy estimates

As in Eq. (3.19) the lowest energy state available to the rotating shell, assuming the rotation is about the z-axis, depends on the expectation value of the angular momentum operator L_z. To calculate this quantity we follow Ref. [115] and consider a single vortex close to the top of the condensate shell so that

$$\langle L_z\rangle = \int f^* e^{-iS}(-i\hbar\partial_\phi)fe^{iS} = \hbar\rho_{2D}\int\int R^2\sin\theta d\theta d\phi\partial_\phi S. \tag{8.28}$$

Since

$$\vec{v} = \frac{\hbar}{m}\nabla S = \frac{\hbar}{m}\frac{1}{R}\partial_\theta S\hat{\theta} + \frac{\hbar}{m}\frac{1}{R\sin\theta}\partial_\phi S\hat{\phi} \tag{8.29}$$

we can rewrite the previous equation as

$$\langle L_z\rangle = \hbar^2\rho_{2D}\int_0^\pi R^2\sin\theta d\theta\int R\sin\theta v_\phi d\phi = \hbar^2\rho_{2D}\int_0^\pi R^2\sin\theta d\theta\int(d\vec{l}\cdot\vec{v})_\phi \tag{8.30}$$

where the last term is a loop around some fixed angle θ. If the vortex is situated at $\theta = \theta_v$ then condensate density should vanish for $\theta > \theta_c$ with θ_c reflecting the size of the vortex $\theta_c \approx \xi/2R$ (see Sec. 3.2). Otherwise, the integral should simply produce $2\pi\ell$. In other words,

$$\langle L_z\rangle = \frac{\hbar}{m}2\pi\ell\rho_{2D}R^2\cos\theta_c \tag{8.31}$$

For the equatorially symmetric vortex antivortex pair we scale Eq. (8.31) by a factor of two and conclude that

$$E_{\rm rot} = \Omega\langle L_z\rangle = \frac{\hbar}{m}4\pi\ell\Omega\rho_{2D}R^2\cos\theta_c \tag{8.32}$$

This term has a geometrical interpretation

$$E_{\rm rot} = \frac{\hbar}{m}\Omega\ell\rho_{2D}(A_{\rm tot} - A_{\rm vort}) \tag{8.33}$$

where $A_{\rm tot}$ is the total surface area of the shell and $A_{\rm vort}$ is the are taken up by the two vortices. More precisely, the difference in Eq. (8.33) mutliplied by the (two-dimensional) condensate density gives the number of atoms that are rotating, taking into account density depletions at the positions of the vortices. Approximating vortices as point-like, we take

$$E_{\rm rot} \approx 4\frac{\hbar}{m}\pi\ell\Omega\rho_{2D}R^2\cos\alpha. \tag{8.34}$$

This expression also lends itself to a simple interpretation as $\cos\alpha$ gives the fraction of angular momentum about the z-axis an atom at $\theta = \alpha$ would locally experience as the whole condensate shell is rotating.

Now we can consider the total condensate energy: the cost of vortex cores, the kinetic interaction energy

between the pair and the rotation term calculated in Eq. (8.34)

$$E_{\rm tot} = 2E_{\rm core} + E_{\rm vortex-vortex} - E_{\rm rot}$$
$$E_{\rm tot} = \frac{2\pi\hbar^2}{m^2}\rho_{\rm 2D}\ell^2\log(R/\xi) + \frac{\pi\hbar^2}{2m^2}\rho_{2D}\log(1+\cos(2\alpha)) - \frac{\hbar}{m}\Omega\rho_{2D}4\pi R^2\cos\alpha. \tag{8.35}$$

Here, $E_{\rm core}$ denotes the energy cost of maintaining the vortex core, as discussed in Sec. 3.2. This quantity is set by the healing length of the condensate and depends on the type of atoms used and the inter-atomic interaction so we take it to be the same as in a flat BEC. It is further appropriate to make this approximation since we are assuming that all vortices being discussed are point-like or at least significantly smaller than the size of the condensate.

A plot of this energy, Eq. (8.35), as a function of α and three rotation rates Ω, is shown in Fig. 8.3. Depending on the rotation rate, it can have at most two distinct minima: one for the configuration where the vortex anti-vortex pair is aligned with the poles of the shell and one when $\alpha = \pi/2$ i.e. the two defects overlap at the shell equator and the flows associated with them cancel out. There are no minima corresponding to intermediate α for which the vortex antivortex configuration could be stable.

While numerical studies [79] show that a vortex antivortex pair characterized by $\alpha \neq 0$ is typically not the lowest energy state of the rotating condensate shell, if such a pair were engineered through some experimental technique any increase in rotation speed of the whole system would push them closer and closer to the rotation axis. This follows from considering the angular momentum term in Eq. (8.35). This term – $\Omega\langle L_z\rangle$ – decreases the total energy of the condensate the most when the vortex antivortex pair is situated on respective poles of the condensate shell. When Ω is large, this term is large as well and the vortices align with the rotation axis. More intuitively, given the geometrical interpretation of Eq. (8.31), increasing $\Omega\langle L_z\rangle$ increases the number of atoms rotating around the z-axis which accounts for the vortices (sourcing a flow that is "tilted" compared to a swirl about the z-axis) being pushed towards it.

More rigorously, we identify a critical rotation frequency $\Omega^{\rm c}_{\alpha=0}$ at which condensate shell energy first features a local minimum for $\alpha = 0$, in addition to $\alpha = \pi/2$. To that end we expand the total energy of the condensate hosting a vortex antivortex pair for small α. As the energy cost of maintaining the two vortex cores does not depend on α, this calculation captures exactly the competition between the rotation (pushing the vortices toward the rotation axis) and the vortex-vortex interaction (pulling the pair closer to each other). From the expansion

$$E = \text{const} + \frac{\pi\hbar\rho_{2D}}{m}\left[\frac{-\hbar}{2m} + 2\Omega R^2\right]\alpha^2 + \left[-\frac{\hbar}{12m} - \frac{1}{6}\Omega R^2\right]\alpha^4 \tag{8.36}$$

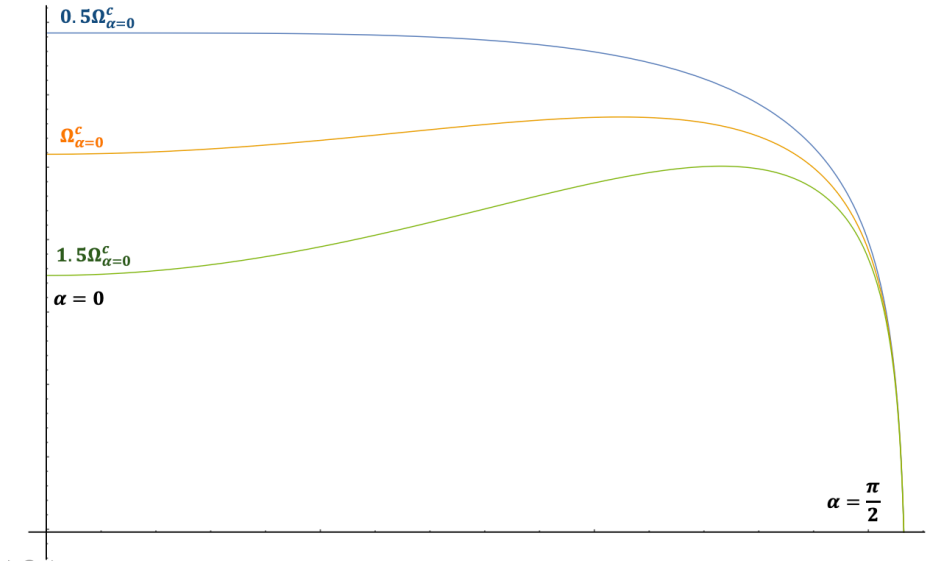

Figure 8.3: Plots of total energy of a rotating two-dimensional condensate shell hosting a vortex anti-vortex pair at $\theta = \alpha$ and $\theta = \pi - \alpha$ for increasing values of rotation frequency. Here, the BEC shell has radius on the order of a micron and consists of $N = 10^5/87$ atoms. We assume that interactions between atoms are strong and calculate ξ to be on the order of 10^{-3} microns. The curve depicted in blue corresponds to half of the critical rotation frequency identified in Eq. (8.37), the one depicted in orange represents a BEC rotating exactly at that frequency while the curve in green shows the total energy for a rotation rate of $\Omega = 1.5\Omega^{\rm c}_{\alpha=0}$. We note that as rotation frequency Ω is increased through $\Omega^{\rm c}_{\alpha=0}$, the more favorable it becomes for the vortex anti-vortex pair to be pinned at the poles i.e. for the flow that they produce to exactly match that due to the rotation.

it is clear that the coefficient of α^2 changes sign and there is a local energy minimum for

$$\Omega^{\rm c}_{\alpha=0} R = \frac{1}{4}\frac{\hbar}{mR}. \tag{8.37}$$

Hence, the vortex and the antivortex align with the rotation axis instead of annihilating at the shell's equator once the linear speed associated with the rotation of the whole system ($v_{\rm lin} = \Omega R$) is of the same order of magnitude as the speed of condensate flow for a vortex antivortex pair positioned exactly along the z-axis ($v^{\rm vort}_{\alpha=0} = \hbar/mR$). This is consistent with studies of two-dimensional rotating BECs where vortex configurations mimicking rigid body rotation have been identified as most energetically favorable [68]. A numerical study complementary to the conclusions of this Section is summarized below.

8.2.2 Numerical energy estimates

In this Section, we numerically calculate the wavefunction $\psi_{\rm 2D}(\theta, \phi)$ of a rotating two-dimensional spherical BEC. This work was primarily carried out by collaborator Dr. K. Sun and it consists of minimizing the energy functional that describes a two-dimensional condensate shell in its rotating frame. For shells rotating

at the angular rate Ω, we have

$$E_{2\mathrm{D}}[\psi] = \int \sin\theta d\theta d\phi \left[|\nabla\psi_{2\mathrm{D}}|^2 + \frac{U_{2\mathrm{D}}}{2}|\psi_{2\mathrm{D}}|^4 + \tilde{\Omega}\psi^*_{2\mathrm{D}}(i\partial_\phi)\psi_{2\mathrm{D}} \right], \tag{8.38}$$

where $U_{2\mathrm{D}}$ is the effective interaction strength in two dimensions. Details of the minimization calculation, addressing mathematical issues with the use of polar coordinates, and the determination of the $U_{2\mathrm{D}}$ value are presented in Appendix C. In our calculations, $U_{2\mathrm{D}}$ is chosen so that the typical ratio of kinetic energy to interaction energy is $\sim 5\%$ i.e. we work in the (Thomas-Fermi) limit of strong inter-atomic interactions. This method – minimizing Eq. (8.38) – is equivalent to solving the GP equation, and we keep all the physical quantities dimensionless by using $E_R = \hbar^2/(2MR^2)$ as the unit of energy and BEC shell radius R as unit length. As in previous Sections, we focus on the vortex-antivortex pair configuration. This structure is imposed by fixing the wavefunction zeros (vortex cores) at $\theta = \alpha$ and $\theta = \pi - \alpha$ respectively, as in Fig. 8.2. While Eq. (8.35) does account for the energy cost of maintaining vortex cores empty of condensate atoms, this minimization approach captures the details of vortex shape and its significance more precisely.

This feature of the numerical calculation enhances the understanding we have gained from the analytical approach leading to Eq. (8.35). Concretely, in Fig. 8.4, we compare energy values for a rotating two-dimensional condensate shell obtained through analytical estimates neglecting vortex cores in panel (a) and values of the energy functional obtained through GP equation calculations that include them in panel (b). In the former case, for clarity of comparison, Fig. 8.4 (a) shows the plot of the energy functional per particle in the rotating frame in a dimensionless form as

$$\varepsilon(\alpha) = \frac{E_{\mathrm{vor-vor}} - E_{\mathrm{rot}}}{NE_R} = \frac{1}{2}\ln(\cos\alpha) - \tilde{\Omega}\cos\alpha, \tag{8.39}$$

where $N = 4\pi R^2\rho_{2\mathrm{D}}$ is the total number of particles and $\tilde{\Omega} = \frac{2m}{\hbar}\Omega R^2$ is a dimensionless angular velocity. This curve and the numerically calculated one in Fig. 8.4 (b) exhibit same behaviors above and below a critical angular velocity $\tilde{\Omega}^c_{\alpha=0} \sim \frac{1}{2}$. Hence, the GP approach confirms the stability of a vortex-antivortex pair at poles of the shell ($\alpha = 0$) when system rotation is fast enough.

Numerical results also show that the sharp decrease of the energy functional to the global minimum at the shell's equator occurs at a larger α than implied by the analytic results in Eq. (8.39). In other words, a vortex-antivortex configuration could be stable against pair annihilation at the equator of the BEC shell for a larger range of α than analytical estimates of the previous Section may imply. We consequently conjecture that the effect of density depletion at the vortex cores moderates the intervortex interaction until the vortices are very close to each other. Notably, for angles near $\alpha = \frac{\pi}{2}$, we cannot disregard vortex core effects, and

the energy functional of Eq. 8.39 is no longer appropriate.

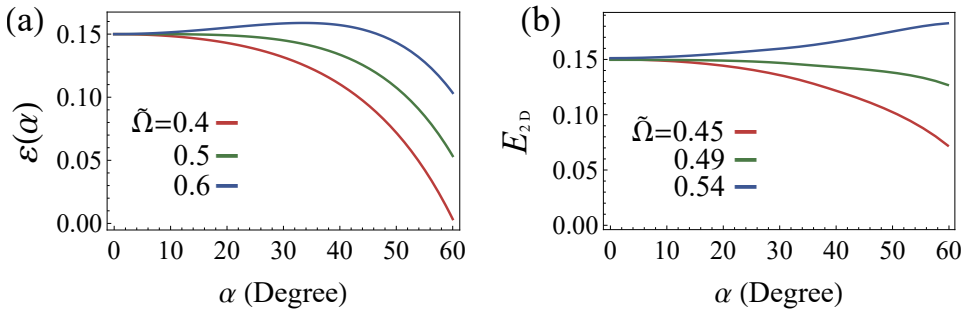

Figure 8.4: **(a)** Energy $\varepsilon(\alpha)$ in Eq. (8.39) of a rotating 2D spherical BEC for angular velocity $\tilde{\Omega}$ above, equal to, and below the critical value $\tilde{\Omega}_c = \frac{1}{2}$. **(b)** Energy E_{2D} in Eq. (8.38) obtained from the numerical GP equation calculations. For a convenient comparison, the energy curves in both panels are levelled up at $\alpha = 0$.

Focusing on the superfluid flow obtained from the GP wavefunction, for any finite α we find that the flow pattern resembles one that rotates about a string through both vortex cores, as illustrated in Fig. 8.2. We employ a variational approach to approximate the wavefunction by considering the shape of such a string, parameterized in a convenient way. This allows us to determine the condensate density and phase, and the associated superfluid flow. We set an arbitrary conic-section curve on the x-z plane ($\phi = 0$ or π) through the vortex cores on the sphere which takes the general form $z^2 = (\lambda - 1)x^2 + 2bx + (1 - \lambda \sin^2\alpha - 2b \sin\alpha)$ with two variational parameters b and λ. We numerically minimize the energy functional of Eq. (8.38) with a variational wavefunction $\psi_{\rm var}(\theta, \phi) = f_{\rm var} e^{iS_{\rm var}}$, where the phase $S_{\rm var}$ is now the azimuthal angle with respect to the variational curve, and the amplitude $f_{\rm var}$ has a variational depletion at the vortex cores. Specifically, $f_{\rm var}(\theta, \phi) = A \frac{\sigma_\alpha}{\sqrt{\zeta^2 + {\sigma_\alpha}^2}} \times \frac{\sigma_{\pi-\alpha}}{\sqrt{\zeta^2 + {\sigma_{\pi-\alpha}}^2}}$, where A is the normalization constant, ζ a variational parameter, and $\sigma_\alpha = \cos^{-1}(\cos\alpha\cos\theta + \sin\alpha\sin\theta\cos\phi)$ is the distance from the vortex core at α. We find that the minimum energy state corresponds to a circle string ($\lambda = 1$) passing through the vortex cores and perpendicular to the sphere's surface. Further, these variational results qualitatively agree with the GP results with respect to energy functional curves as well as critical rotation speed.

The variational assumption of a curved string connecting the vortex-antivortex pair relates our analysis to studies of vortex dynamics in filled 3D spherical BECs where a physical vortex string (line) may move off-axis [9, 39] or bend [64, 126, 127] due to interaction or density inhomogeneity effects. Namely, a vortex-antivortex pair on opposite poles of a 2D condensate shell corresponds to a straight on-axis vortex in a 3D BEC, while the pair at angle $\alpha > 0$ corresponds to a bent vortex. This correspondence additionally informs the understanding of vortices on a spherically symmetric BEC undergoing dimensional crossover from a hollow 2D geometry to a shell-shaped condensate having finite thickness and, finally, to a fully filled

spherical BEC. Such crossover could be experimentally achieved by the bubble trap discussed in Sec. 4.2 and Ref. [98].

8.2.3 Effect of rotation on the condensate shell shape

Rotating the condensate shell will not only affect the vortex structures on its surface but also change the shape of condensate density as well. Similar to the geometry of the Earth, we expect the BEC shell to lose perfect spherical symmetry and become an oblate spheroid. To see this, we consider a harmonically trapped spherical BEC. In the Thomas-Fermi approximation, it's surface is determined by

$$\frac{1}{2}m\omega_0^2 r^2 = \frac{1}{2}m\omega_0^2(x^2+y^2+z^2) = \mu \tag{8.40}$$

for μ the chemical potential. In the reference frame rotating with Ω, as in the previous Section, this becomes

$$\frac{1}{2}\omega_0^2 r^2 - \frac{1}{2}m\Omega^2 r^2 \sin^2\theta = \frac{1}{2}m(\omega_0^2-\Omega^2)(x^2+y^2) + \frac{1}{2}mz^2 = \mu'. \tag{8.41}$$

To be more detailed, the confinement in the x and y directions becomes less tight and the $x-z$ and $y-z$ cross-sections of the condensate cloud become elliptical.

From, Ref. [115], we know that the fact that a spheroid does not have a constant Gaussian curvature (like a spherical surface does) will result in there being a geometrical potential that can interact with vortices

$$\begin{aligned} E_{\text{curv}} &\simeq -\sum_i \ell_i^2 U_G(\vec{u}_i) \\ \nabla^2 U_G(\vec{u}_i) &= G(\vec{u}_i) \end{aligned} \tag{8.42}$$

where G is the Gaussian curvature. Thinking about this in terms of an analogy with electromagnetism, the curvature serves as a background charge that can source a potential. Accordingly, the Green's function of Eq. (8.13) can be re-defined as dependent on the Gaussian curvature G

$$\nabla\Gamma(\vec{x},\vec{y}) = -\delta(\vec{x},\vec{y}) + \frac{G(\vec{x},\vec{y})}{4\pi} \tag{8.43}$$

and all relevant energies re-calculated. In doing so, the authors of Ref. [115] find that for spheroids with height-to-length ratio smaller than or equal to 1 (this ratio being equal to 1 corresponds to a perfectly spherical surface), the same trend found in the sphere continues – it is energetically unfavorable for vortices to be positioned at any α other than $\alpha = 0$ (the poles) or $\alpha = \pi/2$ (the equator). Moreover, adding E_{curv}

to Eq. (8.35) for even a small deformation of the condensate shell (slow rotation rate) shows that the vortex anti-vortex pair is even more likely to meet at the equator and annihilate [115].

8.3 Towards rotating three-dimensional condensate shells

In the remainder of this Chapter, we present preliminary work aimed at expanding our discussion of the previous Section to condensate shells having non-negligible thickness. Here, the vortex structures in question are not point-like but rather three-dimensional "empty tubes" i.e they are vortex lines. Given the added radial degree of freedom that three-dimensional condensate shells have, the hollow vortex core takes up a volume rather than an area. The vortex line itself can also be characterized by some curvature. Below, we consider nucleation of such three-dimensional vortex lines and again address the effects of system rotation. We first offer an estimate for the frequency of rotation for which it is energetically favorable for a thin but three-dimensional shell to attain a vortex state in Sec. 8.3.1 then present preliminary results addressing the same question through two separate numerical approaches in Sec. 8.3.2.

8.3.1 Slicing and stacking

We start our analysis of the energetic cost of a vortex line for three-dimensional condensate shells by employing a "slicing and stacking" approach inspired by Ref. [9]. We approximate the condensate shell having some small thickness as a stack of two-dimensional "slices" perpendicular to the z-axis. Assuming that condensate flow parallel to the z-axis vanishes, we model a thin BEC shell having mean radius r_0 (approximately equal to its outer radius R) and shell thickness t pierced by a straight vortex line extending through its center, along the z-axis. Slices perpendicular to the vortex (cross-sections in the $x-y$ plane) are a top and a bottom disk-shaped cap, having an extreme density depletion at the position of the vortex, and a stack of two-dimensional annuli. For the caps, the vortex contribution to condensate energy is the energy cost of maintaining its core (empty of superfluid) as well as the kinetic energy of the flow around it. For the rings only the latter energy is important. We proceed to outline and combine these two estimates.

We assume the shell thickness to be small so that the radius of each cap can be approximated as

$$r_{\mathrm{z,end}} \approx \sqrt{r_0^2 - (r_0 - t)^2} \approx \sqrt{2tr_0}. \tag{8.44}$$

From Ref. [9] and our discussion in Sec. 3.2, the energy cost of a vortex in a uniform condensate reads

$$E_{\mathrm{vortex}} = \rho_{\mathrm{2D}} \pi \frac{\hbar^2}{m} \ln(1.464R/\xi_0) \tag{8.45}$$

for R the radius of the slice, $\rho_{2\mathrm{D}}$ the BEC density and ξ_0 the coherence length at the mean radius of the shell. Consequently we can approximate the energy contribution of each disk-like slice as

$$E_{\mathrm{vortex}}^{\mathrm{cap}} \approx tE_{\mathrm{vortex}} = t\pi\bar{\rho}_{2\mathrm{D}}\frac{\hbar^2}{m}\ln\left(1.464\frac{\sqrt{2tr_0}}{\xi_0}\right) \tag{8.46}$$

where condensate density has been replaced with some appropriate average value $\bar{\rho}_{2\mathrm{D}}$. We proceed to evaluate the energy contribution of ring-like slices where the only energy contribution is that due to the azimuthal condensate flow

$$E_{\mathrm{KE}} = \frac{1}{2}\int_{\mathrm{thickness}} m\rho_{2\mathrm{D}}(\rho)v^2\pi\rho d\rho \tag{8.47}$$

where ρ is the radial coordinate in the $x-y$ plane and

$$v = \frac{\hbar}{m\rho} \approx \frac{\hbar}{mr_z} \tag{8.48}$$

for a very thin shell and a ring slice of mean radius r_z. Under these assumptions we can approximate

$$\int \rho_{2\mathrm{D}}(\rho)2\pi\rho d\rho \approx 2\pi r_z t\bar{n} \tag{8.49}$$

so that the contribution to the total energy of the condensate from each ring slice is

$$dE_{\mathrm{vortex}}^{\mathrm{rings}} = \frac{1}{2}m2\pi r_z t\bar{\rho}_{2\mathrm{D}}\frac{\hbar^2}{m^2r_z^2}dz. \tag{8.50}$$

Integrating over z further gives

$$E_{\mathrm{vortex}}^{\mathrm{rings}} = \int_{r_0-t/2}^{r_0+t/2}\pi\frac{\bar{\rho}_{2\mathrm{D}}\hbar^2}{m}\frac{t}{r_z}dz \approx \frac{\pi\bar{\rho}_{2\mathrm{D}}\hbar^2}{m}t\int_{-r_0}^{r_0}\frac{dz}{\sqrt{r_0^2-z^2}} \approx \frac{\pi^2\bar{\rho}_{2\mathrm{D}}\hbar^2}{m}t. \tag{8.51}$$

The total energy of the thin condensate shell having a straight vortex line along the z-axis follows from combining Eqs. (8.46) and (8.51) as

$$E_{\mathrm{vortex}} = 2E_{\mathrm{vortex}}^{\mathrm{cap}} + E_{\mathrm{vortex}}^{\mathrm{rings}} \tag{8.52}$$

or, more precisely,

$$E_{\mathrm{vortex}} = \bar{\rho}_{2\mathrm{D}}\frac{\pi\hbar^2}{m}t(\pi + 2\ln(1.464\sqrt{2tr_0}/\xi_0). \tag{8.53}$$

As noted above, the critical Ω_c rotation frequency at which this state becomes energetically favorable and a vortex is nucleated is determined by

$$E_{\rm vortex} = E_{\rm rotation} = \Omega_c \langle L_z \rangle \tag{8.54}$$

where the average value of the angular momentum along the z-axis is roughly equal to each atom in the condensate carrying a single unit of angular momentum (for a $\ell = 1$ vortex line)

$$\langle L_z \rangle \approx \hbar \int \rho_{\rm 2D}(\vec{r}) d\vec{r} = \hbar \bar{n} 4\pi r_0^2 t. \tag{8.55}$$

Here we note that $\vec{r}$ is now a three-dimensional vector in spherical polar coordinates. Finally, we estimate

$$\Omega_c^{\rm thinshell} = \frac{\hbar}{4mr_0^2}(\pi + 2\ln(1.464\sqrt{2tr_0}/\xi_0)). \tag{8.56}$$

As the distinguishing feature of the condensate shell under consideration is its having a hollow region, we compare this critical frequency to a fully-filled spherically symmetric BEC for which [9]

$$\Omega_c^{\rm sphere} = \frac{5}{2}\frac{\hbar}{mR^2}\log(0.671R/\xi_0). \tag{8.57}$$

Evaluating Eqs. (8.56) and (8.57) for a number of values representative of feasible experimental studies (such as in Sec. 7.3.1), we find that the latter is always larger. In other words, a vortex state becomes energetically favorable for lower rotation frequencies when the condensate is a thin, hollow shell than when it is a fully filled sphere.

For a more direct analytical comparison, we write

$$E_{\rm vortex}^{\rm sphere}/E_{\rm sphere} \approx \frac{4\pi\hbar^2}{3mU} R \left(\ln \frac{R}{\xi_0} - 0.399 \right). \tag{8.58}$$

Here, U is the 3D interatomic interaction strength and ξ_0 now denotes the coherence length at the center of the vortex-free filled spherical BEC, while R is its outer radius. We note that the vortex core size is set by ξ_0, which should be much smaller than the size of the cloud, $R/\xi_0 \gg 1$. For a thin spherical shell having thickness t, much smaller than outer radius R, the fractional energy cost of the vortex determined by "slicing and stacking" similarly reads:

$$E_{\rm vortex}^{\rm thinshell}/E_{\rm thinshell} \approx \frac{2\pi\hbar^2}{3mU} t \left(\ln \frac{R}{\xi_0} + \ln \frac{t}{\xi_0} + 4.597 \right), \tag{8.59}$$

where ξ_0 is the coherence length at the mean radius of the shell as in Eq. (8.45). We note that, parallel to the fully-filled spherical condensate, we assume $t/\xi_0 \gg 1$. Since $R \gg t$ for a thin shell, the first term in parentheses dominates.

Based on this analytical calculation we conclude that the energy cost of a vortex in a thin shell BEC scales linearly with its thickness. In contrast, the energy cost of a vortex in a filled sphere BEC scales linearly (with log corrections) with its radius R. This result suggests that the dominant cost of a vortex is its core, which has length $2R$ in the filled sphere and only $2t$ for the thin shell. Since in the thin shell limit we assume a hollow BEC thickness much smaller than its radius, the energy cost for a vortex in this geometry will be much lower than for a similarly sized fully filled spherical condensate. The importance of the density depletion at the position of the vortex here is consistent with our discussion of purely two-dimensional shells in Sec. (8.2.2). In that case we found that vortex cores can have a significant effects on the energetics of a vortex-antivortex pair and such a pair represents an extreme limit of a vortex line in a thin condensate shell where the very small shell thickness makes the edges of the line point-like.

8.3.2 Numerical Results for BEC shells of arbitrary thickness

We complete our discussion of vorticity in three-dimensional BEC shells by presenting results of two numerical studies. They access more realistic physical models of the shell's equilibrium density and complement the approximate approach presented above. Calculations of the ground state of the hollow condensate shell obtained by the imaginary-time method, previously discussed for defect-less BECs in Sec. 4.3, have been conducted by collaborator Prof. C. Lannert while work centering numerical solutions to the two-dimensional GP equation on a curved surface and the subsequent local density approximation (LDA) was carried out by collaborator Dr. K. Sun. Both approaches are presented and detailed in Ref. [79]. With these approaches, we aim to refine and strengthen our conclusions following Eq. (8.56) as well as the critical rotation rate estimate. Through imaginary time numerics we corroborate the fact that lower rotation rates result in nucleation of a vortex line in the case of hollow condensate shells, as opposed to fully-filled spherical BECs. The LDA further identifies a relationship between the critical rotation rate and condensate shell thickness.

Critical rotation speed from imaginary time numerics

Numerical solutions of the Gross-Pitaevskii equation found by using an imaginary-time method enable us to extend our analysis beyond the Thomas-Fermi approximation, and to consider shells of arbitrary thickness. We specifically seek numerical solutions corresponding to condensate shells having a vortex along the z-axis with vorticity ℓ. The resulting energy equation for the condensate wavefunction magnitude,

$|\psi|$, can be minimized using an imaginary-time algorithm [104]. By using the bubble-trap of Eq. (4.3), $V_{\rm bubble}(\mathbf{r}) = m\omega_0^2\sqrt{(r^2-\Delta)^2/4+\Omega^2}$, we numerically find the ground state wavefunction amplitude and energy for a harmonically-trapped filled spherical condensate, as well as a shell of arbitrary size and thickness. To make contact with previous discussion, we present results concerning a fairly thin shell having thickness-to-radius ratio $\delta/R \approx 0.3$ and trap confinement frequency $\omega_{sh} = \omega_0$. We compare these results to the case of a condensate sphere confined by the same frequency, ω_0. In these calculations the effective interaction constant U_0 is set by $8\pi N a_s/S_l = 10,000$ where S_l is the oscillator length of the harmonic confining trap. In other words, the numerical solutions obtained here correspond to the strong interaction regime of the BEC as well.

By numerically obtaining the ground state energy for the no-vortex ($\ell = 0$) and single-vortex ($\ell = 1$) cases, we find the critical rotation rate for nucleation of a vortex. For the thin ($t/R \approx 0.3$) condensate shell, we find $\Omega_c^{\rm sh} = 0.02\omega_0$, whereas for the fully-filled spherical BEC we find $\Omega_c^{\rm sp} = 0.2\omega_0$. The factor of ten difference in critical rotation speeds bears out and illustrates the much lower energy cost for a vortex in a hollow shell, compared with a filled sphere BEC. This conclusion is in agreement with the more analytical, albeit approximate, approach of Sec. 8.3.1.

Layered two-dimensional shells and the local density approximation

As a complementary calculation, in this Section, we build on the numerical scheme used in Sec. 8.2.2 and approximate a thick condensate shell as a series of concentric two-dimensional shells. We assume that the superfluid flow along the radial direction and any possible interactions between the layered two-dimensional shells are negligible. These assumptions constitute a local density approximation (LDA), schematically represented in Fig. 8.5.

We denote the shell thickness δ so that the concentric two-dimensional shells have radii ranging between the three-dimensional BEC's inner (Thomas-Fermi) radius $R_{\rm in} = R - \delta$ and its outer (Thomas-Fermi) radius R. The energy functional is evaluated as

$$E_{\rm 3D}^{\rm LDA} = \sum_i E_{\rm 2D}(r_i), \tag{8.60}$$

where $E_{\rm 2D}(r_i)$ is the energy of each 2D shell, taking the same form as Eq. (8.38) with the shell radius being equal to r_i. The effective rotation speed for each two-dimensional shell is here scaled by its radius so that

$$\tilde{\Omega}^{\rm LDA}(r_i) = (r_i^2/R^2)\tilde{\Omega}. \tag{8.61}$$

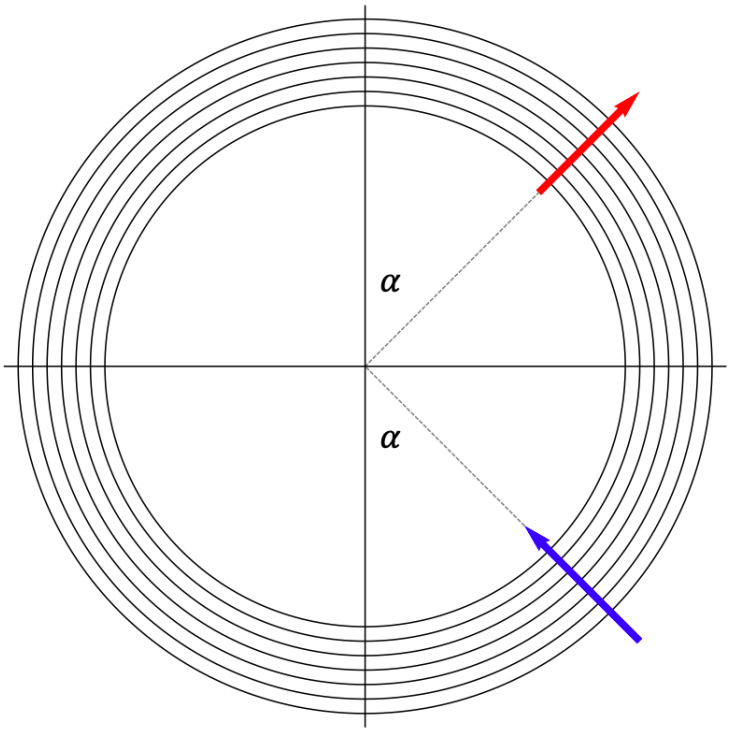

Figure 8.5: Schematic reperesentation of the local density approximation (LDA) discussed in Sec. 8.3.2. Here, a condensate shell having non-negligible thickness is approximated as concentric layers of two-dimensional condensate shells. We assume that flows and interactions between the layers are negligible.

The rotational term in the energy functional of each concentric layer therefore has r-dependence. Therefore, there ought to exist a radius r_c, such that the effective rotation speed is large enough to stabilize a vortex pair on the poles for the layers with $r_i > r_c$ (the 'outer' layers) but not for those with $r_i < r_c$ (the 'inner' layers). Since the vortex line cannot break into parts, its stability is determined by the layers that energetically dominate and thus depends on both the rotation speed $\tilde{\Omega}$ (which determines r_c) and the shell thickness δ (which determines the relative energetic contributions between the outer and inner layers).

Given a fixed rotation speed, the thicker the shell, the more the inner layers contribute to the system's energy. Thus, we expect to identify a critical thickness beyond which the local energy minimum for a vortex line piercing through the poles disappears. Figure 8.6(a) shows the energy functional of shell BECs having various thicknesses at $\tilde{\Omega} = 0.6$ (with the vortex location fixed at $\theta = \alpha$ on each 2D layer). The critical thickness above which the vortex line is no longer stable at the poles in this case corresponds to $\delta/R = 0.222$.

Conversely, for a given thickness, the LDA calculations show a critical rotation speed that determines the stability of the vortex line through the poles. In Fig. 8.6(b), we plot the critical rotation speed as function of BEC shell thickness, and find an approximately linear relationship. This result suggests a non-destructive

way to experimentally probe the thickness of a BEC shell by finding the lowest rotation speed that stabilizes a single vortex aligned with the rotation axis and passing through the poles.

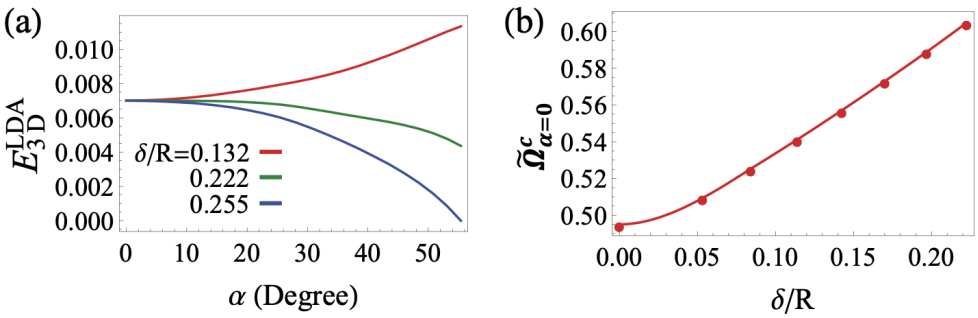

Figure 8.6: **(a)** Energy E_{3D}^{LDA} [in Eq. (8.60)] of 3D shell BECs as a function of vortex location for various shell thickness δ and $\tilde{\Omega} = 0.6$. The data are from the LDA calculation and are levelled up at $\alpha = 0$ **(b)** Critical rotation speed vs shell thickness from the LDA calculation. The leftmost data point is for a pure 2D shell.

In connecting these results with realistic experiments, we note that the LDA ignores coupling between the two-dimensional layer shells. In other words, we ignore any possible radial superfluid flow and associated radial kinetic energy. For a realistic shell BEC having thickness near the critical value, we posit that the competition between the vortex's outer and inner parts (with respect to the radial coordinate r) could not only reduces the force on the whole vortex but also cause bending or tilting of the line-like vortex cores. This effect, somewhat analogus to assigning the vortex core a tension along its length, might increase the life time of the vortex pair staying at a finite angle α in sufficiently thick condensate shells. However, for very thin shells, we do not expect such an effect as radial flow would increase condensate shell energy.

We complete this Section by summarizing our findings. First, the approximate method of "slicing and stacking" of two-dimensional planes in order to model a thin condensate shell and numerical solutions of the Gross-Pitaevskii equation found by an imaginary time algorithm both show that the rotation rate at which a vortex enters a thin condensate shell i.e. a vortex line is nucleated is smaller than in the case of a fully-filled, spherical condensate geometry. Numerical results concretely show this difference to be non-negligible. Further, numerical calculations within the LDA show that the stability of a vortex-antivortex pair at opposite poles of the condensate shell depends on both the rotation rate Ω and its thickness δ. While a vortex line extending along the rotation axis of a hollow BEC shell may nucleate for relatively low system rotation rates, its dynamical behavior and stability depend on the details of the hollow condensate geometry. In this way, as in our discussion of collective modes of hollow spherically-symetric condensates, the existence of the inner surface and the vanishing denisty at the condensate's center (its finite thickness) significantly change the physics of the system when compared to similar fully-filled BECs.

8.4 Further concerns and outlook

Throughout this work, we have discussed vortex nucleation but not the dynamic behavior of point-like vortices and vortex lines. For fully-filled condensates it is known that vortex lines nucleated at a lateral off-set from the rotation axis are not stable in presence of dissipation, which can provide a mechanism for the vortex line to move from a local to a global minimum [9]. Experimental and theoretical studies of vortices in oblate, cigar-shaped, condensates have further shown the tendency of vortices to precess [70, 74]. Previous work has also pointed to vortex bending being energetically favorable in, for instance, prolate harmonically trapped condensates [127, 64, 128, 126]. It is natural to ask whether vortex structures in thin condensate shells exhibit some of these behaviors. We briefly address two such concerns.

First, we consider modeling the condensate shell by stacking horizontal slices that are either two-dimensional condensate disks or annuli as in Sec. 8.3.1. In this scheme, the vortex line is made-out of point-like vortices in each slice. Recalling the arguments of Sec. 3.5, a point vortex in a condensate disk is stationary only when situated at $\rho_v = 0$ (in polar coordinates) while for an annular BEC, the speed of the vortex vanishes for $\rho_v = \sqrt{R_{\rm out}R_{\rm in}}$ (provided there is no additional vorticity about the ring's inner radius $R_{\rm in}$). The somewhat heuristic "slicing and stacking" picture of the vortex line in a condensate shell then implies that it would have to be unstable if nucleated at $\rho_v \neq 0$: its top and bottom segments would be attracted to the condensate edge while the the parts contained in the annular slices would be attracted to different ρ_v since the inner and outer radii of each slice depend on z. Moreover, the point at which the vortex speed in an annular condensate vanishes is not a true minimum of its energy so that the "pull" of the vortex in the slices above and below a given part of the vortex line would be sufficient to make the whole vortex line unstable. Such an instability is consistent with existing literature on vortex lines supporting excitations such as Kelvin waves along the lenght of their cores [74, 129, 130, 131]. We also note that for a vortex line to fully exit the condensate rather than changing shape, dissipation has to be present or otherwise angular momentum is not conserved.

Second, we comment on the possibility of a bent vortex. We model such a vortex line as consisting of two radial segments beginning and ending on boundaries of the condensate shell, as opposed to being parallel to the rotation axis. Using the LDA (disregarding any radial condensate flow) and assuming that the bending angle α is r-independent, we find that the total energy of the vortex only has terms quadratic or quartic in that parameter when it is small. Under these assumptions, it follows from Eq. (8.36) that for a shell having thickness $\delta = R - R_{\rm in}$ the energy functional, up to an additive constant, reads

$$E = \int_{R_{\rm in}}^{R} dr \left\{ \frac{\pi\hbar\rho_{\rm 2D}}{m} \left[-\frac{\hbar}{2m} + 2\Omega r^2 \right] \alpha^2 + \left[-\frac{\hbar}{12m} - \frac{1}{6}\Omega r^2 \right] \alpha^4 \right\} = C_2\alpha^2 + C_4\alpha^4 \tag{8.62}$$

with C_2 and C_4 some properly calculated numerical coefficients. Here, the only global energy minimum occurs for $\alpha = 0$. This bending angle corresponds to the vortex line being straight and extending along the rotation axis. Consequently we suggest that in a realistic experimental situation, a bent vortex would either "straighten out" or self-annihilate in the same way a bent current-carrying wire becomes more bent due to magnetic field effects. As in our discussion above, rotation would be of significant importance for one or the other final fate of the vortex line. Various experiments in related contexts hint at this behavior, such as in Ref. [**?**], where a vortex line in a prolate harmonically trapped BEC becomes more bent and deviates more from the center of the condensate as the angular momentum of the system decreases.

Details of dynamic behavior of vortices in either case are of great interest for future work. Many BEC situations of physical relevance are likely to involve complex multi-vortex dynamics. Vortices are often nucleated as a consequence of perturbing condensates; the dynamical instability of vortex lines presents a starting point for understanding subsequent re-equilibration processes. In the context of BEC shells, we expect diverse dynamic and multi-vortex phenomena that are modified in comparison with the their filled counterparts due to the different geometry and topology. We have shown this to be the case for the vortex-antivortex pair, which in principle could be systematically investigated in the CAL experiment in the future. The work presented in this Chapter also offers a first step towards deconstructing theoretical and experimental multi-vortex dynamic studies in a range of settings from CAL and other ultracold atomic systems to pulsar glitches observed in the context of neutron stars [63, 62].

This Chapter concludes Part I of this thesis. In the seven Chapters that make it up, we presented a detailed and exhaustive study of hollow spherically symmetric Bose-Einstein condensates including their static, dynamic and vortex properties. Our work here clearly establishes the distinction between fully-filled and hollow quantum superfluid topologies and provides avenues for equally rich future work in theory and experiment alike.

In Part II, we shift our attention to a different issue of seemingly simple mathematics that neverthless results in a myriad of complex and intriguing physics phenomena. Namely, the next Part of this thesis focuses on the topic of quasiperiodicity in one-dimensional tight-binding models. Here, we address the ways in which a one-dimensional chain having a periodic on-site modulation with an irrational period – a quaisperiodic modulation – differs from its well-understood rational counterpart. We capture the importance of this irrational parameter by highlighting localization-delocalization physics. To that end, we utilize transfer matrix methods and a correspondence between eigenstates of a given system and curves on a torus. The following Chapter introduces these methods and outlines a number of examples of their use.

Part II: Quasiperiodicity in one-dimension

Chapter 9

Transfer matrices and Curves on a Torus

9.1 Introduction

In this Chapter, we focus on a method for capturing localization physics through geometrical properties of curves on a torus. Generically, for one-dimensional systems quantum states in disordered systems are known to be localized due to celebrated arguments put forward by P. W. Anderson in the late 1950s [2]. In other words, presence of any amount of randomness in these models precludes the possibility of a localization-delocalization transition. However, quasiperiodic systems characterized by deterministic "disorder" rather than true randomness can undergo such a transition even in one dimension. Consequently, localization-delocalization physics is of great interest as means of distinguishing between these different kinds of disorder in addition to having pratical implications with respect to transport in electronic systems. As localization of waves in non-periodic media is often taken as a universal phenomenon, systems in which this process is complicated by different delocalization regimes are of interest as a class of models of their own. We focus on a number of specific quasiperiodic models in the next Chapter and establish techniques for determining their localization properties here. In the remainder of this Section, we present a transfer matrix approach for characterizing localization physics in a geometric way, through studying curves on a torus calculated from transfer matrices. In Sec. 9.2 we concretely apply this approach to obtain toroidal curves corresponding to a number of simple systems that exemplify either localization or delocalization of eigenstates. The following Section, Sec. 9.3, focuses on using the same method in a complementary fashion in that we calculate toroidal curves corresponding to a few specific eigenstate functional forms. The aim of these Sections is to develop a "dictionary of curves" that could serve as a reference point for determining localization properties of more complex systems. The next Chapter centers one such system – the celebrated Aubry-Andre-Harper model.

Presently, we introduce our method connecting eigenstate localization properties and geometrically distinct curves on a torus. This rather visually striking method we present below has been developed based on Ref. [132] and through discussion with Drs. Vatsal Dwivedi, Suraj S. Hegde and Prof. Diptiman Sen. It is based on the transfer matrix formalism. We proceed to briefly introduce this formalism.

Following Ref. [132], we note that most generally, for a tight-binding Hamiltonian of an arbitrary one-dimensional model having finite range hopping and finite size, we can write the Hamiltonian as

$$\mathcal{H} = \sum_{n=0}^{N} \sum_{\alpha,\beta=1}^{q} \sum_{\ell=0}^{R} (c^{\dagger}_{n+\ell,\alpha} t_{\ell,\alpha\beta} c_{n,\beta} + \text{h.c.}) \tag{9.1}$$

where R is the range of the hopping, q counts the internal degrees of freedom in the system, for instance spin or sublattice degrees of freedom, per lattice site and N stands for the number of those sites that make up the system. Considering the action of this Hamiltonian on a (fermionic) state occupied by a single particle

$$|\psi\rangle = \sum_{n=0}^{N} \psi_n c^{\dagger}_n |\Omega\rangle \tag{9.2}$$

where $|\Omega\rangle$ is the empty, vacuum state and $\psi_n \in \mathbb{C}^q$ is the wavefunction at each physical site of the chain described by Eq. (9.1), the eigenvalue problem $\mathcal{H}|\psi\rangle = E|\psi\rangle$ where E is the appropriate eigenvalue can be written as a recursive expression

$$\sum_{\ell=0}^{R} (\mathbf{t}_\ell \psi_{n+\ell} + \mathbf{t}^{\dagger}_\ell \psi_{n-\ell}) \tag{9.3}$$

with $\mathbf{t}$ now denoting a hopping matrix. Specializing to the $R = 1$ case i.e. nearest-neighbor (NN) hopping only greatly simplifes this expression which can then be written in matrix form so that

$$\begin{pmatrix} \psi_{n+1} \\ \psi_n \end{pmatrix} = A_n \begin{pmatrix} \psi_n \\ \psi_{n-1} \end{pmatrix} \tag{9.4}$$

where A_n is a matrix that encodes the recursion relation of Eq. (9.3). Below, we will obtain this recursion from Heisenberg equations of motion and specify the exact form of the transfer matrix for each model under consideration. From Eq. (9.4), it is clear that a full wavefunction can be specified by acting on a vector composed of ψ_1 and ψ_2 by a product $A(N) = \prod_{n=1}^{N} A_n$. Importantly, we can calculate the Lyapunov exponent γ of a total transfer matrix as

$$\gamma = \lim_{N\to\infty} \frac{1}{N} \log(|\lambda_{\max}|), \tag{9.5}$$

where $\lambda_{\max}$ is the larger of the two eigenvalues of $A(N)$. This quantity is equal to the inverse of the localization length of the eigenstate described by $A(N)$. Consequently, given some one-dimensional tight-binding Hamiltonian we can determine the localization character of its eigenstates by first obtaining the

relevant transfer matrix through Eq. (9.3) then finding the Lyapunov exponent by using Eq. (9.5).

In this Chapter, we highlight the fact that a transfer matrix having real entries has to be symplectic and use this property to map it onto a point on a torus. An equivalent statement to the real-valued transfer matrix being symplectic is that its determinant is equal to unity. This is a consequence of quantum mechanical probability current having to be conserved. Due to this property a total transfer matrix can always be written in the form

$$A(N) = \prod_{n=1}^{N} A_n = \begin{pmatrix} a+b & c-d \\ c+d & a-b \end{pmatrix} \tag{9.6}$$

where $(a^2+d^2)-(b^2+c^2)=1$. From here, we define

$$\begin{aligned} a^2+d^2 &= \rho^2 = \cosh^2\eta \\ b^2+c^2 &= \sigma^2 = \sinh^2\eta. \end{aligned} \tag{9.7}$$

and introduce two angular coordinates on a torus, θ_1 and θ_2, by writing

$$\begin{aligned} a &= \cosh\eta\cos\theta_2,\ b = \sinh\eta\cos\theta_1 \\ c &= \sinh\eta\sin\theta_1,\ d = \cosh\eta\sin\theta_2. \end{aligned} \tag{9.8}$$

The two angles, θ_1 and θ_2, are illustrated in Fig. 9.1. We can now describe a toroidal curve by these two angles and a radial coordinate χ by calculating

$$\begin{aligned} &\tan\theta_2 = d/a,\ \tan\theta_1 = c/b \\ &\chi = \frac{1}{2}\left(1+\sqrt{\frac{b^2+c^2}{a^2+d^2}}\right). \end{aligned} \tag{9.9}$$

We note that θ_1, θ_2 and χ are all functions of N. Through our mapping Eq. (9.9), each product of some number of k transfer matrices corresponds to a point on the torus described by $(x,y,z) = ((R+\chi\sin\theta_2)\cos\theta_1, (R+\chi\sin\theta_2)\sin\theta_1, \chi\cos\theta_2)$ where R is the outer radius of the torus. In other words, $\prod_{n=1}^{k} A_n$ and $\prod_{n=1}^{k+1} A_n$ will correspond to distinct points on the torus, not necessarily close to each other. Evaluating the product $A(N)$ in a step-by-step fashion and plotting each partial product as a point on the torus for large N can then trace out a (nearly) continuous trajectory.

Generally, we are interested in calculating $A(N)$ for one-dimensional tight-binding models described by

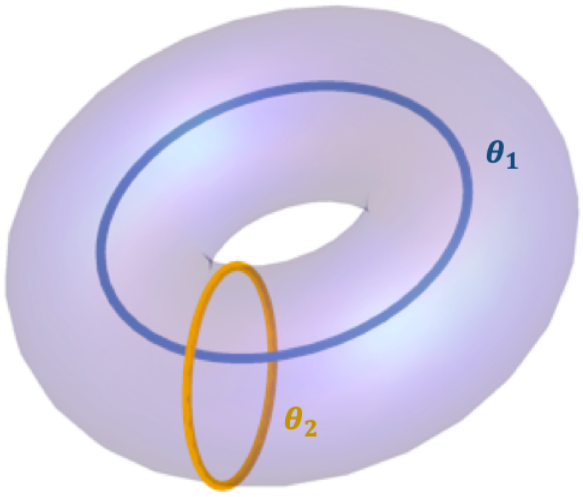

Figure 9.1: Schematic depiction of the two angles on the torus stemming from the parametrization of the total transfer matrix in Eqs. (9.8) and (9.9)

.

Hamiltonians of the form

$$H = -t\sum_n (c_{n+1}^\dagger c_n + \text{h.c.}) + \sum_n \mu_n c_n^\dagger c_n \tag{9.10}$$

where μ_n is a site-dependent term that can encode disorder, quasiperiodicity or a simple periodic lattice. Models captured by Eq. (9.10) are only characterized by nearest-neighbor hopping and more long-ranged Hamiltonians would necessitate a larger transfer matrix with more parameters. More precisely, the size of the transfer matrix for a generic tight-binding model is set as $qR \times qR$ where R denotes the range of hopping and q corresponds to the number of internal degrees of freedom such as spin or sublattice [132].

To derive a transfer matrix corresponding to Eq. (9.10) we first find Heisenberg equations of motion

$$t(c_{n+1} + c_{n-1}) + \mu_n c_n = E c_n. \tag{9.11}$$

The consequent transfer matrix reads

$$A(N) = \prod_{n=1}^{N} \begin{pmatrix} \mu_n & -1 \\ 1 & 0 \end{pmatrix} \tag{9.12}$$

where the hopping amplitude t is used as the energy scale, μ_n has been made dimensionless and we have set

$E = 0$. Trajectories on a torus described by θ_1, θ_2 and χ are hence determined by μ_n. For non-zero energy eigenstates, the Heisenberg equations of motion imply that the correct total transfer matrix reads

$$A(N, E) = \prod_{n=1}^{N} \begin{pmatrix} \mu_n - E & -1 \\ 1 & 0 \end{pmatrix}. \tag{9.13}$$

In the following discussion we clearly indicate the assumptions made about E when calculating the total transfer matrix $A(N, E)$ or $A(N)$. Further, we note that as we are explicitly evaluating a product for N steps – unit cells of the system – this formalism is suited for finitely-sized systems and open boundary conditions.

9.2 Toroidal curves for pre-determined on-site variation: uniform, alternating and single-site

After establishing the equivalence between transfer matrices for one-dimensional tight-binding models of the form Eq. (9.10) and curves on a torus, we can approach calculating the latter in two ways. First, we can fix the form of μ_n and calculate the total transfer matrix Eq. (9.6). Alternatively, we can use the definition of the transfer matrix $\psi_M = A(M)\psi_0$ for systems where the functional form of the eigenstates is known. In this Section, we focus on the former, starting with some simple choices of μ_n for which the product in Eq. (9.12) can be evaluated exactly.

9.2.1 Clean Model

First, we consider the uniform or clean model having $\mu_n = \mu$ for all n. In this simple case, the total transfer matrix product N can be obtained analytically. Carrying out this calculation below, we find the corresponding toroidal curve to be simple and described by one angular coordinate only. As it is known that all eigenstates of this system are extended, this observation serves as a reference point for delocalization regimes of more complex models.

We begin the calculation of $A(N)$ by utilizing the following identity

$$\begin{pmatrix} m_{11} & m_{12} \\ m_{21} & m_{22} \end{pmatrix}^N = \begin{pmatrix} m_{11}U_{N-1}(x) - U_{N-2}(x) & m_{12}U_{N-1}(x) \\ m_{21}U_{N-1}(x) & m_{22}U_{N-1}(x) - U_{N-2}(x) \end{pmatrix} \tag{9.14}$$

where $x = (m_{11} + m_{22})/2$ and $U_j(x)$ are Chebyshev polynomials of the second kind

$$U_j(x) = \frac{\sin((j+1)\cos^{-1}(x))}{\sqrt{1-x^2}}. \tag{9.15}$$

Consequently, for constant on-site variation μ the full transfer matrix is equal to

$$A(N) = \begin{pmatrix} \mu U_{N-1}(x) - U_{N-2}(x) & -U_{N-1}(x) \\ U_{N-1}(x) & -U_{N-2}(x) \end{pmatrix} \tag{9.16}$$

where $x = \mu/2 = \cos\theta$.

It is useful to note here that we can calculate the Lyapunov exponent γ from Eq. (9.16)

$$\gamma = \lim_{N\to\infty} \frac{1}{N} \log(|\lambda_{\max}|), \tag{9.17}$$

where $\lambda_{\max}$ is the larger of the two eigenvalues of $A(N)$. More precisely,

$$\lambda_{\max} = a + \sqrt{a^2 - 1} \tag{9.18}$$

and since

$$a = (\mu/2)U_{N-1}(x) - U_{N-2}(x) = \frac{\cos\theta\sin(N\theta) - \sin((N-1)\theta)}{\sin\theta} = \cos(N\theta) \tag{9.19}$$

it is clear that $|\lambda_{\max}| = 1$. In other words, the Lyapunov exponent γ vanishes. Since the Lyapunov exponent is the inverse of the eigenstates localization length $\gamma = 1/\xi$ and eigenstates of this, clean, model should be plane waves, this conclusion is fully expected.

Turning to the calculation of θ_1, θ_2 and χ, we first note that

$$\tan\theta_1 = c/b = 0 \Rightarrow \theta_1 = 0, \pi \tag{9.20}$$

i.e. the winding of the trajectory in the θ_2 direction does not depend on N – it is "stuck" at these two special points on the torus. Next, we find

$$\tan\theta_2 = \frac{U_{N-1}(\cos\theta)}{\cos\theta U_{N-1}(\cos\theta) - U_{N-2}(\cos\theta)} = \csc\theta\tan N\theta. \tag{9.21}$$

Recalling the identity

$$\tan(N\theta) = \frac{1}{i}\frac{(1+i\tan\theta)^N - (1-i\tan\theta)^N}{(1+i\tan\theta)^N + (1-i\tan\theta)^N} \tag{9.22}$$

and calculating, from the definition of $\cos\theta$,

$$\csc\theta = \frac{2}{\sqrt{4-\mu^2}},\ \tan\theta = \frac{\sqrt{4-\mu^2}}{\mu} \tag{9.23}$$

we can express θ_1 as a function of μ and N only

$$\theta_2(N,\mu) = \arctan\left(\frac{2i}{\sqrt{4-\mu^2}}\frac{(\mu - i\sqrt{4-\mu^2})^N - (\mu + i\sqrt{4-\mu^2})^N}{(\mu - i\sqrt{4-\mu^2})^N + (\mu + i\sqrt{4-\mu^2})^N}\right). \tag{9.24}$$

Further, we find

$$\chi(N,\mu) = \frac{1}{2}\left(1 + \frac{b(N,\mu)}{\sqrt{1+b(N,\mu)^2}}\right) \tag{9.25}$$

where

$$b(N,\mu) = \frac{i}{2^N\sqrt{4-\mu^2}}\left((\mu - i\sqrt{4-\mu^2})^N - (\mu + i\sqrt{4-\mu^2})^N\right). \tag{9.26}$$

Trajectories determined by Eqs. (9.24), (9.20) and (9.26) are shown in Fig. 9.2.

9.2.2 Alternating Model

As a natural generalization of the $\mu_n = \mu$ model we proceed to consider $\mu_{2k-1} = \mu_1$ and $\mu_{2k} = \mu_2$. For simplicty, we assume that N is even so that

$$A(N) = \begin{pmatrix} \mu_1\mu_2 - 1 & -\mu_1 \\ \mu_2 & -1 \end{pmatrix}^{N/2} \tag{9.27}$$

which can again be evaluated by using Chebyshev polynomials

$$A(N) = \begin{pmatrix} (\mu_1\mu_2 - 1)U_{N/2-1}(y) - U_{N/2-2}(y) & -\mu_1 U_{N/2-1}(y) \\ \mu_2 U_{N/2-1}(y) & -U_{N/2-1}(y) - U_{N/2-2}(y) \end{pmatrix} \tag{9.28}$$

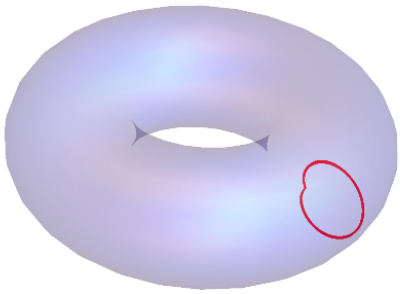

(a)

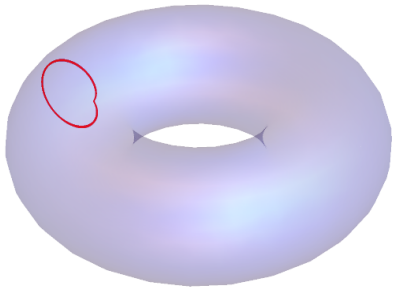

(b)

Figure 9.2: Plot of the trajectory determined by $(x, y, z) = ((R+\chi\sin\theta_2)\cos\theta_1, (R+\chi\sin\theta_2)\sin\theta_1, \chi\cos\theta_2)$ for $\mu_n = 1.5$, $N = 1000$ and **(a)** $\theta_2 = 0$, **(b)** $\theta_2 = \pi$.

where we define $y = (\mu_1\mu_2 - 2)/2 = \cos\phi$. It then follows that

$$\theta_1 = \arctan\frac{\mu_2 - \mu_1}{\mu_1\mu_2} \tag{9.29}$$

so that θ_1 only depends on the chosen values of μ_n and does not change with N. Consequently, the trajectories on the torus will not wind around the hollow portion of the torus in the same way that those shown in Fig. 9.2 do not. Following algebraic manipulations similar to those in the previous Section we evaluate θ_2 as a function of N, μ_1 and μ_2

$$\theta_2(N,\mu_1,\mu_2) = \arctan\Bigg(\Big((\mu_1+\mu_2)/2((\sqrt{\mu_1\mu_2} - i\sqrt{4-\mu_1\mu_2})^N - (\sqrt{\mu_1\mu_2} + i\sqrt{4-\mu_1\mu_2})^N)\Big) \times$$
$$\Big((\mu_1\mu_2-2)/2((\sqrt{\mu_1\mu_2} - i\sqrt{4-\mu_1\mu_2})^N - (\sqrt{\mu_1\mu_2} + i\sqrt{4-\mu_1\mu_2})^N) - (\sqrt{\mu_1\mu_2} - i\sqrt{4-\mu_1\mu_2})^{N-1}$$
$$+(\sqrt{\mu_1\mu_2} + i\sqrt{4-\mu_1\mu_2})^{N-1}\Big)^{-1}\Bigg). \tag{9.30}$$

Similarly, the radial coordinate reads

$$\chi(N,\mu_1,\mu_2) = \frac{1}{2}\left(1 + \sqrt{\frac{b(N,\mu_1,\mu_2)^2 + c(N,\mu_1,\mu_2)^2}{1 + b(N,\mu_1,\mu_2)^2 + c(N,\mu_1,\mu_2)^2}}\right) \tag{9.31}$$

where

$$b(N,\mu_1,\mu_2)^2 + c(N,\mu_1,\mu_2)^2 = \frac{\mu_1^2\mu_2^2 + (\mu_2 - \mu_1^2)}{\mu_1\mu_2(4-\mu_1\mu_2)}\sin^2(N\phi/2) \tag{9.32}$$

and

$$\sin(N\phi/2) = \frac{i}{2^{N+1}}\left((\sqrt{\mu_1\mu_2} - i\sqrt{4-\mu_1\mu_2})^N - (\sqrt{\mu_1\mu_2} + i\sqrt{4-\mu_1\mu_2})^N\right). \tag{9.33}$$

The trajectory on the torus corresponding to Eqs. (9.29), (9.30) and (9.31) is shown in Fig. 9.3. We note that the trajectories determined by the transfer matrix for constant and alternating values of μ_n look rather similar due to the fact that both correspond to systems with fully extended (rather than localized) eigenstates. As expected, in the latter case

$$a = \frac{\cos\phi\sin(N\phi/2) - \sin((N-1)\phi/2)}{\sin\phi} \tag{9.34}$$

and the Lyapunov exponent again vanishes.

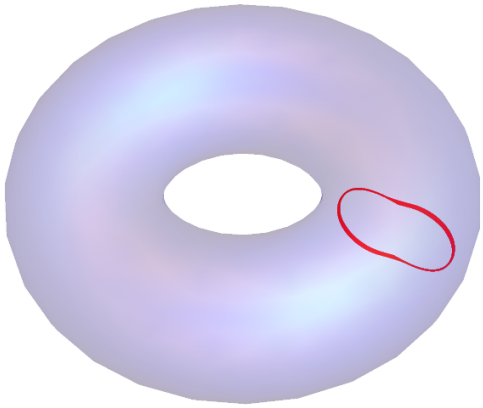

Figure 9.3: Plot of the trajectory determined by $(x, y, z) = ((R+\chi\sin\theta_2)\cos\theta_1, (R+\chi\sin\theta_2)\sin\theta_1, \chi\cos\theta_2)$ for $\mu_{2k-1} = 0.8$, $\mu_{2k} = 1.6$ and $N = 1000$.

Before considering a very different potentia landscape having an extremum at only one isolated site, we comment on more general periodic systems. We expect any model having a finite number of regularly repeating μ_i for $i = 1, 2, ..., N_\mu$ and $N_\mu < N$ to have eigenstate corresponding to curves qualitatively similar to those we have calculated in Fig. (9.3). To be more precise, for any system where Eq. (9.14) can be used to carry out the transfer matrix product some appropriate N_p number of times, we find

$$\begin{aligned} \tan\theta_1 &= \frac{m_{11}+m_{21}}{m_{11}-m_{22}} \\ \tan\theta_2 &= \frac{(m_{21}-m_{12})U_{N_p-1}(x)}{(m_{11}+m_{22})U_{N_p-1}(x) - 2U_{N_p-2}(x)} \end{aligned} \tag{9.35}$$

where m_{ij} are a function of μ_i only. Consequently, when N is divisible by N_μ (so that $N_p = N/N_\mu$) the angle θ_1 on the torus is equal to a discrete number of values and the toroidal curve obtained from $A(N)$ only winds in the θ_2 direction (note that θ_2 does depend on N). This is exactly the character of toroidal curves we have found for the clean model where $\mu_i = \mu$ for all i and the alternating model where $\mu_i = \mu_1, \mu_2$.

9.2.3 Single Site Impurity

In contrast to the previous two examples, we now consider a near-uniform system with an "impurity" located at a single site. More precisely, we take $\mu_n = \mu$ for all $n \neq M$ and $\mu_M \neq \mu$. In this case, the entries of the

full transfer matrix $A(N)$ can be evaluted as

$$\begin{aligned}
a+b = A_{11} &= (\mu_M U_{N-M}(x) - U_{N-M-1}(x))U_{M-1}(x) - U_{M-2}(x)U_{N-M}(x) \\
c-d = A_{12} &= U_{M-1}(x)(U_{N-M-2}(x) - \mu_M U_{N-M-1}(x)) + U_{M-2}(x)U_{N-M-1}(x) \\
c+d = A_{21} &= U_{M-2}(x)(\mu_M U_{N-M}(x) - U_{N-M_1}(x)) - U_{M-3}(x)U_{N-M}(x) \\
a-b = A_{22} &= U_{M-2}(x)(U_{N-M-2}(x) - \mu_M U_{N-M-1}(x)) + U_{M-3}(x)U_{N-M-1}(x)
\end{aligned} \tag{9.36}$$

where, as above, $x = \mu/2 = \cos\theta$.

Using similar arguments as before, we plot this trajectory in Fig. 9.4 for a state with a non-zero eigenenergy obtained through direct diagonalization of the Hamiltonian (Eq. 9.10). Unlike trajectories for models having all extended eigenstates, the trajectory in this case consists of a number of discrete points rather than a connected curve winding around any part of the torus

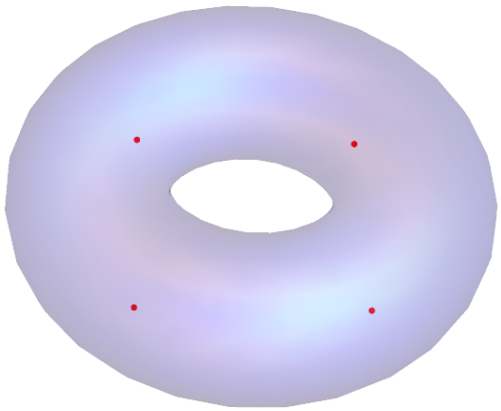

Figure 9.4: Plot of the trajectory determined by $(x, y, z) = ((R+\chi\sin\theta_2)\cos\theta_1, (R+\chi\sin\theta_2)\sin\theta_1, \chi\cos\theta_2)$ for $\mu = E = -10.198$, $\mu_M = -10.198 + 10$, $N = 800$ and $M = 400$.

To better understand this trajectory, we offer the following heuristic argument. Assuming that the wavefunction for a system with one strong impurity is esentially localized over only a few sites, for instance

from some $M < N$ to $M + k$ for $k << N$, and zero everywhere else, we can approximate

$$\begin{pmatrix} \psi_1 \\ \psi_0 \end{pmatrix} \approx \begin{pmatrix} \psi_{M-1} \\ \psi_{M-2} \end{pmatrix} \tag{9.37}$$

and

$$\begin{pmatrix} \psi_{M+k+2} \\ \psi_{M+k+1} \end{pmatrix} \approx \begin{pmatrix} \psi_{N+1} \\ \psi_N \end{pmatrix}. \tag{9.38}$$

By the definition of the transfer matrix then $\prod_{n=1}^{M+k-2} A_n \approx \mathbb{I}$ and $\prod_{n=M+k+1}^{N} A_n \approx \mathbb{I}$. Consequently

$$\prod_{n=1}^{N} A_n \approx \prod_{n=M-1}^{M+k} A_n \tag{9.39}$$

and the entries a, b, c and d of Eq. (9.6) depend on k rather than on N. In the most extreme case, when $k = 2$, the full transfer matrix $A(N)$ consist of a single matrix and all of its entries are constant. In other words, for a wavefunction localized in a way that resembles a Dirac $\delta-$function the coordinates on the torus determined by Eq. (9.9) are all constants. Thus, the corresponding trajectory is not a connected curve and consists of a set of distinct points instead. This is consistent with the claculation illustrated in Fig. 9.4. However, we stress that this argument is less appropriate for less peaked (narrow) localized wavefunctions.

9.3 Toroidal curves for a pre-determined wavefunction form

Having examined a number of cases in which the on-site modulation μ_n is known and drives the physics of the model in question, we move on to discuss a complementary use of the transfer matrix. Here, we start with a known functional form of the system's eigenstates. By definition, the entries of the total transfer matrix after some number of sites M should reflect the spatial properties of the eigenstate of relevant energy as $\psi_M = A(M)\psi_0$. Turning to the toroidal curve formalism at the center of this Chapter, we use this property to work towards a "dictionary of curves" that could lead to better understanding the systems for which toroidal curves have been calculated from a Hamiltonian only. Since the transfer matrix has been shown to be a powerful tool for studying localization-delocalization physics through Lyapunov exponent calculations, in what follows we primarily consider different localized wavefunctions and the toroidal curves that correspond to them.

9.3.1 Exponentially localized wavefunction with a sinusoidal envelope

First, we consider an eigenstate having the spatial form $\psi_n = e^{-n/\xi}\sin(n)$. This wavefunction is localized but has a sinusoidal envelope. To calculate all of the entries of a transfer matrix A_n such that

$$\begin{pmatrix} \psi_{n+1} \\ \psi_n \end{pmatrix} = A_n \begin{pmatrix} \psi_n \\ \psi_{n-1} \end{pmatrix} \tag{9.40}$$

we use the following identities:

$$\begin{aligned} &\psi_{n+1} = e^{-(n+1)/\xi}\sin(n+1) = e^{-(n+1)/\xi}(\sin(n)\cos(1) + \cos(n)\sin(1)) \\ &= e^{-n/\xi}\sin(n)e^{-1/\xi}\cos(1) + \frac{1}{2}\exp -(n+1)/\xi(\sin(n+1) - \sin(n-1)) \\ &= \psi_n e^{-1/\xi}\cos(1) + \frac{1}{2}\psi_{n+1} - \frac{1}{2}e^{-2/\xi}\psi_{n-1} \end{aligned} \tag{9.41}$$

Now, from Eq. 9.40 it is clear that

$$\psi_{n+1} = A^n_{11}\psi_n + A^n_{12}\psi_{n-1}. \tag{9.42}$$

so that comparing this expression to Eq. (9.41) implies that

$$\begin{aligned} A^n_{11} &= 2e^{-1/\xi}\cos(1) \\ A^n_{12} &= -e^{-2/\xi}. \end{aligned} \tag{9.43}$$

The remainder of the entries of A_n can be calculated from

$$\begin{aligned} \psi_n &= A^n_{21}\psi_n + A^n_{22}\psi_{n-1} \\ \det(A_n) &= A^n_{11}A^n_{22} - A^n_{21}A^n_{12} = 1 \end{aligned} \tag{9.44}$$

where the first expression again stems from Eq. (9.40). Consequently, we find

$$A_n = \begin{pmatrix} 2e^{-1/\xi}\cos(1) & -e^{-2/\xi} \\ 1 - (e^{2/\xi} - 1)\frac{\sin(n-1)}{\sin(n+1)} & 2\sinh(1/\xi)\frac{\sin(n)}{\sin(n+1)} \end{pmatrix}. \tag{9.45}$$

The plot of the toroidal curves corresponding to the product of some number N of matrices of this form i.e. the total transfer matrix for a system having N sites is shown in Fig. 9.5. We note that this trajectory

is a closed, connected curve and winds around the hollow region of the torus. It qualitatively differs from the closed toroidal curves corresponding to the clean system (Sec. 9.2.1) or models with on-site modulation commensurate with the underlying one-dimensional lattice (Sec. 9.2.2). To be precise, represetations of extended wavefunctions that characterize those cases differ from the representation of the more localized eigenstates considered here in that they wind in θ_1 rather than θ_2. We note that this trend persists even as the localization length ξ is increased. The dominant effect of this increase, and the eigenstate becoming more similar to an extended state, is the "shedding" of points away from the curve, making it less tight and more similar to a set of diffuse points covering some larger area of the underlying torus.

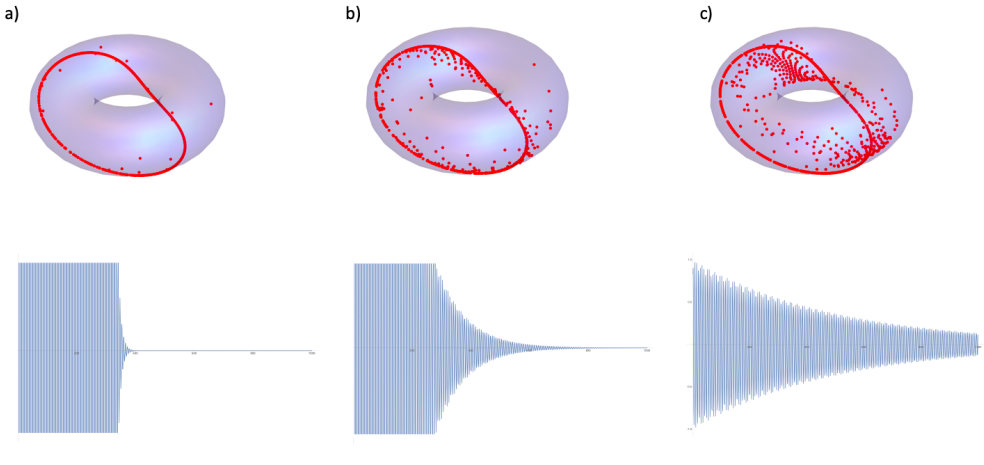

Figure 9.5: Plot of the torus trajectories determined by the total transfer matrix Eq. (9.45) with $N = 1000$ and **(a)** $\xi = 10$, **(b)** $\xi = 100$, **(c)** $\xi = 500$ in the top row while the bottom row shows the corresponding eigenstate wavefunction forms.

9.3.2 Power-law localized wavefunction

Similarly to the discussion above, we can investigate the transfer matrices and their representations as curves on a torus for wavefunctions with power-law spatial dependence: $\psi_n = n^\alpha$ for $\alpha < 0$. For a generic transfer matrix A_n with entries A^n_{ij}, they should be related as

$$\begin{aligned} A^n_{11} &= \frac{(n+1)^\alpha + (n-1)^\alpha}{n^\alpha} - \left(\frac{n^2-1}{n^2}\right)^\alpha A^n_{22} \\ A^n_{12} &= \left(\frac{n+1}{n}\right)^\alpha - 1 \\ A^n_{21} &= 1 - \left(\frac{n-1}{n}\right)^\alpha A^n_{22}. \end{aligned} \tag{9.46}$$

Here, the second diagonal entry is not fixed by the definition of the transfer matrix nor the constraint on its determinant. The same is true when we consider the total transfer matrix $\prod_n T_n$ for a finite-sized model:

$$\begin{pmatrix} \psi_{N+1} \\ \psi_N \end{pmatrix} = \begin{pmatrix} 0 \\ N^\alpha \end{pmatrix} = \begin{pmatrix} a+b & c-d \\ c+d & a-b \end{pmatrix} \begin{pmatrix} \psi_1 \\ \psi_0 \end{pmatrix} = \begin{pmatrix} a+b & c-d \\ c+d & a-b \end{pmatrix} \begin{pmatrix} 1 \\ 0 \end{pmatrix}, \tag{9.47}$$

where $\psi_0 = 0$ and $\psi_{N+1} = 0$ mark the edges of the system. Requiring the determinant to be equal to one implies

$$\begin{aligned} a &= -b \\ d &= \frac{N^{2\alpha} - 1}{2N^\alpha} \\ c &= N^\alpha + \frac{1 - N^{2\alpha}}{2N^\alpha}. \end{aligned} \tag{9.48}$$

While we cannot solve for $a = -b$ as a function of N and α, recalling Eq. (9.9) allows us to write

$$\frac{\tan\theta_1}{\tan\theta_2} = \frac{1 - N^{2\alpha}}{1 + N^{2\alpha}} \tag{9.49}$$

so that for $N >> 1$ it is true that $\tan\theta_1 \approx \tan\theta_2$. Consequently, the toroidal curve corresponding to a very large system having power-law localized eigenstates ought to be similar to a curve defined by $\theta_1 = \theta_2 + k\pi$ for $k \in \mathbb{Z}$. Such a curve is plotted in Fig. 9.6. As this curve is connected and winds around the central hollow region of the torus in a manner not dissimilar from the curve corresponding to localized eigenstates having a sinusoidal envelope (Fig. 9.5), we conclude that the appearance of such curves likely indicates eigenstate localization more generally.

These observations are germane to the study of toroidal curves corresponding to transfer matrices for systems with quasiperiodic modulation μ_n which are the focus of the following Chapter. At the same time, we emphasize that this work is preliminary and ongoing. It is our hope that future projects involving the toroidal curve and transfer matrix methods of this Chapter will add a level of mathematical rigor and make contact with the broader literature concerning symplectic matrices.

At this time, we proceed to apply the methods that we have discussed so far to two one-dimensional tight-binding models — the AAH model and its generalization proposed in Ref. [3] or the GPD model — having quasiperiodic parameters. Such systems are known to have unusual localization properties and have been studied in mathematics and physics literature for over four decades. After reviewing some of these

historical results, we center the next Chapter on analyzing localization physics of the AAH and GPD models by studying toroidal curves stemming from transfer matrices describing these systems. We underscore not only the applicability of our technique but also its ability to capture mobility edge physics i.e. energey eigenvalue dependent state (de)localization.

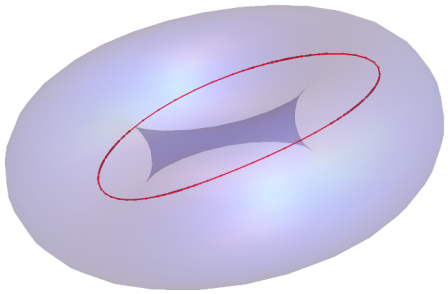

Figure 9.6: Plot of the trajectory determined by $\theta_1 = \theta_2 + k\pi$ for $k = 0$.

Chapter 10

Toroidal Curves and the Aubry-Andre-Harper Model

10.1 Introduction

While periodic structures and crystals are at the core of much of condensed matter and solid state physics, quasiperiodicity and quasicrystals have historically fascinated physicists and mathematicians alike by having much more exotic properties. As Douglas R. Hofstadter noted in his seminal 1976 paper [133], the difference between rational and irrational numbers is rarely physically meaningful and one does not expect it to be – an arbitrarily small change in some irrational parameter makes it rational so a physical effect stemming from the irrationality of this parameter would be everywhere discontinuous. A quasicrystal defined by a periodic modulation having an irrational period should by this reasoning be similar to its rational period counterparts. However, the work of Serge Aubry and Gilles Andre [134] and Phillip G. Harper has shown this to not be the case, contrasting studies of one-dimensional quasiperiodic systems to Anderson's studies of disorder [2] and even making contact with Hofstadter's own work. In this Chapter, we focus on the so-called Aubry-Andre-Harper (AAH) model which in many ways exemplifies the properties of a larger class of one-dimensional quasiperiodic systems (with some exceptions concerning the Fibonacci chain). It has been extensively studied by numerical methods, in the realm of rigorous mathematics and, more recently, through experiments in ultracold atomic, photonic and meta-materials settings.

We write the AAH Hamiltonian as

$$H_{\mathrm{AA}} = -t\sum_j (c_{j+1}^\dagger c_j + \mathrm{h.c.}) + V\sum_j \cos(2j\pi\alpha + \phi)c_j^\dagger c_j \tag{10.1}$$

where α is irrational. Typically, we also set $\phi = 0$. This phase degree of freedom is often utilized in experiments and will be further remarked upon in the following Chapter. The Hamiltonian of Eq. (10.1) is a one-dimensional thight-binding model having an incommensurate on-site modulation. It is self-dual when

$V = 2t$ under the duality transform given by

$$b_n = \sum_j e^{i(2n\pi\alpha+\varphi)j+ij\phi} c_j. \tag{10.2}$$

More explicitly, the dual Heisenberg equations of motion corresponding to H_{AA} are

$$\begin{aligned} t(c_{j+1} + c_{j-1}) + V\cos(2j\pi\alpha + \phi)c_j &= Ec_j \\ \frac{V}{2}(b_{n+1} + b_{n-1}) + 2t\cos(2n\pi\alpha + \varphi)b_n &= Eb_n. \end{aligned} \tag{10.3}$$

At the self-dual point, $V = 2t$, these expression reproduce Harper's equation thus connecting the AAH model to the Hofstadter problem of electrons in a magnetic field in two dimensions. In that setting, α is the ratio of a flux through a lattice cell to one flux quantum and ϕ is a property of plane waves in the direction in which the system is assumed to be translationally invariant. More rigorously, in analyzing the problem of electrons in a magetic field in two dimensions, Harper equation is typically derived after chosing a gauge such that translation operators in only one direction are multiplied by phases that depend on the magnetic field while the other direction remains translation invariant. In Hofstadter's seminal paper Ref. [133] this is achieved by chosing the Landau gauge. Noting the appearance of the Harper equation in this treatment of the two-dimensional electron problem and in Eq. (10.3), we conclude that for irrational α, at the critical point, the energy spectrum of the AAH model is the Hofstadter butterfly. Hence, the model shows multifractality properties at this point and its wavefunctions or, to be more precise, its critical wavefunctions form an uncountable measure-zero set homeomorphic to the Cantor set. In the following discussion, we will often use the term "critical" to denote precisely this type of wavefunction that exhibits multifractality.

Further, the self-dual point idenitifed by Eqs. (10.3) is significant with respect to localization-delocalization properties of the AAH model. It has been commonly accepted in physics literature that for $V < 2t$ all eigenstates of the model are extended while for $V > 2t$ they are all localized. Put more simply, the AAH model undergoes a localization-delocalization transition as the strength of quasiperiodicity is increased. We stress here that this is rather unexpected as the AAH model bears resemblance to disordered models in one-dimension. Famously, Anderson localization theory predicts that a localization-delocalization transition cannot happen in one-dimension but rather that any amount of uncorrelated disorder localizes all eigenstates of the system [2]. In the AAH model, in contrast, small quasiperiodicty strengths do not prohibit extended states. This makes the AAH model of great interest and highlights the difference between quasiperiodicity, which is an inherently deterministic type of near-disorder, and simply random variation that leads to truly disordered systems.

Commonly, the localization-delocalization transition at the critical point is studied with the formula developed by D. J. Thouless that relates the Lyapunov exponent (inverse localization length) $\gamma(E)$to the density of states of the system

$$\gamma(E) = \int dE' \ln |(E - E')/t| \rho(E') \tag{10.4}$$

where $\rho(E')$ is the density of states.

To motivate this formula, we note that for a Schrodinger equation on a regular 1D lattice written in discrete form as

$$\psi_{n+1} + V_n \psi_n = E\psi_n \tag{10.5}$$

having a set of eigenvalues E_α and the NNN hopping parameter set to be the unit of energy and boundary conditions $\psi_0 = \psi_{N+1} = 0$ i.e. a finitely-sized chain, the solution of the intial value problem with $\psi_0(E) = 0$ and $\psi_1(E) = 1$ is characterized by

$$\psi_{N+1}(E) = \prod_{\alpha=1}^{N} (E_\alpha - E). \tag{10.6}$$

Defining the density of states as

$$\rho(\epsilon) = \lim_{N\to\infty} \frac{1}{N} \sum_{\alpha=1} N\delta(E - E_\alpha) \tag{10.7}$$

and assuming that $\psi_{N+1} \propto e^{-i/\xi}$ forξ a localization length so that the Lyapunov exponent reads

$$\gamma(E) = \lim_{N\to\infty} \frac{\ln |\psi_{N+1}(E)|}{N} \tag{10.8}$$

which leads to Eq. (10.4). In his 1972 paper, Ref. [135], Thouless offers an alternative way of arriving at the same conclusion by noting that for G_{ij} the Green function (resolvent) the entry G_{1N} has poles and residues corresponding to ψ_1 and ψ_N and by a cofactor matrix method

$$G_{1N}(E) = \prod_{i=1}^{N-1} t / \prod_{\alpha=1}^{N} (E - E_\alpha). \tag{10.9}$$

Following Thouless' work, this formula has been proven more rigorously in the work of J. Avron and B. Simon [136] and has been used extensively in studies of transport and eigenstate properties in disoredered

and quasiperiodic systems [137].

In the dual model the equivalent of the Thouless formula Eq. (10.4) reads

$$\gamma_{\text{dual}}(E) = \int dE' \ln|2(E-E')/V|\rho(E') \tag{10.10}$$

where the density of states is the same in either representation. From Eqs. (10.4) and (10.10) it follows that

$$\gamma_{\text{dual}}(E) = \gamma(E) + \int dE' \ln|2t/V|\rho(E') \tag{10.11}$$

and the two Lyapunov exponents are equal at the critical point $2t = V$. Further, if the eigenstates of Eq. (10.1) are extended then $\gamma(E) = 0$ and by the duality Eq. (10.2) the eigenstates of the dual have to be localized. Consequently, $\gamma_{\text{dual}}(E) > 0$ and Eq. (10.11) implies that $2t > V$. In the opposite case, when the eigenstates of the dual are extended, the wavefunctions corresponding to Eq. (10.1) are exponentially localized and $\gamma(E) > 0$ so that we conclude that $V > 2t$. This discussion replicates the assertion about different $V/2t$ regimes made above. We note that the Thouless formula used here shows the localization-delocalization physics of the AAH model to be closely related to its self-duality. While this Chapter includes insights on models having self-dualities, in Chapter 11 we focus solely on a larger family of self-dual models where the self-duality plays a similar role with regards to accessing the localization-delocalization transition.

For the reasons outlined above, studies of the AAH model, its generalizations and similarly quasiperiodic one-dimensional systems, for instance the Fibonacci chain, have attracted the attention of both physicists and mathematicians. Before applying our transfer matrix approach to studying localization-delocalization physics in the AAH model, in the remainder of this Chapter, we briefly summarize some of the existing mathematical literature and previously established mathematical and experimental results.

10.1.1 Summary of mathematical results

The interest in the AAH model and the Harper equation in the physics community has historically found an equally rich counterpart in studies of the almost Mathieu operator in mathematics. As an example, "analysis of the almost Mathieu equation" and "Point spectrum in a continuous almost periodic model" were included on Barry Simon's list of problems in mathematical physics [138]. Similarly, in 2014 Artur Avila was honored with a Fields Medal in part for his work proving, together with Svetlana Jitomirskaya, that the spectrum of the almost Mathieu operator is homeomorphic to the Cantor set [139]. Here, we enumerate some of the most recent and most complete results concerning the spectrum of the almost Mathieu operator (energy spectrum of the AAH model). Much of this work leads to refinements to the simple localization-delocalization transition

picture inferred from the Thouless formula Eq. (10.4) presented above. These mathematical studies thus advance physicists' understanding of systems such as the AAH model.

Formally, the almost Mathieu operator is given by

$$(H_{\lambda,\alpha,\theta}u)_n = u_{n+1} + u_{n-1} + 2\lambda\cos 2\pi(n\alpha+\theta)u_n \tag{10.12}$$

which is equivalent to the Heisenberg equations of motion in Eq. (10.3) with $2\lambda = V/t$. In other words, the critical, localization-delocalization transition point $V = 2t$ is equivalent to $\lambda = 1$ in this definition. Here, $\theta, \lambda \in \mathbb{R}$ and $\alpha \in \mathbb{R}/\mathbb{Q}$. The original work of Aubry and Andre in 1980 [134] conjectured the following concerning the spectral measure of $H_{\lambda,\alpha,\theta}$

1. If $\lambda < 1$, then $H_{\lambda,\alpha,\theta}$ has purely absolutely continuous spectrum for all $\alpha \in \mathbb{R}/\mathbb{Q}$, and all $\theta \in \mathbb{R}$.

2. If $\lambda > 1$, then $H_{\lambda,\alpha,\theta}$ has pure point spectrum for all $\alpha \in \mathbb{R}/\mathbb{Q}$, and all $\theta \in \mathbb{R}$.

At this point, it is worth commenting on characterization of spectra in mathematical language as compared to discussions of extended or localized eigenstates (wavefunctions) in physics literature. The spectra under discussion here refer to solutions of $H_{\lambda,\alpha,\theta}u_n = E_n u_n$ and we will denote the spectru of the operator $H_{\lambda,\alpha,\theta}$ as $\sigma(H_{\lambda,\alpha,\theta})$. First, absolutely continuous spectra correspond to extended eigenstates. Here, a distributional derivative of a state is a measure that is arbitrarily small on sets having an arbitrarily small Lebesgue measure. Second, a pure point spectrum is supported on a countable set of points meaning that it is analogous to all wavefunctions of the model being localized. Finally, a singular continuous spectrum is supported on a set of Lebesgue measure zero but gives no weight to individual points. Such a spectrum has been explicitly shown to exist for some choices of λ (V and t) for the almost Mathieu operator (AAH model) An example of a singular continuous spectrum is the Cantor set which is a fractal. Using the Cantor set to illustrate singular continuous spectrum properties, we note that it is prototypical in that it is self-similar: "zooming in" and "out" inside the Cantor set shows a seemingly identical set. Heuristically, it is equal to two copies of itself which have been made three times smaller and translated. Moreover, it is uncountable but has Lebsegue measure zero i.e. it seems to occupy zero length despite being made up of uncountably many points. When a system has a singular continuous spectrum, such as the Cantor set, its wavefunctions are often referred to as critical (between being extended and localized) in physics literature.

Work following the studies of Aubry and Andre showed that considering arithmetic properties of α refines these conclusions. The work of Svetlana Jitomirskaya provided one such refinement in 1995 [140] when she conjectured the following

1. If $1 < \lambda < e^{\beta}$, the spectrum is purely singular continuous for all θ.

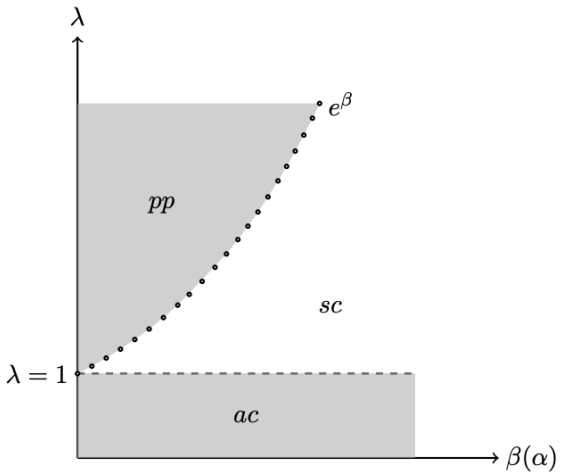

Figure 10.1: Phase transition diagram ilustrating Theorem 1.1. of Ref. [4]. Here *ac* marks the regime having an absolutely continuous spectrum i.e. fully extended eigenstates, *sc* stands for the singularly continuous regime where wavefunctions are multifractal while the region denoted with *pp* corresponds to the purely point specturm with exponentially decaying egeinfunctions.

2. If $\lambda > e^\beta$, the spectrum is pure point with exponential decaying eigenfunctions for almost every θ.

Here the parameter β is defined with respect to the nth convergent of α, denoted as p_n/q_n

$$\beta(\alpha) := \limsup_{n\to\infty} \frac{\ln q_{n+1}}{q_n}. \tag{10.13}$$

In other words, Jitomirskaya conjectured that there is a transition point between a continuous spectrum and a pure point spectrum at $\lambda = e^\beta$ in addition to the $\lambda = 1$ transition point separating the purely absolutely continuous and purely singular continuous spectra. This conjecture was proven by Avila, You and Zhou in Ref. [4]. The full characterization of the spectrum of the almost Mathieu operator is then summarized by Theorem 1.1 in their work as:

Theorem 1. Let $\alpha \in \mathbb{R}/\mathbb{Q}$ with $0 < \beta(\alpha) < \infty$, then we have the following:

1. If $|\lambda| < 1$, then $H_{\lambda,\alpha,\theta}$ has purely absolutely continuous spectrum for all θ
2. If $1 \leq |\lambda| < e^\beta$, then $H_{\lambda,\alpha,\theta}$ has purely singular continuous spectrum for all θ.
3. If $|\lambda| > e^\beta$, then $H_{\lambda,\alpha,\theta}$ has purely point spectrum with exponentially decaying eigenfunctions for almost every θ

In Fig. 10.1 we reproduce the phase transition diagram from Ref. [4] visualizing these conclusions.

Further, more specific statements about the Hausdorff dimension of the spectrum of the almost Mathieu operator, $\dim_H(\sigma(H_{\lambda,\alpha,\theta}))$, have been made by Jitomirskaya and Krasovsky [141], making a conjecture about

the $\lambda = 1$, equivalent to the Hofstadter butterfly, made by Thouless in the early 1980s rigorous. Thouless' claim was that this dimension was equal to 1/2 while Ref. [141] offers proof that for any irrational α and real θ the Hausdorff dimension is less than or equal to 1/2. The Hausdorff dimension agrees with the usual sense of dimensions for smooth shapes or objects with a small number of corners such as lines or regular n-gons. At the same time, self-similar objects and fractals are known to have non-integer Hausdorff dimensions. We highlight that the proof in Ref. [141] consequently fully establishes the fractal and self-similar nature of the energy spectrum of the AAH model at its critical point. While Hofstadter [133] observed a self-similar structure through his numerical work with the butterfly plot, this work established it with high amount of rigor. Jitomirskaya and Liu [142] have also been able to determine exact exponential asymptotics of eigenfuncions and corresponding transfer matrices of the almost Mathieu operators for all α in the localized regime, showing that they are goverened by the continued fraction expansion of this irrational parameter. The work of Jitomirskaya and collaborators on the hierarchical structure of quasiperiodic wavefunctions and spectral transitions is ongoing [143, 144] and the mathematics of the almost Mathieu operator, including many implications for Hofstadter, Quantum Hall and AAH physics, continues to be a rich and growing field.

Of particular interest to some of our work presented below are studies of generalized (having more than one quasiperiodic on-site term) and extended (having beyond nearest-neighbor hoppings) carried out by some of these authors. In Ref. [145] Jitomirskaya and Liu obtain a lower bound for the Lyapunov exponent for a family of discrete Schrodinger operators

$$(Hu)_n = u_{n+1} + u_{n-1} + 2a_1 \cos 2\pi(\theta + n\alpha)u_n + 2a_2 \cos 4\pi(\theta + n\alpha)u_n \tag{10.14}$$

and similar work has been carried out by Marx, Shou and Wellens [146]. These results are of note as the Lyapunov exponent is the inverse of the localization length for the eigenstates of the system and therefore captures localization physics of the model, as depending on quasiperiodicity strengths a_1 and a_2. The extended Harper's model, expressed as

$$(H_{\lambda,\alpha,\theta}u)_n = c_\lambda(\theta + n\alpha)u_{n+1} + \tilde{c}_\lambda(\theta + (n-1)\alpha)u_{n-1} + 2\cos 2\pi(\theta + n\alpha)u_n, \tag{10.15}$$

where

$$\begin{aligned} c_\lambda(\theta) &= \lambda_1 e^{-2i\pi(\theta+\alpha/2)} + \lambda_2 + \lambda_3 e^{2i\pi(\theta+\alpha/2)} \\ \tilde{c}_\lambda(\theta) &= \lambda_3 e^{-2i\pi(\theta+\alpha/2)} + \lambda_2 + \lambda_1 e^{2i\pi(\theta+\alpha/2)} \end{aligned} \tag{10.16}$$

encode the hoppings in the physical model: nearest-neighbor hopping is captured by λ_2 while $\lambda_{1,3}$ determine the amplitude of next-nearest-neighbor (NNN) hopping. Typically the coupling constant space for Eq. (10.15) is divided into three regions informed by the duality map $(\lambda_1, \lambda_2, \lambda_3) \to (\lambda_3/\lambda_2, 1/\lambda_2, \lambda_1/\lambda_2)$ as follows

- **Region I** $0 \leq \lambda_1 + \lambda_3 \leq 1, 0\lambda_2 \leq 1$,
- **Region II** $0 \leq \lambda_1 + \lambda_3 \leq \lambda_2, 1 \leq \lambda_2$
- **Region III** $\max\{1, 2\} \leq \lambda_1 + \lambda_2, \lambda_2 > 0$.

This is illustrated in Fig. 10.2 from Ref. [5]. Here, I°, II° and III° denote interiors of the three regions and for $\sigma(K)$ the notation for a spectrum of some operator K, we also have $\sigma(I^\circ) = II^\circ$, $\sigma(L_I) = L_{III}$ and $\sigma(L_{II}) = L_{II}$. Currently proven spectral behavior of Eq. (10.15) can then be summarized by

Theorem 2:

1. For $\lambda \in II^\circ \cup III^\circ_{\lambda_1 \neq \lambda_3}$ for all α and almost every θ, $H_{\lambda,\alpha,\theta}$ has a purely absolutely continuous spectrum [147]
2. For $\lambda \in III^\circ_{\lambda_1=\lambda_3} \cup L_I \cup L_{II} \cup L_{III}$, for all α and almost every θ, $H_{\lambda,\alpha,\theta}$ has a purely singular continuous spectrum [147, 148]
3. 17, 13For $\lambda \in I^\circ$. If $\beta(\alpha) < L(\lambda)$, the for almost every θ, $H_{\lambda,\alpha,\theta}$ has a pure point spectrum. If $\beta(\alpha) > L(\lambda)$, then for almost every θ, $H_{\lambda,\alpha,\theta}$ has a purely singular continuous spectrum, with $L(\lambda)$ the Lyapunov exponent [149, 150]

and, for $\lambda \in I^\circ$, it has been shown that [5]

Theorem 3:

1. for a dense subset of $\{\alpha : \beta(\alpha) = L(\lambda)\}$, $H_{\lambda,\alpha,\theta}$ has a purely singular continuous spectrum for any θ in a full measure set Θ
2. for a dense subset of $\{\alpha : \beta(\alpha) = L(\lambda)\}$, $H_{\lambda,\alpha,\theta}$ has a purely point spectrum for almost every θ.

In other words, at the level of rigrorous spectral theory, the eigenstates of the extended AAH model show the same three regimes – extended, localized and multifractal – as the AAH model itself, depending on the strength of hoppings λ_i and arithmetic properties (rational approximation) of α in a rather complex way. It is of particular note that the spectrum $\Sigma_{\lambda,\alpha}$ of Eq. (10.15) is related to its dual in a simple way, $\Sigma_{\lambda,\alpha} = \lambda_2 \Sigma_{\sigma(\lambda),\alpha}$, thus perserving a notion of duality discussed for Eq. 10.1. Moreover, Jitomirskaya and Marx have been able to derive the exact form of the Lyapunov exponent for $H_{\lambda,\alpha,\theta} u = Eu$ and $E \in \Sigma_{\lambda,\alpha}$

and show it only depends on λ_i rather than E itself so there are no mobility edges (special E delineating parts of the spectrum that change and do not change their localization properties) in this model. While our work in the following Sections is somewhat preliminary and significantly more heuristic than any of the references in this short overview, we do aim to address the emergence of mobility edges below as well.

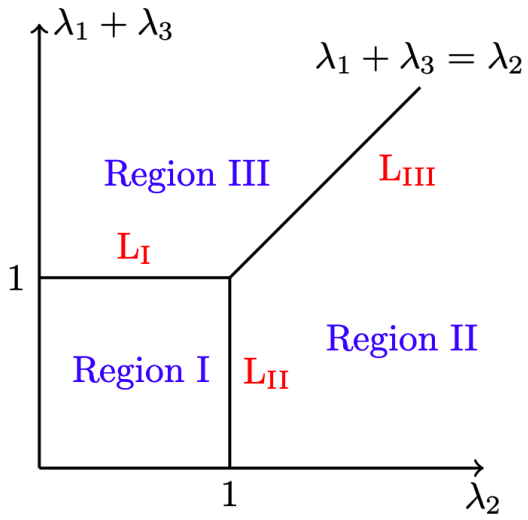

Figure 10.2: Phase transition diagram ilustrating Theorem 1.1. of Ref. [5]. Regions denoted by Roman numerals denote different NNN hopping amplitude regimes: **(I)** $0 \leq \lambda_1 + \lambda_3 \leq 1, 0\lambda_2 \leq 1$, **(II)** $0 \leq \lambda_1 + \lambda_3 \leq \lambda_2, 1 \leq \lambda_2$ and $\max\{1,2\} \leq \lambda_1 + \lambda_2, \lambda_2 > 0$. Interiors of these regions and their unions with lines L_i correspond to different spectral properties of $H_{\lambda,\alpha,\theta}$ i.e. different localization properties of the eigenstates for the Hamiltonian equivalent to the operator in Eq. (10.14).

As a final remark, we note that the almost Mathieu operator and the related Eqs. (10.14) and (10.15) are not the only quasiperiodic operators that have attracted the attention of mathematicians. Extensive work has been done on the Fibonacci Hamiltonian showing that for all parameter values, all spectral measures for this model are purely singular continuous i.e. the spectrum is always a Cantor set [151]. This is somewhat remarkable as prior to the 1980s it was believed that such a model could not be physically relevant, and contemporary research now suggests that there are even ways to interpolate between the Fibonacci chain and the AAH model [152].

10.1.2 Some experimental advances

We finish this Section by recounting some experimental advances in realizing and studying quasiperiodic systems. Thus far, ultracold atomic and photonic settings have proven fruitful for these studies. Further, developments in the field of meta-materials have marked these essentially classical systems as promising new testbeds for analyzing quasiperiodicity and multifractality as well.

In the realm of photonics, experiments have directly observed the localization-delocalization transition in photonic crystals [153] and probed the topological nature of the Hofstadter Hamiltonian (and the critical point of the AAH model) by injecting light at a specific site (photonic waveguide) and determining the position of localized edge states based on whether it spreads to neighboring sites [152]. Ultracold atomic studies have explored the Hofstadter Hamiltonian by engineering two-dimensional atomic lattices, even in the limiting case of huge magnetic fields not experimentally accessible for electrons in metals [154, 155]. Such studies have also simulated the AAH model in one-dimensional Bose-Einstein condensates. Here, researchers have been able to measure transport properties in the presence of precisely tailored disorder through expansion dynamics similar to the photonic technique mentioned above [156, 157, 158]. Finally, reconfigurable one-dimensional acoustic arrays [159, 160] have been used to map the multifractal butterfly spectrum by measuring acoustic density of states while varying the long-range order of the array. Another type of meta-materials, identical coupled mechanical resonators having collective dynamics fully determined by the controllable pattern in which they are arranged [7] have also proven to be well-suited for investigations of quasiperiodic systems. All three types of experiments– ultracold atomic, photonic and meta-material – continue to be investigated as potential simulators for quasiperiodicity and multifractality inherent to the AAH model and its generalizations. Quasiperiodic systems hosting mobility edges or having long-ranged hoppings between atoms which we discuss in some of the following Sections are therefore good candidates for a whole host of experimental realizations and have been explored as such already [161].

10.2 Toroidal curves for models with quasiperiodic on-site modulation

In this Section we employ the transfer matrix toroidal curve techniques discussed in Chapter 9 to study the AAH model and a closely related self-dual system, proposed in Ref. [3], which is known to have mobility edges. The latter model is also the focus of the collaborative experimental study described in Chapter 11.

10.2.1 AAH Model

First, we explore the localization-delocalization transition of the AAH model Eq. (10.1) as a geometrical transition between two qualitatively different sets of points on the surface of a torus. Fig. 10.3 depicts the three regimes of the model: (a) all eigenstates are localized for $V/t > 2$, (b) $V/t = 2$ corresponds to the system's critical wavefunction regime and (c) all the wavefunctions are fully extended for $V/t < 2$. We compute the total transfer matrix $A(N)$ for a system with $N = 1000$ sites using Eq. (9.13) as a starting

point. In these calculations E is a nonzero energy eigenvalue obtained by directly diagonalizing the AAH Hamiltonian. The qualitative difference between the three regimes is rather striking: as the ratio $V/2t$ decreases the toroidal curve character changes from a "tight" line winding around the central hollow region of the torus to a fairly diffuse set of points. We note that the curves corresponding to the localized regime in Fig. 10.3 (a) are qualitatively similar to the two types of localized curves we studied in Secs. 9.3.2 and 9.3.1 i.e exponentially localized wavefunctions having a sinusoidal envelope and power-law localized wavefunctions, respectively. This indicates that the wavefunctions corresponding to $V > 2t$ are likey to vary as a function of lattice site in a way more complex than a simple exponential decay. Further, we highlight the difference between Figs. 10.3 (b) and (c) in that the critical regime, equivalent to the Hofstadter problem, corresponds to a set of points that cover the most area on the torus most evenly, while in the delocalized regime some more densly covered regions are present.

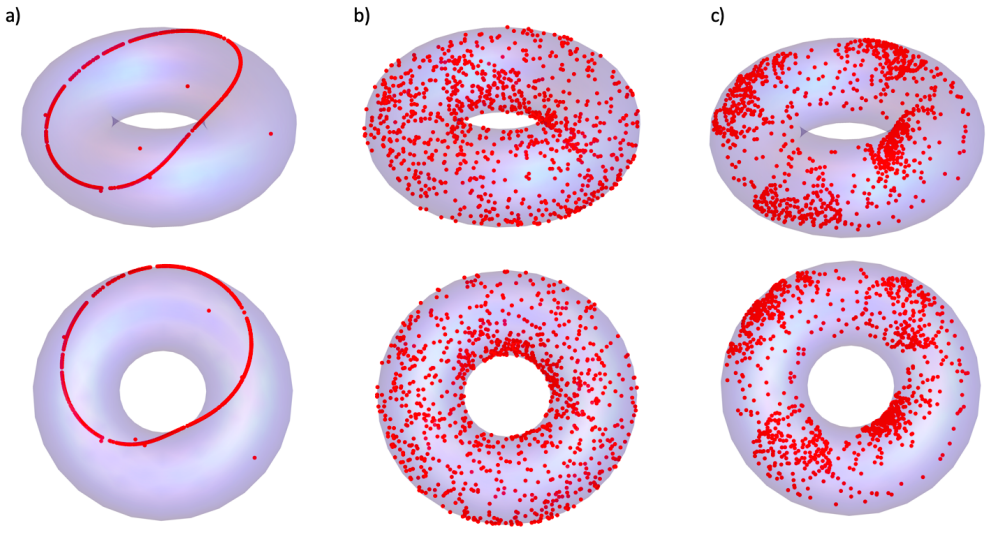

Figure 10.3: Side and top view of toroidal curves determined by $(x, y, z) = ((R + \chi \sin\theta_2)\cos\theta_1, (R + \chi \sin\theta_2)\sin\theta_1, \chi\cos\theta_2)$ for $N = 1000$ and an energy eigenvalue corresponding to the middle of the energy spectrum of the AAH Hamiltonian having quasiperiodicity strength **(a)** $V/t = 2.5$, **(b)** $V/t = 2$, **(c)** $V/t = 1.5$. The qualitative difference between the three regimes illustrates localized, critical and delocalized eigenstates of the system as captured by the full transfer matrix of Eq. (9.6)

Finally, to illustrate the absence of mobility edges in this system, we calculate the same three transfer matrices and plot the corresponding curves on the torus for three different eigenstates energies. To that end, Fig. 10.4 shows the same three regimes of quasiperiodicity strength for states close to the either edge of the energy spectrum in addition to a mid-spectrum state. While the curves determined by different states are not identical, they depict the same trend as quasiperiodicity strength is decreased. Recalling that for systems without mobility edges all eigenstates undergo a localization-delocalization transition, this

geometrical representation of the transition is consistent with theoretical predictions for the AAH model. We draw the same conclusion by studying a wider range of energy states for the AAH model as depicted in Fig. 10.5. Here, comparing Figs. 10.5 (a) and (b), the qualitative difference between toroidal curves corresponding to extended states (covering a wide are of the torus or similar to the clean and periodic cases of Secs. 9.2.1 and 9.2.2) and those reflecting the localized regime (tight and almost fully connected), is particularly salient regardless of the eigenenergies used to calculate them. We proceed to generalize and complicate these observations by studying the GPD model which reduces to the AAH model for a specific choice of system parameter values.

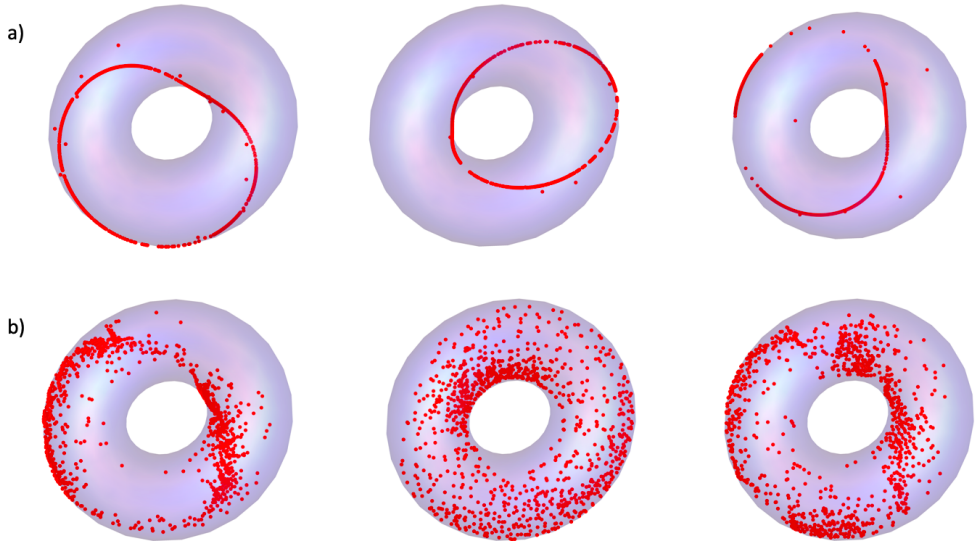

Figure 10.4: Plot of the toroidal curves determined by $(x, y, z) = ((R + \chi \sin\theta_2)\cos\theta_1, (R + \chi \sin\theta_2)\sin\theta_1, \chi\cos\theta_2)$ for $N = 1000$ and determined by the total transfer matrix for a state close to the bottom (left), middle (center) and top (right) of the energy spectrum as quasiperiodicity strenght is varied from **(a)** $V = 2.5t$ to **(b)** $V = 1.5t$. The similarity between the different energy eigenstates points towards the absence of a mobility edge.

10.2.2 Self-dual model having exact mobility edges

In this Section, we focus on transfer matrices and toroidal curves pertaining to a self-dual generalization of the AAH model described by S. Ganeshan, J. Pixley and S. Das Sarma in Ref. [3] i.e. the GPD model. Namely, we take the on-site modulation to have the form

$$\mu_n(\alpha, \phi) = 2\lambda \frac{\cos(2n\pi b + \phi)}{1 - \alpha\cos(2n\pi b + \phi)} \tag{10.17}$$

where $-1 < \alpha < 1$. Each value of α describes a different one-dimensional tight binding model and $\alpha = 0$ reproduces the AAH model of Eq. (10.1) as a limiting case. We note that for this choice of μ_n, the localization-

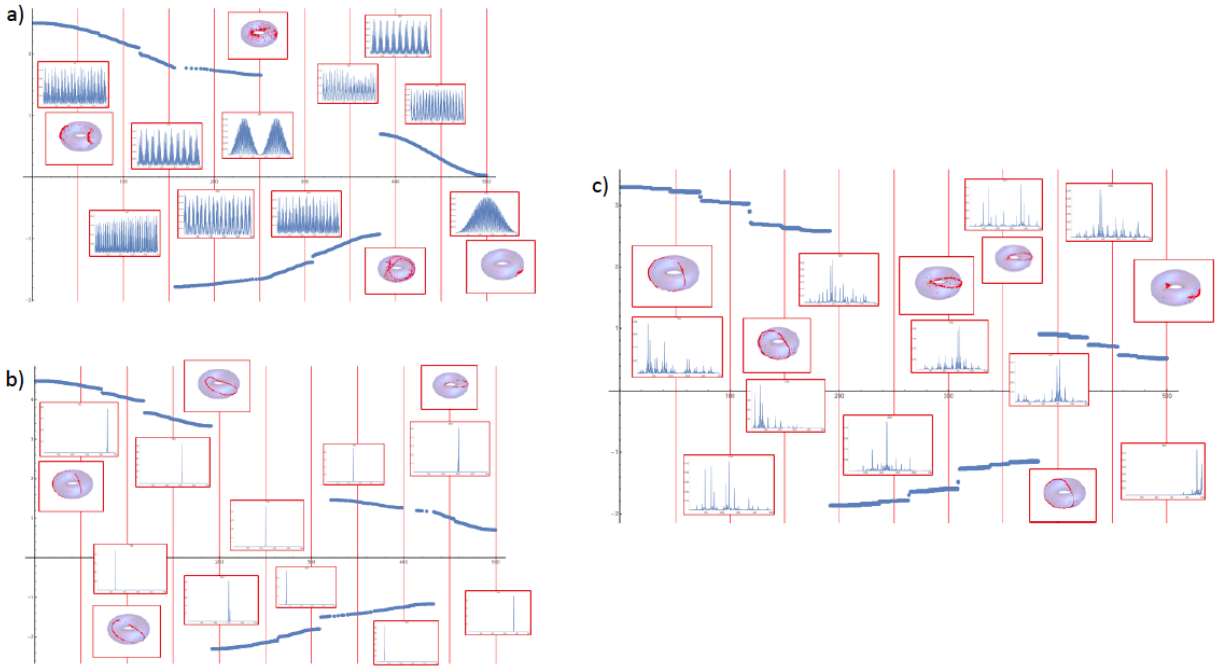

Figure 10.5: Plots of toroidal curves determined by $(x, y, z) = ((R + \chi \sin\theta_2)\cos\theta_1, (R + \chi \sin\theta_2)\sin\theta_1, \chi\cos\theta_2)$ for $N = 1000$ and determined by the total transfer matrix and their corresponding wavefunctions overlaid on top of the energy spectrum of the AAH Hamiltonian for **(a)**$V = t$ **(b)** $V = 3.0t$ and **(c)** $V = 1.98t$. The change in the geometry of the toroidal curves as well as the localization of the eigenstates of the AAH Hamiltonian clearly indicates a localization-delocalization transition for $V = 2t$.

delocalization transition of all eigenstates of the system occurs for $\alpha = 0$ and $\lambda = t$ when b is irrational (typically the Golden Ratio). In Ref. [3] it is precisely proven that a set of Heisenberg equations of motion for this model is self-dual under a series of Fourier-like transforms for all values of α. Further, for $\alpha \neq 0$ this model has a mobility edge described by a surprisingly simple closed form expression

$$\alpha E = 2\text{sgn}(\lambda)(|t| - |\lambda|). \tag{10.18}$$

Concretely, solving Eq. (10.18) for E identifies a point in the energy spectrum of this quasiperiodic model that separates eigenstates that will and will not undergo a (de)localization transition as the system parameters are tuned through the critical point $\lambda = t$.

The self-dual property is here critical for determining the localization physics in a manner similar to our discussion of the Thouless formula in Eqs. (10.4) and (10.4). To be more precise, from those expressions we know that identifying a self-dual point of a quasiperiodic or disored system implies that $\gamma = \gamma_{\text{dual}}$ at that point as wel. As the model and its dual have opposite localization behaviors, the self-dual point thus demarcates the localized and delocalized regimes of the model in question. In the case of the AAH model expemplified in Eqs. (10.4) and (10.10) the self-dual point is set by system parameters and independent of eigenstate energies so there is no mobility edge. In the case of the GPD model, having quasiperiodic modulation of the form given in Eq. (10.17) this is no longer the case. Namely, as in Ref. [3] we can re-write the discrete Schrodinger equation with the on-site modulation as in Eq. (10.17) in the form

$$t(u_{p-1} + u_{p+1}) + g\chi_p(\beta)u_p = (E + 2\lambda\cosh\beta)u_p \tag{10.19}$$

where $\chi_p = \sinh\beta/(\cosh\beta - \cos(2\pi pb + \phi))$ and we further define $\cosh\beta = 1/\alpha$ and $g = 2\lambda\cosh\beta/\tanh\beta$. Following a series of transform described in Ref. [3] this system of equations becomes

$$t(f_{k+1} + f_{k-1}) + g\frac{\sinh\beta}{\sinh\beta_0}\chi_k(\beta_0)f_k = 2t\cosh\beta f_k \tag{10.20}$$

with $2t\cosh\beta_0 = E + 2\lambda\cosh\beta$. Expressions given in Eqs. (10.19) and (10.20) are explicitly self-dual to each other when $\beta = \beta_0$. This condition is equivalent the the mobility edge equation Eq. (10.18).

To illustrate the existence of the mobility edge, we determine the energies of the lowest and highest energy states of a non-interacting one-dimensional tight binding Hamiltonian having on-site terms as in Eq. (10.17) and use them to plot toroidal curves at different values of λ via our transfer matrix method Eqs. (9.6) and (9.9). These two states are expected to lie on opposite sides of the mobility edge within the system's

energy spectrum and consequently exhibit distinct localization properties as the strength of quasiperiodicity is increased. Our transfer matrix method can capture these differing behaviors as a geometrical difference between curves on a torus. Further, we use transfer matrices to calculate the Lyapunov exponent at either energy eigenvalue while varying α. When an eigenstate becomes delocalized for some α, we expect the Lyapunov exponent to sharply decrease and near-vanish. This is depicted for lowest energy state of in Fig. 10.6 (a) and for the highest energy state in Fig. 10.6 (b). Further emphasizing the difference between the model having $\alpha \neq 0$ and the AAH model discussed in the previous Section, calculations depicted in these figures have been carried out for $\lambda = 0.9t$ – at this point all AAH eigensates are delocalized, and the Lyapunov exponent nearly vanishes but this is not the case for the GPD model. This mobility edge behavior is clearly reflected in the nature of the toroidal curves which become more tight and connected as the Lyapunov exponent increases.

The trend in the character of these curves, and the Lyapunov exponent, as illustrated by Fig. 10.6 is the opposite due to a symmetry of the Hamiltonian that exchanges the lowest and the highest energy state as $\alpha \to -\alpha$. In order to see this, it is sufficient to note that in Eq. 10.17 taking $\alpha \to -\alpha$ is equivalent to shifting $\phi \to \phi - \pi$. The shift in ϕ exchanges a minimum of the potential for a maximum (or vice versa) thus exchanging a high energy and a low energy state of the system.

We end this Section by noting that the Ganeshan, Pixley and Das Sarma (GPD) model can be experimentally realized in ultracold atomic settings and preliminary exploration of its properties has been conducted in the group of Prof. B. Gadway already. A comparison between these findings and theoretical predicitions is presented in detail in the next Chapter, but we note that the two eigenstates of this model considered here have been calculated with realistic experimental values for t. While we ignore the interactions between atoms in Figs. 10.6, they can be taken as limiting cases of a more physical system where those interactions shift the mobility edges and enhance the difference in behavior between the lowest and highest energy states of the model. We focus on these two states in particular in order to provide a setting for further discussion of those interactions in Chapter 11. Accordingly, we obtain their eigenenergies by an imaginary-time method within which the strength of interactions can be tuned precisely.

10.3 Rational approximation and tightness of toroidal curves

In previous Sections, we have presented a number of computational results supporting the notion that the localization-delocalization transition in quasiperiodic tight-binding models can be captured by a geometrical change of a set of curves on a torus. Here, as a complementary and more analytical approach, we outline

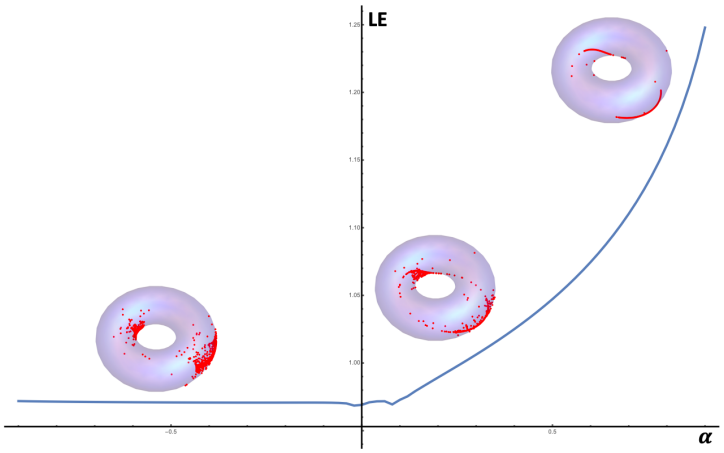

(a)

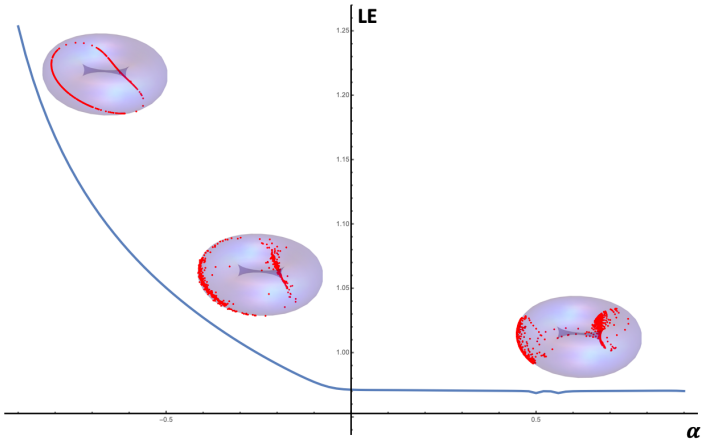

(b)

Figure 10.6: Plot of the Lyapunov exponent and the toroidal curves determined by $(x, y, z) = ((R + \chi \sin\theta_2)\cos\theta_1, (R+\chi\sin\theta_2)\sin\theta_1, \chi\cos\theta_2)$ as a function of α calculated from the full transfer matrix for the **(a)** lowest energy state of a non-interacting, one-dimensiona tight binding model with μ_n as in Eq. (10.17) and **(b)** its highest energy state. For all α, we set $\lambda = 0.9t$. As the Lyapunov exponent increases, the lowest energy eigenstate becomes more localized as illustrated by the tighter toroidal curves on the right hand side of the plot. The highest energy state exhibits the opposite trend.

an argument due to Prof. Diptiman Sen concerning the difference between $\alpha = p/q (b = p/q)$ for some co-prime integers p and q and irrational $\alpha(b)$. Thus, we end this Chapter with an eye towards other more mathematical arguments that could formalize the notion of toroidal curves "tightening" (presenting as a single curve rather than a two-dimensional set) when they correspond to regimes of some given model where its eigenstates are localized.

We consider the model in Eq. (10.1) and aim to calculate the total transfer matrix $A(N, E)$ for $\alpha = p/q$ with $p, q \in \mathbb{Z}$ and having no shared divisors. The number of sites in the system N and, equivalently, the number of transfer matrices making up the product $A(N, E)$ (Eq. (9.6)) can be written as $N = rq + s - 1$

for r and s integers such that $1 \neq s \neq q$. Defining

$$M = A_q A_{q-1} \cdots A_2 A_1 \tag{10.21}$$

we can re-write

$$A(N, E) = A_{s-1} \cdots A_a M^r \tag{10.22}$$

so that some of the properties of $A(N, E)$ can be understood by studying M. Being a product of transfer matrices, M is symplectic and has real entries and unit determinant. Consequently, we can write its eigenvalues as λ and $1/\lambda$ and three possibilities are allowed: (1) $\lambda \in \mathbb{R}$ and $\lambda > 1$, (2) $\lambda \in \mathbb{R}$ and $\lambda < -1$, and (3) $|\lambda| = 1$ so that $\lambda = e^{i\phi_\lambda}$. If the eigenvalues of M are not degenerate ($\lambda \neq \pm 1$), it will have two indpendent eigenvectors

$$\begin{aligned} M x_1 &= \lambda x_1 \\ M x_2 &= (1/\lambda) x_2. \end{aligned} \tag{10.23}$$

Suppose that we can find some other pair of vectors $x_{1,2}^{'}$ such that $x_i^{iT} x_j = \delta_{ij}$. It then follows that

$$\begin{aligned} M &= \lambda x_1 x_1^{'T} + (1/\lambda) x_2 x_2^{'T} \\ M^r &= \lambda^r x_1 x_1^{'T} + (1/\lambda)^r x_2 x_2^{'T}. \end{aligned} \tag{10.24}$$

. If the eigenstates of the system are localized i.e. $|\lambda| > 1$ and $|1/\lambda| < 1$ then the Lyapunov exponent, set by the logarithm of λ, is large as well. For a sufficiently large r we can approximate Eq. (10.24) as

$$M^r \approx \lambda^r x_1 x_1^{'T} \tag{10.25}$$

so that parametrizing M^r as we have done in the previous Chapter (Chapter 9) we conclude that $\eta \to \infty$ and $\chi \to 1$ as $r \to \infty$. More concretely, the point corresponding to M^r will reside on the surface of the torus and only the two angles θ_1 and θ_2 that describe its position can vary. Further, for $\lambda > 1$, these angles will not change either and it is only for $\lambda < -1$ that the signs of a, b, c and d of Eq. (9.8) will change as r (N) changes. Equivalently, θ_1 and θ_2 will change in discrete increments of $r\pi$ and the point on the torus they describe will flip between diametrically opposite points on the torus as r changes from odd to even and vice versa.

Turning to the full transfer matrix as written in Eq. 10.22 we first note that since all A_i for $1 \leq i \leq q$ are on the order of unity, in the limit of large r, multiplying M^r by the product of A_i will not change $\chi = 1$ for any value of s. Hence, $A(N, E)$ also corresponds to a point on the surface of the torus. However, the angles θ_1 and θ_2 will shift on the surface of the torus as s ranges from 1 to q. We conclude that as s varies the point on the torus under consideration takes on q values. In other words, in carrying out the plotting procedures of the previous Sections, once N becomes large, the toroidal curve corresponding to $A(N, E)$ whould be restricted to q points only. Further, as q becomes large so the choice of $\alpha = p/q$ gives the system near-quasiperiodic properties, this set of q points become dense and fills up a "tight" curve on the torus. This is illustrated in the top row of Fig. 10.7.

Finally, we turn to $\lambda = e^{i\phi_\lambda}$. Here, M^r cannot be approximated by neglecting either term in Eq. (10.24) so that the point on the torus corresponding to M^r on the torus does not stay fixed on its surface (η and χ can change). In this case then, both the variation in r (as N is increased to get the next point on the torus) and the variation of s from 1 to q move the point corresponding to $A(N, E)$. We conclude that for large q and with increasing N, the point will cover an essentially two-dimensional set on the torus. This is illustrated in the bottom row of Fig. 10.7. As this eigenvalue of the transfer matrix corresponds to an extended eigenstate of the system, we establish an approximate equivalence between torioidal curve plots that are diffuse and cover a large area on the torus and eigenstate delocalization.

We conclude our study of AAH-like quasiperiodic models by turning to an experimental realization of the model described by Eq. (10.17) in the next Chapter. Here, we consider not only the realistic physical constraints on possible observations of multifractal wavefunctions and mobility edge physics but also the effect of interactions between atoms.

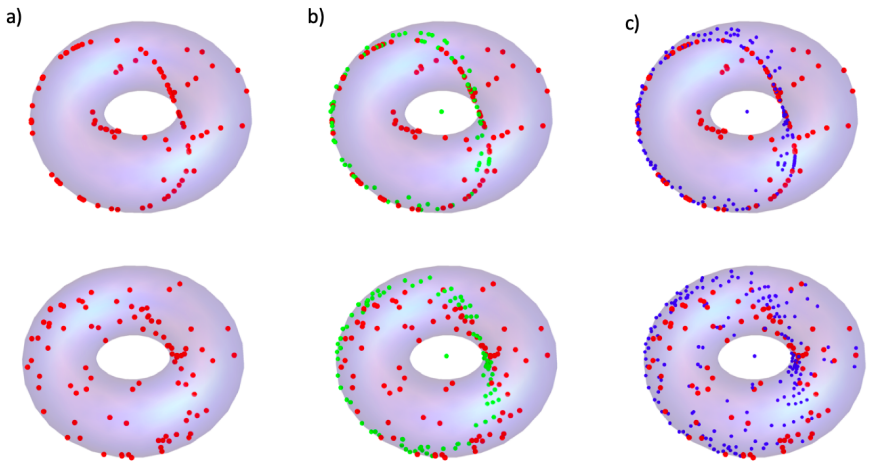

Figure 10.7: Toroidal curves corresponding to the transfer matrix for the model in Eq. (10.1) with the irrational period approximated as $\alpha = 144/89$. The top row shows toroidal curves for $V = 2.6t$ i.e. the localized regime while the curves in the bottom row were calculated with $V = 1.6t$ i.e. the extended regime. The number of transfer matrices used in calculating the full transfer matrix increases from left to right with **(a)** $N = 90$, **(b)** $N = 180$, and **(c)** $N = 270$. Colors indicate the points added to the curve with each increase in N: points in blue are calculated for a larger N than points in green and the points in green are calculated for a larger N than points in red. We observe that the blue points in the top row roughly trace the same curve as points calculated for smaller N while in the bottom row the area of the torus covered by the points corresponding to total transfer matrices consistently increases with increasing N. These computational observations are consistent with the discussion presented in Sec. 10.3.

Chapter 11

Interaction-shifted mobility edges in a generalized Aubry-Andre model

11.1 Introduction

In this Chapter, we focus on AAH-like quasiperiodic systems having mobility edges and address a specific experimental realization of one such model in an ultracold atomic setting. This discussion is a product of an on-going collaboration with the experimental research group of Prof. B. Gadway [161] at UIUC.

Ultracold atomic systems have historically not only been a fruitful context for realizing quasiperiodicity due to their high degree of experimental control, but quasiperiodic modulation has also been used to emulate disorder in these experiments. The precise properties of localization-delocalization physics in quasiperiodic ultracold atomic systems are then of both theoretical (as a test of theories of multifractality) and experimental (as a tool for studying disorder) interest. Presence of mobility edges in these system is of particular relevance since even prototypical examples such as the AAH model, Eq. (10.1), itself have been theoretically predicted [162, 163] and exprimentally observed [164] to feature them away from the tight binding limit. Namely, when the primary lattice potential is not very deep, the AAH model manifests a single-particle mobility edge (critical energy) separating delocalized and localized states instead of featuring a single sharp localization-delocalization transition for all energy eigenstates. Presence of any tunneling terms beyond nearest-neighbor that appear naturally in ultracold atomic implementations of generalized AAH models can also give rise to mobility edges, as we have noted in our discussion in Chapter 10.

While this Chapter centers on the model proposed in Ref. [3] and explicitly expressed in Eq. (10.17) – the GPD model – where the exact energy value for the mobility edge has been theoretically determined, we note that current discussion strongly implies that mobility edges are somewhat generic as features of quasiperiodic ultracold atom experiments. Finally, as many of these experiments involve interacting atoms, it is relevant to inquire whether single-particle mobility edges are stable to effects of nonlinear inter-particle interactions. This concern is related to the issue of many-body-localization as well. Below, we detail the experimental realization of the GPD model in a highly tunable momentum-space lattice holding a rubidum BEC [161]. We explicitly address interaction effects by including them in numerical simulations. We find good qualitative

agreement between experimental data and simulations and conclude that interactions between the ultracold atoms preserve but shift mobility edges. Further, we find that interactions can give rise to mobility edges in cases where they would not be present in the non-interacting model (ex. AAH model or the $\alpha = 0$ limit of the GPD model).

This Chapter is organized as follows. First, we summarize the momentum space lattice technique used in ultracold atomic experiments in the Gadway research group in Sec. 11.2. Here, we rely on commony used formalism for describing atom-light interactions that are the main tool for manipulating BECs and mainly draw from Ref. [6]. In Sec. 11.2.1 we present the specific application of this technique to the GPD model then enumerate consequent experimental observations in Sec. 11.3. Experimental work presented in this Sections was carried out by F. A. An, E. Meier and B. Gadway. We finish this Chapter by discussing effects of inter-atomic interactions in Sec. 11.4. Our analysis in this Section is based on numerical simulations and constitute the main theoretical contribution to the collaborative study at the center of this Chapter. The imaginary time propagation method we use in these simulations is outlined in Sec. 11.4.1 and the full details of the mobility edge shift are given in Sec. 11.4.2 Finally, in Sec. 11.5, we summarize our findings and suggest some possible avenues for future experimental and theoretical work.

11.2 Simulating tight-binding models with momentum-space lattices

The purpose of this Section is to outline the basic experimental technique used by the Gadway research group in order to study effects of quasiperiodicity in one-dimensional ultracold atomic lattices [161]. This technique is based on standard experimental methods utilizing atom-light interactionsand highly versatile when it comes to designing systems described by various tight-binding models [6, 165]. It essentially employs a discrete set of free-particle momentum states coupled through two-photon Bragg transitions to engineer a momentum space lattice. These transitions are driven by pairs of interfering laser beams that can be controlled precisely. In effective tight-binding models that are accessible through this experimental scheme, the momentum-space lattice setup allows for a local and time-dependent control over all system parameters such as tunneling amplitudes, tunneling phases and site energy differences. More precisely, these parameters can be varied for each link between lattice sites thus allowing for realization of many patterns. Further, single-site resolved detection of atomic populations is possible [6].

The basic idea behind the momentum-space lattice setup is shown in Fig. (11.1). Here, we consider a generic two-level system of atoms having a single internal ground state $|g\rangle$ and a single internal excited state

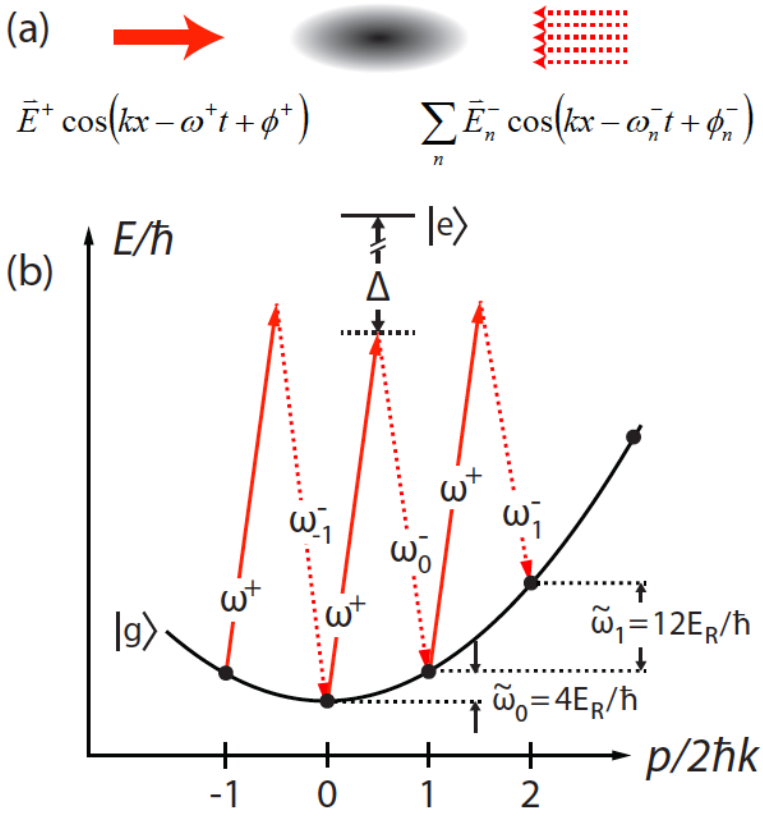

Figure 11.1: Schematic of the experimental scehme for studying lattice-driven momentum-space dynamics from Ref. [6]. In panel **(a)** it is shown how atomic matter waves are driven by a pair of counter-propagating laser beams, one of which (shown on the top right of the schematic) is made up of a number of distinct frequency components while panel **(b)** depicts the energy-momentum dispersion. All lasers fields are detuned far away from the atomic resonance between the ground $|g\rangle$ and excited $|e\rangle$ state by an amount Δ. Stimulated two-photon Bragg transitions are engineered by using pairs of interfering lasers. They couple plane-wave momentum states separated by two photon momenta $2\hbar k$. The two-photon Bragg resonance condition here reads $\hbar\tilde{\omega}_n = (2n+1)4E_R$ for each link between neighboring sites with E_R the single-photon recoil energy, $\tilde{\omega}_n$ the Doppler frequency shift of the transition from the $|n\rangle$ to the $|n+1\rangle$ state and $|n\rangle$ labeling the discrete basis of plane-wave momentum states having $\vec{p}_n = 2n\hbar k\hat{x}$.

$|e\rangle$. We denote their energies as $\hbar\omega_g$ and $\hbar\omega_e$, respectively, and atomic mass as M. Shining a laser beam on these atoms induces electric dipole moments so the atom-light interaction can be expressed through a dipole operator. The two states here are distinct hyperfine energy level used in laser cooling, for instance $5S_{1/2}$ and $5P_{3/2}$ states in ^{87}Rb. Neglecting spontaneous emission and assuming that the dipole approximation holds, the single-particle two-level Hamiltonian is

$$\hat{H} = \frac{\hat{p}^2}{2M} + \hbar\omega_e|e\rangle\langle e| + \hbar\omega_g|g\rangle\langle g| - \vec{d}\cdot\vec{E} \tag{11.1}$$

where $\vec{p}$ is the free particle momentum of the atoms, $\vec{d}$ the atomic dipole operator and $\vec{E}$ the driving electric (laser) field. The dipole approximation assumes that the radiation used to manipulate the atoms, the laser beam $\vec{E}$, has a wavelength greater than the size of the atom. We model the electric field $\vec{E}$ as compsed of a right-traveling field $\vec{E}^+(\vec{x},t)$ having a single frequency component and a left-traveling field $\vec{E}^-(x,t)$ composed of several discrete frequency components. As indicated in Fig. 11.1 this amounts to taking

$$\vec{E}^+(\vec{x},t) = \vec{E}^+\cos(\vec{k}^+\cdot\vec{x} - \omega^+ t + \phi^+) \tag{11.2}$$

$$\vec{E}^-(\vec{x},t) = \sum_j \vec{E}^-\cos(\vec{k}_j^-\cdot\vec{x} - \omega_j^- t + \phi_j^-) \tag{11.3}$$

Without loss of generality, Eq. (11.2) assumes that the fields propagate along the x-axis and that they are nearly monochromatic so that $\vec{k}^+ = k\hat{x}$ and $\vec{k}_j^- \approx -k\hat{x}\forall j$ with $k = 2\pi/\lambda$ the wavevector of the laser light having wavelength λ. Further, we assume that all laser frequencies are detuned from atomic resonance by nearly the same amout – labeling the resonance as $\omega_{eg} = \omega_e - \omega_g$, we take the detuning to be $\Delta = \omega_{eg} - \omega^+ \approx \omega_{eg} - \omega_j^-\forall j$. For every frequency component we also define the respective resonant Rabi couplings to be $\Omega^+ = -\langle e|\vec{d}\cdot\vec{E}^+|g\rangle/\hbar$ and $\Omega_j^- = -\langle e|\vec{d}\cdot\vec{E}_j^-|g\rangle/\hbar$ and take the single-photon detuning from resonance to be much larger: $|\Delta| >> |\Omega_j^\pm|\forall j$. Consequently, the direct population of the atomic excited state $|e\rangle$ is negligible in this model and we can formulate an effective ground state Hamiltonian $\hat{H}_{\text{eff}} = \hat{H}_0 + \hat{H}_{\text{int}}$. In this approximation, $\hat{H}_0$ is the free-particle kinetic energy term while $\hat{H}_{\text{int}}$ describes light-atom interactions. These interactions drive two-photon, Bragg scattering-like, processes that change the atomic momenta by $\pm\hbar\vec{k}_{\text{eff}} = \pm 2\hbar k\hat{x}$ while leaving the internal state unchanged. This process consists of virtual absorption of a photon from one laser field and stimulated emission into the other. In experiments, the atoms in question reside in a Bose-Einstein condensate so it is reasonable to assume a small momentum spread among them (the momentum spread of trapped BECs is typically much smaller than the single photon recoil momentum $2\sigma_p << \hbar k$). We can then define a discrete basis (labeled by an integer) of plane-wave momentum states $|n\rangle$ having momenta $\vec{p}_n = 2n\hbar k\hat{x}$. This set of allowed, quantized, momentum states forms the lattice sites

of the momentum-state lattice used to experimentally realize tight-binding models such as those having quasiperiodic on-site modulation that are of interest in this Chapter. For each of these states, we have $E_n = \langle n|\hat{H}_0|n\rangle = n^2(4E_R)$ for $E_R = \hbar^2k^2/(2M)$ the single-photon recoil energy.

Given the form of the driving laser field $\vec{E}$ stated in Eq. (11.2), terms that increase the momentum of $|n\rangle$ states can be a result of absorption of a photon from the right-traveling field and consequent stimulated emission into any of the various frequency fields making up the left-traveling laser beam. Formally, we can define a two-photon Rabi coupling

$$\tilde{\Omega}_j e^{i\tilde{\phi}_j} = \frac{\Omega_j^* - \Omega^+}{2\Delta} e^{i(\phi^+ - \phi_j^-)} \tag{11.4}$$

where we take $\tilde{\Omega}_j$ to be real and positive and ϕ^+ and ϕ_j^- are phases of the two lasers that can be controlled experimentally [6]. These parameters set the phase shift associated with the absorption and emission process. Moving to the interaction picture where both system operators and state vectors carry time dependence, the nearest-neighbor off-diagonal elements of the interacting Hamiltonian $\hat{H}^I_{\text{eff}}$ take the time-dependent form

$$\langle n+1|\hat{H}^I_{\text{eff}}|n\rangle/\hbar = \sum_j \tilde{\Omega}_j e^{i\tilde{\phi}_j} e^{-i\delta_j^{(n)}t}. \tag{11.5}$$

Here, $\delta_j^{(n)} = \omega^+ - \omega_j^- - \tilde{\omega}_n$ is the two-photon detuning of the jth frequency component from the $|n\rangle$ to $|n+1\rangle$ transition and $\tilde{\omega}_n$ denotes the Doppler frequency shift of the same transition (recall that the atoms being affected by laser light are moving). The latter quantity can be explicitly calculated as [6]

$$\tilde{\omega}_n = (2n+1)4E_R/\hbar \tag{11.6}$$

which defines the two-photon Bragg resonance condition for the $|n\rangle$ to $|n+1\rangle$ transition. In other words, there is a unique state-to-state frequency shift that can be used to control the off-diagonal Hamiltonian elements (hopping amplitudes in a tight-binding model) with great precision. As in Ref. [6], we assume that the two-photon detuning between each frequency component j from the left-traveling field and the right traveling field approximately satisfies the condition identified in Eq. (11.6). To be more precise, for every jth frequency component, we take

$$\omega^+ - \omega_j^- = \tilde{\omega}_j - \xi_j \tag{11.7}$$

where ξ_j is a small detuning from the Bragg resonance that can be varied in experiments. On-site energies

in thight-binding models can be implemented through ξ_j [6] since

$$E_(j+1) - E_j = \xi_j. \tag{11.8}$$

This feature of the momentum-space lattice technique is germane for realization of quasiperiodic models such as in Eqs. (10.1) and (10.17) where the details of the on-site modulation determine the localization physics of the system. In the limit of 'weak-driving' i.e. $\hbar\tilde{\Omega}_j << 8E_R \forall j$, the bandwith of the two-photon transitions coupling nearby momentum-lattice sites is narrow enough that we can assume that at most one frequency component of the laser field substantially contributes to each off-diagonal coupling. The interaction picture Hamiltonian in Eq. (11.5) can consequently be re-written as [6]

$$\langle n+1|\hat{H}^I_{\text{eff}}|n\rangle/\hbar \approx \tilde{\Omega}_n e^{i\tilde{\phi}_n} e^{i\xi_n t}. \tag{11.9}$$

Assuming that $\xi_j = 0$ for all j ($\omega^+ - \omega_j^- = \tilde{\omega}_j$) or that, equivalently, all frequency components of the applied laser field precisely satisfy the two-photon Bragg resonance condition, we finally arrive at a description of a tight-binding Hamiltonian

$$\hat{H}^I_{\text{eff}} \approx \sum_j t_j (e^{i\phi_j} \hat{c}^\dagger_{j+1} \hat{c}_j + \text{h.c.}) \tag{11.10}$$

with tunneling amplitudes given by $t_j = \hbar\tilde{\Omega}_j$ and tunneling phases equal to $\phi_j = \tilde{\phi}_j$.

As noted at the beginning of this Section, Eq. (11.10) shows that the momentum space lattice exprimental scheme can be used to build up individual links between lattice sites of discrete momentum states with high degree of local control. From Eq. (11.10) it is clear that this can be done through engineering of many interfering laser frequency components – hopping amplitudes and tunneling phases are controlled in a link-dependent way through adjusting the laser field $\vec{E}^-(\vec{x}, t)$. Namely, setting each component E_j^- of the right-propagating laser field in Fig. 11.1 sets the corresponding parameters t_j and ϕ_j. Practically, this can be done by, for instance, passing a single laser beam through a pair of acousto-optic modulators driven by precisely calibrated radiofrequency signals [6, 166]. Such tailored radiofrequency signal can be smoothly varied in time so that the paramaters t_j and ϕ_j of the tight-binding system being emulated can be made time-dependent. This allows for both slow, adiabatic changes and rapid quenches through different phases or regimes of the system, which is of great interest in studies of localization-delocalization physics in quasiperiodic models. Before turning to particular examples such as the GPD model, however, we emphasize that this experimental scheme permits the study of almost any one-dimensional system and is

a great advance in ultracold atomic simulation of tight-binding models, including those having topological properties or characterized by presence of disorder. This approach can also be extended to higher dimensions and used to study, for instance, two-dimensional Abelian U(1) lattice models exhibiting the integer Quantum Hall effect [6, 158, 157].

11.2.1 GPD model realized in a momentum-space lattice

To experimentally realize the model proposed in Ref. [3], Gadway research group used the momentum space lattice technique with ultracold ^{87}Rb atoms and counter-propagating lattice beams of wavelength $\lambda = 1064$ nm. The detuning ξ_j defined by Eqs. (11.7) and (11.9) was set to be non-zero so that "site"-energies could be implemented via Eq. (11.8). In this way, the generalized AAH on-site potential landscape of Eq. (10.17) was emulated. More concretely, the appropriate tight-binding Hamiltonian reads

$$H_{GPD} = -t \sum_n \left(c_{n+1}^\dagger c_n + \text{h.c.} \right) + \sum_n \varepsilon_n c_n^\dagger c_n, \tag{11.11}$$

where the onsite variation ε_n is as in Eq. (10.17), namely,

$$\varepsilon_n = \lambda \frac{\cos(2\pi n b + \phi)}{1 - \alpha \cos(2\pi n b + \phi)}. \tag{11.12}$$

While Ref. [3] assumes $b = (\sqrt{5} - 1)/2$, the experimental study employs the inverse of this number. However, either choice results in a system having three bands in its energy spectrum. Further, the analysis of localization physics and mobility edge energy values in Ref. [3] does not hinge on the precise value of b but rather its being irrational. The potential landscape realized in experiment is further formulated so that the localization-delocalization transition in the AAH model takes place for $\lambda_e/t = 2$ rather than $\lambda/t = 1$ as in our discussion above. For this reason we denote the experimental quasiperiodicty strength as λ_e/t and explictly address this discrepancy when appropriate.

To experimentally determine the localization behavior of different eigenstates of the GPD model, the entire population of condensed atoms was initiated at the central lattice site i.e. in the state having $\vec{p} = 0$, then adiabatically loaded into some other desired eigenstate by slowly ramping the tunneling amplitude t from 0 to some final value t_f while quasiperiodicty strength λ was held fixed. This is equivalent to decreasing λ/t from some very large value, deep in the localized phase of the system, to the final value λ/t_f. Here, the slow ramp ensures that the system starts in an eigenstate of the Hamiltonian with λ/t and ends in the corresponding eigenstate of the Hamiltonian having λ/t_f i.e. adiabaticity of the process. Snce the ramp starts in the highly localized regime, after λ/t_f was reached, the system was allowed time to equilibrate. In

cases where the ramp led to a regime in which the state being studied was delocalized, it would "spread out" during this equilibration time. The atomic population was imaged by standard methods following such equilibration. Optical density images obtained in this way thus clearly indicate whether the system is in a localized (atom population does not spread across the one-dimensional lattice) or a delocalized (atom population spreads across the one-dimensional lattice) regime.

We only consider this procedure for the lowest energy state of the system (its ground state, denoted GS) and it highest excited energy state (denoted ES) as other eigenstates could not be exprimentally accessed due to limitations on experimental timescales [6, 161]. To ensure that the central lattice site where the atom population was initiated had the lowest energy, the phase degree of freedom in Eq. (10.17) was set to $\phi = \pi$ while to access the highest excited state of the system at the same lattice site this quantity was tuned to $\phi = 0$. In principle, varying ϕ should allow this experimental ramp to start wih any eigenstate. However, the ramp duration as currently implemented is too short compared to difference in energy between non-extreme eigenstates leading to poor overlap between the atom population and the desired eigenstate [161]. The ramp procedure is illustrated in Fig. 11.2 (a).

Since the mobility edge is expected to lie between the two extreme eigenenergies studied in experiment (minimum and maximum of the energy spectrum), observing distinct localization-delocalization patterns between the two supports its existence in this model. The exact value of the mobility edge depends on the parameter α as stated in Eq. (10.18) and illustrated by toroidal curve studies in Figs. 10.6 so the ramp procedure was performed for values ranging from $\alpha = -0.5$ to 0.5. Consequently, the symmetry of the GPD model exchanging the lowest and highest energy state of the models as $\alpha \to -\alpha$ noted in Sec. 10.2.2 was also experimentally investigated.

11.3 Experimental Findings

Having outlined the experimental procedure used by the Gadway research group to investigate the GPD model, we proceed to enumerate some observations from it [161]. Discussion and results presented in this Section stem from a collaboration with this group as well as with Profs. J. H. Pixley at Rutgers Univeristy and S. Ganeshan at City College of New York. At the time of writing of this thesis, a manuscript of a publication is being prepared together with these co-authors.

Main results of the experiment are summarized by Figs. 11.2 (c) and 11.3. Here, we use the participation ratio (PR) in order to distinguish localized and delocalized states. More explicitly,

$$\mathrm{PR} = 1/\Sigma_n |\psi_n|^4 \ . \tag{11.13}$$

is calculated from experimental data and we extract it from numerical simulations as well. For a finite-sized system having N sites, the PR takes values ranging from 1 for fully localized states to N for fully extended states. When an eigenstate of the system is tightly localized to a single site, $n = n_0$, the sum in Eq. (11.13) becomes $\Sigma_n |\psi_n|^4 = |\psi_{n0}|^4 = 1$ and the PR is equal to unity. In contrast, for a wavefunction evenly distributed across all sites in the system i.e. $\psi_n = 1/N$ for any n, it follows that $\Sigma_n |\psi_n|^4 = 1/N$ and the participation ratio is equal to system size N. Panel (c) of Fig. 11.2 shows the measured values of this parameter for the ground state and the highest excited state of the GPD model together with theoretically obtained predictions (using exact numerical diagonalization and the imaginary time propagation technique discussed in more detail in Sec. 11.4.1 below). Here, we recall that in the experimental realization of the AAH limit ($\alpha = 0$) of the GPD model, the localization-delocalization transition takes place for $\lambda_e/t = 2$ rather than $\lambda/t = 1$ as in Chapter 10.

While all three parts of this plot show both states localizing as λ_e/t_f becomes larger, we highlight that the localization transition happens at approximately the same quasiperiodicity amplitude for the ground state and the highest excited state only when $\alpha = 0$ (we attribute the small discrepancy between the two to the effect of nonlinear inter-atomic interactions and discuss it further in Sec. 11.4.2). At this point, the experimental system is equivalent to the AAH model of Eq. (10.1) where mobility edges are effectively absent and all states presumed to exhibit the same localization-delocalization physics. For $\alpha = -0.5$, the ground state localizes for smaller λ_e/t_f than the highest excited state. The opposite is true for $\alpha = 0.5$, in accordance with our discussion of the $\alpha \to -\alpha$ symmetry in Sec. 10.2.2.

Considering the PR of either state as function of λ_e/t, as shown in Fig. 11.2 (b), we see that for $\alpha = -0.5$ the ground state (localizing near $\lambda_e/t = 1$ or $\lambda/t = 1/2$) and the highest excited state (localizing near $\lambda_e/t = 3$ or $\lambda/t = 3/2$) of the system eventually cross the mobility edge. These two plots therefore provide experimental support for a parameter-tuned mobility edge. This conclusion is further strengthened by Fig. 11.3 which shows a localization-delocalization phase diagram with both α and λ_e/t varied. To summarize, experimental data shows that for negative values of α this systems features a mobility edge and as α is increased, the mobility edge moves closer to the zero energy eigenvalue. For positive α, the mobility edge inverts so that high energy states localize at smaller quasiperiodicity strengths λ/t than the low energy states.

To gain insight into different localization behaviors for positive and negative α, we consider the distribution of lattice site energies in either case, as depicted in Fig. 11.4 (a). In this figure, the GPD on-site quasiperiodic term of Eq. (11.12) is shown overlaid on top of the regular one-dimensional lattice. It exhibits a more peaked character for $\alpha < 0$. Lattice site energies in this case are mostly high, in a heuristic picture

of the quasiperiodic lattice being a sequence of potential wells, most states "sit" on top of the wells rather than at their bottoms. The opposite is true for $\alpha > 0$ where the distribution of lattice site energies is such that most states are characterized by low energy eigenvalues. Consequently, for negative α, a high quasiperiodicity strength is required to achieve localization as there are many nearby wavefunctions (having similar, high energies) that overlap thus being likely to produce an extended state. Low energy states, in contrast, are fewer and further apart thus leading to localization even for weaker quasiperiodicity. Since changing the sign of α inverts the distribution of low and high energy states, we expect the opposite localization trends, as in Fig. 11.2 (c), by the same argument. We have previously exhibited this inverse localization-delocalization behavior when comparing the two states in Chapter 10 by using the transfer matrix formalism; Fig. 10.6 illustrates it in the language of Lyapunov exponents.

We proceed to discuss the effects of interactions between condensed atoms that are relevant for localization-delocalization physics as most clearly evidenced by the experimental observations in the $\alpha = 0$ limit. To pin-point these effects, we turn to numerical simulations.

11.4 Effect of interactions

In this Section, we discuss the effects of interactions between atoms in the momentum-space lattice experimental realization of the GDP model. They are an important factor for its localization-delocalization physics and contribute to the emergence of mobility edges. In particular, as we comment below, in the absence of interactions mobility edges can be tuned by the parameter α while for $\alpha = 0$ they are purely a consequence of the presence of inter-atomic interactions. We elaborate on this finding by considering experimental results and numerical simulations carried out with realistic experimental parameters.

The interactions between atoms in the various momentum orders interacting through s-wave collisions [167] is in general given by

$$H_{\text{int}} = (U/2N) \sum_{i,j,k,l} c_i^\dagger c_j^\dagger c_k c_l, \tag{11.14}$$

where $U = g\rho$ is the mean-field interaction energy per atom for N atoms occupying the same momentum state. Here ρ is the atomic number density and $g = 4\pi\hbar^2 a_s/M$ captures interactions term as in Sec. 2.1 (M is the atomic mass, and a_s the scattering length for ^{87}Rb atoms).

As written, Eq. 11.14 relates to a spatially uniform density ρ and mean-field energy U. For the one-dimensional configuration of coupled momentum states employed by the Gadway group, only collisions that do not change the momentum mode occur within the set of states considered. Furthermore, mode-changing collisions out of this subspace are highly suppressed relative to these mode-conserving collisions. When com-

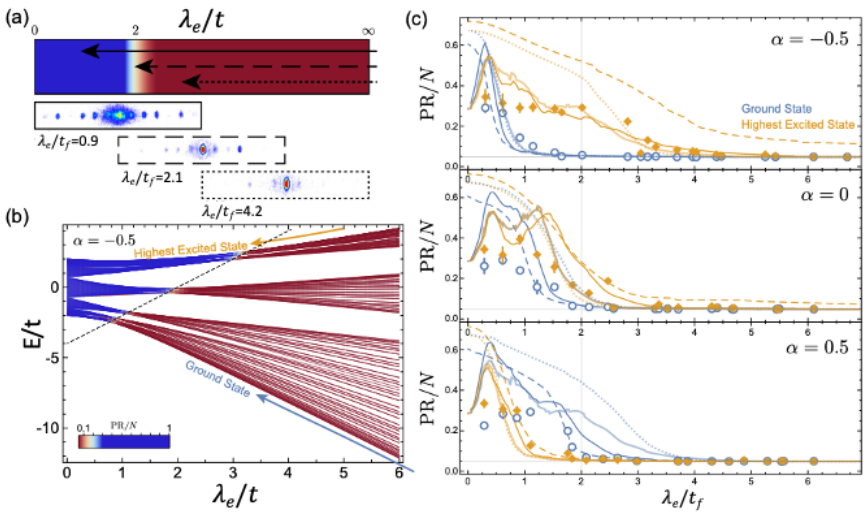

Figure 11.2: **(a)** Cartoon of effective experimental sequence for the Gadway group study: population of condensed atoms starts as fully localized in the high disorder regime ($\lambda_e/t \gg 2$), the tunneling between lattice sites is then slowly tuned to some final value λ_e/t_f. This procedure may cross a transition to a delocalized regime, pictured here at $\lambda_e/t_{\rm crit} = 2$ for $\alpha = 0$. In the experiment, tunneling is ramped linearly from 0 to t_f over 0.75 ms, while λ_e is held fixed. The population is imaged after another 1.25 ms duration. Population is shown, from left to right, for the highest energy state under λ_e/t_f ending in the delocalized metallic regime ($\lambda_e/t_f = 0.9$), near the transition ($\lambda_e/t_f = 2.1$), and in the localized regime ($\lambda_e/t_f = 4.2$). **(b)** Eigenenergies of a 21-site GPD model lattice with uniform tunneling values t, for $\alpha = -0.5$ and $\phi = \pi$. Colors represent the participation ratio (PR) of each eigenstate, where blue is delocalized (high PR) and red is localized (low PR). Initially, atom population is in the ground state of the $t = 0$ Hamiltonian (bottom curve) and follows this state through the ramp, ending in the ground state of the full Hamiltonian ($t \neq 0$). By setting $\phi = 0$, atom population is initialized in the highest energy state so that its localization-delocalization physics is observed as well (top curve). **(c)** PR/N vs. λ_e/t for the lowest energy state (open blue circles) and the highest energy state (yellow diamonds) under $\alpha = -0.5, 0, 0.5$. This plot shows evidence for a parameter-tuned mobility edge as the two states localized at different λ_e/t when α is varied. Dashed lines represent eigenstates under a homogeneous mean-field energy $U = 300$ Hz calculated with imaginary time propagation, and solid lines show numerical tight-binding simulations including the tunneling ramp taking either $U = 0.48t$ (thin solid) or $U = 0$ (thick solid) used in experiments.

paring theoretical treatment and experimental measurements, we consequntly make the simplifying assumption to only consider mode-conserving collisions. Furthermore, the typical occupation of the experimental momentum modes – the 21-site momentum-space lattice – is large, such that $|\langle c_i \rangle| \approx |\langle c_i^\dagger \rangle| \approx |\psi_i| \times N$. This makes it appropriate to theoretically treat interactions through a mean-field Gross-Pitaevskii formalism, where the normalized complex wave function ψ is a solution of the corresponding non-linear Schrodinger equation. In other words, for this experimental system more general, mode-dependent interactions can be effectively recast as a purely local intra-mode attraction, with scale $U = g\rho$. This treatment ignores many details of the experiment (like the non-uniform atomic density, quantum correlations, additional mode-dependence to the interactions due to superfluid screening [167], and changes to the real-space atomic distribution throughout the dynamics), but it does succesffuly provide a simple mean-field-level comparison

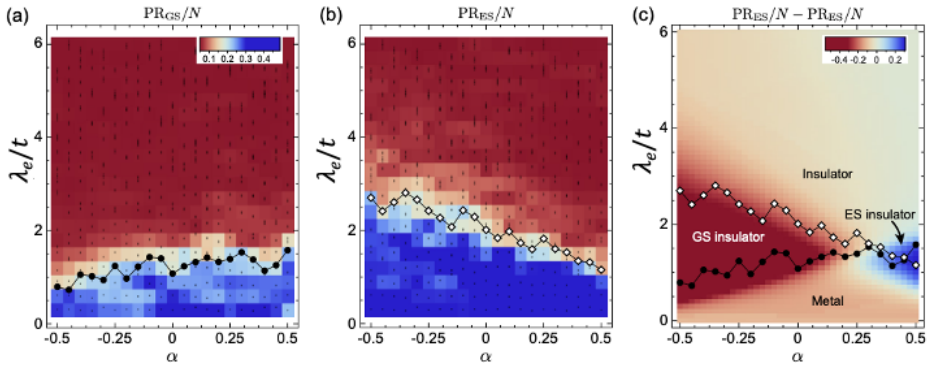

Figure 11.3: **(a,b)** Two-dimensional phase diagrams showing PR vs. λ_e/t and α for the (a) lowest energy state (marked as GS) and (b) highest energy state (marked as ES) of the GPD system. Filled circles and open diamonds mark the "critical" disorder for each α value, calculated by finding where the PR decreases below a threshold $\mathrm{PR_{thres}} = 0.19$. **(c)** Critical disorder values for the lowest energy state and highest energy state cases (filled circles and open diamonds, respectively), overlaid on interacting eigenstate simulation results (obtained through imaginary time propagation) showing the difference in PR between the two states (in color). The critical disorder "lines" do not coincide, showing a mobility edge. They cross away from $\alpha = 0$ due to screening and self-trapping effects stemming from inter-atomic interactions. The two states exhibit opposite localization trends as α changes sign.

that captures most of the salient features.

Concretely, we implement this Gross-Pitaevskii treatment by carrying out numerical simulations via the imaginary time propagation method. Prior to discussing numerical findings for the interacting GPD model, and their comparison with experimental measurements, we first review this method itself.

11.4.1 Imaginary time propagation

Imaginary time propagation primarily consists of substituting complex, imaginary time for real time in the time-dependent Schrodinger equation. In this way the Schrodinger problem can be reformulated so that all energy states except the one having the lowest energy eigenvalue i.e. the ground state of the system being studied, decay exponentially. In other words, the imaginary time calculation yields an approximation for the ground state wavefunction and its corresponding energy.

To derive this method we start with a basic quantum mechanical formulation

$$i\hbar\partial_t\psi = H\psi \tag{11.15}$$

for H some Hamiltonian and the wavefunction ψ expressed as a sum of its eigenfunctions ψ_i (having energy eigenvalues E_i) in a standard way

$$\psi = \sum_i c_i \psi_i. \tag{11.16}$$

For each eigenfunction, Schrodinger equation expressed in terms of an imaginary time derivative reads

$$\partial_{it} \psi_i = -H\psi_i/\hbar = -E_i \psi_i/\hbar, \tag{11.17}$$

which is an equation solved by an exponentional wavefunction. Defining $\tau = it/\hbar$, we can further write

$$\psi_i(\tau) = e^{-\tau E_i}\psi_i(0) = e^{-\tau H}\psi_i(0) \tag{11.18}$$

$$e^{-\tau H} = \sum_{n=0}^{\infty} \frac{(-\tau)^n H^n}{n!}. \tag{11.19}$$

From Eq. (11.18) it is clear that when propagated in imaginary time each eigenfunction decays exponentially and the rate of that decay depends on its energy. Denoting the ground state as ψ_0 we then have

$$\frac{\psi_i(\tau)}{\psi_0(\tau)} \propto e^{-\tau(E_i - E_0)} \tag{11.20}$$

and conclude that all states having energies higher than that of the ground state vanish exponentially quickly. For some general state ψ then

$$\psi(\tau) = \sum_i e^{-\tau E_i} c_i \psi_i(0) \tag{11.21}$$

so that for imaginary time propagation, the coefficients $c_i e^{-\tau E_i}$ for the scattering components of the wavefunction approach zero while those corresponding to bound states approach infinity. Thus, starting with some trial wavefunction ψ the large τ limit yields a state proportional to the ground state wavefunction. More formally,

$$\psi(\tau) = c_0 e^{-\tau H}\psi_0(0) + \mathcal{O}(e^{-\tau(E_1 - E_0)}). \tag{11.22}$$

Additionally, if the overlap c_0 between the trial wavefunction and the ground state wavefunction is non-zero,

we can calculate the exact ground-state wavefunction as

$$\psi_0(0) = \lim_{\tau\to\infty} \frac{\psi(\tau)}{\sqrt{\psi(\tau)|\psi(\tau)}}. \tag{11.23}$$

As discussed above, the experimental method used to study the GPD model allows for observations of the behavior of not only the ground state but also the highest excited state of the system. To target this state we adapt the imaginary time propagation method with $\tau \to -\tau$. Further, all of our simulations are iterative in the sense that once this approach has been applied to the trial wavefunction, the resulting approximate ground (highest excited) state is used in place of that trial wavefunction in the next simulation run. This approximate state is appropriately normalized at the end of each calculation (before being used as the next trial wavefunction) so that the iterative process does not result in erroneously large wavefunction amplitudes. Typically we carry out on the order of 100 loops.

We employ imaginary time propagation for timescales 10 or more times larger than the timescale associated with the tunneling amplitude t to ensure reasonable convergence to the ground (highest excited) state of the GPD system. In all simulations, our trial wavefunction is simply evenly distributed across all lattice sites and system size is taken to be either 51 sites (Fig. 11.4 (c) and (e)) or 21 sites (Fig. 11.2 (c-e) and Fig. 11.3 (c)). By chosing this wavefunction form for the first "guess" we ensure that there will be some overlap with the true system eigenstate regardless of its localization character.

To account for the presence of interactions between the atoms, we use a Hamiltonian corresponding to the Gross-Pitaevskii equation, Eq. (2.10). In other words, we include a term akin to $-U|\psi(\mathbf{r})|^2\psi(\mathbf{r})$ where U depends on the s-wave scattering length as in Eq. (2.7). This treatment of interacting BEC, as we have previously outlined, is essentially a mean-field approach. We chose values of U in accordance with experimental data, expressed in units of t (typically $U = 0.48t$). Each step in the iterative process employs the $|\psi|^2\psi$ form calculated in the previous application of the imaginary time scheme.

11.4.2 Shifting of mobility edges

Having elaborated on the imaginary time numerical technique we use to simulate the (mean-field) interactions in the GPD model, we proceed to discuss the results of these simulations and how they compare to experimental findings.

First, we note that as the $\alpha = 0$ case reduces to the standard AA model. In the absence of interactions, all energy eigenstates for this value of α should undergo a delocalization transition at the same critical value of $\lambda_e/t = 2$. In other words, we anticipate localization behavior illustrated in Fig. 11.4 (d). However, as

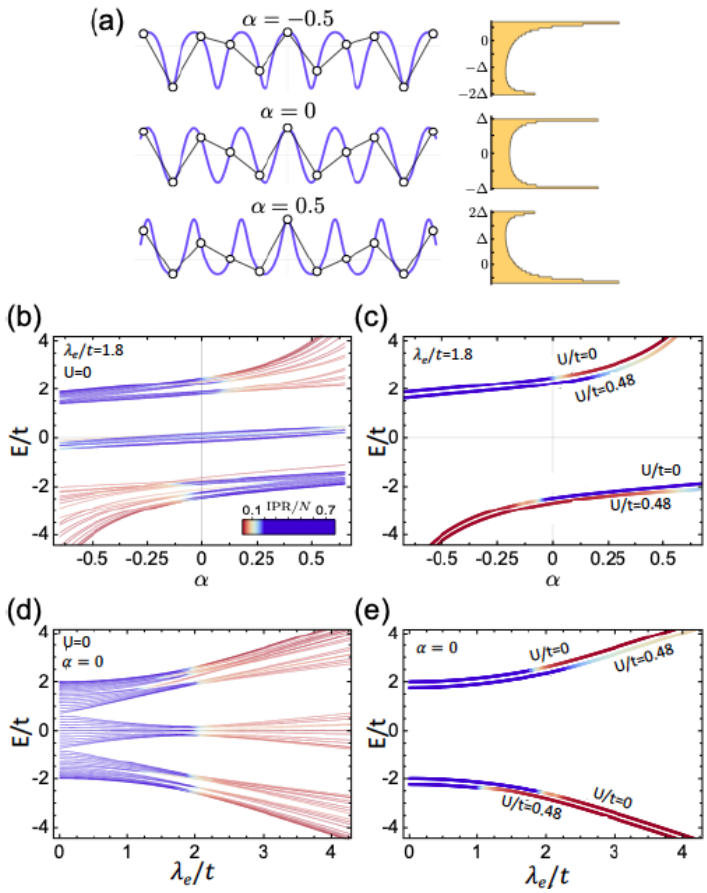

Figure 11.4: **(a)** Potential of GPD model for $\alpha = -0.5, 0, 0.5$, with corresponding distributions of lattice site energies. **(b)** Calculated eigenenergies and participation ratios (PRs) vs. α for a non-interacting model just below the critical quasiperiodicity strength at $\lambda_e/t = 1.8$ ($N = 51$ sites). Away from $\alpha = 0$, eigenstates localize at different energies, forming a mobility edge. **(c)** Same parameters as (b), showing lowest and highest energy eigenstates for an interacting model, calculated using imaginary time propagation. Under a uniform mean-field interaction strength $U/t = 0.48$, the mobility edge moves towards lower energy values as evidenced by the lowest energy state being localized for nearly all α values when $U \neq 0$. **(d)** Calculated eigenenergies and participation ratios (PRs) vs. quasiperiodicity strength λ_e/t for a non-interacting model at a fixed $\alpha = 0$ ($N = 51$ sites). This plot depicts the physics of the standard AAH model so there are no mobility edges and all energy states undergo a localization transition (color-coded as a change from blue to red) for the same λ_e/t value. **(e)** Same parameters as (d), showing lowest and highest energy eigenstates for the interacting GPD model, calculated using imaginary time propagation. Though setting $\alpha = 0$ describes the AAH model, presence of nonlinear inter-atomic interactions results in different localization physics for the two depicted states, in contrast to (d).

shown in the central panel of Fig. 11.2 (c), experimental measurements inidicate that the transition in fact splits for the lowest and highest energy states, signalling a mobility edge that arises solely from interactions between atoms in the momentum-state lattice [168, 167]. Repulsive interactions are stronger between atoms in different momentum modes than for atoms within the same mode, due to the added contribution Effective attarctive interactions have distinct influences on the low and high energy states, respectively. The same

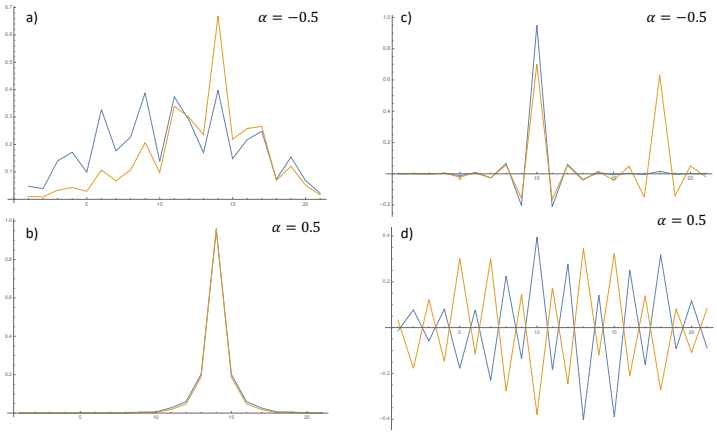

Figure 11.5: **(a,b)** Plot of the spatial profile of the wavefunction corresponding to the lowest energy state of the GPD model, calculated by the imaginary time propagation method with realistic experimental parameters and $\lambda_e/t = 0.9$. The calculation carried out in the absence of inter-atomic interactions is shown in blue while the interacting simulation produced the curve depicted in yellow. Here, for negative α in **(a)** the wavefunction is more peaked for $U \neq 0$ leading to lower PR values. As discussed in the text, for positive α in **(b)** this effect is significantly less prominent. **(c,d)** Plot of the spatial profile of the wavefunction corresponding to the highest energy state of the GPD model, calculated and color-coded as in **(a,b)**. Here, the effect of changing the sign of α is rather dramatic, leading to low PR values for $\alpha < 0$ in **(c)** and high PR values for for $\alpha > 0$ in **(d)**.

effect is captured through numerical simulations in Fig. 11.4 (e). Here it is evident that the ground state achieves low PR values for values of λ_e/t lower than in the non-interacting model while the opposite is true for the highest excited state which is characterized by relatively high PR values for virtually all α in the presence of interactions. For states at low energy, the chemical potential shifts due to interactions further inhibit delocalization in the synthetic lattice. This instability towards self-trapping for attractive interactions [169] shifts the ground state localization transition towards lower quasiperiodicity strengths. In general, it is known in the literature [168, 170, 171] that nonlinear interactions in optical lattices can lead to spontaneously localizing excitations, what we refer to as self-trapping. In contrast, for states at high energy, attractive interactions can effectively screen the GPD quasiperiodic potential, leading to enhanced delocalization. We remark that this screening by attractive interactions for high energy states proceeds in much the same manner as the screening by repulsive interactions for low energy states [169, 172]. As shown in Fig. 11.2 (c), these qualitative considerations are in good agreement with the shifts of the localization transitions of the ground state and highest excited state observed in the experiment and our theoretical calculations.

As in our previous arguments for the effect of changing the sign of α, we recall that for $\alpha < 0$ there are more high energy states while for positive α there are more low energy states in the spectrum of the GPD model. Fig 11.5 shows the effect of interactions on the ground state and the highest excited state of

the system calculated by the imaginary time propragation method. For these calculations, we fix λ/t at a value such that for the $\alpha = 0$ the system would be approaching its fully localized regime for any increase in quasiperiodicity strength. In the presence of interactions and negative α, the highest excited energy state can then be a superposition of states at lattice sites that are close to U in energy. Hence we see mostly extended states for all negative α in Fig. 11.4 (c) and the same trend persists even as this parameter takes on small positive values due to screening.

For $\alpha = +0.5$ (bottom of Fig. 11.2(c)), experimental data show an inversion of the mobility edge: the excited state localizes at a weaker quasiperiodicity amplitude than the ground state. This inversion is expected due to a symmetry of the non-interacting Hamiltonian (H_{GPD}) that exchanges the lowest and the highest energy state as $\alpha \to -\alpha$, further highlighting that the GPD mobility edge is parameter-tunable with respect to α. However, as the experiment demonstrates, while there is still an inversion of the mobility edge, this symmetry is strongly broken for $\alpha = +0.5$ as the ground state localization transition is strongly shifted relative to the highest excited state at $\alpha = -0.5$ (top panel of Fig. 11.2 (c)). This is a clear manifestation of many-body (interaction) effects on the localization transition: the interacting model has an enlarged symmetry that requires $U \to -U$ for $\alpha \to -\alpha$. Last, we observe that the ground state transition for $\alpha = +0.5$ is significantly shifted away from the non-interacting limit, demonstrating another signature of interaction effects in the experimental study.

Overall, the qualitative agreement between experimental data and simulation curves is rather good, though we note that the calculated behavior of the highest excited state for $\alpha = -0.5$ deviates from both the data and numerical simulations. For this α value, we have seen in Fig. 11.4 (a) that there are many lattice sites lying at high energy, and that the role of interactions is to screen the quasiperiodic potential. Taken together, this results in the highest energy state being localized and restricted to the highest energy sites for large λ_e/t, but still populating multiple high energy sites whose site energy differences fulfill $\lambda_e \epsilon \lesssim U$.

Figure 11.3 provides a more comprehensive picture for the localization properties of the low- and high-energy states prepared by our loading procedure over a range of α and λ_e/t values. We plot the measured PR values for these states (on a color scale, based on data sampled at parameter values corresponding to the overlaid black points) as a function of the quasiperiodicity strength λ_e/t and the parameter α that controls the precise shape of the GPD potential. The state preparation ramp, starting from the infinite disorder limit, is the same as described for Fig. 11.2. The black line-connected data points in panels (a) and (b) denote the critical λ_e/t values, determined for each α column by determining where the PR exceeds a threshold value set to 0.19. The shift of the delocalization transition for these two states show opposite trends as the GPD tuning parameter α is varied, consistent with our previous discussion. The lowest and highest excited state

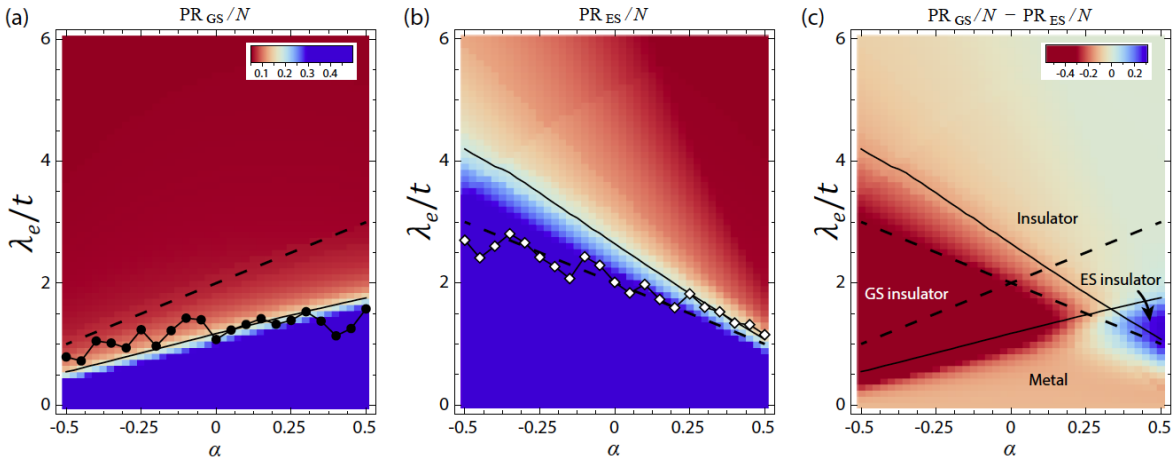

Figure 11.6: **Numerical simulations of localization phase diagrams.** The color in (a,b) represents PR/N of the interacting eigenstates calculated by imaginary time propagation. The line-connected black circles and white in (a) and (b) are the transition curves found for the lowest and the highest excited state from experiment, as in Fig. 11.3. Dashed lines represent the non-interacting transition lines determined based on the mobility edge relation Eq. (10.18). Solid lines represent the critical λ_e/t transition values, as determined for the interacting eigenstates (for $U = 0.48J$) by determining where PR/N crosses the threshold value of 0.19. (c) The color shows the difference in the PR/N for the lowes and highest excited state with interactions. Overlaid on this PR difference diagram are the theoretical critical delocalization boundaries, from (a) and (b).

critical delocalization boundaries are plotted together in panel (c), showing a crossing for values of $\alpha \sim 0.3$. Also shown, underneath, is the numerically determined difference in PR of the calculated (by imaginary time propagation) low- and high-energy eigenstates for an interaction energy $U/t = 0.48$ ($U/h = 300$ Hz). Taken together, these plots can be viewed as the localization diagram for the two extremal states of the interacting model characterized by Eq. (10.17) and $U/t = 0.48$.

Further, Fig. 11.6 shows the numerically-calculated (by imaginary time propagation) localization phase diagrams for the eigenstates of the interacting GPD model, assuming a homogeneous mean-field interaction energy $U = 0.48J$. Along with the simulation results, we show experimental transition curves as in Fig. **??** for comparison (circles and diamonds indicate critical λ_e/t values for the ground and highest excited state, respectively). The background color in Figure 11.6 (a,b) represent the PR/N for the lowest state and the highest excited state. Dashed lines indicate the expected $U = 0$ transition lines of $(\lambda_e/t)_c = 2(1 \pm \alpha)$ for the lowest (highest excited) state, anticipated based on the GPD mobility edge relation of Eq. (10.18). Solid lines show critical λ_e/t values for the *interacting* eigenstates (calculated by imaginary time propagation), determined by comparison to a threshold value of PR/N. The discrepancy between the dashed (non-interacting) and solid (interacting) lines underscores the shifting of the mobility edge due to interactions.

As the experimental data for the lowest energy state agrees with the interacting theory curves, we

conclude that we see clear effects of self-trapping in experiment. In contrast, for the highest excited state (in particular for $\alpha \lesssim 0$), experimental results align more with the expected non-interacting transition curve than the one incorporating screening effects. This signifies that the experimental state preparation procedure used was likely unable to capture the exact behavior of the true highest escited state across the full parameter space, due to initial conditions and the effects of screening on the true excited state.

In experiment, atomic population was initialized on only one lattice site. Then the tunneling t was ramped from zero to some final strength. As the quasiperiodicity amplitude λ_e was fixed for each ramp, this effectively ramped from the limit $\lambda_e/t = \infty$, where all eigenstates are site-localized in the absence of interactions, to some final λ_e/t value. However, the existence of a fixed interaction strength U throughout the ramp, and thus a non-zero U/λ_e, makes it difficult and unlikely to prepare the true highest energy eigenstate by using this experimental procedure. A more ideal ramp procedure would lower both λ_e/t and λ_e/U from the infinite quasiperiodicity limit, to account for the fact that population needs to spread from the initial single site due to screening. This experimental ramping procedure, however, was not a problem for the ground state preparation, as the effectively attractive interactions promote self-trapping for low-energy states.

11.5 Conclusions and outlook

In this Chapter, we have presented an experimental study [161] investigating a one-dimensional quasiperiodic system having a mobility edge and modeled nonlinear interactions between atoms through numerical simulations. This collaborative work with the Gadway experimental research group presents a strong starting point for future work focusing on both mobility edges and realistic qusiperiodic models. Observations that we have enumerated here imply the existence of the mobility edge in the GPD model that has so far only been studied theoretically and highlight the importance of inter-atomic interactions that has not been addressed beyond our numerical work yet. Arguing in the spirit of self-trapping and screening, we have concluded that interactions shift mobility edges in such a way that the lowest energy state of the system localizes for lower quasiperiodicity strengths while the highest energy state exhibits the opposite trend. This observation holds for the AAH model of Eq. (10.1) as well and has been strengthened by the same trends being evident in numerical simulations and calculations employing imaginary time propagation.

As this work only addresses localization-delocalization physics of the two extreme states of the GPD model, it is of great future interest to probe and observe more intermediate energy states and their response to differing values of quasiperiodicity stregth and interactions between the atoms. Experimentally, this could

be achieved by implementing counterdiabatic driving [161] to lengthen observation timescales. This may allow for precise determination of the energy of the mobility edge in this and other quasiperiodic models. Furthermore, by variation of the phason (ϕ) and incommensurability (b) parameters of the AA model, such experimental improvements should make it possible to explore the dimensionally-reduced Hofstadter model and it's butterfly energy spectrum [133, 173]. Future theoretical approaches may be related to our work with the transfer matrix foralism and its representation with toroidal curves discussed in Chapters 10 and 9.

In the next two Chapters, we focus on topological ladder models comprised of Su-Schrieffer-Heeger chains. We study the existence and robustness of localized edge modes, the physics of disorder and quasiperiodicity when those modes are present and connect with experimental studies in reconfigurable, classical meta-materials.

Part III: Topological Ladder Models

Chapter 12

Topological phases, edge modes, and the Hofstadter butterfly in coupled Su-Schrieffer-Heeger systems

12.1 Introduction

The advent of the Su-Schrieffer-Heeger (SSH) model [174, 175] as a description of organic chains was a milestone in the study of condensed matter systems as it offered one of the first realizations of charge fractionalization. It was shown that a simple tight-binding chain having two different alternating bond strengths between lattice sites hosts localized bound states at its edges, enabling fractionalization for charge at these ends. Subsequently, the model has been studied as a prototype for fractionalization and associated topological properties characterized by band-structure based invariants and localized edge modes. Recent experimental developments in diverse disciplines, ranging from photonic to mechanical setups, have revealed aspects of the SSH model and related systems in a variety of fascinating ways. In cold atomic setting, measurements of topological invariants, such as the Zak phase have been performed [176]. Further, topologically robust charge pumping has been observed in such systems [177, 178, 179]. Here, the transported charge is quantized and solely determined by the topology of the pump cycle. Equally striking, topological systems carrying dispersionless edge modes have been realized in magneto-optical photonic crystals [180], classical acoustic meta-materials [181, 182] and even tunable mechanical systems of granular particles [183]. The solitonic state distinguishing the topological phase of the SSH model in particular, has also been observed in cold atomic systems [184, 185] through time-of-flight imaging and in photonic quantum walks [186].

Here, we show that the simplest of next steps in these studies—coupling two SSH chains [187, 188, 189, 190, 191, 192]— gives rise to rich behavior. We investigate salient features of such "SSH ladder systems", theoretically studying several physical properties with an eye towards realizing them in the experimental settings ranging from ultracold atomic and photonic studies to experiments involving meta-materials. This work has previously been collected and presented in Ref. [193] and is a product of collaboration with Drs. Suraj S. Hegde and Wade DeGottardi as well as Prof. Smitha Vishveshwara. The discussion presented here is based on this publication.

In this Chapter, we chart out the phases exhibited by the the SSH ladder and the phase boundaries

separating them as characterized by a gap in the energy spectrum. We determine the topological nature of these phases. Further, we identify the nature and behavior of bound states localized at the ends of the ladder which ought to be realizable in cold atomic, photonic and mechanical settings. We focus on three noteworthy aspects of the SSH ladder. i) The most general phase diagram for the SSH ladder hosts phases that go beyond that of a single chain. These phases show the distinction between completely trivial phases characterized by the absence of edge modes, robust topological phases having topologically protected edge modes, and an intermediate coupling regime having unprotected edge modes (analogous to a weak topological insulator). ii) The SSH ladder can act as a model of the Kitaev wire by mimicking its traits in the sense of the Kitaev wire hosting Majorana bound states, which have historically been of much interest and continue to drive new research. iii) The SSH ladder system has enough degrees of freedom to exhibit marked effects of inhomogeneous couplings—in the case of quasiperiodicity its topological phase diagram exhibits multifractality.

In motivating the work presented in this Chapter, we particularly stress parallels between the SSH ladder and the Kitaev chain. The Kitaev chain [194] has come to the forefront as a key model for capturing essential features of topological superconductors. A distinctive feature of the model is a clean phase diagram separating trivial phases from topological ones in which the chain harbors end bound states. These states are, in the case of the Kitaev chain, the right combination of particle-like and hole-like excitations for forming charge neutral Majorana fermionic states. The phase diagram for the Kitaev chain, the nature of edge modes and their experimental realization have been thoroughly studied and the Majorana edge states themselves are known to have unique properties [194, 195, 196, 197, 198]. For the Kitaev chain, a basis can be chosen so that the system admits a ladder description [199]. Remarkably, we find that the SSH ladder is capable of mimicking this Kitaev chain ladder when subject to restricted intra-chain couplings. Below, we demonstrate how these parallels become manifest. A significant distinction is that the bound states of the SSH ladder are not Majorana fermions but number-conserving states, either fermionic or bosonic in nature. Nevertheless, the SSH ladder provides a concrete experimentally realizable system that can map the phase diagram for the Kitaev chain and the spatial structure of its localized bound edge states.

Extensive work on the Kitaev chain has revealed the manner in which inhomogeneities can greatly alter topological phase diagrams, for instance, periodic variations or disorder [199]. Borrowing from these insights, we show that indeed spatially varying couplings in the SSH ladder system can produce dramatically different phase diagrams. We employ a transfer matrix technique to directly target the fate of localized end modes in the presence of such spatial variations. Further, we find that quasiperiodic variations across the ladder reflect the mathematical structure of Harper's equation and its physical manifestation in Hofstadter's

butterfly pattern [133] – one of the most well-known examples of fractals in condensed matter physics. While cold atomic systems are well suited for clean achievement of such self-similar patterns (otherwise experimentally rather challenging in electronic systems), experiments concerning the Hofstadter Hamiltonian so far [200, 155, 201, 154] have not included any direct measurements of its fractal nature. As the topological phases of the SSH ladder can be identified through direct observation of edge wavefunction spatial profiles, our proposal provides a novel possibility of probing this fractal diagram through time-of-flight imaging.

This Chapter is organized as follows. In Sec. 12.2 we introduce the SSH ladder Hamiltonian and outline the use of the momentum space dispersion relation, the chiral index topological invariant and the tranfer matrix formalism in obtaining its phase diagram. In Sec. 12.3 we briefly review the properties of a single, uncoupled, SSH chain and proceed to discuss the more complex phase diagram of the coupled system in Sec. 12.4. In this Section, we identify three distinct regimes (topological, topologically trivial and weakly topological) as determined by differing edge mode structures. In Sec. 12.5 we focus on the phase of the ladder hosting edge modes with wavefunctions having spatial profiles matching those of the localized Majorana modes of the Kitaev chain. Further, in Sec 12.6 we employ transfer matrix methods to discuss the response of this Kitaev chain analog phase to inhomogenous couplings, disorder and quasiperiodicity. Finally, in Sec. 12.7 we bring our discussion closer to experimental studies of SSH models by considering finite size effects and offer an outlook on possible future experimental work in Sec. 12.8. One specific possibility for such work is explored in more detail in Ch. 13.

12.2 Model and Methods

The system at the focus of this Chapter, shown in Fig. (12.1), is a fermionic ladder composed of two coupled SSH chains. It exhibits a particle-hole symmetry due to the bipartite nature of its Hamiltonian. Consequently, its energy spectrum is symmetric about zero energy. As detailed in Sec. 12.5, when the inter-chain and intra-chain couplings within the ladder respect certain constraints, the system is a close analog to the celebrated superconducting Kitaev chain. In this case, particle-hole symmetry is a natural consequence of superconductivity, as captured by the Bogoliubov-de Gennes form of the Kitaev chain Hamiltonian. The close relationship between the two systems gives rise to a clear correspondence between their respective topological phases. However, in this Chapter we show that rather than hosting Majorana fermions, the topological phases of the SSH ladder are characterized by Dirac fermions localized at the system edge. As detailed in Sec. 12.4, the more generalized ladder system shows a rich phase diagram. Further, several of single-particle properties studied in what follows apply to bosonic systems as well. Some similar models have

been explored in Ref. [187, 188, 189].

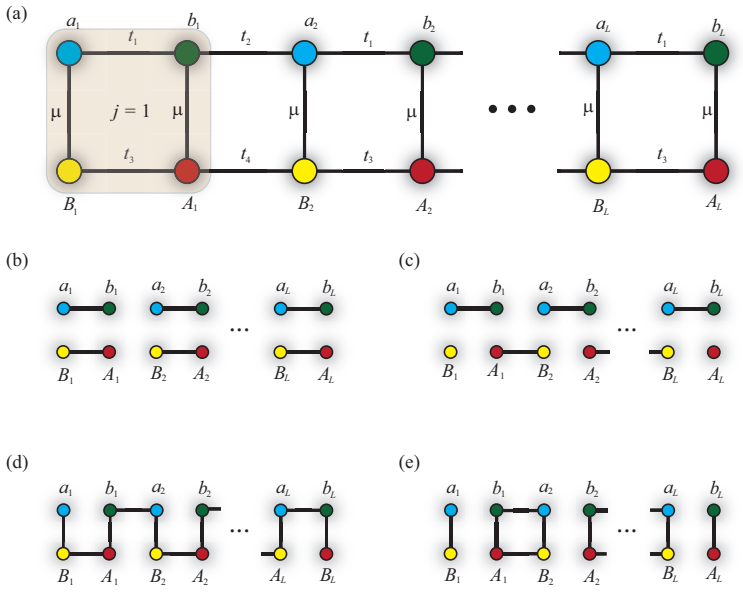

Figure 12.1: Pictorial representation of the fermion couplings in the SSH ladder model, as represented by the Hamiltonian of Eq. (12.1) for **(a)** generic couplings, for the decoupled case havin $t_2 = t_4 = 0$ where the two legs of the ladde are made-up of dimers only in**(b)**, in **(c)** for the decoupled case with the special values of couplings $t_2 = t_3 = 0$ characterized by $N_S = 1$ exhibiting a single fermion end mode, **(d)** coupled SSH ladder for $t_1 = t_4 = 0$ and $t_2 = t_3 = t$. For $|\mu| < 2|t|$, the system exhibits a Kitaev-like topologically protected zero mode. **(e)** For $t_1 = t_3 = 0$ and $|\mu| \ll t_2, t_4$, the system exhibits mid-gap states that are not topologically protected.

12.2.1 Model

The unit cell for the SSH ladder is a plaquette composed of four fermions: for the j^{th} plaquette, the operators a_j, b_j are fermion annihilation operators for sites on the top leg (SSH chain), while the operators B_j and A_j reside on the bottom leg (SSH chain). The Hamiltonian is given by

$$H = \sum_j (t_1 b_j^\dagger a_j + t_2 a_{j+1}^\dagger b_j + t_3 A_j^\dagger B_j + t_4 B_{j+1}^\dagger A_j + \text{h.c.}) + \mu \sum_j (a_j^\dagger B_j + b_j^\dagger A_j + \text{h.c.}). \tag{12.1}$$

It is characterized by five real couplings: four hopping amplitudes t_1, t_2, t_3, and t_4 and an inter-chain coupling μ. The system is bi-partite in that it decouples into two interpenetrating sub-lattices, a/A and b/B coupled to each other but not within themselves. This bi-partite nature of the model guarantees that the

spectrum respects particle-hole symmetry. Fourier transforming Eq. (12.1) yields

$$H_k = \frac{1}{2}\tau_z \otimes [((t_1 - t_3) + (t_2 - t_4)\cos k)\sigma_x + (t_2 + t_4)\sin k\, \sigma_y] + \frac{1}{2}\mathbb{I} \otimes [((t_1 + t_3) + (t_2 + t_4)\cos k)\sigma_x + (t_2 - t_4)\sin k\sigma_y] + \mu\tau_x \otimes \sigma_x \tag{12.2}$$

where the Pauli matrices τ_i and σ_i act in the ladder leg and ladder sublattice spaces, respectively.

Our analyses of the phases of the SSH ladder and their properties primarily employ three methods. First, for systems respecting translational invariance, energy dispersions obtained in momentum space identify gapless energy contours which delineate phase boundaries. Second, a topological invariant enables us to identify topological aspects of the phases. Finally, as a third method, the transfer matrix technique charts out the existence and nature of possible localized end bound states in some phases through Lyapunov exponents. We proceed to elaborate on each of these methods.

12.2.2 Dispersion

First, to establish phase boundaries, we consider the dispersion relation corresponding to Eq. (12.2). Contours in parameter space along which the bulk energy gap closes delimit different phases of the system. In the most general case, the SSH ladder has a four-band energy dispersion

$$E^2 = \mu^2 + \frac{1}{2}(|\rho_1|^2 + |\rho_2|^2) \pm \frac{1}{2}\sqrt{(2\mu^2 + |\rho_1|^2 + |\rho_2|^2)^2 + 4(\rho_1\rho_2 - \mu^2)(\mu^2 - \rho_1^*\rho_2^*)} \tag{12.3}$$

where

$$\rho_1 = \rho_1(k) = t_1 + t_2 e^{-ik}$$
$$\rho_2 = \rho_2(k) = t_3 + t_4 e^{+ik}. \tag{12.4}$$

Here, the gap in the energy spectrum closes at $k = 0$ for $\mu^2 = (t_1 + t_2)(t_3 + t_4)$ while the same happens for $\mu^2 = (t_1 - t_2)(t_3 - t_4)$ and $k = \pi$. Additionally, the energy spectrum is gapless for $t_1 t_4 = t_2 t_3$ and $k = (1/2)\cos^{-1}(\mu^2 - t_1 t_3 - t_2 t_4)/(t_1 t_4 + t_2 t_3))$.

Following Ref. [202], we parameterize the couplings in Eq. (12.1)

$$t_1 = (t + \Delta)(1 - \eta),\ \ t_2 = (t - \Delta)(1 + \eta),$$
$$t_3 = (t - \Delta)(1 - \eta),\ \ t_4 = (t + \Delta)(1 + \eta). \tag{12.5}$$

with $|\eta| < 1$ and $|\Delta| < t$. In Sec. 12.4, we offer a physical interpretation for these two parameters in terms of competing energy gaps. Various topological and topologically trivial phases of the ladder are separated by regions in the (μ, Δ, η, t) parameter space satisfying

$$\begin{aligned} &\mu^2 = 4(t^2 - \Delta^2\eta^2), \\ &\mu^2 = 4(t^2\eta^2 - \Delta^2), \text{ for } t|\eta| > |\Delta| \\ &\Delta = 0. \end{aligned} \tag{12.6}$$

12.2.3 Topological invariant

Phases of the SSH ladder can be characterized by a topological invariant. The over-arching Hamiltonian of Eq. (12.1) belongs to the BDI symmetry class and has phases described by a $\mathbb{Z}-$valued topological invariant. Following Refs. [203, 202] we consider the chiral index associated with a generic symmetry operator S with the properties $SH_kS^{-1} = -H_k$, $S^2 = \mathbb{I}$. The topological invariant is given by

$$N_S = \mathrm{Tr} \int_{-\pi}^{\pi} \frac{dk}{4\pi i} S g^{-1} \partial_k g \tag{12.7}$$

where $g(k) = H^{-1}(k)$ is the Green's function at zero energy.

12.2.4 Transfer matrix

The transfer matrix formalism extensively used in studies of localized states in 1D systems, especially in the presence of complex potential landscapes, is applicable to this ladder model as well. We employ this formalism to study the effects of spatial modulation of the inter-chain coupling μ in Sec. 12.6. This method has been further developed as a tool in studies of Majorana modes in the Kitaev wire by two of our collaborators in Refs. [196, 199, 204].

Within this formalism, the presence of localized zero energy edge modes is determined by the growth or decay of the eigenfunctions of the transfer matrix. To construct the matrix, we start with the zero-energy Heisenberg equations of motion, $[a_j, H] = 0$, $[b_j, H] = 0$, for

$$H = -\sum_j [t_1(b_{j+1}^\dagger a_j + B_{j+1}^\dagger A_j) + t_2(a_{j+1}^\dagger b_j + A_{j+1}^\dagger B_{2,j})] + \sum_j \mu_j a_j^\dagger B_j + \text{h.c.}$$

where the inter-chain coupling μ_j now varies throughout the ladder. The zero energy equations of motion couple the a_i and A_i fermions and the b_i and B_i fermions, but these two sets of equations have no mutual

couplings. The equations of motion for operators a_j are second-order difference equations of the form

$$t(1+\delta)a_{j-1} + t(1-\delta)a_{j+1} + \mu_j A_j = 0. \tag{12.8}$$

Here we have taken $t_1 = t(1+\delta)$ and $t_2 = t(1-\delta)$ This can be cast into the form of transfer matrices:

$$\begin{pmatrix} a_{j-1} \\ A_j \end{pmatrix} = A_j \begin{pmatrix} A_j \\ a_{j+1} \end{pmatrix}, \; \mathcal{A}_j = \begin{pmatrix} \frac{\mu_n}{t(1+\delta)} & -\left(\frac{1-\delta}{1+\delta}\right) \\ 1 & 0 \end{pmatrix}. \tag{12.9}$$

Thus, the transfer matrix relates wavefunction amplitudes between one unit-cell-wide "slice" of the ladder and its adjacent one. Its multiplicative nature allows us to study the manner in which the wavefunction varies along the ladder. For localized states, such variation is an exponential decay and can be ascertained based on the eigenvalue structure of the transfer matrix. Such an analysis will be presented in more detail and used extensively in following Sections involving inhomogenous variations in the SSH ladder (Sec. 12.6).

12.3 Single SSH chain

Before discussing the intricacies of the full SSH ladder model, we recapitulate the properties of a single SSH chain having coupling t_1 and t_2. The chain possesses two topologically distinct phases. Here, the topological and trivial phases are characterized by the presence and absence of end zero modes, respectively. For instance, in the case in which $t_2 = 0$, and $t_1 \neq 0$, the system is described by pairs of coupled fermions. This corresponds to the top chain schematic in panel (c) of Fig. 12.1. In contrast, for $t_1 = 0$ and $t_2 \neq 0$, the system forms pairs of dimers with the exception of the modes a_1 and b_L, with L being the length of the ladder, which are left uncoupled to the rest of the chain. Such a configuration is akin to the bottom chain in in panel (c) of Fig. 12.1. More formally, the operators corresponding to the end modes commute with the single-chain Hamiltonian when $t_1 = 0$. Particle-hole symmetry guarantees that they are zero energy modes.

The existence of these end bound state fermions is protected by the existence of the bulk energy gap. Tuning away from the special case in which $t_1 = 0$, the end zero mode is a linear combination of modes near the edge of the system. These modes persist as long as the bulk gap does not close. The spectrum of the single SSH chain is given by $E = \pm\sqrt{t_1^2 + t_2^2 + 2t_1 t_2 \cos k}$, and thus the bulk gap closes at $k = \pm\pi$ for $t_1 = t_2$. This condition separates the trivial phase from the topological phases. For $t_1 > t_2 > 0$, the system is trivial. For $t_2 > t_1 > 0$, the system is topological and possesses a single Dirac fermion at each of its ends.

We note that our assignment of phases as topological and topologically trivial depends on where, within

the unit cell, we propose a measurement to detect the zero edge state should occur (where a "cut" occurs). In other words, determining the wavefunction spatial profile at a site off-set by half of the unit cell width would result in a different characterization of the phases of the SSH ladder. However, the two previously discussed phases, remain *topologically distinct* regardless. Below, we use a convention consistent with studying the zero mode wavefunctions at the left-most and right-most sites of the SSH ladder.

12.4 Phases of the SSH Ladder

As in our discussion of the phase diagram of the single, uncoupled SSH chain, the topology of the ladder system strongly depends on the relative strengths of the couplings t_1, t_2, t_3, and t_4. In this Section, we find three distinct physical regimes: a topological phase analogous to the Kitaev chain hosting localized zero energy edge modes, a topologically trivial phase and a regime analogous to a weak topological insulator having unprotected edge modes resembling a "twin-SSH" construction. To provide an intuitive picture for these phases, in considering Fig. 12.1, it is clear that in addition to a topologically trivial phase having no localized edge modes (Fig. 12.1 (b)) the SSH ladder can host a single localized mode at each edge (Fig. 12.1 (c)) or two pairs of localized modes at each edge as in Fig. 12.1 (e).

Parameters Δ and η introduced in Eq. (12.5) quantify the relative strengths of the various dimerization patterns the SSH ladder can exhibit. The quantity η is indicative of the relative strength of inter-plaquette and intra-plaquette couplings, while Δ is a measure of how strongly the upper and lower legs of the ladder have opposite dimerization patterns. In particular, increasing Δ, for $t, \Delta > 0$ tends to give rise to a single end mode on each end of the chain. This mode has weight on the a_i, A_i modes on the left-hand side of the chain and the b_i, B_i modes on the right-hand side. Similarly, decreasing Δ for $\Delta < 0$ tends to localize a single fermion with the roles of a_i, A_i and b_i, B_i interchanged. The parameter η treats the upper and lower legs symmetrically. For $\eta > 0$, there is a tendency to localize two fermionic modes to each end of the ladder.

The topological nature of the phases can be characterized by tailoring the topological invariant introduced in Eq. 12.7 to the SSH ladder. In particular, identifying $S = \mathbb{I} \otimes \sigma_z$, we obtain

$$N_S = -\int_{-\pi}^{\pi} \frac{dk}{2\pi i} \partial_k \log(t_1 t_3 + t_2 t_4 + t_2 t_3 e^{-ik} + t_1 t_4 e^{ik} - \mu^2). \tag{12.10}$$

The topological index N_S is thus the winding number of an ellipse in the complex plane. If the ellipse does not enclose the origin, the system is trivial and $N_S = 0$. This occurs for

$$\mu^2 > (t_1 + t_2)(t_3 + t_4) = 4(t^2 - \Delta^2 \eta^2). \tag{12.11}$$

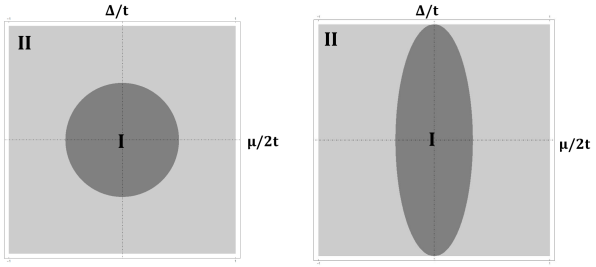

(a)

(b)

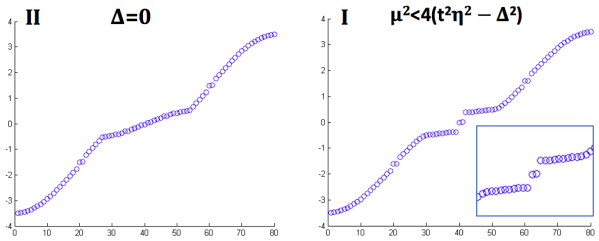

(c)

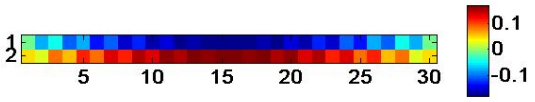

(d)

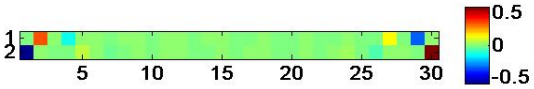

(e)

Figure 12.2: **(a)** Phase diagram of the general SSH ladder for $|\Delta| < |\eta|t$. This parameter regime corresponds to a ladder configuration composed of two *identical* SSH chains, as in Fig. 12.1 (b). Here, phase I hosts a single pair of zero energy edge modes while phase II is topologically trivial having no zero edge mode structure. **(b)** Phase diagram of the general SSH ladder for $|\Delta| > |\eta|t$. Here, the SSH ladder is in a regime illustrated by Fig. 12.1 (c) where the two SSH chains that comprise it are *offset* with respect to the relative strength of couplings: if the bottom chain starts with a weaker coupling then the top starts with the stronger one. As in (a), phase I hosts a single pair of zero energy edge modes and phase II supports no zero edge modes. **(c), (d) and (e)** Energy spectra and spatial wavefunction profiles obtained by numerical diagonalization of the Hamiltonian Eq. (12.2), corresponding to the phases in (a) and (b). In either parameter regime $\Delta = 0$ describes a gapless line in the phase diagram, having the same dispersion relation as the topologically trivial phase II, as illustrated in (d). The sign of Δ determines whether a_i, A_i or b_i, B_i modes are localized to a particular side of the ladder. (e) shows an example of a topologically nontrivial phase with localized zero energy modes at the edge.

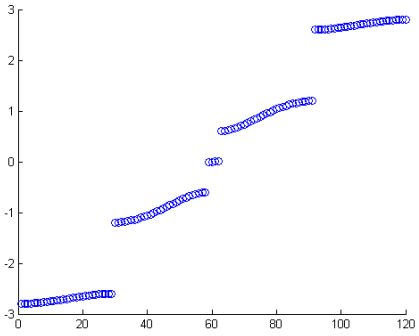

(a)

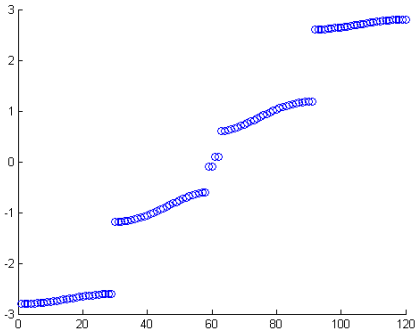

(b)

Figure 12.3: Energy spectra obtained by numerical diagonalization of the Hamiltonian Eq. (12.2), for **(a)** a fully decoupled SSH ladder $\mu = 0$ and **(b)** a weakly coupled $\mu \ll 1$ SSH ladder. A non-zero value of the inter-chain coupling μ causes the four zero energy states to hybridize, resulting in non-zero energy mid-gap edge modes.

In contrast, for

$$(t_1 - t_2)(t_3 - t_4) = 4(t^2\eta^2 - \Delta^2) < \mu^2 < (t_1 + t_2)(t_3 + t_4) = 4(t^2 - \Delta^2\eta^2), \tag{12.12}$$

the ellipse encloses the origin and $N_S = \text{sgn}(t\Delta)$. We conclude that the sign of N_S determines whether a_i, A_i or b_i, B_i modes are localized to a particular side of the ladder. These two possible cases are topologically distinct and separated by a gapless line $\Delta = 0$ in the topological phase diagram as in, for instance, Fig. (12.2).

Given that the ladder model at the center of this Chapter is essentially two coupled SSH chains i.e. a doubling of a well-understood model hosting one or zero localized modes at each of its ends, intuitively the ladder system seems capable of hosting zero, one or two localized modes at each of its ends. Our analysis of the topological invariant N_S shows that this expectation is not quite accurate. We find that there are two distinct topological phases which exhibit single fermionic zero modes at each end of the ladder. At the same time, the ladder system cannot host more than one fermionic mode at each end. In particular, the form of N_S in Eq. (12.10) makes it clear that only if the ladder has longer range hopping can $|N_S| > 1$. We note that this is conistent with the classification of the SSH ladder as a BDI topological insulator in Sec. 12.2.3.

We can also address the fate of the zero modes for two SSH chains, each in the topological phase, when they are coupled. The two end modes can hybridize and form an analog of a weak topological insulator, as shown in Fig. 12.1 (e). A single fermion mode, as opposed to a pair, is however protected given that for a spectrum with particle hole symmetry and an odd number of states there must be at least one zero energy state. This argument is readily generalized: for a system of N chains coupled by weak inter-chain couplings, we anticipate that a topological phase (with a single topological edge mode) will result if and only if the number of chains that are topological is odd, a natural consequence of fermion parity and particle-hole symmetry. Further, we note that while the hybridization of edge states in the case of two coupled chains does not allow for a topological phase hosting zero energy edge states, the resulting regime is distinct from the trivial regime in that there is a non-zero energy bound state at each ladder end. As shown in Fig. 12.3, hybridization causes the bound edge states to move away from zero energy but they still form low-energy mid-gap states. Further, the energy spectrum retains an energy gap despite this hybridization (in the regime of weak inter-chain coupling). Transitioning into the trivial state having no boundary modes whatsoever requires the closing of the bulk energy gap.

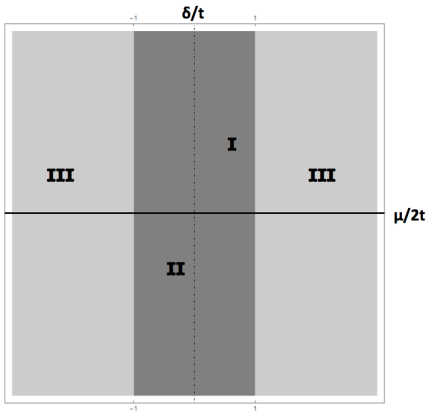

(a)

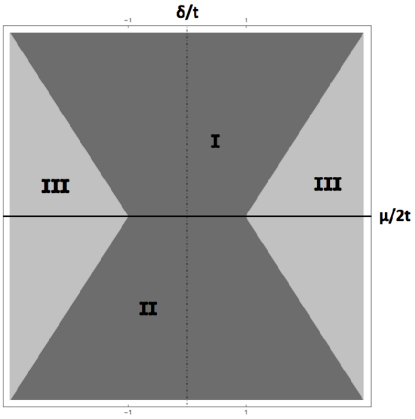

(b)

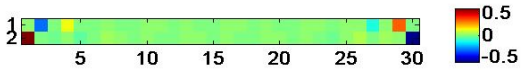

(c)

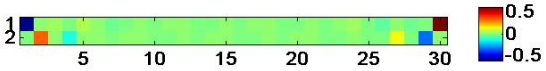

(d)

Figure 12.4: **(a)** Phase diagram for an infinitely long SSH ladder with $t_1 = t_3$ and $t_2 = t_4$, **(b)** phase diagram for an SSH ladder with hopping parameters as in (a) and a finite size L. The slope of the phase boundaries is linear in L. **(c) and (d)** Spatial wavefunction profiles corresponding to the two topologically non-trivial phases (I and II in (a)) of the reduced SSH ladder.

12.5 Kitaev Chain Analog

Having identified the topological properties and edge mode structures of the most general SSH ladder, we now specialize to the case in which $\eta = 0$. We take $t_1 = t_4 = t(1-\delta)$, $t_2 = t_3 = t(1+\delta)$, where $\delta = \Delta/t$. As discussed in the previous Section, δ measures the tendency of the SSH ladder to have the opposite dimerization patterns on its upper and lower legs, respectively. Thus, larger $|\delta|$ tends to stabilize topologically non-trivial phases.

This special, restricted set of couplings offers a means of probing the phase diagram of the Kitaev chain, a prototype for studying Majorana wires and physics of Majorana fermionic bound states [194, 205]. The Kitaev chain consists of a single chain of electrons possessing on-site local chemical potential μ that can tunnel between sites (for instance, with strength t) and experience nearest neighbour p-wave pairing (for instance, of strength Δ). Its Hamiltonian in the Dirac fermion basis takes the form

$$H = \sum_{n=1}^{N-1}(-tc_{n+1}^{\dagger}c_n + \Delta c_{n+1}^{\dagger}c_n^{\dagger} + \text{h.c.}) - \sum_{n=1}^{N}\mu_n(c_n^{\dagger}c_n - 1/2) \tag{12.13}$$

When represented in terms of pairs of Majorana fermions on each site, the physical construction exactly maps on to the SSH ladder with the identification $t_{1/2} = t \pm \Delta$ [199]. Concretely, introducing $2N$ Majorana operators $a_n = c_n + c_n^{\dagger}$ and $b_n = i(c_n^{\dagger} - c_n)$ such that $a_n^{\dagger} = a_n$, $b^{\dagger_n} = b_n$ and $\{a_n, a_m\} = \{b_n, b_m\} = 2\delta_{mn}$ we find

$$H_{\text{M}} = -\frac{i}{2}\sum_{n=1}^{N-1}\Big[(t-\Delta)a_n b_{n+1} - (t+\Delta)b_n a_{n+1}\Big] - \sum_{n=1}^{N}\frac{i\mu_n}{2}a_n b_n. \tag{12.14}$$

This expression is clearly equivalent to the Hamiltonian in Eq. (12.8). Given this equivalency, we conclude that electronic bound states at the ends of the SSH ladder map to Majorana fermionic bound states at the end of the Majorana wire. Most importantly, the dispersions for both systems are identical and equivalent phase boundaries serve to demarcate topological phases from trivial ones.

Specifically, in the Kitaev chain analog limit, the energy dispersion of the SSH ladder takes the form

$$E_{\pm}(k) = \pm t\sqrt{(2\cos(k) + \mu/t)^2 + (2\delta\sin(k))^2}. \tag{12.15}$$

As in Sec. 12.4, the loci of energy gap closing points form the phase boundaries between different topological phases of the system and are given by : $\mu = \pm 2t$ at $k = 0, \pi$ and $\delta = 0$ at $k = \cos^{-1}(-\mu/2t)$. The phase diagram determined by these curves is shown in Fig. 12.4 (a). The topological characters of the various parts of the phase diagram are readily established by considering simple cases. Setting $\delta = -1$ corresponds

to the case shown in Fig. 12.1 (d) which can be viewed as a single SSH chain weaving between the upper and lower legs of the ladder. In accordance with findings for a single, disconnected SSH chain the system is topologically non-trivial in this case provided that $|\mu| < 2|t|$.

To re-emphasize the connections and differences between the SSH ladder and the Kitaev chain, the Dirac fermionic end modes in the SSH ladder correspond to phases with end Majorana modes in the Kitaev chain. We note that these modes of the SSH ladder could be realized in some bosonic systems as well. Though sometimes attributed to the $\mathbb{Z}_2$ character of the Kitaev chain (a system in class D), we see that its topological property is actually due to particle-hole symmetry and fermionic parity. Indeed, when the superconducting order parameter is taken to be real in the Kitaev chain, the Hamiltonian is also in the BDI class.

12.6 Inhomogeneous Couplings and the Hofstadter Butterfly

We proceed to further expand our discussion of varying couplings essential for the determination of the properties of the SSH ladder by considering effects of spatial inhomogeneity in a specific coupling term in this Section. More specifically, we remain within the Kitaev chain analog limit of $t_1 = t_4$, $t_2 = t_3$ and consider periodicity, quasi-periodicity, and disorder in the inter-chain coupling μ. Our reason for this is three-fold. First, we wish to preserve particle-hole symmetry and the bipartite nature of the lattice and thus do not include an actual on-site chemical potential. Second, variation in μ for the ladder system exactly maps on to such a variation in a potential landscape in the Kitaev chain, thus enabling us to parallel Majorana fermion physics in the presence of potential landscapes and disorder [206, 199**? ?** , 207]. Third, of the vast parameter space for inhomogeneities, we narrow our study to the most natural choice and show that even varying a single parameter results in a rich phase diagram structure.

Explicitly, the inter-chain coupling in our model Hamiltonian of Eq. (12.1) takes the form

$$\sum_{j=1} (\mu_{2j-1} a_j^\dagger B_j + \mu_{2j} b_j^\dagger A_j + \text{h.c.}). \tag{12.16}$$

The topology of the disordered chain is most conveniently found by employing the transfer matrix method, discussed in Sec. 12.2.4. We define the Lyapunov exponent of the transfer matrix as

$$\gamma(\{\mu_j\}, \delta, L) = \lim_{L\to\infty} \frac{1}{L} \ln |\lambda|, \tag{12.17}$$

where λ is its highest eigenvalue. This exponent is the inverse of the localization length of the edge-mode wavefunction in the topological phase. The phase boundaries separating the topologically trivial and non-

trivial phases are thus determined by $\gamma = 0$, corresponding to a diverging localization length at the transition point.

To probe the fate of the topological phase diagram when inhomogeneities are present, we make use of a similarity transformation given in Ref. [196]. Explicitly, the similarity transformation on the full chain transfer matrix reads

$$\mathcal{A}(\mu_n, \delta) = \left(\frac{1-\delta}{1+\delta}\right)^{N/2} S\tilde{\mathcal{A}}(\mu_n/\sqrt{1-\delta^2}, \delta = 0)S^{-1} \tag{12.18}$$

where

$$S = \mathrm{diag}(\ell_\delta^{1/4}, 1/\ell_\delta^{1/4}), \tag{12.19}$$

the function ℓ_δ is defined by $\ell_\delta = \frac{1-\delta}{1+\delta}$ and we have set $t = 1$. The matrix $\tilde{\mathcal{A}}_n$ is the transfer matrix for a normal tight-binding model – in the context of quasi-periodicity, a Harper model – in the absence of a dimerization δ. The model's on-site chemical potential terms are re-scaled by the transformation $\mu_n \to \mu_n/\sqrt{1-\delta^2}$. This map allows the Lyapunov exponent to be written as a sum of two components, $\gamma(\mu, \delta) = \gamma_\delta + \gamma_0$, one that depends purely on the dimerization γ_δ and $\gamma_0(\mu/\sqrt{1-\delta^2})$, which is the Lyapunov exponent for a system having no dimerization and a rescaled locally varying chemical potential. Thus, knowing wavefunction properties for the non-dimerized system enables identifying localized wavefunctions in an SSH ladder having the same spatial variation.

One-dimensional fermionic systems are especially sensitive to non-uniform potentials and disorder. The similarity transformation quantifies the fact that the tendency to localize fermions directly competes with the topological phases. The transfer matrix formalism is particularly well-suited to the study of spatially varying potentials as the topological phases can be determined by considering the eigenvalues of $\prod_i \mathcal{A}_i$, where the product runs over the full extent of the system in question, one unit cell at a time.

To be more concrete, we elaborate on transfer matrix calculations aimed at determining edge mode physics. If both eigenvalues of $\mathcal{A}$ have a magnitude less than 1, this indicates that the a_i/A_i zero mode decays as it extends into the bulk of the system from the right. Since the transfer matrix governing the b_i/B_i mode is given by $\mathcal{A}^{-1}$, in this case the b_i/B_i mode would be localized to the right-hand side of the system. If however $\mathcal{A}$ has one eigenvalue that is larger than 1 in magnitude and another that is smaller than 1, then the zero modes are not normalizable. This case corresponds to the topologically trivial phase.

Physically, the topology of the Kitaev-like ladder is dictated by the competition between the coupling parameters μ/t and $\delta = \Delta/t$. The parameter δ breaks the symmetry between the a_1 and B_1 modes at the

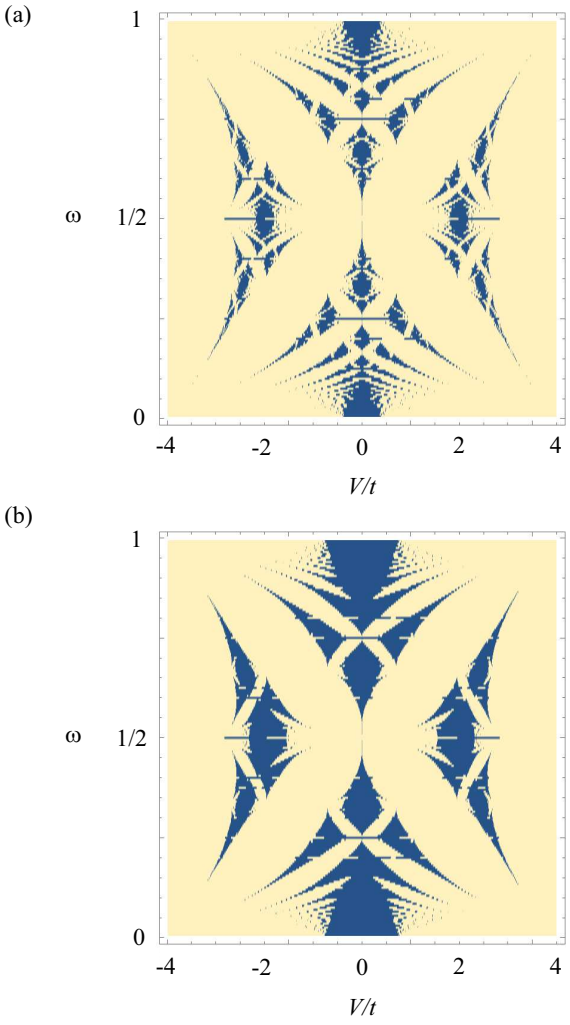

Figure 12.5: The phase diagram for a quasiperiodically varying inter-chain coupling $\mu_n/t = V/t + 2\cos(2\pi\omega n)$, where $2t = t_1 + t_2$, reflects the Hofstadter butterfly pattern. The lighter regions indicate the places where the bulk gap closes and the Lyapunov exponent vanishes i.e. the topologically trivial regions. The Hofstadter butterfly pattern shows loci in parameter space where available energy states exist in the limit $\delta = t_1 - t_2 = 0$. These loci seed topological phases, which occupy larger regions of the phase diagram as δ grows larger between panels **(a)** $\delta = 0.1$ and **(b)** $\delta = 0.2$.

left end of the chain. In the limit $\delta = 0$, the Hamiltonian treats the a_i/A_i and b_i/B_i modes symmetrically, and thus must be trivial since the topologically non-trivial regimes are characterized by a *single* end mode. For $0 < \delta \leq 1$, the coupling of the a_1 mode to the rest of the chain is weakened relative to the B_1 mode, and thus in this case any topological phase will have $N_S = 1$.

We begin our investigation of inhomogenously coupled SSH chains with a particulary simple case which illustrates the relevant physics. Consider the case in which $\delta = -1$ (recall that we have set $t = 1$) and μ_n is some arbitrary configuration (either periodic, quasiperiodic, or disordered). As discussed above, this case can be considered as a single connected chain, as in Fig. 12.1 (d). In this case, the product of transfer matrices can be carried out explicity

$$\prod_{n=1}^{N} \mathcal{A}_n = \frac{1}{(2t)^N} \prod_{n=1}^{N} \mu_i \begin{pmatrix} 1 & 0 \\ 2t/\mu_1 & 0 \end{pmatrix}. \tag{12.20}$$

The eigenvalues of the resultant matrix are $\frac{1}{(2t)^N} \prod_{n=1}^{N} \mu_n$ and zero. The phase is topological provided that the nonzero eigenvalue has magnitude less than 1. The condition that the system is topological can be expressed as

$$\langle \ln (|\mu_n|/t) \rangle \leq \ln 2, \tag{12.21}$$

a condition that is applicable to periodic, quasiperiodic, and disordered potentials. We point out that this special case ($\delta = -1$) can be mapped to the disordered quantum Ising model. In this correspondence, the topological phase in the fermionic system corresponds to the ferromagnetic phase in the spin model.

12.6.1 Quasiperiodic modulation

In discussing modulations of the inter-chain coupling μ_n, of particular note is the case in which

$$\mu_n/t = V/t + 2\cos(2\pi\omega n). \tag{12.22}$$

This variation is of particular interest in the context of localization physics and arises in the problem of an electron on a two-dimensional lattice in a magnetic field. The spectrum of the latter is fractal and is known as Hofstadter's butterfly. (We address the issue of quasiperiodicity and fractality in more depth in Chapter 10.) The fractal pattern arises due to ω continuously tuning through quasi-periodic and periodic modulations with respect to the underlying lattice. In the present notation, Hofstadter's butterfly is made up of regions in which the Lyapunov exponent for Eq. (12.22) and δ are zero. Given the similarity transformation discussed in

Eqs. (12.18) and (12.19), knowing Lyapunov exponents in the Hofstadter case enables us to derive Lyapunov exponents for non-zero δ. This in turn enables us to determine the regions of parameter space that support localized end bound states and are thus topological.

We have plotted the topological phase diagram in the $V - \omega$ plane for two values of δ in Fig. 12.5. As δ is increased from zero, the mapping to Hofstadter's model indicates that the regions corresponding to the lowest Lyapunov exponent get filled in first. Thus, as δ is increased from zero, regions of the phase diagram nearest to available energy states reflected in the Hofstadter butterfly pattern become topological first. As noted above, increasing δ tends to isolate an a_i/A_i mode, giving rise to more regions which are topological (i.e. host localized edge modes). The phase diagram shown in Fig. 12.5 ultimately arises as a result of the competition between the localizing potential μ_n given by Eq. (12.22) and the effects of nonzero δ or the tendency of the system to become topological.

Our treatment above of spatial variations in the inter-chain coupling μ is generic and allows for different forms of variation. Disorder in μ is another natural choice. Extensive treatments of such a case for the Kitaev chain [196] immediately translate to the phase diagrams expected for the SSH ladder system.

We highlight that the effects of disorder are a ubiquitous concern in experiments. Further, ultracold atomic, photonic and meta-materials realizations of the SSH ladder are all systems typically characterized by high levels of experimental control and reconfigurability. In other words, not only is studying disorder informative for experimental studies but they could also be used to target specific cases such as the quasiperiodic modulation of the inter-chain coupling in the SSH ladder. The discussion presented in this Section consequently allows us to connect our analysis to realistic physical systems. We expand on some concrete future directions along these lines in Sec. 12.8 and spend the following Section focusing on finitely-sized systems which are another point where our work closely parallels experimental efforts.

12.7 Finite Size Effects

In experimental setups, for instance cold-atomic optical lattices, the number of lattice sites in the system is typically quite small due to limitations of experimental techniques. Consequently, finite size effects are a significant consideration in experimental observation of topological phases. In this Section, we derive the structure of edge mode wavefunctions for a system of size 'L' and demonstrate how a boundary between a regime hosting and lacking localized edge modes can be effectively obtained through finite-size analyses. While a finitely-sized system does not undergo a true topological phase transition but rather a crossover between these two regimes, we find that representing this process in parameter space of μ/t and δ amounts

to a linear slant in the phase boundaries of the infinite SSH ladder.

We focus our discussion of finite size effects on the reduced SSH ladder model – the analogue of the Kitaev wire discussed in Sec. 12.5 – where it is sufficient to consider the Fourier space Hamiltonian

$$\hat{H}_k^1 = \begin{pmatrix} 0 & \rho(k) \\ \rho^*(k) & 0 \end{pmatrix} \tag{12.23}$$

with $\rho(k) = t_1 e^{ika} + t_2 e^{-ika} + \mu$ and $\rho(k) = |\rho(k)|e^{i\phi(k)}$. This Hamiltonian, Eq. (12.23), connects to the larger Hamiltonian of Eq. (12.2) through a unitary transformation U that renders the latter off-diagonal and defines A and B sub-lattices that are linear combinations of a and A (b and B):

$$U^\dagger \hat{H}_k U = \begin{pmatrix} \hat{H}_k^1 & 0 \\ 0 & \hat{H}_k^1 - 2\mu\sigma_x \end{pmatrix} \tag{12.24}$$

and $(A_k^\dagger, B_k^\dagger) = \frac{1}{\sqrt{2}}(a_k^\dagger + A_k^\dagger, b_k^\dagger + B_k^\dagger)$.

The eigenstates of Eq. (12.23), corresponding to two eigenvalues $\pm E$, are of the form:

$$|u_k, \pm\rangle = \frac{1}{\sqrt{2}} \begin{pmatrix} e^{-i\phi(k)} \\ \pm 1 \end{pmatrix}. \tag{12.25}$$

Here, the phase $\phi(k)$ is implicitly given by

$$\cot\phi(k) = \frac{t_1 + t_2}{t_1 - t_2} \cot k + \frac{\mu}{t_1 - t_2} \csc k. \tag{12.26}$$

We construct the edge mode states as linear combinations $|v_k, \pm\rangle = C_+|u_k, \pm\rangle + C_-|u_{-k}, \pm\rangle$. Further, in terms of lattice wavefunctions [208]:

$$|u_k, \pm\rangle = \sqrt{\frac{1}{2L}} \sum_{j=1}^{L} \begin{pmatrix} e^{-i\phi(k)} \\ \pm 1 \end{pmatrix} \times (e^{ikj}|j, A\rangle, e^{ik(j+1)}|j+1, B\rangle) \tag{12.27}$$

where A and B denote the same sublattices as above.

To analyze the effects of the ladder's finite size we impose open boundary conditions and require that

the wave functions vanish for sites $j = 0, L+1$. More precisely, we set

$$\begin{aligned} \langle 0, B|v_k, \pm\rangle &= 0 \\ \langle (L+1), A|v_k, \pm\rangle &= 0. \end{aligned} \tag{12.28}$$

Enforcing the first of these conditions we find $C_+ = -C_- = 1/\sqrt{2}$ while enforcing the second implies

$$k(M_L + 1)a - \phi(k) = n\pi \tag{12.29}$$

for n some integer. Recalling the definitions of t_1 and t_2 we can re-write this expression as

$$k(L+1)a - n\pi = \cot^{-1}\left(\frac{(t_1+t_2)\cos(k)+\mu}{(t_1-t_2)\sin(k)}\right) = \cot^{-1}\left(\frac{2t\cos(k)+\mu}{\delta\sin(k)}\right). \tag{12.30}$$

We note that for $k = \pi$, if $t_1 + t_2 = 2t < \mu$ then $\phi(\pi) = 0$ and in Eq. (12.30) $n = L+1$ while for $2t_0 > \mu$ the same equation, now with $\phi(\pi) = \pi$ gives $n = L$. Consequently, we conclude that some states are "lost" as the ratio of $2t$ and μ goes through 1. These states are precisely the mid-gap, localized edge modes.

In order to solve Eq. (12.30) we consider setting the slopes of its right-hand and left-hand sides equal (note that if these slopes are equal then the curves corresponding to each side of the equation are parallel and cannot intercept) at $k = \pi$ then gives

$$\frac{t_1 - t_2}{t_1 + t_2 - \mu} = \frac{\delta}{2t - \mu} = L + 1. \tag{12.31}$$

This expression should be taken as defining phase boundaries in a way that depends on L i.e. the number of sites in the ladder. In other words, for an edge state to be present the values of μ, δ and t have to satisfy $\delta/(2t-\mu) < L+1$. The phase diagram accounting for this feature is show in Fig. 12.4 (b). From this plot, it is clear that for the Kitaev wire analogue SSH ladder having finitely many lattice sites, the slope of phase boundaries is linear in system size. Here, we again note that while crossing these boundaries does not amount to a rigorous phase transition since the system is finitely-sized and some overlap between the localized edge modes is inevitable, the lines determined by Eq. (12.31) still demarcate a crossover between rather different edge mode structure regimes that could be distinguished in real physical systems. For large system sizes ($L \to \infty$), these boundary lines become vertical and match the phase boundaries in the thermodynamic limit.

Further, enforcing Eq. (12.28) enables us to obtain the form of the wavefunctions of zero energy edge

modes:

$$|v_{k_\lambda}, \pm\rangle = \frac{1}{\sqrt{L}} \sum_{j=1}^{L} \begin{pmatrix} \sinh(\lambda_\xi a(L+1+j)) \\ \pm \sinh(\lambda_\xi (j+1)a) \end{pmatrix} \times (|j, A\rangle, |j+1, B\rangle) \tag{12.32}$$

where λ_ξ is the inverse of the localization length ξ for the edge state. In other words, λ_ξ is equivalent to the Lyapunov exponent γ of Sec. 12.5.

When $L >> \xi$ i.e. the system size is much larger than the localization length, the difference in energy of the modes corresponding to the two states in Eq. (12.32) decreases exponentially fast with increasing L so that for a large yet finitely-sized system the edge modes are effectively degenerate states with vanishing energies. The "bending" of the phase boundaries compared to the phase diagram of Fig. 12.4 (a) for a ladder with a finite size and the qualitative shape of the edge-mode wavefunction in Eq. (12.32) are germane to experimental studies of the SSH ladder system.

Further, we use the same formalism to compare the general SSH ladder to its decoupled $\mu \to 0$ limit. Considering the case in which the decoupled system consists of two topological chains i.e. two chains hosting a pair of zero egde modes, these four modes can be described by the wavefunctions

$$|v^{\mathrm{ab}}_{k_\lambda}, \pm; v^{\mathrm{AB}}_{k_\lambda}, \pm\rangle = \sum_{j=1}^{L} \frac{(-1)^{j+1}}{\sqrt{L}} \begin{pmatrix} \sinh(\lambda_\xi (L+1-j)) \\ \pm \sinh(j\lambda_\xi) \\ \sinh(j\lambda_\xi) \\ \pm \sinh(\lambda_\xi (L-j+1)) \end{pmatrix} \times (|j, a\rangle, |j, b\rangle, |j, A\rangle, |j, B\rangle) \tag{12.33}$$

with λ_ξ as above. An addition of a small inter-chain coupling μ can then be treated perturbatively. Consequently, we see that regardless of the size of the SSH ladder, the four dispersionless edge states acquire an energy shift linear in μ. In other words, these modes hybridize and the energy spectrum does not possess any zero modes but rather two pairs of non-zero energy midgap states, as shown in Fig. (12.3). This observation is consistent with our previous discussion of pairs of zero edge modes not being topologically protected, as in Sec. 12.4.

12.8 Outlook

We close this Chapter by summarizing our findings and discussing future experimental and theoretical work that could build on the rich physics we have presented here. Concretely, we have analyzed the SSH ladder as a natural extension of the well-studied SSH chain, paying particular regard to topological and edge state

properties. We have charted the phase diagram exhibited by such a ladder system and pinpointed the nature of the topological phases as a function of various inter-chain and intra-chain couplings. Under a restricted set of couplings, the ladder serves as an analogue for the Kitaev chain and associated Majorana physics. In this regime, we have investigated the effect of inhomogeneity and the possibility of a *topological Hofstadter butterfly phase diagram* for quasiperiodic variations. With an eye towards realizing these features in a variety of experimental systems, we have discussed the role played by finite size effects. This discussion leads us to posit that some of the topological features discussed in the thermodynamic limit would remain observable even for much smaller and much more experimentally feasible ladder systems.

One particularly elegant realization of localized edge modes in the context of cold atomic experiments has already been achieved in Ref. [184], where these topological features of a single SSH chain have been confirmed through direct imaging. The procedure of directly detecting edge-localization entails loading condensate atoms on a particular momentum-space lattice site, which in this experimental set-up corresponds to a discrete momentum state as is described in Sec. 11.2, and suddenly turning on, or quenching, the desired coupling between sites. Observing consequent population decay, or the lack thereof, to the neighboring sites through time-of-flight absorption imaging then indicates whether or not a zero energy edge mode is supported for this point in the space of couplings. Such images comprise a direct observation of an edge mode and confirm that the system is in a topologically nontrivial phase. An extension of such methods to our SSH ladder would required a set-up capable of realizing two coupled chains and the ability to tune through parameter space in order to access our predicted phase diagrams.

A similar procedure for observing edge modes has been used in a photonic system [186], where a photon is initialized next to the boundary between two topologically distinct quantum walks and observed to not spread ballistically when a bound edge state is present. In meta-materials of Ref. [182], the zero modes are found to localize in the corners of a more two-dimensional system and to be robust to mechanical deformations corresponding to changes in the space of inter- and intra-chain couplings. In another metamaterial system explored in Ref. [7], topologically protected edge modes of a single SSH chain are observed as persistent mechanical resonator vibrations. Experimental systems mentioned here thus offer various means of manifesting Kitaev chain analogues through SSH ladder realizations. The Majorana fermion bound states in these cases would translate to Dirac fermionic, bosonic, and even classical mechanical localized modes confined to ends of the ladder.

Turning to inhomogeneity, the appearance of the Hofstadter butterfly is one of many exotic features arising from the rich mathematical structure of the Harper equation and related quasiperiodicity (as discussed in detail in Chapter 10). So far, there have been experimental works on realising a quasiperiodic system

through a Hofstadter Hamiltonian in cold atomic systems [200, 155]. Even though cold atomic systems are well suited for realizations of complex structures such as the Hofstadter butterfly in contrast to electronic systems, as of now, studies centered on the Hofstadter Hamiltonian have not included any direct measurements of the fractal character of the system's wavefunctions. Our model of coupled SSH chains provides a novel possibility of realizing this striking self-similar diagram through observation of topological phases driven by direct time-of-flight imaging and related experimental techniques described above.

While we have outlined a number of potential candidate systems for experimental work exploring the Kitaev-like and the quasiperiodic SSH ladder, in the following Chapter we focus on one particular realization in meta-materials. Detailing the experimental setup and procedure at the core of an ongoing collaboration, we complete Part III of this thesis with a look towards beginnings of rich future works and further succesful exploration of topological ladder systems.

Chapter 13

Coupled Ladders and Topological Phases in Meta-Materials

13.1 Introduction

In this Chapter, we build on our discussion of experimental prospects for realizing the SSH ladder model analyzed at length in Chapter 12 by focusing on classical meta-materials systems. Remarkably, mechanical systems can exhibit characteristics analogous to those of electronic topological insulators. The latter class of materials is marked by the property that they conduct electricity along their edges despite being insulators in the bulk or host localized Majorana edge modes. In recent years, this phenomenon has been showed to not be restricted to electronic systems only. For instance, specially designed photonic crystals can support robust, topological electromagnetic wave-modes along their edges [209, 210, 211, 183]. The same is true of topological phonon modes in mechanical lattices [212, 213, 214]. Topological effects are typically associated with quantum mechanical systems, but the existence of edge and surface phonon modes exhibiting topological properties is not rare in mechanical systems and even analogues of the Quantum Hall Effect have been observed in acoustic systems in a magnetic field [215, 216]. Mechanical meta-materials have consequently been used to realize and study a plethora of topological systems, including those featuring higher order topological phases [217]. They have also proven to be a fruitful setting for modeling biologically motivated structures such as Microtubules – a biomaterial synthesized by all living cells having dynamical behavior strongly influenced by topological edge modes [212, 218].

Taking a longer view and focusing on theoretical work, a classical analog of the classification of strong topological condensed matter systems into 10 distinct classes [219, 220] has been generated as well. Namely, in Ref. [221], a reformulation and generalization of the Susstrunk-Huber technique [181] has been used to establish an algorithmic procedure to translate any strong topological electronic system from the ten-fold way classification into an equivalent topological classical metamaterial. In these works [181, 221], authors develop a map connecting the dynamical matrix that encodes classical equations of motion to the one appearing in the quantum mechanical, Hamiltonian eigenproblem. The latter formalism can be summarized

by the Schrodinger equation of the form

$$i\hbar\dot{\psi}_i^{\alpha} = \mathcal{H}_{ij}^{\alpha\beta}\psi_j^{\beta} \tag{13.1}$$

with ψ_{i^α} the wave-function amplitude for an electron having spin α on a lattice site labeled i. Here, $\mathcal{H}_{ij}^{\alpha\beta}$ is the Hamiltonian of the system. A classical system, for instance one consisting of a collection of oscillators or resonators, is governed by Newton's equations of motion

$$\ddot{x}_i = -\mathcal{D}_{ij}x_j \tag{13.2}$$

with x_i the resonator coordinate and $\mathcal{D}_{ij}$ the dynamical matrix. The entries of $\mathcal{D}$ are the couplings between the oscillators. In either system – classical meta-material or electronic quantum mechanical – existence and properties of edge modes are features of the eigenstates of $\mathcal{H}$ or $\mathcal{D}$ and do not depend on the precise interpretation of ψ_{i^α} or x_i, treated as just an appropriate eigenvector, nor the nature of the dynamics encoded in the first or second time-derivative in Eqs. (13.1) and (13.2). In other words, $\mathcal{D}$ can be designed to include topological properties [181]. Here, the challenge is in achieving broken symmetries, such as time-reversal symmetry, crucial for emergence of topological properties. This obstacle is removed by the theoretical study in Ref. [221] where in addition to a map between a formulation of $\mathcal{H}$ and $\mathcal{D}$ spectral projector operators are used to identify sectors of the eigenstate space (subspaces) having appropriate symmetries. In other words, if an electronic Hamiltonian has symmetries informing its topological classification, then it can be mapped to a Hamiltonian having same symmetries when projected to one of these sectors with this mapped Hamiltonian being formulated in a way that allows simple experimental implementation with classical meta-materials [221]. Consequently, efforts to realize topological models such as the SSH ladder in these systems rest on a well-studied theoretical foundation and present a new and fast-advancing frontier for researching topological phenomena.

In this Chapter, we focus specifically on a meta-materials system made up of magnetically coupled spinners. Coupled spinner chains are a promising candidate for realizing topologically non-trivial phases of the SSH ladder in ways that may be experimentally more feasible than in, for instance, cold atomic environments where the restriction to nearest-neighbor hoppings only and the need for long systems sizes present a challenge. Mechanical spinners, on the other hand, are more easily configurable and can be engineered at any scale. In discussing their properties below, we draw heavily on the work of collaborators Profs. C. Prodan and E. Prodan in Ref. [7].

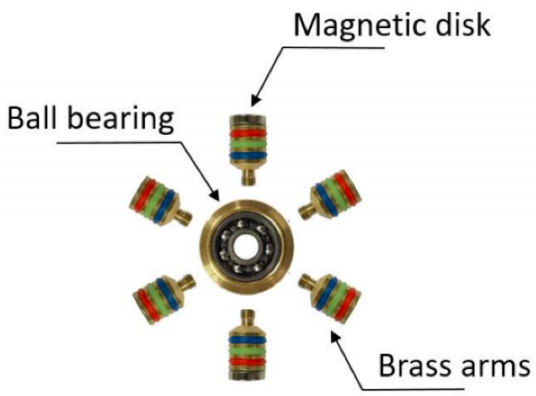

Figure 13.1: Example of a mechanical spinner used as a building block for the meta-materials implementation of the SSH ladder discussed in this Chapter. The arms are detachable thus allowing for refitting of the spinner and high adaptability of the structures made up of such resonators. This schematic has been adapted from Ref. [7].

13.2 Magnetically coupled spinners

The appeal of using coupled mechanical resonators or spinners, as proposed in Ref. [7], primarily lies in their versatility. As a platform for realizing topological and other systems, they can be easily reconfigured, engineering patterns with predefined internal structures and couplings. Thus, the degree of experimental control is rather high in studies that employ them and promises good agreement with theoretical predictions. A configurable spinner is made up of a stainless steel ball-bearing mounted in a threaded brass encapsulation. In constructing lattice-like patterns, centers of spinners are pinned down but they can still be adapted with a multitude of components. Here, we focus on spinners with six grooved indentations and heavy brass arms fastened in the encapsulation. Two of the arms are fitted with neodymium magnetic disks which facilitates magnetic coupling between neighboring resonators. A single resonator outfitted in this way is shown in Fig. 13.1. Each spinner has one rotational degree of freedom denoted by φ so that by stacking and magnetically coupling individual spinners, systems of any complexity can be built one degree of freedom at time. Consequently, controlling the couplings between spinners enables experimentalists to implement any quadratic Hamiltonian in the small oscillation regime of the coupled resonators [7].

Theoretically, the magnetic couplings between magnetically coupled spinners can be measured by mapping the resonant modes of a dimer (spinner pair φ_1 and φ_2) having dynamics governed by the Lagrangian

$$\mathcal{L}(\varphi_1, \varphi_2, \dot{\varphi}_1, \dot{\varphi}_2) = \frac{1}{2} I \dot{\varphi}_1^2 + \frac{1}{2} I \dot{\varphi}_2^2 - V(\varphi_1, \varphi_2) \tag{13.3}$$

where I denotes the moment of inertia of each spinner. In the regime of small oscillations around $\varphi_1 = \varphi_2 = 0$ it is appropriate to further approximate [7]

$$V(\varphi_1, \varphi_2) = \frac{1}{2}\alpha(\varphi_1^2 + \varphi_2^2) + \beta\varphi_1\varphi_2. \tag{13.4}$$

The resonant modes of the spinner pair can be computed explicitly as

$$f_\pm = \sqrt{\frac{\alpha \pm \beta}{4\pi^2 I}}. \tag{13.5}$$

Since resonant frequencies $f_\pm$ can be measured as a function of distance d between the magnets (arms of spinners) and Eq. (13.5) can be inverted to solve for parameters α and β, it is possible to use experimental data to determine the functional dependencies $\alpha(d)$ and $\beta(d)$ of the coupling coefficients on the physical distance between the spinners in the desired experimental configuration.

Assuming that the spinner centers are pinned to form some one-dimensional pattern $\omega = x_{n\,n\in\mathbb{Z}}$, the Lagrangian of the system reads

$$\mathcal{L} = \sum_{n\in\mathbb{Z}} \left[\frac{1}{2}I\dot{\varphi}_n^2 - (\alpha(d_n - 1) + \alpha(d_n))\varphi_n^2 - \beta(d_n)\varphi_n\varphi_{n+1}\right] \tag{13.6}$$

where $d_n = x_{n+1} - x_n - D$ and D denotes the diameter of a single spinner. From the Lagrangian in Eq. (13.6), we proceed to obtain the equations of motion governing the system

$$-I\ddot{\varphi}_n = (\alpha(d_{n-1} + \alpha(d_n))\varphi_n + \beta(d_{n-1})\varphi_{n-1} + \beta(d_n)\varphi_{n+1}. \tag{13.7}$$

Here, as in Ref. [7], all coupling functions are presented in units of $2\pi^2 I$. To move to a Hamiltonian formalism, we encode the degrees of freedom of the spinner system into a column vector

$$|\varphi\rangle = (\dots, \varphi_{-1}, \varphi_0, \varphi_1, \dots)^{\mathrm{T}}, \tag{13.8}$$

and set $|n\rangle$ to be another column vector with 1 at position n and zeroes as all other entries. Taking

$$\begin{aligned} |\varphi\rangle &= \sum_n \varphi_n |n\rangle \\ |\varphi(t)\rangle &= \mathrm{Re}\left[e^{i2\pi f t}|\psi\rangle\right] \end{aligned} \tag{13.9}$$

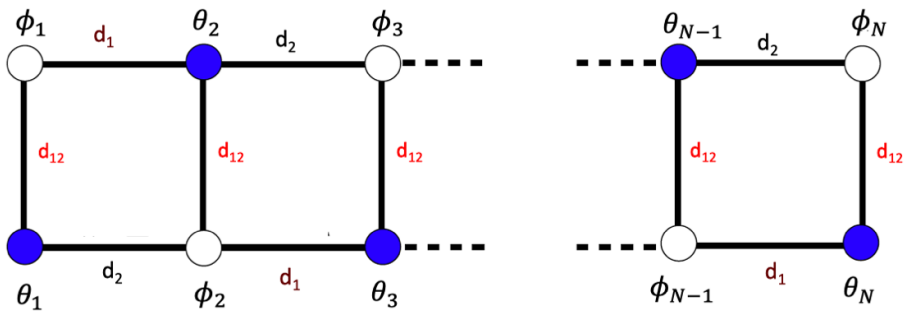

Figure 13.2: Schematic representation of the SSH ladder as implemented by magnetically coupled mechanical resonators. Distances d_i for $i = 1, 2$ and $i = 12$ denote the physical distances between individual resonators horizontally and vertically. Here, spinners are colored white and blue to highlight the sublattice symmetry characterizing the system when the hoppings on the top (bottom) leg of the ladder take two alternating values.

the system of equations of motion from Eq. (13.7) becomes $f^2|\psi\rangle = H|\psi\rangle$ with

$$H = \sum_{n\in\mathbb{Z}} \Big[(\alpha(d_{n-1}) + \alpha(d_n))|n\rangle\langle n| + \beta(d_{n-1})|n\rangle\langle n-1| + \beta(d_n)|n\rangle\langle n+1| \Big], \tag{13.10}$$

a Hamiltonian in the Hilbert space $\ell^2(\mathbb{Z})$. This Hamiltonian only encodes nearest-neighbor interactions, but an analogous calculation could be made for more complex and long-ranged spinner configurations. In the following Section, we specialize this formalism to the case of the SSH ladder in its Kitaev-like phase discussed in Sec. 12.5.

13.3 Towards spinner ladder realizations

To implement the iteration of the SSH ladder analogous to the Kitaev chain (Majorana wire), we re-write the Lagrangian of Eq. (13.6) in terms of two degrees of freedom ϕ_j and θ_j. This reflects the sublattice symmetry of the system and is illustrated in Fig. 13.2.

Accordingly, the Lagrangian of the system becomes

$$\mathcal{L} = \sum_{n\in\mathbb{Z}} \frac{1}{2} I(\dot{\phi}_j^2 + \dot{\theta}_j^2) - \frac{1}{2}(\alpha(d_1) + \alpha(d_2) + \alpha(d_{12}))\theta_j^2 - (\beta(d_1)\phi_{j-1} + \beta(d_2)\phi_{j+1} + \beta(d_{12})\phi_j)\theta_j \tag{13.11}$$

and the equations of motion governing zero energy modes i.e. modes with $\omega = 0$ read

$$I\ddot{\phi}_j = (\alpha(d_1) + \alpha(d_2) + \alpha(d_{12}))\theta_j - (\beta(d_1)\phi_{j-1} + \beta(d_2)\phi_{j+1} + \beta(d_{12})\phi_j). \tag{13.12}$$

We focus on zero energy states as they are meant to reflect the spatial wavefunction structure of the dispersionless edge modes present in the Kitaev chain and the fermionic (or bosonic) SSH ladder. We recall, from our discussion in Sec. 12.5, that inter- and intra-chain couplings of the SSH ladder can be tuned to render its topological phase diagram analogous to that describing the Kitaev chain. In either case, topological invariants are assigned to these phases based on band-structure properties and topological phase transitions require the closing of a spectral gap. As the Kitaev chain hosts exponentially localized Majorana mode wavefunctions at its edges in its topological phases [194], this parallel behavior lends importance to experimental measurements of edge mode structures in SSH ladder realizations. Experimentally confirming the presence of modes described by Eq. (13.12) amounts to establishing the mechanical resonator system to be in a topologically non-trivial phase that is a counterpart to the topological phases of the Kitaev chain. As our previous work, elaborated on in Ch. 12 and by collaborators in Refs. [205, 199], established the exact parameters at which the topological phase transition occurs, we can compare Eq. (13.12) to Eq. (12.8) and Sec. 12.5 in order to develop a dictionary reformulating the transition as a function of physical distance between spinners instead of hopping amplitudes. More precisely, we identify

$$\begin{aligned} t(1+\delta) &\Longleftrightarrow \beta(d_1) \\ t(1-\delta) &\Longleftrightarrow \beta(d_2) \\ |\mu| &= \beta(d_{12}). \end{aligned} \tag{13.13}$$

Here, we recall that the parameter μ quantifies the strength of the coupling between the two SSH chains making up the ladder, t sets the scale for intra-chain hoppings and the amplitude of δ indicates how opposite the dimerization patterns of the upper and lower legs of the ladder are, respectively. Referring to the phase diagram in Fig. 12.4, we conclude that the critical line separating topological and topologically trivial phases occurs for

$$\left|\frac{\mu}{2t}\right| = 1 \Longleftrightarrow \frac{\beta(d_{12})}{\beta(d_1)+\beta(d_2)} = 1. \tag{13.14}$$

The two distinct edge mode structure regimes that this condition demarcates can be experimentally accessed by fixing d_1 and d_2 and performing measurements at the ends of the spinner ladder at various values of d_{12}. In cases when actuating a spinner at the ladder's edge results in vibration that stops afer a few sites into the system's bulk (where the frequency of oscillation of each can be measured), we can conclude that the spinner ladder is in a phase having edge modes i.e. the finite-size equivalent of a topologically non-trivial phase. We expand on details of experiments of this sort in the following Section.

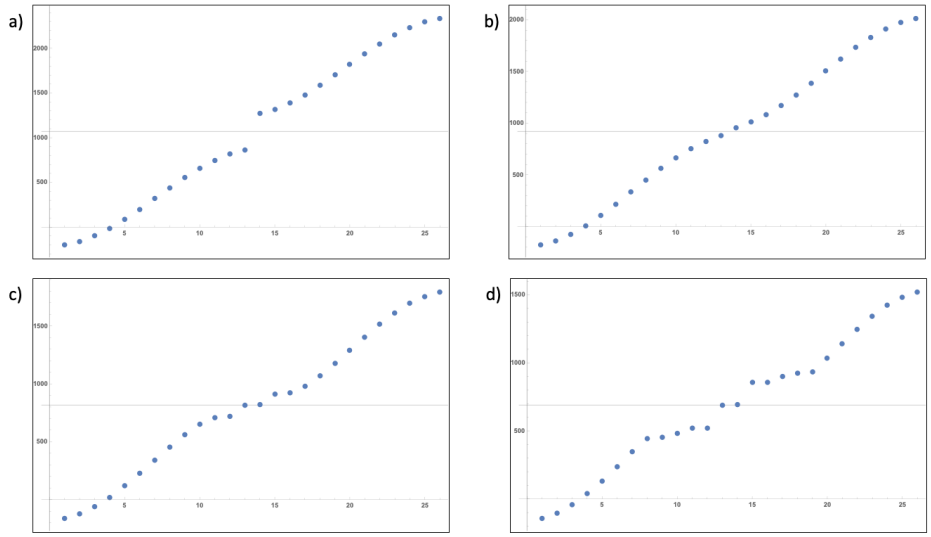

Figure 13.3: Energy spectra for a mechanical spinner ladder system obtained through direct diagonalization for $d_1 = 5$mm, $d_2 = 7$mm and **(a)** $d_{12} = 3.5$mm, **(b)** $d_{12} = 4.0$mm, **(c)** $d_{12} = 4.5$mm and **(d)** $d_{12} = 5.5$mm. As the symmetry (middle of energy gap) point is set by $E_\alpha = \alpha(d_1) + \alpha(d_2) + \alpha(d_{12})$, all of the depicted energy spectra are centered about different energy values set by d_{12}. Here, direct diagonalization is carried out for a system of 26 spinners (two coupled chains of 13) and, taking finite size effects into account, a crossover into a regime hosting topologically protected edge modes is expected for $d_{12} = 4.0$mm. In (b) it is clear that the energy gap closes at this value of inter-chain distance while two nearly degenerate mid-gap states are discernible in (c) and (d). In these calculations, we use functions α and β informed by the experimental work of collaborators in the Prodan research group.

In comparing Eq. (13.12) we further highlight an important difference between the mechanical spinner ladder and the Kitaev chain, or the analogous SSH ladder configuration, that is particularly relevant for experimental meta-materials studies – the presence of the on-site term $(\alpha(d_1) + \alpha(d_2) + \alpha(d_{12}))\theta_j$. This term indicates a constant energy off-set at each site of the spinner ladder and sets the energy of the localized edge modes. Here, edge modes still occur in the energy gap in the spinner ladder energy spectrum but the gap itself is not centered around zero energy. This energy spectrum shift is shown in Fig. 13.3. It is of special importance for experimental studies as it informs energy values at which localized edge modes may be detected. In a procedure where d_1 and d_2 are fixed but d_{12} is varied, while sweeping through various values of d_{12} the topologically protected edge modes can be measured only for values close to $E_\alpha = \alpha(d_1) + \alpha(d_2) + \alpha(d_{12})$. In other words, a topological phase transition may appear to be missing if measurements seeking edge modes are taken near zero energy only despite the distance between the two spinner chains being changed.

Finally, in discussing experimental concerns, it is important to again acknowledge finite size effects i.e. changes to the topological phase diagram of the SSH (and spinner) ladder due to modeling systems with a

small number of sites. This us depicted in the two top panels of Fig. 12.4. To be very precise, the ladder system here undergoes a crossover from a state hosting no mid-gap edge modes to one where they are present rather than a true topological phase transition. The crossover line determining this change can be explicitly calculated as in Eq. (12.31). Translating this expression to spinner ladder parameters, using Eqs. (13.13) and (13.14), leads to

$$\beta(d_{12}) = \frac{\beta(d_2) - \beta(d_1)}{L+1} + (\beta(d_1) + \beta(d_2)) \tag{13.15}$$

where L counts the number of sites in the system (spinners in a single leg of the ladder). Using this expression we are able to predict physical spinner configurations that will result in the appearance of localized edge modes. For instance, for a system consisting of two rows of 13 coupled spinners, patterned with alternating inter-chain distances as in Fig. 13.1, we expect the crossover to the topologically non-trivial phase to occur for $d_1 = 5.0$ mm, $d_2 = 7.0$ mm and $d_{12} = 4.0$ mm. A plot of Eq. (13.15) implying this conclusion is shown in Fig. 13.4 while the energy spectra confirming the appearance of localized edge modes are shown in Fig. 13.3.

13.4 Outlook

Discussion of implementing the SSH ladder model of Chapter 12 (and hence the Kitaev wire) in a mechanical meta-materials system of reconfigurable spinners presented in this Chapter reflects an on-going collaboration with the research groups of Profs. C. and E. Prodan at NJIT and Yeshiva University, respectively. Past work by these collaborators has proven the feasibility of spinner systems for experimental realization of localized, topological edge modes. For instance, they have successfully implemented complex systems such as a bipartite honeycomb lattice exhibiting the Quantum Valley Hall Effect (QVHE) [222]. Experiments in the same group have further successfully realized aperiodic patterns in spinner chains producing excitation spectrum measurements in good agreement with theoretical predictions [7]. A preliminary experimental setup for the realization of the SSH ladder in the Prodan research group is shown in Fig. 13.5. This ladder consist of 26 freely rotating spinners and 4 fixed ends. As noted above, the interactions between nearest-neighbor spinners are realized through magnetic discs attached to their arms. Coupling between the two spinner SSH chains making up the ladder is therefore variable by changing the spacing between these magnets – the distance d_{12} can be varied as we have discussed and modeled in Sec. 13.3. Planned experiments include studying ladder spacings from $d_{12} = 1.0$ mm to 7.0 mm in 1.0 mm increments. In order to detect a localized mode, a spinner at some pre-determined site is actuated with low-power sinusoidal waves and the vibration strengths of other spinners in the system are subsequently measured by light-weight accelerometers attached

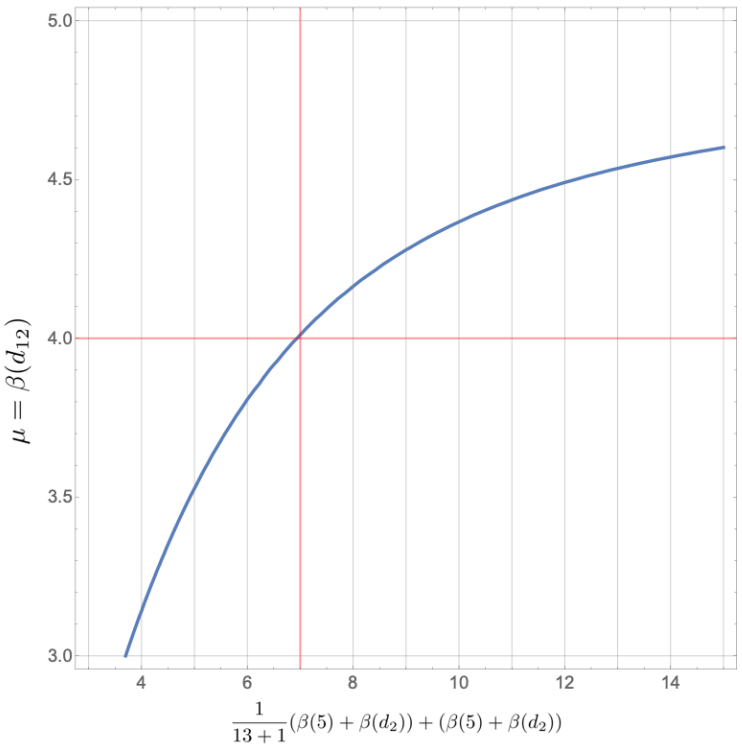

Figure 13.4: Plot of Eq. (13.15) for a spinner ladder consisting of 26 sites. Red lines denote a crossover point between a regime not having and having localized edge modes. The intersection of the three lines corresponds to Fig. 13.3 b) where the energy gap closes at the transition between the topologically trivial and the topologically non-trivial regime of the spinner ladder. In these calculations, we use functions α and β informed by the experimental work of collaborators in the Prodan research group.

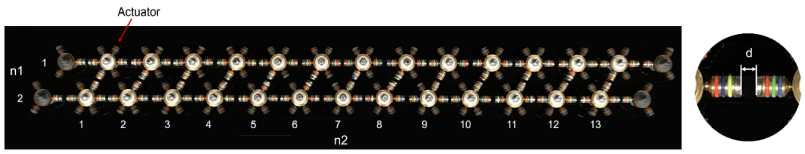

Figure 13.5: Photograph of the experimental spinner ladder configuration from the Prodan research group. Here, spinners and coupled arms are highlighted while the darker spinners at the edges are fixed and hence provide the system with a sharp, exact boundary.

to their arms. For example, in the topological phase of the spinner ladder actuating the spinner labeled by $(1, 1)$ in the notation of Fig. 13.5 is expected to result in rapidly diminishing amplitudes of vibration as spinners more than a few sites away from the actuator are measured. Additionally, full excitation spectra akin to Fig. 13.3 can be obtained by actuating and measuring each spinner.

At the time of writing of this thesis, experimental work on the spinner ladder is in progress. In the future, we hope to maintain this collaboration with the Prodan group and generalize the system under study to include more varied hoppings $t_{1,2} \neq t_{3,4}$, as in Sec. 12.4, and disorder or quasiperiodicity in the intra-chain coupling μ. Either could be implemented by physical patterning of spinners in real space i.e. a change in distances $d_{1,2}$ and d_{12}.

The platform provided to condensed matter theorists by relatively simple systems such as the spinner ladder described in this Chapter is a rather powerful one. Here, we have shown that it can be used to realize an analogue of the Kitaev (Majorana) wire which is in itself a celebrated and important model. Using the SSH ladder proposed in our work (Ref. [193] and Ch. 12) as an intermediate step sets up the spinner ladder as a veritable playground for many other models that may be "translated" in the same way. Thinking beyond realizations of topological systems, be they marked by dispersionless edge modes or more complex higher-order structures [217, 182, 223], the spinner ladder is particularly promising for studies of quasiperiodicity and similarly aperiodic structures. As these can be built-up one spinner at a time, one-dimensional patterns such as the Fibonacci sequence [152, 224] could be realized as well as two-dimensional tilings that may present a much more severe experimental challenge in other highly-controlled experimental systems such as ultracold atomic environments [225].

Chapter 14

References

[1] R. Carollo, M. Gold, X. Jiang, K. Padavic, S. Vishveshwara, C. Lannert, D. Aveline, and N. Lundblad. Shell-geometry Bose-Einstein condensates in microgravity. *APS March Meeting* E01.99131, May 2019.

[2] P. W. Anderson. Absence of diffusion in certain random lattices. *Phys. Rev.*, 109:1492–1505, Mar 1958.

[3] S. Ganeshan, J. H. Pixley, and S. Das Sarma. Nearest neighbor tight binding models with an exact mobility edge in one dimension. *Phys. Rev. Lett.*, 114:146601, Apr 2015.

[4] A. Avila, J. You, and Q. Zhou. Sharp phase transitions for the almost Mathieu operator. *Duke Math. J.*, 166(14):2697–2718, Oct 2017.

[5] F. Yang. Spectral transition line for the extended Harper's model in the positive Lyapunov exponent regime. *J. Funct. Anal.*, 275(3):712 – 734, Aug 2018.

[6] B. Gadway. Atom-optics approach to studying transport phenomena. *Phys. Rev. A*, 92:043606, Oct 2015.

[7] D. J. Apigo, K. Qian, C. Prodan, and E. Prodan. Topological edge modes by smart patterning. *Phys. Rev. Materials*, 2:124203, Dec 2018.

[8] U. R. Fischer and G. Baym. Vortex states of rapidly rotating dilute Bose-Einstein condensates. *Phys. Rev. Lett.*, 90:140402, Apr 2003.

[9] C. J. Pethick and H. Smith. *Bose-Einstein Condensation in Dilute Gases*. Cambridge University Press, 2 edition, 2008.

[10] S. J. Bereta, L. Madeira, V. S. Bagnato, and M. A. Caracanhas. Boseeinstein condensation in spherically symmetric traps. *American Journal of Physics*, 87(11):924–934, 2019.

[11] W. D. Phillips. Nobel lecture: Laser cooling and trapping of neutral atoms. *Rev. Mod. Phys.*, 70:721–741, Jul 1998.

[12] M. H. Anderson, J. R. Ensher, M. R. Matthews, and E. A. Wieman, C. E.and Cornell. Observation of Bose-Einstein condensation in a dilute atomic vapor. *Science*, 269(5221):198–201, Jul 1995.

[13] K. B. Davis, M. O. Mewes, M. R. Andrews, N. J. van Druten, D. S. Durfee, D. M. Kurn, and W. Ketterle. Bose-Einstein condensation in a gas of sodium atoms. *Phys. Rev. Lett.*, 75:3969–3973, Nov 1995.

[14] A. E. Leanhardt, T. A. Pasquini, M. Saba, A. Schirotzek, Y. Shin, D. Kielpinski, D. E. Pritchard, and W. Ketterle. Cooling Bose-Einstein condensates below 500 picokelvin. *Science*, 301(5639):1513–1515, Sep 2003.

[15] M. Lewenstein, A. Sanpera, V. Ahufinger, B. Damski, A. Sen(De), and U. Sen. Ultracold atomic gases in optical lattices: mimicking condensed matter physics and beyond. *Advances in Physics*, 56(2):243–379, Jul 2007.

[16] S. Jochim, M. Bartenstein, A. Altmeyer, G. Hendl, S. Riedl, C. Chin, J. Hecker Denschlag, and R. Grimm. Bose-Einstein condensation of molecules. *Science*, 302(5653):2101–2103, Dec 2003.

[17] M. Greiner, C. A. Regal, and D. S. Jin. A molecular Bose-Einstein condensate emerges from a Fermi sea. arXiv cond-mat/0311172, Nov 2003.

[18] D. G. Fried, T. C. Killian, L. Willmann, D. Landhuis, S. C. Moss, D. Kleppner, and T. J. Greytak. Bose-Einstein condensation of atomic hydrogen. *Phys. Rev. Lett.*, 81:3811–3814, Nov 1998.

[19] K. Casella, E. Scott, and D. Stamper-Kurn. Towards a quantum degenerate gas of ^{48}Ti. DAMOP Q07.00001, May 2019.

[20] A. Görlitz, J. M. Vogels, A. E. Leanhardt, C. Raman, T. L. Gustavson, J. R. Abo-Shaeer, A. P. Chikkatur, S. Gupta, S. Inouye, T. Rosenband, and W. Ketterle. Realization of Bose-Einstein condensates in lower dimensions. *Phys. Rev. Lett.*, 87:130402, Sep 2001.

[21] M. Greiner, I. Bloch, O. Mandel, T. W. Hänsch, and T. Esslinger. Exploring phase coherence in a 2d lattice of Bose-Einstein condensates. *Phys. Rev. Lett.*, 87:160405, Oct 2001.

[22] S. Dettmer, D. Hellweg, P. Ryytty, J. J. Arlt, W. Ertmer, K. Sengstock, D. S. Petrov, G. V. Shlyapnikov, H. Kreutzmann, L. Santos, and M. Lewenstein. Observation of phase fluctuations in elongated Bose-Einstein condensates. *Phys. Rev. Lett.*, 87:160406, Oct 2001.

[23] G. Hechenblaikner, J. M. Krueger, and C. J. Foot. Properties of quasi-two-dimensional condensates in highly anisotropic traps. *Phys. Rev. A*, 71:013604, Jan 2005.

[24] N. L. Smith, W. H. Heathcote, G. Hechenblaikner, E. Nugent, and C. J. Foot. Quasi-2D confinement of a BEC in a combined optical and magnetic potential. 38(3):223–235, Jan 2005.

[25] S. Gupta, K. W. Murch, K. L. Moore, T. P. Purdy, and D. M. Stamper-Kurn. Bose-Einstein condensation in a circular waveguide. *Phys. Rev. Lett.*, 95:143201, Sep 2005.

[26] A. Ramanathan, K. C. Wright, S. R. Muniz, M. Zelan, W. T. Hill, C. J. Lobb, K. Helmerson, W. D. Phillips, and G. K. Campbell. Superflow in a toroidal Bose-Einstein condensate: An atom circuit with a tunable weak link. *Phys. Rev. Lett.*, 106:130401, Mar 2011.

[27] A. L. Gaunt, T. F. Schmidutz, I. Gotlibovych, R. P. Smith, and Z. Hadzibabic. Bose-Einstein condensation of atoms in a uniform potential. *Phys. Rev. Lett.*, 110:200406, May 2013.

[28] Y. Shin, M. Saba, T. A. Pasquini, W. Ketterle, D. E. Pritchard, and A. E. Leanhardt. Atom interferometry with Bose-Einstein condensates in a double-well potential. *Phys. Rev. Lett.*, 92:050405, Feb 2004.

[29] J. Hecker Denschlag, J. E. Simsarian, H. Hffner, C. McKenzie, A. Browaeys, D. Cho, K. Helmerson, S. L. Rolston, and W. D. Phillips. A Bose-Einstein condensate in an optical lattice. *Journal of Physics B: Atomic, Molecular and Optical Physics*, 35(14):3095–3110, Jul 2002.

[30] C. Fort, F. S. Cataliotti, L. Fallani, F. Ferlaino, P. Maddaloni, and M. Inguscio. Collective excitations of a trapped Bose-Einstein condensate in the presence of a 1D optical lattice. *Phys. Rev. Lett.*, 90:140405, Apr 2003.

[31] D. Jaksch, C. Bruder, J. I. Cirac, C. W. Gardiner, and P. Zoller. Cold bosonic atoms in optical lattices. *Phys. Rev. Lett.*, 81:3108–3111, Oct 1998.

[32] H. Gimperlein, S. Wessel, J. Schmiedmayer, and L. Santos. Ultracold atoms in optical lattices with random on-site interactions. *Phys. Rev. Lett.*, 95:170401, Oct 2005.

[33] C. Fort, L. Fallani, V. Guarrera, J. E. Lye, M. Modugno, D. S. Wiersma, and M. Inguscio. Effect of optical disorder and single defects on the expansion of a Bose-Einstein condensate in a one-dimensional waveguide. *Phys. Rev. Lett.*, 95:170410, Oct 2005.

[34] P. Massignan and Y. Castin. Three-dimensional strong localization of matter waves by scattering from atoms in a lattice with a confinement-induced resonance. *Phys. Rev. A*, 74:013616, Jul 2006.

[35] M. White, M. Pasienski, D. McKay, S. Q. Zhou, D. Ceperley, and B. DeMarco. Strongly interacting bosons in a disordered optical lattice. *Phys. Rev. Lett.*, 102:055301, Feb 2009.

[36] L. W. Clark, L. Feng, and C. Chin. Universal space-time scaling symmetry in the dynamics of bosons across a quantum phase transition. *Science*, 354(6312):606–610, Nov 2016.

[37] C. Raman, J. R. Abo-Shaeer, J. M. Vogels, K. Xu, and W. Ketterle. Vortex nucleation in a stirred Bose-Einstein condensate. *Phys. Rev. Lett.*, 87:210402, Nov 2001.

[38] E. Hodby, G. Hechenblaikner, S. A. Hopkins, O. M. Maragò, and C. J. Foot. Vortex nucleation in Bose-Einstein condensates in an oblate, purely magnetic potential. *Phys. Rev. Lett.*, 88:010405, Dec 2001.

[39] P. Rosenbusch, V. Bretin, and J. Dalibard. Dynamics of a single vortex line in a Bose-Einstein condensate. *Phys. Rev. Lett.*, 89:200403, Oct 2002.

[40] P. C. Haljan, I. Coddington, P. Engels, and E. A. Cornell. Driving Bose-Einstein condensate vorticity with a rotating normal cloud. *Phys. Rev. Lett.*, 87:210403, Nov 2001.

[41] C. Raman, J. R. Abo-Shaeer, J. M. Vogels, K. Xu, and W. Ketterle. Vortex nucleation in a stirred Bose-Einstein condensate. *Phys. Rev. Lett.*, 87:210402, Nov 2001.

[42] O. Oladehin. *Producing smooth flow in atom circuits by stirring.* Master's thesis, Spring 2018.

[43] Y. Wang, X. Zhang, T. A. Corcovilos, A. Kumar, and D. S. Weiss. Coherent addressing of individual neutral atoms in a 3D optical lattice. *Phys. Rev. Lett.*, 115:043003, Jul 2015.

[44] R. Dumke, M. Volk, T. Müther, F. B. J. Buchkremer, G. Birkl, and W. Ertmer. Micro-optical realization of arrays of selectively addressable dipole traps: A scalable configuration for quantum computation with atomic qubits. *Phys. Rev. Lett.*, 89:097903, Aug 2002.

[45] H. C. Nägerl, D. Leibfried, H. Rohde, G. Thalhammer, J. Eschner, F. Schmidt-Kaler, and R. Blatt. Laser addressing of individual ions in a linear ion trap. *Phys. Rev. A*, 60:145–148, Jul 1999.

[46] J. Beugnon, C. Tuchendler, H. Marion, A. Gaetan, Y. Miroshnychenko, Y. R.P. Sortais, A. M. Lance, Matthew P.A. Jones, G. Messin, A. Browaeys, and P. Grainger. Two-dimensional transport and transfer of a single atomic quit in optical tweezers. *Nature Phys.*, 3:696, Aug 2007.

[47] T. L. Gustavson, A. P. Chikkatur, A. E. Leanhardt, A. Görlitz, S. Gupta, D. E. Pritchard, and W. Ketterle. Transport of Bose-Einstein condensates with optical tweezers. *Phys. Rev. Lett.*, 88:020401, Dec 2001.

[48] H. Labuhn, S. Ravets, D. Barredo, L. Béguin, F. Nogrette, T. Lahaye, and A. Browaeys. Single-atom addressing in microtraps for quantum-state engineering using Rydberg atoms. *Phys. Rev. A*, 90:023415, Aug 2014.

[49] K. S. Kleinbach, F. Engel, T. Dieterle, R. Löw, T. Pfau, and F. Meinert. Ionic impurity in a Bose-Einstein condensate at submicrokelvin temperatures. *Phys. Rev. Lett.*, 120:193401, May 2018.

[50] J.-Y. Choi, S. Hild, J. Zeiher, P. Schauß, A. Rubio-Abadal, T. Yefsah, V. Khemani, D. A. Huse, I. Bloch, and C. Gross. Exploring the many-body localization transition in two dimensions. *Science*, 352(6293):1547–1552, Jun 2016.

[51] S. S. Kondov, W. R. McGehee, W. Xu, and B. DeMarco. Disorder-induced localization in a strongly correlated atomic Hubbard gas. *Phys. Rev. Lett.*, 114:083002, Feb 2015.

[52] M. P.G. Robbins, N. Afshordi, and R. B. Mann. Bose-Einstein condensates as gravitational wave detectors. *Journal of Cosmology and Astroparticle Physics*, 2019(07):032–032, Jul 2019.

[53] A. Di Carli, C. D. Colquhoun, S. Kuhr, and E. Haller. Interferometric measurement of micro-g acceleration with levitated atoms. *New Journal of Physics*, 21(5):053028, May 2019.

[54] S. Boixo, A. Datta, M. J. Davis, A. Shaji, A. B. Tacla, and C. M. Caves. Quantum-limited metrology and Bose-Einstein condensates. *Phys. Rev. A*, 80:032103, Sep 2009.

[55] M. F. Riedel, P. Bohl, Y. Li, T. W. Hansch, A. Sinatra, and P. Treutlein. Atom-chip based generation of entanglement for quantum metrology. *Nature*, 464:1170, Apr 2010.

[56] N. Lundblad, R. A. Carollo, C. Lannert, M. J. Gold, X. Jiang, D. Paseltiner, N. Sergay, and D. C. Aveline. Shell potentials for microgravity Bose-Einstein condensates. *npj Microgravity*, 5, Apr 2019.

[57] A. E. Leanhardt, A. Görlitz, A. P. Chikkatur, D. Kielpinski, Y. Shin, D. E. Pritchard, and W. Ketterle. Imprinting vortices in a Bose-Einstein condensate using topological phases. *Phys. Rev. Lett.*, 89:190403, Oct 2002.

[58] E. C. Samson, K. E. Wilson, Z. L. Newman, and B. P. Anderson. Deterministic creation, pinning, and manipulation of quantized vortices in a Bose-Einstein condensate. *Phys. Rev. A*, 93:023603, Feb 2016.

[59] O. Gessner and A. F. Vilesov. Imaging quantum vortices in superfluid helium droplets. *Annual Review of Physical Chemistry*, 70(1):173–198, 2019. PMID: 31174460.

[60] S. Grebenev, J. P. Toennies, and A. F. Vilesov. Superfluidity within a small helium-4 cluster: The microscopic Andronikashvili experiment. *Science*, 279(5359):2083–2086, Mar 1998.

[61] J. P. Toennies, A. F. Vilesov, and B. K. Whaley. Superfluid helium droplets: An ultracold nanolaboratory. *Physics Today*, 54(2):31–37, 2001.

[62] A. K. Verma, R. Pandit, and M. E. Brachet. Rotating self-gravitating Bose-Einstein condensates with a crust: a minimal model for pulsar glitches, 2020. arXiv 2005.13310.

[63] V. Khomenko and B. Haskell. Modelling pulsar glitches: The hydrodynamics of superfluid vortex avalanches in neutron stars. *Publications of the Astronomical Society of Australia*, 35:E020, May 2018.

[64] A. Aftalion and T. Riviere. Vortex energy and vortex bending for a rotating Bose-Einstein condensate. *Phys. Rev. A*, 64:043611, Sep 2001.

[65] D.J. Acheson and F.D.J. Acheson. *Elementary Fluid Dynamics*.

[66] H. Lamb. *Hydrodynamics*. Dover Books on Physics. Dover publications, 1945.

[67] N.-E. Guenther, P. Massignan, and A. L. Fetter. Quantized superfluid vortex dynamics on cylindrical surfaces and planar annuli. *Phys. Rev. A*, 96:063608, Dec 2017.

[68] A. L. Fetter. Low-lying superfluid states in a rotating annulus. *Phys. Rev.*, 153:285–296, Jan 1967.

[69] K. W. Schwarz. Three-dimensional vortex dynamics in superfluid ^{4}He: Line-line and line-boundary interactions. *Phys. Rev. B*, 31:5782–5804, May 1985.

[70] P. G. Kevrekidis, W. Wang, R. Carretero-González, D. J. Frantzeskakis, and S. Xie. Vortex precession dynamics in general radially symmetric potential traps in two-dimensional atomic Bose-Einstein condensates. *Phys. Rev. A*, 96:043612, Oct 2017.

[71] B. P. Anderson, P. C. Haljan, C. E. Wieman, and E. A. Cornell. Vortex precession in Bose-Einstein condensates: Observations with filled and empty cores. *Phys. Rev. Lett.*, 85:2857–2860, Oct 2000.

[72] D. V. Freilich, D. M. Bianchi, A. M. Kaufman, T. K. Langin, and D. S. Hall. Real-time dynamics of single vortex lines and vortex dipoles in a Bose-Einstein condensate. *Science*, 329(5996):1182–1185, Sep 2010.

[73] J.-K. Kim and A. L. Fetter. Dynamics of a single ring of vortices in two-dimensional trapped Bose-Einstein condensates. *Phys. Rev. A*, 70:043624, Oct 2004.

[74] A. A. Svidzinsky and A. L. Fetter. Dynamics of a vortex in a trapped Bose-Einstein condensate. *Phys. Rev. A*, 62:063617, Nov 2000.

[75] B. Jackson, J. F. McCann, and C. S. Adams. Vortex line and ring dynamics in trapped Bose-Einstein condensates. *Phys. Rev. A*, 61:013604, Dec 1999.

[76] D. M. Jezek and H. M. Cataldo. Vortex velocity field in inhomogeneous media: A numerical study in Bose-Einstein condensates. *Phys. Rev. A*, 77:043602, Apr 2008.

[77] K. Padavic, K. Sun, C. Lannert, and S. Vishveshwara. Physics of hollow Bose-Einstein condensates. *Europhys. Lett.*, 120(2):20004, Oct 2017.

[78] K. Sun, K. Padavic, F. Yang, S. Vishveshwara, and C. Lannert. Static and dynamic properties of shell-shaped condensates. *Phys. Rev. A*, 98:013609, Jul 2018.

[79] K. Padavic, K. Sun, C. Lannert, and S. Vishveshwara. Vortex-antivortex physics in shell-shaped Bose-Einstein condensates, 2020. arXiv 2005.13030.

[80] D. van Oosten, P. van der Straten, and H. T. C. Stoof. Quantum phases in an optical lattice. *Phys. Rev. A*, 63:053601, Apr 2001.

[81] M. Greiner, O. Mandel, T. Esslinger, T. W. Hansch, and I. Bloch. Quantum phase transition from a superfluid to a Mott insulator in a gas of ultracold atoms. *Nature*, 415:39, Jan 2002.

[82] M. Greiner. *Ultracold quantum gases in three-dimensional optical lattice potentials*. PhD thesis, April 2003.

[83] Matthew P. A. Fisher, Peter B. Weichman, G. Grinstein, and Daniel S. Fisher. Boson localization and the superfluid-insulator transition. *Phys. Rev. B*, 40:546–570, Jul 1989.

[84] K. Sheshadri, H. R Krishnamurthy, R. Pandit, and T. V Ramakrishnan. Superfluid and insulating phases in an interacting-boson model: Mean-field theory and the RPA. *Europhys. Lett,*, 22(4):257–263, May 1993.

[85] J. K Freericks and H. Monien. Phase diagram of the Bose-Hubbard model. *Europhy. Lett.*, 26(7):545–550, jun 1994.

[86] G. G. Batrouni, V. Rousseau, R. T. Scalettar, M. Rigol, A. Muramatsu, P. J. H. Denteneer, and M. Troyer. Mott domains of bosons confined on optical lattices. *Phys. Rev. Lett.*, 89:117203, Aug 2002.

[87] B. DeMarco, C. Lannert, S. Vishveshwara, and T.-C. Wei. Structure and stability of Mott-insulator shells of bosons trapped in an optical lattice. *Phys. Rev. A*, 71:063601, Jun 2005.

[88] G. K. Campbell, J. Mun, M. Boyd, P. Medley, A. E. Leanhardt, L. G. Marcassa, D. E. Pritchard, and W. Ketterle. Imaging the Mott insulator shells by using atomic clock shifts. *Science*, 313(5787):649–652, Aug 2006.

[89] R. A. Barankov, C. Lannert, and S. Vishveshwara. Coexistence of superfluid and Mott phases of lattice bosons. *Phys. Rev. A*, 75:063622, Jun 2007.

[90] K. Sun, C. Lannert, and S. Vishveshwara. Probing condensate order in deep optical lattices. *Phys. Rev. A*, 79:043422, Apr 2009.

[91] K. Mølmer. Bose condensates and Fermi gases at zero temperature. *Phys. Rev. Lett.*, 80:1804–1807, Mar 1998.

[92] S. Ospelkaus, C. Ospelkaus, L. Humbert, K. Sengstock, and K. Bongs. Tuning of heteronuclear interactions in a degenerate Fermi-Bose mixture. *Phys. Rev. Lett.*, 97:120403, Sep 2006.

[93] B. Van Schaeybroeck and A. Lazarides. Trapped phase-segregated Bose-Fermi mixtures and their collective excitations. *Phys. Rev. A*, 79:033618, Mar 2009.

[94] F. Weber. Strange quark matter and compact stars. *Progress in Particle and Nuclear Physics*, 54(1):193 – 288, Mar 2005.

[95] C. J. Pethick, T. Schaefer, and A. Schwenk. Bose-Einstein condensates in neutron stars, 2015. arXiv 1507.05839.

[96] Y. Colombe, E. Knyazchyan, O. Morizot, B. Mercier, V. Lorent, and H. Perrin. Ultracold atoms confined in rf-induced two-dimensional trapping potentials. *Europhys. Lett.*, 67(4):593–599, Aug 2004.

[97] K. Merloti, R. Dubessy, L. Longchambon, A. Perrin, P.-E. Pottie, V. Lorent, and H. Perrin. A two-dimensional quantum gas in a magnetic trap. *New Journal of Physics*, 15(3):033007, mar 2013.

[98] O. Zobay and B. M. Garraway. Two-dimensional atom trapping in field-induced adiabatic potentials. *Phys. Rev. Lett.*, 86:1195–1198, Feb 2001.

[99] O. Zobay and B. M. Garraway. Atom trapping and two-dimensional Bose-Einstein condensates in field-induced adiabatic potentials. *Phys. Rev. A*, 69:023605, Feb 2004.

[100] G. Nandi, R. Walser, E. Kajari, and W. P. Schleich. Dropping cold quantum gases on Earth over long times and large distances. *Phys. Rev. A*, 76:063617, Dec 2007.

[101] M. Mihm, J. P. Marburger, A. Wenzlawski, O. Hellmig, O. Anton, K. Dringshoff, M. Krutzik, A. Peters, P. Windpassinger, and the MAIUS Team. ZERODUR based optical systems for quantum gas experiments in space. *Acta Astronautica*, 159:166 – 169, Jun 2019.

[102] D. Becker, M. D. Lachmann, E. M. Rasel, and the MAIUS Team. Space-borne Bose-Einstein condensation for precision interferometry. *Nature*, 562:391, Oct 2018.

[103] T.G. Wang, A.V. Anilkumar, C.P. Lee, and K.C. Lin. Core-centering of compound drops in capillary oscillations: Observations on USML-1 experiments in space. *Journal of Colloid and Interface Science*, 165(1):19 – 30, Jun 1994.

[104] M. L. Chiofalo, S. Succi, and M. P. Tosi. Ground state of trapped interacting Bose-Einstein condensates by an explicit imaginary-time algorithm. *Phys. Rev. E*, 62:7438–7444, Nov 2000.

[105] U. Al Khawaja, C. J. Pethick, and H. Smith. Surface of a Bose-Einstein condensed atomic cloud. *Phys. Rev. A*, 60:1507–1512, Aug 1999.

[106] M.-O. Mewes, M. R. Andrews, N. J. van Druten, D. M. Kurn, D. S. Durfee, C. G. Townsend, and W. Ketterle. Collective excitations of a Bose-Einstein condensate in a magnetic trap. *Phys. Rev. Lett.*, 77:988–991, Aug 1996.

[107] M. M. Cerimele, M. L. Chiofalo, F. Pistella, S. Succi, and M. P. Tosi. Numerical solution of the Gross-Pitaevskii equation using an explicit finite-difference scheme: An application to trapped Bose-Einstein condensates. *Phys. Rev. E*, 62:1382–1389, Jul 2000.

[108] S. Stringari. Collective excitations of a trapped Bose-condensed gas. *Phys. Rev. Lett.*, 77:2360–2363, Sep 1996.

[109] D. S. Jin, J. R. Ensher, M. R. Matthews, C. E. Wieman, and E. A. Cornell. Collective excitations of a Bose-Einstein condensate in a dilute gas. *Phys. Rev. Lett.*, 77:420–423, Jul 1996.

[110] D. S. Lobser, A. E. S. Barentine, E. A. Cornell, and H.J. Lewandowski. Observation of a persistent non-equilibrium state in cold atoms. *Nature Physics*, (11):1009, Oct 2015.

[111] C. J. E. Straatsma, V. E. Colussi, M. J. Davis, D. S. Lobser, M. J. Holland, D. Z. Anderson, H. J. Lewandowski, and E. A. Cornell. Collapse and revival of the monopole mode of a degenerate Bose gas in an isotropic harmonic trap. *Phys. Rev. A*, 94:043640, Oct 2016.

[112] M. Cozzini, B. Jackson, and S. Stringari. Vortex signatures in annular Bose-Einstein condensates. *Phys. Rev. A*, 73:013603, Jan 2006.

[113] R. Dubessy, T. Liennard, P. Pedri, and H. Perrin. Critical rotation of an annular superfluid Bose-Einstein condensate. *Phys. Rev. A*, 86:011602, Jul 2012.

[114] J. Schneider and A. Schenzle. Output from an atom laser: theory vs. experiment. *App. Phys. B*, 69:353, Dec 1991.

[115] A. M. Turner, V. Vitelli, and D. R. Nelson. Vortices on curved surfaces. *Rev. Mod. Phys.*, 82:1301–1348, Apr 2010.

[116] J.-M. Park and T. C. Lubensky. Topological defects on fluctuating surfaces: General properties and the Kosterlitz-Thouless transition. *Phys. Rev. E*, 53:2648–2664, Mar 1996.

[117] K. Kasamatsu, M. Tsubota, and M. Ueda. Giant hole and circular superflow in a fast rotating Bose-Einstein condensate. *Phys. Rev. A*, 66:053606, Nov 2002.

[118] A. L. Fetter, B. Jackson, and S. Stringari. Rapid rotation of a Bose-Einstein condensate in a harmonic plus quartic trap. *Phys. Rev. A*, 71:013605, Jan 2005.

[119] H. Fu and E. Zaremba. Transition to the giant vortex state in a harmonic-plus-quartic trap. *Phys. Rev. A*, 73:013614, Jan 2006.

[120] J. A. Sauls. *Superfluidity in the Interiors of Neutron Stars*, pages 457–490. Springer Netherlands, Dordrecht, 1989.

[121] A. Tononi and L. Salasnich. Bose-Einstein condensation on the surface of a sphere. *Phys. Rev. Lett.*, 123:160403, Oct 2019.

[122] R. D. Kamien. The geometry of soft materials: a primer. *Rev. Mod. Phys.*, 74:953–971, Sep 2002.

[123] M. Nestler, I. Nitschke, S. Praetorius, and A. Voigt. Orientational order on surfaces: The coupling of topology, geometry, and dynamics. *Journal of Nonlinear Science*, 28(1):147–191, Jul 2018.

[124] V. Vitelli and D. R. Nelson. Nematic textures in spherical shells. *Phys. Rev. E*, 74:021711, Aug 2006.

[125] S. Prabhakar, R. P. Singh, S. Gautam, and D. Angom. Annihilation of vortex dipoles in an oblate Bose-Einstein condensate. *Journal of Physics B: Atomic, Molecular and Optical Physics*, 46(12):125302, May 2013.

[126] A. Aftalion and I. Danaila. Three-dimensional vortex configurations in a rotating Bose-Einstein condensate. *Phys. Rev. A*, 68:023603, Aug 2003.

[127] Pricoupenko L. Modugno, M. and Y. Castin. Bose-Einstein condensates with a bent vortex in rotating traps. *Eur. Phys. J. D*, 22:235, Feb 2003.

[128] A. Aftalion and R. L. Jerrard. Shape of vortices for a rotating Bose-Einstein condensate. *Phys. Rev. A*, 66:023611, Aug 2002.

[129] Makoto T., Kenichi K., and Michikazu K. Quantized vortices in superfluid helium and atomic Bose-Einstein condensates, 2010. arXiv 1004.5458.

[130] N.R. Cooper. Rapidly rotating atomic gases. *Advances in Physics*, 57(6):539–616, 2008.

[131] A. L. Fetter. Rotating trapped Bose-Einstein condensates. *Laser Physics*, 18(1):1–11, Jan 2008.

[132] V. Dwivedi and V. Chua. Of bulk and boundaries: Generalized transfer matrices for tight-binding models, 2015. arXiV 1510.04279.

[133] D. R. Hofstadter. Energy levels and wave functions of Bloch electrons in rational and irrational magnetic fields. *Phys. Rev. B*, 14:2239–2249, Sep 1976.

[134] S. Aubry and G. Andre. Analyticity breaking and Anderson localization in incommensurate lattices. *Ann. Israel Phys. Soc.*, 3(133), Dec 1980.

[135] D J Thouless. A relation between the density of states and range of localization for one dimensional random systems. *Journal of Physics C: Solid State Physics*, 5(1):77–81, Jan 1972.

[136] J. Avron and B. Simon. Almost periodic Schrodinger operators ii. the integrated density of states. *Duke Math. J.*, 50(1):369–391, 03 1983.

[137] J.B Sokoloff. Unusual band structure, wave functions and electrical conductance in crystals with incommensurate periodic potentials. *Physics Reports*, 126(4):189 – 244, Sep 1985.

[138] B. Simon. Fifteen problems in mathematical physics. *Oberwolfach Anniversary Volume*, 187(3):423–454, 1984.

[139] International Mathematical Union. Fields medals 2014, 2014.

[140] S. Jitomirskaya. Almost everything about the almost Mathieu operator. *Proceedings of XI International Congress of Mathematical Physics*, pages 373–382, 1995.

[141] S. Jitomirskaya and I. Krasovsky. Critical almost Mathieu operator: hidden singularity, gap continuity, and the Hausdorff dimension of the spectrum, 2019. arXiv 1909.04429.

[142] S. Jitomirskaya and W. Liu. Universal hierarchical structure of quasiperiodic eigenfunctions. *Annals of Mathematics*, 187(3):721–776, Mar 2018.

[143] S. Jitomirskaya and W. Liu. Universal reflective-hierarchical structure of quasiperiodic eigenfunctions and sharp spectral transition in phase, 2018. arXiv 1802.00781.

[144] S. Jitomirskaya, H. Kruger, and W. Liu. Exact dynamical decay rate for the almost Mathieu operator, 2018. arXiv 1812.02860.

[145] S. Jitomirskaya and W. Liu. A lower bound on the Lyapunov exponent for the generalized Harper's model. *Journal of Statistical Physics*, 166(3):609–617, Feb 2017.

[146] C. A. Marx, L. H. Shou, and J. L. Wellens. Subcritical behavior for quasi-periodic Schrdinger cocycles with trigonometric potentials, 2015. arXiv 1509.05279.

[147] A. Avila, S. Jitomirskaya, and C. A. Marx. Spectral theory of extended Harper's model and a question by Erdős and Szekeres. *Inventiones mathematicae*, 210(1):283–339, Oct 2017.

[148] R. Han. Absence of point spectrum for the self-dual extended Harpers model. *International Mathematics Research Notices*, 2018(9):2801–2809, Jan 2017.

[149] R. Han and S. Jitomirskaya. Full measure reducibility and localization for quasiperiodic Jacobi operators: A topological criterion. *Advances in Mathematics*, 319:224 – 250, Oct 2017.

[150] S. Jitomirskaya, D. A. Koslover, and M. S. Schulteis. Localization for a family of one-dimensional quasiperiodic operators of magnetic origin. *Ann. Henri Poincare*, 6:103–124, Feb 2005.

[151] D. Damanik, A. Gorodetski, and W. Yessen. The Fibonacci Hamiltonian. *Inventiones mathematicae*, 206(3):629–692, Dec 2016.

[152] Y. E. Kraus and O. Zilberberg. Topological equivalence between the Fibonacci quasicrystal and the Harper model. *Phys. Rev. Lett.*, 109:116404, Sep 2012.

[153] Y. Lahini, R. Pugatch, F. Pozzi, M. Sorel, R. Morandotti, N. Davidson, and Y. Silberberg. Observation of a localization transition in quasiperiodic photonic lattices. *Phys. Rev. Lett.*, 103:013901, Jun 2009.

[154] D. Jaksch and P. Zoller. Creation of effective magnetic fields in optical lattices: the Hofstadter butterfly for cold neutral atoms. *New Journal of Physics*, 5(1):56, May 2003.

[155] H. Miyake, G. A. Siviloglou, C. J. Kennedy, W. C. Burton, and W. Ketterle. Realizing the Harper Hamiltonian with laser-assisted tunneling in optical lattices. *Phys. Rev. Lett.*, 111:185302, Oct 2013.

[156] G. Roati, C. D'Errico, L. Fallani, M. Fattori, C. For, M. Zaccanti, G. Modugno, M. Modugno, and M. Ignuscio. Anderson localization of a non-interacting Bose-Einstein condensate. *Nature*, 453:895–898, Jun 2008.

[157] F. A. An, E. J. Meier, and B. Gadway. Diffusive and arrested transport of atoms under tailored disorder. *Nat. Commun.*, 8:325, Aug 2017.

[158] F. A. An, E. J. Meier, and B. Gadway. Engineering a flux-dependent mobility edge in disordered zigzag chains. *Phys. Rev. X*, 8:031045, Aug 2018.

[159] X. Ni, K. Chen, M. Weiner, D. J. Apigo, C. Prodan, A. Alu, E. Prodan, and A. B. Khanikaev. Observation of Hofstadter butterfly and topological edge states in reconfigurable quasi-periodic acoustic crystals. *Commun. Phys. 2*, 55, Jun 2019.

[160] D. J. Apigo, W. Cheng, K. F. Dobiszewski, E. Prodan, and C. Prodan. Observation of topological edge modes in a quasiperiodic acoustic waveguide. *Phys. Rev. Lett.*, 122:095501, Mar 2019.

[161] F. A. An, K. Padavic, E. J Meier, S. Hegde, S. Ganeshan, J. H. Pixley, S. Vishveshwara, and B. Gadway. Observation of tunable mobility edges in generalized Aubry-Andre lattices. In preparation, 2019.

[162] X. Li, X. Li, and S. Das Sarma. Mobility edges in one-dimensional bichromatic incommensurate potentials. *Phys. Rev. B*, 96:085119, Aug 2017.

[163] J. Biddle and S. Das Sarma. Predicted mobility edges in one-dimensional incommensurate optical lattices: An exactly solvable model of Anderson localization. *Phys. Rev. Lett.*, 104:070601, Feb 2010.

[164] H. P. Lüschen, S. Scherg, T. Kohlert, M. Schreiber, P. Bordia, X. Li, S. Das Sarma, and I. Bloch. Single-particle mobility edge in a one-dimensional quasiperiodic optical lattice. *Phys. Rev. Lett.*, 120:160404, Apr 2018.

[165] E. J. Meier, F. A. An, and B. Gadway. Atom-optics simulator of lattice transport phenomena. *Phys. Rev. A*, 93:051602, May 2016.

[166] N. Gemelke, X. Zhang, C.-L. Hung, and C. Chin. *In situ* observation of incompressible Mott-insulating domains in ultracold atomic gases. *Nature*, 460, Aug 2009.

[167] R. Ozeri, N. Katz, J. Steinhauer, and N. Davidson. Colloquium: Bulk Bogoliubov excitations in a Bose-Einstein condensate. *Rev. Mod. Phys.*, 77:187–205, Apr 2005.

[168] F. A. An, E. J. Meier, J. Ang'ong'a, and B. Gadway. Correlated dynamics in a synthetic lattice of momentum states. *Phys. Rev. Lett.*, 120:040407, Jan 2018.

[169] Thierry Giamarchi. *Quantum physics in one dimension.* Oxford University Press, Oxford, 1st edition, Nov 2003.

[170] H. Hennig and R. Fleischmann. Nature of self-localization of Bose-Einstein condensates in optical lattices. *Phys. Rev. A*, 87:033605, Mar 2013.

[171] M. Bruderer, W. Bao, and D. Jaksch. Self-trapping of impurities in Bose-Einstein condensates: Strong attractive and repulsive coupling. *Europhys. Lett.*, 82(3):30004, Apr 2008.

[172] B. Deissler, M. Zaccanti, G. Roati, C. D'Errico, M. Fattori, M. Modugno, G. Modugno, and M. Inguscio. Delocalization of a disordered bosonic system by repulsive interactions. *Nat. Phys.*, 6(5):354–358, May 2010.

[173] S. V. Rajagopal, T. Shimasaki, P. Dotti, M. Račiūnas, R. Senaratne, E. Anisimovas, A. Eckardt, and D. M. Weld. Phasonic spectroscopy of a quantum gas in a quasicrystalline lattice. *Phys. Rev. Lett.*, 123:223201, Nov 2019.

[174] W. P. Su, J. R. Schrieffer, and A. J. Heeger. Solitons in polyacetylene. *Phys. Rev. Lett.*, 42:1698–1701, Jun 1979.

[175] A. J. Heeger, S. Kivelson, J. R. Schrieffer, and W. P. Su. Solitons in conducting polymers. *Rev. Mod. Phys.*, 60:781–850, Jul 1988.

[176] M. Atala, M. Aidelsburger, J. T. Barreiro, D. Abanin, T. Kitagawa, E. Demler, and I. Bloch. Direct measurement of the Zak phase in topological bloch bands. *Nature Physics*, 9(12):795, Oct 2013.

[177] M. Lohse, C. Schweizer, O. Zilberberg, M. Aidelsburger, and I. Bloch. A Thouless quantum pump with ultracold bosonic atoms in an optical superlattice. *Nature Physics*, 12(4):350, Dec 2016.

[178] S. Nakajima, T. Tomita, S. Taie, T. Ichinose, H. Ozawa, L. Wang, M. Troyer, and Y. Takahashi. Topological Thouless pumping of ultracold fermions. *Nature Physics*, 12(4):296, Jan 2016.

[179] L. Wang, M. Troyer, and X. Dai. Topological charge pumping in a one-dimensional optical lattice. *Phys. Rev. Lett.*, 111:026802, Jul 2013.

[180] Z. Wang, Y. Chong, J. D. Joannopoulos, and M. Soljačić. Observation of unidirectional backscattering-immune topological electromagnetic states. *Nature*, 461:772 EP, Oct 2009.

[181] R. Süsstrunk and S. D. Huber. Observation of phononic helical edge states in a mechanical topological insulator. *Science*, 349(6243):47–50, Jul 2015.

[182] W. C. Peterson, W. A. Benalcazar, T. L. Hughes, and G. Bahl. Demonstration of a quantized microwave quadrupole insulator with topologically protected corner states. *Nature*, 555, Mar 2017.

[183] R. Chaunsali, E. Kim, A. Thakkar, P. G. Kevrekidis, and J. Yang. Demonstrating an in situ topological band transition in cylindrical granular chains. *Phys. Rev. Lett.*, 119:024301, Jul 2017.

[184] E. J. Meier, F. A. An, and B. Gadway. Observation of the topological soliton state in the Su-Schrieffer-Heeger model. *Nature Communications*, 7:13986, Dec 2016.

[185] M. Leder, C. Grossert, L. Sitta, M. Genske, A. Rosch, and M. Weitz. Real-space imaging of a topologically protected edge state with ultracold atoms in an amplitude-chirped optical lattice. *Nature Communications*, 7:13112, Oct 2016.

[186] T. Kitagawa, M. A. Broome, A. Fedrizzi, M. S. Rudner, E. Berg, I. Kassal, A. Aspuru-Guzik, E. Demler, and A. G. White. Observation of topologically protected bound states in photonic quantum walks. *Nature Communications*, 3:882, Jun 2012.

[187] L. Li, Z. Xu, and S. Chen. Topological phases of generalized Su-Schrieffer-Heeger models. *Phys. Rev. B*, 89:085111, Feb 2014.

[188] S.-L. Zhang and Q. Zhou. Two-leg Su-Schrieffer-Heeger chain with glide reflection symmetry. *Phys. Rev. A*, 95:061601, Jun 2017.

[189] J.-Y. Zou and B.-G. Liu. Hidden chiral symmetry protected $\mathbb{Z} \oplus \mathbb{Z}$ topological insulators in a ladder dimer model. June 2015. ArXiv 1506.06626.

[190] J.-W. Rhim, J. H. Bardarson, and R.-J. Slager. Unified bulk-boundary correspondence for band insulators. *Phys. Rev. B*, 97:115143, Mar 2018.

[191] D. Bercioux, O. Dutta, and E. Rico. Solitons in one-dimensional lattices with a flat band. *Annalen der Physik*, 529(9):1600262, 2017.

[192] J. I. Vayrynen and T. Ojanen. Chiral topological phases and fractional domain wall excitations in one-dimensional chains and wires. *Phys. Rev. Lett.*, 107:166804, Oct 2011.

[193] K. Padavić, S. S. Hegde, W. DeGottardi, and S. Vishveshwara. Topological phases, edge modes, and the Hofstadter butterfly in coupled Su-Schrieffer-Heeger systems. *Phys. Rev. B*, 98:024205, Jul 2018.

[194] A.Y. Kitaev. Unpaired Majorana fermions in quantum wires. *Phys. Usp.*, 44:131, 2001.

[195] J. Alicea. New directions in the pursuit of Majorana fermions in solid state systems. *Reports on Progress in Physics*, 75(7):076501, Jun 2012.

[196] W. DeGottardi, M. Thakurathi, S. Vishveshwara, and D. Sen. Majorana fermions in superconducting wires: Effects of long-range hopping, broken time-reversal symmetry, and potential landscapes. *Phys. Rev. B*, 88:165111, Oct 2013.

[197] S. R. Elliott and M. Franz. *Colloquium*: Majorana fermions in nuclear, particle, and solid-state physics. *Rev. Mod. Phys.*, 87:137, Feb 2015.

[198] M. Leijnse and K. Flensberg. Introduction to topological superconductivity and Majorana fermions. *Semiconductor Science and Technology*, 27(12):124003, Nov 2012.

[199] W. DeGottardi, D. Sen, and S. Vishveshwara. Majorana fermions in superconducting 1d systems having periodic, quasiperiodic, and disordered potentials. *Phys. Rev. Lett.*, 110:146404, 2013.

[200] M. Aidelsburger, M. Atala, M. Lohse, J. T. Barreiro, B. Paredes, and I. Bloch. Realization of the Hofstadter Hamiltonian with ultracold atoms in optical lattices. *Phys. Rev. Lett.*, 111:185301, 2013.

[201] K. Osterloh, M. Baig, L. Santos, P. Zoller, and M. Lewenstein. Cold atoms in non-abelian gauge potentials: From the Hofstadter "moth" to lattice gauge theory. *Phys. Rev. Lett.*, 95:010403, Jun 2005.

[202] R. Wakatsuki, M. Ezawa, Y. Tanaka, and N. Nagaosa. Fermion fractionalization to Majorana fermions in a dimerized Kitaev superconductor. *Phys. Rev. B*, 90:014505, Jul 2014.

[203] V. Gurarie. Single-particle Green's functions and interacting topological insulators. *Phys. Rev. B*, 83:085426, Feb 2011.

[204] W. DeGottardi, D. Sen, and S. Vishveshwara. Topological phases, Majorana modes and quench dynamics in a spin ladder system. *New J. Phys.*, 13:065028, Jun 2011.

[205] S. S. Hegde and S. Vishveshwara. Majorana wave-function oscillations, fermion parity switches, and disorder in Kitaev chains. *Phys. Rev. B*, 94:115166, Sep 2016.

[206] J. Sau and E. Demler. Bound states at impurities as a probe of topological superconductivity in nanowires. *Phys. Rev. B*, 88:205402, Nov 2013.

[207] P. Neven, D. Bagrets, and A. Altland. Quasiclassical theory of disordered multi-channel Majorana quantum wires. *New Journal of Physics*, 15(5), May 2013.

[208] P. Delplace, D. Ullmo, and G. Montambaux. Zak phase and the existence of edge states in graphene. *Phys. Rev. B*, 84:195452, Nov 2011.

[209] F. D. M. Haldane and S. Raghu. Possible realization of directional optical waveguides in photonic crystals with broken time-reversal symmetry. *Phys. Rev. Lett.*, 100:013904, Jan 2008.

[210] S. Raghu and F. D. M. Haldane. Analogs of quantum-Hall-effect edge states in photonic crystals. *Phys. Rev. A*, 78:033834, Sep 2008.

[211] A. P. Slobozhanyuk, A. N. Poddubny, A. E. Miroshnichenko, P. A. Belov, and Y. S. Kivshar. Subwavelength topological edge states in optically resonant dielectric structures. *Phys. Rev. Lett.*, 114:123901, Mar 2015.

[212] E. Prodan and C. Prodan. Topological phonon modes and their role in dynamic instability of microtubules. *Phys. Rev. Lett.*, 103:248101, Dec 2009.

[213] C. L. Kane and T. C. Lubensky. Topological boundary modes in isostatic lattices. *Nat. Phys.*, 10:39, Dec 2014.

[214] V. Peano, C. Brendel, M. Schmidt, and F. Marquardt. Topological phases of sound and light. *Phys. Rev. X*, 5:031011, Jul 2015.

[215] C. Strohm, G. L. J. A. Rikken, and P. Wyder. Phenomenological evidence for the phonon Hall effect. *Phys. Rev. Lett.*, 95:155901, Oct 2005.

[216] A. V. Inyushkin and A. N. Taldenkov. On the phonon hall effect in a paramagnetic dielectric. *JETP Letters*, 86:379, Nov 2007.

[217] C. W. Peterson, W. A. Benalcazar, T. L. Hughes, and G. Bahl. A quantized microwave quadrupole insulator with topologically protected corner states. *Nature*, 555:346, Mar 2018.

[218] N. Berg, K. Joel, M. Koolyk, and E. Prodan. Topological phonon modes in filamentary structures. *Phys. Rev. E*, 83:021913, Feb 2011.

[219] S. Ryu, A. P. Schnyder, A. Furusaki, and A. W. W. Ludwig. Topological insulators and superconductors: tenfold way and dimensional hierarchy. *New J. Phys.*, 12:065010, Jun 2010.

[220] X.-L. Qi, T. L. Hughes, and S.-C. Zhang. Topological field theory of time-reversal invariant insulators. *Phys. Rev. B*, 78:195424, Nov 2008.

[221] Y. Barlas and E. Prodan. Topological classification table implemented with classical passive metamaterials. *Phys. Rev. B*, 98:094310, Sep 2018.

[222] K. Qian, D. J. Apigo, C. Prodan, Y. Barlas, and E. Prodan. Topology of the valley-Chern effect. *Phys. Rev. B*, 98:155138, Oct 2018.

[223] W. A. Benalcazar, B. A. Bernevig, and T. L. Hughes. Quantized electric multipole insulators. *Science*, 357(6346):61–66, Jul 2017.

[224] L. Dal Negro, C. J. Oton, Z. Gaburro, L. Pavesi, P. Johnson, A. Lagendijk, R. Righini, M. Colocci, and D. S. Wiersma. Light transport through the band-edge states of Fibonacci quasicrystals. *Phys. Rev. Lett.*, 90:055501, Feb 2003.

[225] L. Mingarelli and R. Barnett. Exotic vortex lattices in binary repulsive superfluids. *Phys. Rev. Lett.*, 122:045301, Jan 2019.

Appendix A

Finite-difference method

In this Appenidx, we present the details for the finite-difference method we use to solve the differential equation Eq. (5.2) for the collective modes throughout Part I of this thesis. The Sturm–Liouville equation has a general form of

$$[p(x)y']' + q(x)y = -\lambda w(x)y, \tag{A.1}$$

where the eigenvalues λ and corresponding eigenfunctions $y(x)$ are to be determined. With a small interval ε, we can approximate the differential term as

$$py'|_x = p(x)\frac{y(x+0.5\varepsilon) - y(x-0.5\varepsilon)}{\varepsilon}, \tag{A.2}$$

and hence

$$\begin{aligned}(py')'|_x &= \frac{py'|_{x+0.5\varepsilon} - py'|_{x-0.5\varepsilon}}{\varepsilon} \\ &= \frac{p(x+0.5\varepsilon)\frac{y(x+\varepsilon)-y(x)}{\varepsilon} - p(x-0.5\varepsilon)\frac{y(x)-y(x-\varepsilon)}{\varepsilon}}{\varepsilon} = \frac{p(x+0.5\varepsilon)y(x+\varepsilon)}{\varepsilon^2} - \frac{[p(x+0.5\varepsilon)+p(x-0.5\varepsilon)]y(x)}{\varepsilon^2} \\ &+ \frac{p(x-0.5\varepsilon)y(x-\varepsilon)}{\varepsilon^2}.\end{aligned} \tag{A.3}$$

If the domain is sectioned into many lattice sites with lattice spacing ε, a function f can be represented by a vector $\mathbf{f} = \{f_i\}$ such as $f_i = f(x)$ and $f_{i\pm1} = f(x \pm \varepsilon)$. We then turn Eq. (A.3) to

$$(py')'_i = \frac{p_{i+0.5}y_{i+1} - (p_{i+0.5} + p_{i-0.5})y_i + p_{i-0.5}y_{i-1}}{\varepsilon^2}. \tag{A.4}$$

Using the rule of Eq. (A.4) and treating $q(x)$ and $w(x)$ as diagonal matrices, we can turn Eq. (A.1) into a generalized eigen problem for a finite-size matrix. The accuracy can be increased by decreasing ε. By

comparing Eq. (A.1) with Eq. (5.2) multiplied by r^2, we obtain

$$p = r^2 \left[V(R) - V(r) \right], \tag{A.5}$$

$$q = -l(l+1) \left[V(R) - V(r) \right], \tag{A.6}$$

$$w = r^2, \tag{A.7}$$

$$\lambda = m\omega^2. \tag{A.8}$$

Therefore, one can calculate the collective modes by solving the generalized eigen problem for a finite matrix.

Appendix B

Evaluation of matrix elements in the perturbative approach to gravitational hydrodynamic equations

In this Appendix, we provide a detailed calculation of the matrix elements of Eq. (7.14). More precisely, to leading order in the thickness of the condensate shell, we set out to calculate

$$\langle \delta n(r,\theta,\phi)^{l}_{\nu,m}|V_g(r,\theta)|\delta n(r,\theta,\phi)^{l'}_{\nu',m'}\rangle \approx \frac{g}{S_l}\langle \delta n(\mathbf{r})^{l}_{\nu,m}|-\frac{1}{r}\sin\theta\frac{\partial}{\partial\theta}-\frac{l'(l'+1)}{r}\cos\theta|\delta n(\mathbf{r})^{l'}_{\nu',m'}\rangle. \tag{B.1}$$

To that end, we recall

$$\delta n(r,\theta,\phi)^{l}_{\nu,m}=\sqrt{\frac{\nu(\nu+1)}{2}}P_\nu\left(\frac{r-r_0}{\delta}\right)Y^{l}_{m_\ell}(\theta,\phi) \tag{B.2}$$

and, further, express the spherical harmonics as

$$Y^{l}_{m}(\theta,\phi)=(-1)^m\sqrt{\frac{2l+1}{4\pi}\frac{(l-m)!}{(l+m)!}}P^m_l(\cos\theta)e^{im\phi} \tag{B.3}$$

so that the matrix elements we are interested in require evaluating an integral over the polar and azimuthal angles and the radial coordinate. In order to evaluate the first term in Eq. (B.1) we start by evaluating the integral over ϕ as

$$\int_0^{2\pi}e^{i(m-m')\phi}d\phi=2\pi\delta_{m,m'}. \tag{B.4}$$

We proceed to utilize the differential identity

$$\sin\theta\frac{\partial}{\partial\theta}P^m_l(\cos\theta)=\frac{1}{2l+1}[l(l-m+1)P^m_{l+1}(\cos\theta)-(l+1)(l+m)P^m_{l-1}(\cos\theta)] \tag{B.5}$$

and the orthogonality relation

$$\int_{-1}^{1}P^m_k(\cos\theta)P^m_l(\cos\theta)\sin\theta d\theta=\frac{2(l+m)!}{(2l+1)(l-m)!}\delta_{k,l} \tag{B.6}$$

for the integral over θ. Furthermore, to evaluate the radial integral we carry out a change of variable $x = \frac{r-r_0}{\delta}$ and write

$$\int P_\nu\left(\frac{r-r_0}{\delta}\right) P_{\nu'}\left(\frac{r-r_0}{\delta}\right) r dr = \delta \int P_\nu(x) P_{\nu'}(x)(\delta x + r_0) dx \tag{B.7}$$

where the factor $\delta x + r_0$ can be expressed as a sum over the Legendre polynomials $P_0(x)$ and $P_1(x)$. More precisely,

$$\delta x + r_0 = \delta P_1(x) + r_0 P_0(x) \tag{B.8}$$

so that the integral in Eq. (B.7) can be evaluated by recalling that an integral of three Legendre polynomials is proportional to the square of a Wigner-j symbol

$$\int_{-1}^{1} P_k(x) P_l(x) P_m(x) dx = 2 \begin{pmatrix} k & l & m \\ 0 & 0 & 0 \end{pmatrix}^2 . \tag{B.9}$$

The Wigner-j symbol itself is related to a Clesbsh-Gordan coefficient

$$C(j_1, j_2, j_3 | m_1, m_2, -m_3) = \langle j_1 m_1, j_2 m_2 | j_3, -m_3 \rangle \tag{B.10}$$

by the definition

$$\begin{pmatrix} j_1 & j_2 & j_3 \\ m_1 & m_2 & m_3 \end{pmatrix} = \frac{(-1)^{j_1 - j_2 - m_3}}{(2j_3+1)^{1/2}} C(j_1, j_2, j_3 | m_1, m_2, -m_3). \tag{B.11}$$

We can therefore evaluate the integral in Eq. (B.7) as

$$\int P_\nu(x)(\delta x + r_0) P_{\nu'}(x) dx = \frac{2r_0}{2\nu+1} \delta_{\nu,\nu'} + 2\delta \begin{pmatrix} \nu & 1 & \nu' \\ 0 & 0 & 0 \end{pmatrix}^2 \tag{B.12}$$

Combining Eqs. (B.5), (B.7), (B.8), and (B.12), we then obtain, to leading order in c^{-1},

$$\begin{aligned} &\langle \delta n(\mathbf{r})^l_{\nu,m} | \frac{g}{r S_l} \sin\theta \frac{\partial}{\partial \theta} | \delta n(\mathbf{r})^{l'}_{\nu',m'} \rangle \approx \frac{g\delta r_0}{S_l} \frac{\nu(\nu+1)}{2\nu+1} \sqrt{\frac{(l'-m)!(l+m)!}{(2l+1)(2l'+1)(l'+m)!(l-m)!}} \\ &\times \left[(l'+1)(l'+m)\delta_{l,l-1} - l'(l-m+1)\delta_{l,l'+1} \right]. \end{aligned} \tag{B.13}$$

We move on to calculate the second term in Eq. (B.1). First, we note that the integral over the azimuthal

angle is equal to $2\pi\delta_{m,m'}$ as above. We then use the recursive identity

$$xP_m^l(x) = \frac{l-m+1}{2l+1}P_{l+1}^m(x) + \frac{l+m}{2l+1}P_{l-1}^m(x) \tag{B.14}$$

in order to evaluate the integral over the polar angle

$$\int P_l^m(\cos\theta)P_m^{l'}(\cos\theta)\cos\theta\sin\theta d\theta \tag{B.15}$$

by again using the orthogonality relation of Eq. (B.6). We conclude that the total angular contribution to this term reads

$$\int Y_m^{l'*}(\theta,\phi)Y_m^l(\theta,\phi)\cos\theta\sin\theta d\theta d\phi = -\sqrt{\frac{(l+m)!(l'-m)!}{(2l+1)(2l'+1)(l-m)!(l'+m)!}} \times \left[(l'-m+1)\delta_{l,l'+1} + (l'+m)\delta_{l,l'-1}\right], \tag{B.16}$$

while the radial contribution is given by Eq. (B.12). The total contribution of this term is then equal to

$$\begin{aligned}\langle\delta n(\mathbf{r})_{\nu,m}^l|\frac{gl'(l'+1)}{rS_l}\cos\theta\frac{\partial}{\partial\theta}|\delta n(\mathbf{r})_{\nu',m'}^{l'}\rangle &\approx \frac{-g\delta r_0}{S_l}\frac{\nu(\nu+1)}{2\nu+1}\sqrt{\frac{(l'-m)!(l+m)!}{(2l+1)(2l'+1)(l-m)!(l'+m)!}} \\ \times[l'(l'+1)(l'-m+1)\delta_{l,l'+1} + l'(l'+1)(l'+1)\delta_{l,l'-1}]&.\end{aligned} \tag{B.17}$$

We conclude that to leading order in c^{-1}, or equivalently the shell thickness δ, the matrix element of Eq. (B.1) reads

$$\begin{aligned}\langle\delta n(\mathbf{r})_{\nu,m}^l|V_g(r,\theta)|\delta n(\mathbf{r})_{\nu',m'}^{l'}\rangle &\approx \frac{g\delta r_0}{S_l}\frac{\nu(\nu+1)}{2\nu+1}\sqrt{\frac{(l'-m)!(l+m)!}{(2l+1)(2l'+1)(l-m)!(l'+m)!}} \\ \times\left[l'(l'-m+1)(l'+2)\delta_{l,l'+1} + (l'+m)(l'^2-1)\delta_{l,l'-1}\right]&.\end{aligned} \tag{B.18}$$

Appendix C

Conformal Projection and GPE on 2D Spherical Shells

In this Appendix we outline the setup for numerically solving the GP equation on a two-dimensional shell of radius R used in Ch. 8. In spherical polar coordinates, this equation reads

$$-\frac{\hbar^2}{2m}\frac{1}{R^2\sin^2\theta}\left[\left(\sin\theta\frac{\partial}{\partial\theta}\right)^2+\frac{\partial^2}{\partial\phi^2}\right]\psi+U|\psi|^2\psi=\mu\psi. \tag{C.1}$$

Since the azimuthal angle ϕ is not defined at the two poles, $\theta=0$ and $\theta=\pi$, numerical solutions of Eq. (C.1) generally diverge at these points. This divergence can be avoided by using Cartesian coordinates on a flat plane. To that end, we take a conformal projection of the North hemisphere, $0\leq\theta\neq\pi/2$ onto a flat unit disk $D:0\leq\rho\leq1$ by defining $\rho=\tan(\theta/2)$. The Laplacian operator can then be written in terms of Cartesian coordinates $(x,y)=(\rho\cos\phi,\rho\sin\phi)$ and the GP equation of Eq. (C.1) becomes

$$-\left(\frac{\partial^2}{\partial x^2}\right)\psi+\omega(x,y)\tilde{U}|\psi|^2\psi=\omega(x,y)\tilde{\mu}\psi \tag{C.2}$$

where $\tilde{U}=2mR^2U/\hbar^2$, $\tilde{\mu}=2mR^2\mu/\hbar^2$ and $\omega(x,y)=4/(x^2+y^2+1)^2$. This expression is a generalized eigenvalue problem of the Sturm-Liouville form with the orthonormal condition

$$\int_D\psi_i^*\psi_j\omega(x,y)dxdy=\delta_{ij} \tag{C.3}$$

for δ_{ij} the Kronecker delta function. Now, the energy of the condensate shell can be calculated by evaluating

$$\tilde{E}=\int_D\left[\left|\frac{\partial\psi}{\partial x}\right|^2+\left|\frac{\partial\psi}{\partial y}\right|^2+\omega(x,y)\frac{\tilde{U}}{2}|\psi|^4\right] \tag{C.4}$$

and if the condensate shell is rotating, since the rotational term $-\Omega L_z$ does not change through the conformal transformation, the GP equation we numerically solve in Secs. 8.2.2 and 8.3.2 finally reads

$$-\left(\frac{\partial^2}{\partial x^2}+\frac{\partial^2}{\partial y^2}\right)\psi+w(x,y)\tilde{U}|\psi|^2\psi+i\omega(x,y)\tilde{\Omega}\left(x\frac{\partial}{\partial y}-y\frac{\partial}{\partial x}\right)\psi=\omega(x,y)\tilde{\mu}\psi \tag{C.5}$$

where the rotation rate of the shell has been rescaled as $\tilde{\Omega} = 2mR^2\Omega/\hbar$.

Appendix D

Coolest Physics You've Ever Heard Off

This Appendix contains a re-print of a popular science article the author of this thesis has written for the Scientific American Opinions blog. It was originally published on January 20th, 2020.

When it comes to furthering our overall understanding of the physical world, ultracold quantum gases are awfully promising. As the famous physicist Richard Feynman argued, to fully understand nature, we need quantum means of simulation and computation. Ultracold atomic systems have, in the last 30 years, proven to be amazing quantum simulators. The number of applications for these systems as such simulators is nothing short of overwhelming, ranging from engineering artificial crystals to providing new platforms for quantum computing. In its brief history, ultracold atomic experimental research has enhanced physicists understanding of a truly vast array of important phenomena.

One of the revelations of quantum mechanics is that any object can be seen as a wave (even you!) when an appropriate experimental test is used. Properties of these co-called matter waves depend on their temperature; at large temperatures they have short wavelengths and look and behave particlelike because all the peaks and valleys are so close together that they cannot be told apart. If we lower temperature to much less than a single kelvin, the wave nature of matter becomes more pronounced and wavelike behaviors more important. What happens then with a large collection of very cold atoms that behave like a large collection of waves? They can all align and overlap to form a single wave, something that was historically called a macroscopic wave function. Such a systema condensate in physics parlanceis a fundamentally quantum state of matter.

Quantum condensates were theoretically predicted in the mid-1920s, but it was only in the late 1990s that experimental physicists kicked off a revolution (recognized by two Nobel prizes) by using lasers and magnets to reach sufficiently low temperatures for the transition to these phases of matter to happen. Light can interact with atoms and thus change their energies. Atoms also experience forces when placed in nonuniform magnetic fields. Physicists used these two properties to trap clouds of atoms such as rubidium and eventually lower their temperature to picokelvinstrillionths of a degree above absolute zero. Remarkably,

experiments in which these extremely low temperatures can be reached, and quantum states of matter are engineered, fit in an average-sized room, on a large table with the ultracold atom gas frequently visible to the naked eye. The coldest places in the universe can often be found in a room on your local college campus, and they are likely controlled by a graduate student.

But its not just making something the coldest or the most quantum that excites physicists; its that ultracold atoms can be controlled and manipulated very precisely. Theoretical physicists have been especially emboldened by the possibility of engineering a quantum system by moving ultracold atoms around and fine-tuning the way in which they interact. To a theorist, a physical system such as a novel material that has some odd or unexpected property, is a frustrating black box that is hard to describe with mathematical equations.

An ultracold atomic experiment can be the exact opposite, bringing equations to life and determining whether they measure up to nature. Many minimal, prototypical models, extensively studied at the level of mathematical equations but not necessarily matched by any naturally found material, can be engineered in ultracold atomic experiments. Since the late 1990s, physicists of all sorts have embraced this idea and pushed it in every direction they could imagine.

As one example, adding counterpropagating laser beams to an ultracold atomic sample creates an optical lattice and turns the system into an artificial crystal. While a physical crystal has to be grown carefully, an ultracold artificial crystal can be changed from one shape to another by adjusting laser beams. Even more advantageously, such artificial crystals are typically very clean, and researchers can add in disorder by using more lasers. This means they can reverse engineer some of the effects of disorder. If a crystal is grown and then studied, it can be difficult to determine how much dirt in that sample actually matters for experimental outcomes. If researchers can control the disorder, then they can be very precise about determining its consequences.

From the very first ultracold atomic experiments, they have been really important for studying fluids having zero viscosity or superfluids. When does a normal fluid become a superfluid? Can something similar to sound propagate through a superfluid? What happens if a container of superfluid is rotated? Many such fundamental questions have been answered through simulations with ultracold atoms.

For instance, rotating a superfluid has been predicted to give rise to appearance of vorticessmall hurricanes of quantum fluidas a consequence of basic properties of the macroscopic wave function. Researchers are learning about quantum turbulence by observing and manipulating these vortices, thinking of them as controllable building blocks of more chaotic superfluid flows. Precise models for turbulent quantum flows have historically eluded theorists, which makes ultracold atomic simulations the first line of attack for this

difficult problem.

As with studies of superfluids, many efforts have been made to simulate superconductors. They are perfect conductors having no resistance; no energy is wasted as electric current runs through them. As this is in contrast with all conductors used to supply electricity to businesses and households, it is a very active area of research to try and simulate a superconductor that does not have to be very cold. While a physicists notion of very cold may not quite match the colloquial use of the phrase (a cold atom in physics jargon is millions of times colder than a cold pint of ice cream in your fridge), even a few kelvin worth of difference could be meaningful for applications of superconductors outside the lab.

Theoretical physicists have debated various high-temperature superconducting models for years, and ultracold atomic studies have been one of the prime ways to put those, sometimes conflicting, theories to test. Experimental physicists can also make a superfluid of ultracold atoms become something like a superconductor in a process called BEC-BCS crossover. This crossover has been theorized in semiconductors and neutron stars but never unequivocally confirmed in any system other than ones consisting of ultracold atoms.

Superconductors and superfluids are both fundamentally quantum phases of matter, making up something like a quantum expansion of the liquid-solid-vapor list of phases you may have learned in school. Ultracold atomic experiments continue to simulate even more novel quantum phases of matter. One striking example from 2019 is simulation of a quantum supersolid. A supersolid, like a superfluid, flows without any friction between the atoms that make it up, but also has a periodic, crystal-like structure like solids do. It is a seemingly paradoxical state of matter whose existence was debated for almost 50 years before ultracold atomic experiments provided a definitively affirmative conclusion.

Many so-called topological phases of matter have also been realized in ultracold systems. Some of these experiments simulate, and generalize, the quantum hall effect, which was first observed in more traditional experiments with semiconductors. Since many topological states of matter have properties unaffected by disorder, they are a very promising setting for quantum computation. In this way, realizing topological models in very tunable ultracold atomic system means that physicists are not only able to simulate a new phase of matter but also immediately put it to use, getting closer to making a quantum computer.

Even if ultracold atomic systems have not been turned into quantum computation machines just yet, they can often be used to beat classical supercomputers in terms of enabling researchers to learn something new about fundamental physics. One example is that of many-body physics. In quantum mechanics, a system that has more than a few interacting particles is almost always a system where it is very difficult to calculate, and therefore predict, anything precisely. However, real materials consist of millions of atoms!

Ultracold atomic systems have been invaluable for studying highly interacting many-body systems, uncovering phenomena such as systems failing to reach thermal equilibrium and never losing memory of their initial state. Physicists often resort to computational methods and supercomputers in order to study these systems, but a simulation with ultracold atoms can be a more direct way to attack some of their questions. Failure to equilibrate is of great interest in statistical physics, and the advent of ultracold atomic experiments has reinforced it as a very active field of contemporary physics research.

As for me personally, despite being trained in the broader discipline of condensed matter physics, I spent my six years as a graduate student coming back to ultracold atoms over and over again. Mostly, I have been studying superfluid bubbles (hollow shells) made of ultracold atoms. This led me to the work of NASA scientists who launched an ultracold atom experiment into space to explore how it will be affected by extremely low gravity. This experiment is still ongoing aboard the International Space Station, and theorists like me who made predictions about what it will find are anxiously awaiting results.

In a way, it is fitting that studying hollow ultracold shells ended up having me think about space, as part of the motivation for this research lies with neutron stars. Physicists dont really know what you would find if you could observe the inside of neutron star, but many theories suggest that it looks like an onion with layers of superconductors and superfluids. Studying superfluid shells in laboratories could then lead to a better understanding of some of these layers that reside in stars that are so far away that scientists may never be able to study them directly. Moreover, measurements of radio signals coming from neutron stars suggest that superfluid vortices within them may affect their rotation.

Ultracold atomic experiments have excelled in studying exactly those vortices with great precision. In the past few years, I have been working on mathematical arguments for what a vortex in a hollow shell of ultracold atoms might do if the whole thing started rotating. I have badgered a fair number of my experimental colleagues with questions about engineering such a system in their labs, and the fact that this is even something we can talk about, some semblance of simulating the quantum innards of a neutron star, still seems to me a little bit like science fiction.

My latest ultracold obsession came when I learned about quasiperiodicity in one-dimensional chains of ultracold atoms. The puzzle hiding behind the jargon is simple: physicists know well how structures of atoms in which they repeat with a regular period behave in nature, but what happens if that period is an irrational number? Such systems are called quasiperiodic, and studying them led Douglas Hofstadter in 1976 to discover a famous fractal plot latter dubbed as his butterfly. Hofstadters plot is self-similar: if you zoom in or zoom out any amount, it still looks the same.

This property implies that physical states having fractional dimensions can exist in nature, a revelation

that jump-started a search for more physical systems where that can happen. Two years ago, another graduate student mentioned to me that they had simulated a quasiperiodic system in their ultracold atomic research lab, and I too have not stopped chasing the Hofstadter butterfly since. Why would nature care about the difference between rational and irrational numbers so much as to allow for fractional dimensions to be more than a mathematical oddity? Ultracold atomic studies are likely to help physicists answer that question, and I hope to be around to hear about them.

My experience as a researcher has included only a sliver of many topics in modern physics for which ultracold atomic experiments are meaningful. The possibilities are truly numerous. And the quantum simulation revolution is nowhere near over! Researchers continue to push the limits of existing technology to cool gases made up of more elements, and execute more manipulations.

Next steps? Quantum chemistry, where molecules form at ultracold temperatures. Ultracold quantum systems that are so large they cannot be called microscopic despite quantum mechanics always being assumed to only describe the smallest of objects. Ultracold systems that can be used to measure fundamental constants in tabletop experiments instead of large accelerators (like the Large Hadron Collider). Ultracold experiments where a single atom can be poked, prodded, moved around and imaged. And whatever else can give us a window into the fundamentals of our (quantum) world.